



**HAL**  
open science

# Multi-scale investigation and analysis of the friction behavior and wear in the manufacturing of the woven composite reinforcements

Yu Wang

► **To cite this version:**

Yu Wang. Multi-scale investigation and analysis of the friction behavior and wear in the manufacturing of the woven composite reinforcements. Mechanics of materials [physics.class-ph]. Université de Haute Alsace - Mulhouse; Université de Tianjin, 2024. English. NNT : 2024MULH7126 . tel-04799067

**HAL Id: tel-04799067**

**<https://theses.hal.science/tel-04799067v1>**

Submitted on 22 Nov 2024

**HAL** is a multi-disciplinary open access archive for the deposit and dissemination of scientific research documents, whether they are published or not. The documents may come from teaching and research institutions in France or abroad, or from public or private research centers.

L'archive ouverte pluridisciplinaire **HAL**, est destinée au dépôt et à la diffusion de documents scientifiques de niveau recherche, publiés ou non, émanant des établissements d'enseignement et de recherche français ou étrangers, des laboratoires publics ou privés.

## UNIVERSITÉ DE HAUTE-ALSACE

UNIVERSITÉ DE STRASBOURG

**THESE**

Pour l'obtention du grade de

**DOCTEUR DE L'UNIVERSITÉ DE HAUTE-ALSACE****ECOLE DOCTORALE : Mathématiques, Sciences de l'Information et de l'Ingénieur (ED 269)**

Discipline : Mécanique

Présentée et soutenue publiquement

par

**Yu WANG**

Le 27 September 2024

---

**Multi-scale investigation and analysis of the friction behavior and wear  
in the manufacturing of the woven composite reinforcements**

---

Sous la direction des Prof. Peng WANG et Prof. Yanan JIAO

## Jury:

Prof. Olga Klinkova	Institut supérieur de mécanique de Paris, France	Rapporteure
Prof. Huaiwen Wang	Tianjin University of Commerce, China	Rapporteur
Prof. Nahiene Hamila	Institut de Recherche Dupuy de Lôme, France	Examineur
Prof. Chung-Hae Park	IMT Nord Europe, France	Examineur
Prof. Ying Sun	Tiangong University, China	Examinatrice
Prof. Libo Yan	Technische Universität Braunschweig, Germany	Invité
Prof. Peng Wang	Université de Haute-Alsace, France	Directeur de thèse
Prof. Yanan Jiao	Tiangong University, China	co-Directrice de thèse

# ACKNOWLEDGEMENTS

Maybe “Congratulations!” was the best word what I want when I was a first-year PhD student. At that time, I was very worried that I would not be able to graduate. No one can imagine what I went through. To be honest, I have been a lot, which teach me a lot. Only then I can be who I am now. Hence, I first want to appreciate myself. Also, I will appreciate everyone who help me a lot.

## **For supervisors,**

Appreciating Prof. Peng Wang and Prof. Yanan Jiao for giving me opportunity to study in France, Germany, which broaden my horizons. They teach how to be a researcher and conduct research. Besides, they also provide patient guidance and supervision throughout my PhD research and encouraged to try new ideas. The guidance, encourage and vision inspire me step further. Also, thanks to Prof. Libo Yan for guidance, care and suggestions during the exchange in Germany.

## **For families,**

Appreciating my parents for supporting and encouraging whatever in finance and spirit during my PhD. Also, I would like to thank my girlfriend for her companionship, care, and help. The period that we solve problems together cannot be forgot.

## **For colleagues and friends,**

Appreciating my colleagues and friends for help in research and life, including Associate Prof. Gilles Arnold, Prof. Michel Tournalias, Sascha Krugl, Théo Perrin, Benoit Schrab, Aurélie Decker, Tannaz Girard Tavakoli, Jinlei Li, Jian Hu, Jingshu Lu, Mengqing He et al. in France and Wenzhuo Ma, Haoze Chen, Ali Nemati Giv, Si Chen, Xueying Zhao et al. in Germany and Assistant Professor. Mengru Li, Associate Prof. Shenglei Xiao in China.

Last but not least, I don't worry about graduation, as what I wanted, I'm getting closer to “Congratulations!”. However, the new problem of future will need to be worried. Like I am back at the beginning again. So, maybe it is my life route, however, it is mine how can it not be the most? This is the end of my doctorate, but also a new beginning in my life. At such a crossroads where time and space meet, I will say to my future, be brave, you can do it! Finally, I will put my motto here, “日拱一卒 (One step forward every day)”.

## Abstract

In the manufacturing process of textile reinforcements, friction between twisted yarns is a critical factor that significantly influences the mechanical properties of fiber-reinforced composites. Excessive friction can deteriorate these properties. This study develops a comprehensive analytical framework to understand the friction behavior in the manufacturing of textile reinforcements, a key determinant in the mechanical integrity of fiber-reinforced composites. A novel analytical model based on Hertzian contact theory is introduced to depict the interaction between twisted yarns. This model accounts for the micro-meso scale contact dynamics influenced by the contact angle and orientation of fibers due to twisting. Experimental validations confirm the model's efficacy, offering a detailed characterization of yarn/yarn friction under various conditions like orthogonal and non-orthogonal contacts and differing twist levels and directions. This insight is pivotal for optimizing the textile preform forming process and subsequently enhancing the mechanical properties composites.

Further, friction properties under different fabric architectures and yarn pre-tensions were explored using a novel micro-meso theoretical model based on Peirce's geometrical model. The study revealed that yarn pre-tensions, a critical parameter, increased friction force across all fabric architectures, directly affecting yarn friction performance. This theoretical model also predicted friction properties during 3D fabric manufacturing, showing that fabric architecture significantly influences friction behavior, dependent on yarn dimensions and preform parameters such as layer number, thickness, and binding pattern.

Additionally, an innovative modeling approach for predicting yarn friction and wear behavior was introduced, incorporating both geometric and mechanical components. A yarn model, considering fiber damage behavior based on the Timoshenko beam principle and Ductile Criterion, was developed to explore friction and wear during reinforcement manufacturing. The model effectively addresses penetration problems through self-coding and was validated by experimental results and micro-CT imaging, confirming its accuracy. This method provides valuable insights into the mechanical response of yarns during reinforcement manufacturing, allowing for an in-depth understanding of the effect of yarn geometrical and mechanical parameters on friction and wear behavior.

Collectively, these integrated models provide a robust framework for predicting and managing friction in yarn interactions during textile reinforcement manufacturing, which is crucial for enhancing the quality and performance of fiber-reinforced composites. In the future, the model can be improved constantly to characterize the friction behavior of composite forming. And be employed to optimize the manufacturing process for promoting longer product lifespans and reduced waste.

## Résumé

Dans le processus de fabrication des renforcements textiles, le frottement entre les fils tordu est un facteur critique qui influence de manière significative les propriétés mécaniques des composites renforcés par des fibres. La friction excessive peut détériorer ces propriétés. Cette étude développe un cadre analytique complet pour comprendre le comportement de friction dans la fabrication des renforts textiles, un déterminant clé de l'intégrité mécanique des composites renforcés par des fibres. Un nouveau modèle analytique basé sur la théorie du contact de Hertz est présenté pour décrire l'interaction entre les fils tordues. Ce modèle explique la dynamique de contact de l'échelle micro-meso influencée par l'angle de contact et l'orientation des fibres due à la torsion. Des validations expérimentales confirment l'efficacité du modèle, offrant une caractérisation détaillée de la friction de fil et de fil dans diverses conditions telles que les contacts orthogonaux et non orthogonaux et les différents niveaux et directions de twist. Cette compréhension est essentielle pour optimiser le processus de préformage du textile et améliorer par la suite les propriétés mécaniques du composite.

En outre, les propriétés de friction sous différentes architectures de tissu et les pré-tension de fil ont été explorées en utilisant un nouveau modèle théorique de micro-meso basé sur le modèle géométrique de Peirce. L'étude a révélé que la pré-tension du fil, un paramètre critique, augmentait la force de friction dans toutes les architectures de tissu, affectant directement les performances de la friction du fil. Ce modèle théorique a également prédit les propriétés de friction lors de la fabrication de tissus 3D, montrant que l'architecture du tissu influence considérablement le comportement de la friction, en fonction des dimensions du fil et des paramètres de préforme tels que le nombre de couches, l'épaisseur et le motif de liaison.

En outre, une méthode de modélisation innovante pour prédire la friction et l'usure du fil a été introduite, incorporant à la fois des composants géométriques et mécaniques. Un modèle de fil, en tenant compte du comportement des dommages des fibres basé sur le principe du faisceau de Timoshenko et le critère ductile, a été développé pour étudier la friction et l'usure pendant la fabrication de renforts. Le modèle s'attaque efficacement aux problèmes de pénétration grâce à l'auto-codage et a été validé par des résultats expérimentaux et une micro-CT, confirmant son exactitude. Cette méthode fournit des informations précieuses sur la réponse mécanique des fils lors de la fabrication de renforts, permettant une compréhension approfondie de l'effet des paramètres géométriques et mécaniques des fils sur le comportement de friction et d'usure.

Ensemble, ces modèles intégrés fournissent un cadre solide pour prédire et gérer les frictions dans les interactions de filetage lors de la fabrication du renforcement textile, essentiel pour améliorer la qualité et les performances des composites renforcés par les fibres. Ensuite, le modèle peut être constamment

amélioré pour caractériser le comportement de friction de la formation composite. Et être employé pour optimiser le processus de fabrication pour promouvoir des durées de vie plus longues des produits et réduire les déchets.

# CONTENTS

ACKNOWLEDGEMENTS .....	I
Abstract.....	II
Résumé .....	III
CONTENTS .....	V
<b>Chapter 1 Literature review</b> .....	1
1.1 Introduction to the textile composites .....	5
1.1.1 The composites and their application .....	5
1.1.2 The textile reinforcements of composites .....	6
1.2 Mechanical behavior during the weaving process .....	9
1.3 Friction behavior between yarns/fibers .....	12
1.3.1 Friction research statue .....	12
1.3.2 Friction test methods .....	12
1.3.3 Friction influence factors .....	20
1.3.4 Friction analytical models .....	24
1.4 Modeling and simulation of woven reinforcement.....	28
1.4.1 Modeling and simulation at micro-scale.....	28
1.4.2 Modeling and simulation at meso scale.....	32
1.4.3 Modeling and simulation at macro-scale.....	37
1.5 Summary of Chapter 1 .....	40
<b>Chapter 2 Yarn to Yarn Friction Analysis Considering the Weaving Process of Textile Fabrics at micro-meso scale</b> .....	42
2.1 Introduction.....	46
2.2 A modified contact model of single non-twisted yarn.....	48
2.2.1 Modified model based on Hertz contact principle.....	48
2.2.2 Experiment research for contact behavior .....	50
2.3 A modified analytical model of friction for single twisted yarn .....	53
2.3.1 Fiber scale modeling .....	56
2.3.2 Yarn scale modeling.....	58
2.3.3 Materials and Experiment .....	61
2.4 Results and discussion .....	63
2.4.1 Consistency analysis .....	63
2.4.2 Friction behavior between the yarns with the same twist level and the same twist direction ...	67

2.4.3 Friction behavior between the yarns with a different twist level and the same twist direction .	68
2.4.4 Friction behavior between the yarns with a different twist level and a different twist direction	70
2.5 Summary of Chapter 2 .....	71
<b>Chapter 3 Yarn-to-yarn friction behavior during the manufacturing of woven fabrics at meso-macro scale .....</b>	<b>74</b>
3.1 Introduction.....	78
3.2 Methodology .....	81
3.2.1 Materials and samples manufacturing .....	81
3.2.2 Experiment setup and procedure .....	82
3.2.3 Micro-meso theoretical model.....	84
3.3 Significance of configuration on friction behavior based on pre-tension .....	90
3.3.1 Influence of S-cell reinforcement configuration.....	90
3.3.2 Influence of D-cell reinforcement configuration .....	92
3.4 Comparison Analysis of the friction behavior .....	93
3.5 Approximate solution of friction behavior based on micro-meso analytical model .....	95
3.5.1 Theoretical examples for 2D configurations .....	95
3.5.2 Theoretical examples for 3D configurations orthogonal .....	96
3.6 Summary of Chapter 3 .....	100
<b>Chapter 4 Numerical simulation and experimental validation of yarn/yarn friction considering fiber damage and wear prediction .....</b>	<b>101</b>
4.1 Introduction.....	105
4.2 Simulation investigations .....	107
4.2.1 Fundamental theory.....	107
4.2.2 Virtual Fiber Method.....	108
4.2.3 Constitutive law .....	109
4.2.4 Geometric description of virtual yarn.....	112
4.2.5 Solution to inter penetration problem.....	114
4.3 Experimental investigations .....	116
4.3.1 Materials preparation .....	116
4.3.2 In situ Micro-CT scanning .....	117
4.3.3 Friction test .....	117
4.4 Consistency Analysis .....	118
4.4.1 Geometric verification .....	118
4.4.2 Mechanical verification.....	120
4.5 Effect of coupling factors on friction behavior.....	122



4.5.1 Normal load .....	122
4.5.2 Pretension.....	123
4.6 Damage behavior prediction .....	125
4.7 Summary of Chapter 4 .....	128
<b>Chapter 5 Conclusions and Perspectives.....</b>	<b>130</b>
5.1 Conclusions.....	131
5.2 Perspectives .....	132
References .....	134

# LIST OF FIGURES

## Chapter 1 Literature review

Fig. 1. 1. Multi-domain properties of composite materials. ....	6
Fig. 1. 2. Classification of textile composites. ....	8
Fig. 1. 3. Representative 2D weave textile. ....	8
Fig. 1. 4. Representative 3D weave textile. ....	9
Fig. 1. 5. Technical path of research .....	12
Fig. 1. 6. Research progress of friction methods during textile composites forming for yarns in recent 10 years: (a) published items and citations in each year; (b) key publications of friction methods during textile composites forming for yarns [obtained from the Web of Science Core Collection with the following keywords: friction methods, yarn and fiber (updated on 25/03/2024)] .....	14
Fig. 1. 7. (a) Schematic diagram of testing method for fiber frictional properties [65]; (b) capstan method for yarns [72]; (c) wear-resistant device schematic [63]; (d) schematic of three angles of wrap; (e) classification of friction according to directions [96]; (f) l-l friction principle [63]; (g) l-t friction principle [97]; (h) t-t friction principle [96]; (i) fixture on machine; (j) schematic diagram of key dimensions of lower fixture; (k) effects of inter-yarn angle on yarn friction [63]; (l) figure of the upper and lower fixture; (m) average cyclic curve of friction coefficient versus angular position for SM single fiber friction with different oscillation frequencies [95]; (n) effect of friction velocity on friction coefficient of carbon yarns; (o) Schematic description of friction experiment between fibers [98]; (p) friction force as a function of pre-tension load [98]; (q) Influence of the normal load on the average cycle in terms of normal force [75]; (r) photograph of experimental rig mounted on friction tester. ....	19
Fig. 1. 8. Basic concepts of the digital element method. (a) Virtual fiber (b) Contact relationship [118].	29
Fig. 1. 9. Different microscopic models based on DEA. (a) Huang’s model[113] (b) Döbrich’s model[115].....	29
Fig. 1. 10. Diagram of virtual fiber of truss element (a) Daelemans’ method[119] (b) Ying’s method[120]. ....	30
Fig. 1. 11. Different microscopic models based on truss element. (a) Daelemans’ model[119] (b) Ying’s model[120].....	30
Fig. 1. 12. The virtual fiber models of (a) non-crimp fabric[127] and (b) weft knitted fabric[128]. ....	31
Fig. 1. 13. The simulation results of 3D fabric meso-geometry by different geometric methods. (a) Stig’s model[136] (b) Wendling’s model[137] (c) Wintiba’s model [138] (d) Nilakantan’s method [139](e) Pierreux’s model[140]. ....	34
Fig. 1. 14. (a)3D reconstruction of the six layer dry preform[147]; (b) 3D tomography reconstruction of orthogonal non-crimp woven fabric image[144].....	36
Fig. 1. 15. The different reconstruction results of 3D fabric using micro-CT. (a) Naouar’s model[144] (b) Straumit’s model[148] (c) Huang’s model[149] (d) Wijaya’s model [150] (e) Wintiba’s model[152] (f) Ricks’s model [153].....	37
Fig. 1. 16. Height node hexahedral finite element containing fibrous yarns (a) Initial and deformed, (b) Simulation of hemisphere formability and (c) Forming of a twisted plate[155].....	39
Fig. 1. 17. (a) DKT6 plate finite element, (b) corresponding prismatic element[159].....	39
Fig. 1. 18. Influence of shear angle on the onset of wrinkling using the second gradient model[169]. ....	40
<b>Chapter 2 Yarn to Yarn Friction Analysis Considering the Weaving Process of Textile Fabrics at microscale</b>	
Fig. 2. 1. Evidence of damage on fibers during weaving[59,172]. ....	46
Fig. 2. 2. Experimental figures: (a) schematic of the experimental fig; (b) schematic of yarns mesoscopic contact; (c) schematic drawing of yarns mesoscopic contact .....	51

Fig. 2. 3. Experimental method for extracting fiber contact surface.....	51
Fig. 2. 4. Contact analysis method .....	52
Fig. 2. 5. Schematic of contact fiber track.....	53
Fig. 2. 6. Schematic diagrams of non-orthogonal contact between twisted yarns: (a) three-dimensional diagram, (b) top viewpoint diagram. (Notes: <b>S</b> means the direction from the upper left to the lower right; <b>Z</b> means the direction from the upper right to the lower left) .....	55
Fig. 2. 7. A diagram of angle analysis during the contact phase of twisted yarns: (a) S-S or Z-Z, (b) S-Z or Z-S.....	56
Fig. 2. 8. Enlarged view of the arrangement to arrive at the relationship: (a) a deformation description under the normal load $F\cos\theta$ and (b) a schema of fiber arrangements (based on the viewpoint in Fig. 2. 6). .....	58
Fig. 2. 9. The description of dimensional parameters during the friction process based on Fig. 2. 10. ....	60
Fig. 2. 10. Kinematic description of the yarn friction process which includes three characteristic locations where force and contact situation are shown.....	60
Fig. 2. 11. A picture of the tribometer dedicated to twisted yarn-yarn friction tests.....	62
Fig. 2. 12. Schematic diagram of one cycle for the friction test. ....	62
Fig. 2. 13. Hertz model, modified model and experiment contact area under different (a) contact angle and (b) pre-tension.....	65
Fig. 2. 14. Comparison of the analytical and experimental results on friction force by different tests mentioned in Table 2. 3 (average of five measurements): (a) one cycle of friction, (b) sliding distance versus velocity curve and (c) average error of friction force in the characteristic area.....	66
Fig. 2. 15. The realistic contact area of yarn $A_{r/yarn}$ of a typical friction cycle with the same twist (horizontal comparison: same color in three figures; vertical comparison: three colors in one figure). ....	67
Fig. 2. 16. A typical friction cycle with the same twist: (a-c) friction force and (d-f) <i>COF</i> . (Note: Friction condition for test 4 was employed to analyze). ....	68
Fig. 2. 17. The realistic contact area of yarn $A_{r/yarn}$ of a typical friction cycle with the different twist levels. ....	69
Fig. 2. 18. A typical friction cycle with the different twist levels: (a-c) friction force and (d-f) <i>COF</i> . (Note: Friction condition for test 4 was employed to analyze).....	70
Fig. 2. 19. The realistic contact area of yarn $A_{r/yarn}$ of a typical friction cycle with the different twist directions. ....	71
Fig. 2. 20. A typical friction cycle with the different twist directions: (a-c) friction force and (d-f) <i>COF</i> . (Note: Friction condition for test 4 was employed to analyze).....	71
<b>Chapter 3 Yarn-to-yarn friction behavior during the manufacturing of woven fabrics at mesoscale</b>	
Fig. 3. 1. Multi-scale preparation description of composites: (a) overview of multi-scale; (b) schematic of the weaving process. ....	80
Fig. 3. 2. Friction device with yarn pre-tension dedicated to the beating-up friction test.....	83
Fig. 3. 3. Schematic diagram of one cycle for the friction test. ....	84
Fig. 3. 4. Overview of the contact types between yarns in different fabric architectures: (a) representative architectures and (b) contact types. ....	85
Fig. 3. 5. Geometric diagram of one interweaving point: (a) contact mode type 1, (b) contact mode type 2 and (c) top view for the contact zone. ....	89
Fig. 3. 6. The key parameters of contact zone from (a) cross-section view of warp yarn and (b) cross-section view of weft yarn. ....	90
Fig. 3. 7. Single cell of representation reinforcement based on the actual weaving process: (a) plain (b) satin and (c) twill. ....	91

Fig. 3. 8. Influence of Friction behavior as a function on pre-tension: (a)-(c) $F_f$ vs LVDT and (a')-(c') experimental observation. ....	92
Fig. 3. 9. Double cell of representation reinforcement based on the actual weaving process: (a) plain (b) satin and (c) twill. ....	92
Fig. 3. 10. The friction forces of D-cell of representation configurations under different pre-tension. ....	93
Fig. 3. 11. Comparison of the theoretical and experimental results on friction force under different configurations. ....	94
Fig. 3. 12. Predicted trend in $COF$ with different S-cell configurations under different pre-tension: (a) plain (b) satin and (c) twill. ....	96
Fig. 3. 13. Schematic diagram of representative 3D fabric architectures (a & b) and weft cross-section (a' & b'): (a) LTL Stru 5-3 (b) A-L Stru 5-3 (c) and (d) Orth. 5-3. ....	97
Fig. 3. 14. Predicted contact area (a) and $COF$ (b) of representative 3D configurations. ....	99
<b>Chapter 4 Numerical simulation and experimental validation of yarn/yarn friction considering fiber damage and wear prediction</b>	
Fig. 4. 1. Typical stress-strain curve of yarn tensile behavior. ....	109
Fig. 4. 2. Flowchart of calling VUMAT in Abaqus as implemented. ....	112
Fig. 4. 3. Virtual fiber and yarn model. ....	114
Fig. 4. 4. Simplified procedure on yarn model by active separation process (ASP). ....	116
Fig. 4. 5. Experimental equipment and method: (a) Micro-CT testing of yarn and (b) diagram of the tribometer with upper and lower upper setup. ....	118
Fig. 4. 6. The geometric comparison results between simulation and experiment: (a) the experimental value, (b) the simulated value and (c) cross-sectional statistics. ....	119
Fig. 4. 7. The comparison of (a) original and (b) modified cross-section viewpoint for yarn. ....	120
Fig. 4. 8. Representative cycle of the friction experiment and simulation results of yarns at a normal load of 2.8 N and pretension of 1.5-1.5 N. ....	121
Fig. 4. 9. Morphologies of friction simulation at different stages. ....	121
Fig. 4. 10. Evolution of friction force on normal load for different twist yarn (a* 50tpm; b* 100tpm; c* 200 tpm), (a-c) friction force versus displacement and (a'-c') twist angle of different twist of yarn. ....	123
Fig. 4. 11. Evolution of friction force on pretension for different twist yarn (a* 50tpm; b* 100tpm; c* 200 tpm), (a-c) same pretension of yarns and (d-f) different pretension of yarns. ....	125
Fig. 4. 12. The results comparison of yarns with different twist for friction and wear behavior before and after 25, 30 cycles (a* 50tpm; b* 100tpm; c* 200 tpm). ....	126
Fig. 4. 13. Number cycles as a function of the dissipated energy(a) and damage variable (b) for different for different twists of yarns. ....	126
Fig. 4. 14. The DUCTCRT distribution of contact zone of yarns with different twist: (a) 50, (b) 100 and (c) 200 tpm. ....	127

# LIST OF TABLES

## **Chapter 1 Literature review**

Table 1. 1 Application scope, advantages and disadvantages of friction test methods..... 13

## **Chapter 2 Yarn to Yarn Friction Analysis Considering the Weaving Process of Textile Fabrics at microscale**

Table 2. 1 Main physical properties of high-molecular-weight polyethylene (HMWPE) fiber and yarns. 61

Table 2. 2 The friction tests with different conditions to validate the developed analytical model. .... 63

Table 2. 3 Hertz contact area between carbon tows and round roller under different contact conditions .. 64

Table 2. 4 Modified contact area between carbon tows and round roller under different conditions ..... 65

Table 2. 5 Tukey-test parameters of three models under different contact conditions..... 65

## **Chapter 3 Yarn-to-yarn friction behavior during the manufacturing of woven fabrics at mesoscale**

Table 3. 1 Material properties for HMWPE (Spectra® 900) Yarn and Fabric. .... 81

Table 3. 2 Contact properties of binding warp and weft yarns in representative 3D reinforcement configurations. .... 98

## **Chapter 4 Numerical simulation and experimental validation of yarn/yarn friction considering fiber damage and wear prediction**

Table 4. 1 The main material parameters of HMWPE. .... 116

# **Chapter 1 Literature review**

## Résumé en français

Les composites textiles, constitués de matériaux renforcés par des fibres comme la fibre de carbone et l'aramide, représentent une avancée importante dans le domaine des matériaux. Ces matériaux composites combinent des propriétés physiques et chimiques distinctes au niveau macroscopique, offrant des caractéristiques mécaniques supérieures qui surpassent celles de leurs composants individuels. Les composites ont gagné une place prépondérante dans divers secteurs industriels, allant de l'aérospatiale à la fabrication de véhicules, en passant par la construction et les équipements sportifs. Leur résistance élevée, leur rigidité, leur faible densité, ainsi que leur excellente résistance à la chaleur et à la corrosion, en font des matériaux de choix pour des applications exigeantes comme la fabrication d'avions, de fusées et de véhicules spatiaux.

Les avancées récentes dans la technologie des matériaux ont permis le développement de composites sophistiqués, notamment ceux renforcés par des fibres de carbone, des fibres d'aramide, et des fibres de polyéthylène de très haute densité. Ces matériaux sont utilisés pour fabriquer des structures porteuses primaires et secondaires, offrant des qualités de rigidité et de résistance équivalentes, voire supérieures, à celles des composites en alliage d'aluminium. Par exemple, les composites en fibre de carbone sont largement utilisés dans les ailes et les fuselages d'avions, améliorant ainsi l'efficacité énergétique et les performances de vol grâce à leur poids réduit et leur excellente résistance à la chaleur. De même, les voitures de course haute performance et les voitures de luxe intègrent des composites pour réduire le poids et améliorer la sécurité et l'efficacité énergétique.

Dans le domaine de la construction, les composites sont utilisés pour fabriquer divers composants structurels, tels que des poutres, des colonnes et des panneaux. Ces matériaux offrent des qualités mécaniques exceptionnelles et une résistance à la corrosion, ce qui améliore la durabilité et la sécurité des structures. Dans l'industrie de l'énergie, les composites servent à fabriquer des pales d'éoliennes et des panneaux solaires, offrant une résistance mécanique et une durabilité accrues face aux intempéries, ce qui améliore l'efficacité et la longévité des équipements énergétiques.

Cependant, malgré leurs avantages potentiels, la production de composites présente des obstacles, notamment la nécessité de réguler méticuleusement les procédures de conception et de fabrication pour garantir les performances du produit final. Les composites peuvent se détériorer dans des conditions environnementales sévères, comme des températures élevées ou une humidité excessive, ce qui impacte la durabilité du produit final. En résumé, l'étude des composites et de

leurs utilisations pratiques représente un domaine riche en défis et en opportunités. Avec les avancées technologiques et l'exploration de nouveaux matériaux, les composites joueront un rôle de plus en plus important dans le progrès futur de la science et de la technologie.

Le processus de tissage des matériaux de renforcement détermine les caractéristiques communes de la forme structurelle des textiles à plusieurs niveaux et échelles. À l'échelle macroscopique, le tissu se manifeste comme un ensemble de systèmes de fils entrelacés; à une échelle plus fine, il se manifeste comme un fil unique, et pour les tissus avec une structure périodique, il peut être représenté par une cellule unitaire représentative (RUC). À l'échelle microscopique, les fibres monofilaments ont des diamètres de l'ordre du micromètre. Les formes structurelles des textiles peuvent être divisées en tissus tissés, tricotés et tressés selon les techniques de tissage, et en tissus bidimensionnels et tridimensionnels en fonction des dimensions du tissu.

L'industrie des composites textiles connaît une demande croissante pour des composites aux propriétés mécaniques améliorées. Une attention particulière est accordée à l'utilisation de structures de fibres tridimensionnelles préfabriquées pour renforcer les composites textiles. Ces composites sont très résistants au délaminage et aux dommages d'impact et possèdent des caractéristiques de forme quasi-nette. La structure de renforcement tridimensionnelle inclut des fils entrelacés qui traversent à la fois la "couche" et la "pli" dans le sens de l'épaisseur, en plus des fils de chaîne et de trame à la surface. Cette caractéristique structurelle intrinsèque permet de surmonter les inconvénients des composites bidimensionnels, tels que des performances intercalaires inférieures et une vulnérabilité au délaminage et aux fissures.

Le comportement mécanique des tissus tissés est crucial pendant le processus de tissage, car il détermine l'efficacité et la qualité de la fabrication des tissus. Les propriétés mécaniques telles que la résistance à la traction, la rigidité au cisaillement et la rigidité en flexion du tissu tissé sont influencées par des facteurs tels que la géométrie des fils et des tissus, la structure du tissage et les propriétés des matériaux des fibres. Le processus de tissage impose des contraintes, des compressions et des flexions aux fils, influençant la distribution des contraintes et des déformations dans le tissu. La compréhension du comportement mécanique des tissus tissés est essentielle pour améliorer le processus de tissage et réduire les coûts de fabrication.

Il est également important de considérer les dommages potentiels aux préformes causés par divers comportements mécaniques pendant le tissage. Les préformes en fibres servent de cadre structurel aux composites, et les fils, qui sont les composants fondamentaux des préformes, subissent des



frictions, des compressions et des flexions pendant le processus de tissage et de formation, ce qui réduit leurs propriétés mécaniques. Des études ont montré que le processus de tissage tridimensionnel peut entraîner une diminution significative de la résistance des fils secs porteurs de charge, de la résistance des fils de chaîne dans les tissus formés et de la résistance des fils normaux.

Enfin, la recherche sur le comportement de friction entre les fils et les outils de tissage est essentielle pour comprendre et optimiser le processus de formation des préformes textiles tridimensionnelles. La caractérisation de la friction et de l'usure des fils pendant le processus de tissage permet d'évaluer quantitativement les dommages aux fils, d'optimiser le processus de formation des préformes textiles tridimensionnelles et d'améliorer les caractéristiques mécaniques des composites.

En conclusion, les composites textiles continuent de jouer un rôle crucial dans le développement de solutions matérielles avancées. Les recherches futures devront se concentrer sur l'amélioration des techniques de fabrication, l'optimisation des processus de tissage et l'exploration de nouvelles applications pour maximiser les avantages de ces matériaux innovants.

**Mots-clés:** Micro–meso échelle; Tissus/textiles; Fils torsadés; Modélisation de la friction; Mécanisme de contact

## 1.1 Introduction to the textile composites

### 1.1.1 The composites and their application

Composite material is a novel substance consisting of two or more constituent materials, which retain their individual physical and chemical properties at a macroscopic level. However, the composite material exhibits exceptional qualities that surpass those of its components. Composite materials have emerged as a significant area of study and implementation within the discipline of materials science[1–3]. Significant advancements have been achieved throughout the past several decades in the creation and utilization of composites. Composites have become ubiquitous in several industries, ranging from aerospace and vehicle manufacturing to construction and sports equipment. These composites possess exceptional mechanical characteristics, including superior strength, stiffness, and low density[4–6]. Additionally, they exhibit commendable heat resistance, corrosion resistance, and dimensional stability. Consequently, they find extensive application in the production of airplanes, rockets, and space vehicles, rendering them highly suitable materials for such purposes. Equation Chapter 1 Section 1

Materials technology has experienced significant advancements in recent years, particularly in the field of sophisticated composite materials. Advanced composite materials are specifically utilized for fabricating primary and secondary bearing structures, and they possess stiffness and strength qualities that are equivalent to or beyond those of aluminum alloy composites. Currently, it mostly pertains to reinforced composites that utilize carbon fiber, aramid fiber, ultra-high molecular weight polyethylene fiber, and other reinforced composites with exceptional strength and modulus[3,7–10]. Carbon fiber composites are utilized in the wings and fuselage of numerous airplanes, offering exceptional strength, low weight, and excellent heat resistance. This application enhances the fuel efficiency and flight performance of airplanes[11,12]. Similarly, high-performance racing cars and luxury cars employ composites in the production of their bodies and interiors to reduce weight and enhance safety and fuel efficiency. Composites are employed in construction to fabricate diverse structural components, including beams, columns, and panels [13–17]. These composite materials provide exceptional mechanical qualities and resistance to corrosion, hence enhancing the longevity and safety of structures. Composites are utilized in the energy industry to fabricate wind turbine blades and solar panels. These composite materials provide exceptional mechanical qualities and resistance to weathering, which enhance the effectiveness and durability of energy equipment[18–21].

Nevertheless, despite the favorable potential uses of composites, some obstacles persist in their production procedure[22–24]. For instance, the design and manufacturing procedures of composites necessitate meticulous regulation to guarantee the performance of the final product, shown as Fig. 1. 1. Composites can deteriorate in severe environmental conditions, such as elevated temperatures or excessive humidity, which will likewise impact the durability of the final product[25–27]. In summary, the study of composites and their practical uses presents a domain replete with both obstacles and prospects. Due to technological advancements and the exploration of novel materials, composites will assume a more significant role in the future progression of science and technology.



Fig. 1. 1. Multi-domain properties of composite materials.

### 1.1.2 The textile reinforcements of composites

The weaving process of reinforcing materials determines the common characteristics of its structural form with multi-level and multi-scale, the fabric in the macroscopic scale is manifested as a collection of interwoven yarn systems; the fine scale is manifested as a single yarn and fabrics with a periodic structure, it can be replaced by a representative unit cell (Representative Unit Cell, RUC); the microscopic scale can be discretized into fiber monofilaments with diameters at the  $\mu\text{m}$  level, such as commonly used carbon fiber and aramid fiber with diameters of  $5\sim 7\mu\text{m}$ ,  $5\sim 25\mu\text{m}$

and 10~20 $\mu\text{m}$  respectively[28]. For the diameter of the fiber monofilament at the  $\mu\text{m}$  level, which includes frequently used carbon fiber, glass fiber, and aramid fiber, the diameters ranged from 5 to 7  $\mu\text{m}$ , 5 to 25  $\mu\text{m}$ , and 10 to 20  $\mu\text{m}$  respectively. We must take into consideration the behavior of the many scales of the level of the material when we are studying the macro-mechanical behavior of the fabric. This is because the fabric has multi-scale features. The structural forms of textiles may be divided into woven, knitted, and Braided fabrics according to the weaving techniques[29]. Textiles can also be classified into two-dimensional and three-dimensional fabrics when the dimensions of the fabric are taken into consideration, as shown in Fig. 1. 2. Dixit [30] et al. have made a presentation of the forms and characteristics of woven, woven, and knitted structures, of which woven fabrics have more advantages than weaving and knitting in terms of manufacturing cost, weaving efficiency, and overall performance, and are the Among them, woven fabrics have more advantages than woven and knitted in terms of manufacturing cost, weaving efficiency and overall performance, and are the most widely used form of fabric structure. Fig. 1. 3. illustrates the plain, twill, and satin textiles that are used in the production of two-dimensional woven fabrics. All three structures have comparable qualities, including the fact that the warp and weft yarn systems are perpendicular to one another. The warp and weft yarns of plain weave fabrics intertwine with each other at the top and bottom, and the interweaving points of the warp and weft yarns and the curls of the yarns are the most numerous among the three configurations; additionally, the degree of compactness of the fabrics is the highest; however, each of the three structures possesses its unique characteristics. the surface of twill fabrics shows a diagonal pattern composed of consecutive interweaving points, which is less in number of interweaving points and less compactness compared to that of plain weave fabrics; there is also a diagonal pattern on the surface of satin fabrics, however, these patterns are not continuous, and the patterns of satin fabrics are not continuous, and they have the same characteristics as that of flat fabrics[31]. The degree of compactness is likewise the lowest among the three designs, and these patterns are not continuous. Additionally, the number of interwoven points in these patterns is the least of the three fabrics.

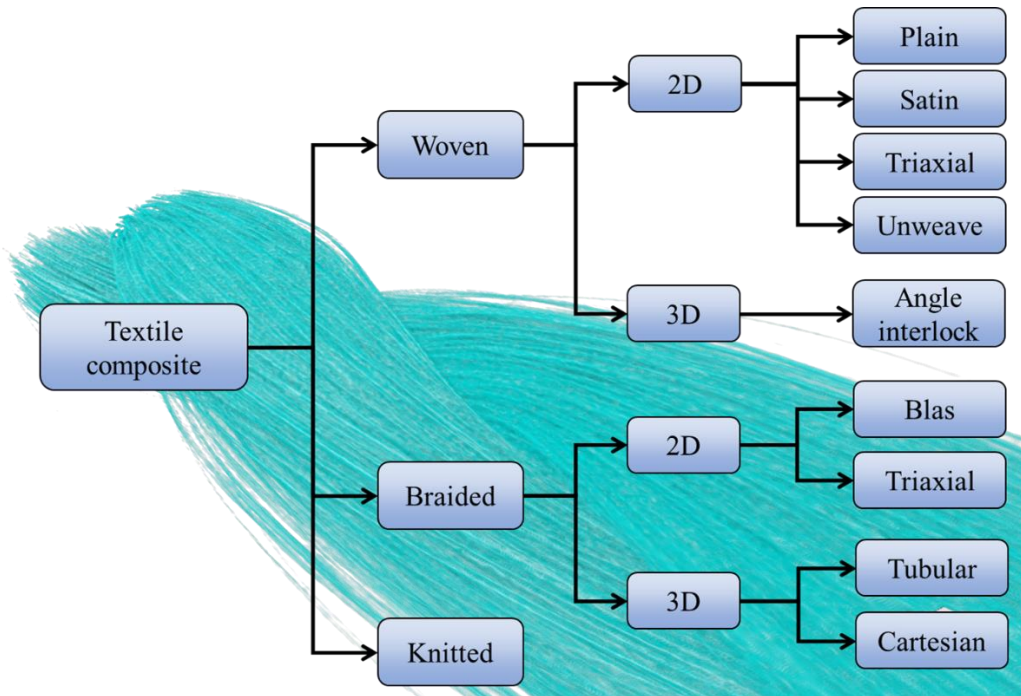


Fig. 1. 2. Classification of textile composites.

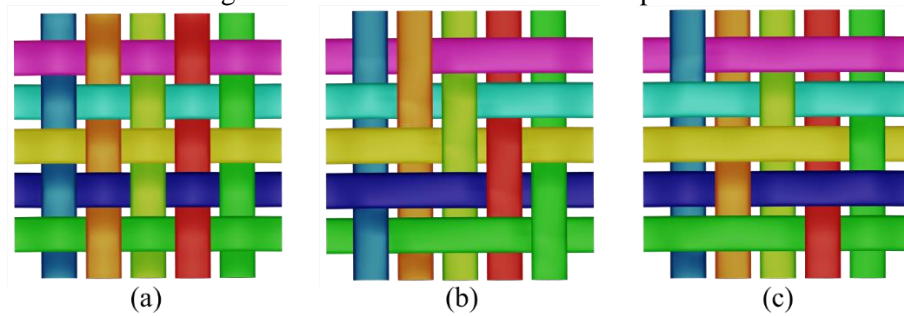


Fig. 1. 3. Representative 2D weave textile.

As the textile composites industry has advanced, there is a growing demand for composites with improved mechanical properties [3,32,33]. One area of research that has gained attention is the use of three-dimensional (3D) fiber structure prefabricated body-reinforced textile composites. These composites are highly resistant to delamination and impact damage, and they also have near-net-shape characteristics[34–36]. Furthermore, the reinforcing structure includes interlacing yarns that traverse both the "layer" and "ply" in the direction of thickness, in addition to the warp and weft yarns on the surface. By virtue of its inherent structural characteristic, this tridimensional composite material effectively mitigates the drawbacks associated with two-dimensional composites, such as subpar interlayer performance, susceptibility to delamination, and vulnerability to cracking, among others. The primary structural configurations of 3D reinforcing

materials consist of orthogonal and angular interlocking structures, as seen in Fig. 1. 4. The orthogonal fabrics consist of warp yarn, weft yarn, and knot yarn that are arranged in a straight and perpendicular manner to each other[37,38]. On the other hand, the angle interlocking fabrics have straight weft yarn and bent warp yarn, with the warp and weft intersecting at a right angle. Additionally, the warp yarn is not only arranged along the length of the fabric, but also intertwines with the weft yarn at a certain depth and angle along the thickness of the fabric[39,40].

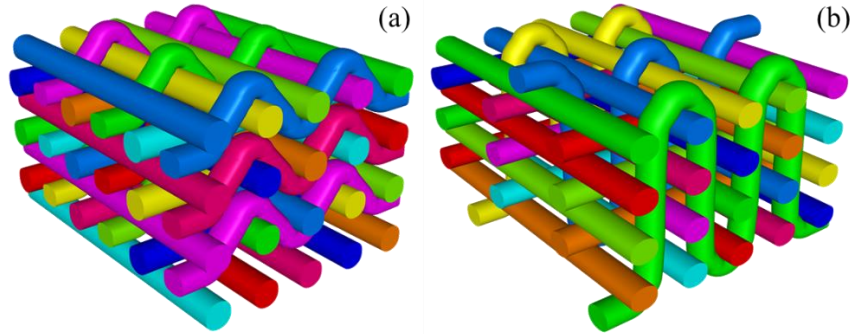


Fig. 1. 4. Representative 3D weave textile.

As an example, satin textile yarns have more straight section parts than plain textiles, which have the best tensile properties and are more suitable for regions of a larger stretch than plain textiles. The fabric structure is one of the most important factors that affect the moldability and mechanical properties of textile composites, and it also determines the different occasions in which their applications are most likely to occur[41,42]. The yarns of satin textiles are organized with the least amount of compactness possible. This makes the yarns more prone to sliding and misalignment, which in turn lowers the quality of the molding being produced. Plain textiles offer the maximum tightness and the best resistance to yarn movement, which makes it simpler to regulate the movement of the yarns throughout the molding process. Plain fabrics are also the most expensive kinds of fabrics. On the other hand, yarn alignment tightness that is too high leads to the poorest lying qualities and is the most likely to result in wrinkles[43,44]. Twill textiles are often used to mold a wide variety of shaped and curved components because they have the highest degree of deformability and can handle massive shear deformations. Additionally, the incorporation of normal yarns into 3D textile reinforcement materials results in an improvement of the mechanical characteristics of these materials in the normal direction. Consequently, these materials are increasingly used in aeronautical applications[45,46].

## 1.2 Mechanical behavior during the weaving process

The mechanical properties of woven fabric are crucial in the weaving process since they dictate the efficiency and quality of fabric manufacturing. Throughout the process of weaving, the fabric experiences numerous factors that impact its structure, including the tension in the warp and weft yarns, as well as the frictional forces between the yarns and the loom components. Understanding the mechanical properties of woven fabric is crucial to improving the weaving process and decreasing manufacturing costs. The tensile strength, shear stiffness, and bending stiffness of the woven fabric are influenced by factors such as the yarn and fabric geometry, weave structure, and material properties of the fibers. Throughout the process of weaving, the yarns experience tension, compression, and bending, which influences the distribution of stress and strain in the fabric. The tensile behavior of the yarns determines the fabric's ability to endure the stress during weaving and maintain its dimensional stability. The shear stiffness of a fabric directly influences its ability to drape and deformation, whereas the bending stiffness of the fabric affects its behavior specifically during the weaving process.

The mechanical properties of woven fabric are also affected by the weaving process factors, including the weaving velocity, the distance between picks, and the shape of the shed. The shape of the shed dictates the force required for weaving, while the spacing between the picks impacts the stiffness of the fabric in terms of shear and bending. The velocity at which the fabric is woven has an impact on the dynamic characteristics of both the fabric and the loom components, potentially resulting in structural distortion of the fabric. The mechanical behavior of woven fabric is complex and multifaceted, as it is affected by the material properties, the weaving process, and the fabric geometry. By understanding the mechanical behavior of woven fabric, we can optimize the weaving process, improve the fabric's quality, and reduce production costs.

The structural variety of reinforcing materials is determined by the weaving process. However, it is important to additionally consider the potential damage to the preforms caused by various mechanical behaviors during weaving. Fiber preforms serve as the structural framework of composites, and yarns, which are the fundamental components of preforms, experience friction, compression, and bending during the weaving and forming process, leading to a reduction of their mechanical properties by approximately 5% to 30% based on previous research[47–49]. Lamon et al. conducted a study on the flaw strength distributions of different kinds of fibers. They developed empirical distributions of flaw strength, which can be used to assess Weibull plot and Maximum Likelihood Estimation techniques based on sample size and composition. Wang et al.[49]

introduced an analytical model grounded on statistical theory to illustrate the unpredictable tensile characteristics of natural fiber yarns. This was achieved by defining the crimp strain of fibers and the effective elastic modulus of yarns as stochastic variables representing damage indicators. Hemmer et al.[50] experimentally presented a simple mechanical method, known as Just-In-Time (JIT), to replicate the changes in width and thickness of E-glass and carbon yarns during through-thickness compression. The researchers developed an analytical framework that was used for the analysis of fiber/yarn, in conjunction with the experimental findings[51]. Furthermore, the mechanical behavior of the yarn leads to changes in its structure. Therefore, comprehending and forecasting the mechanical properties of yarns is an essential aspect of composite molding study.

When weaving 3D textiles, the fibers undergo repetitive weaving movements, resulting in damage and degradation of their qualities, as opposed to 2D fabrics. Clark et al. [52] performed tensile tests on glass fiber samples obtained from three-dimensional weaving. The results demonstrated that the weaving process led to a 30% decrease in the strength of the dry load-bearing yarns, a 30% decrease in the strength of the warp yarns in the shaped fabrics, and a 50% decrease in the strength of the normal yarns. The researchers determined that the significant decrease in strength of the regular yarns was attributed to two factors: firstly, the regular yarns had a lower fineness compared to the warp yarns, and secondly, the regular yarns had more bending deformations than the warp yarns. Lee et al. [53] did research on weaving damage using two carbon fibers. The findings revealed a 12% decrease in the tensile strength of one of the fibers. The study also highlighted that the decline in strength was attributed to abrasion and bending of the fibers during the weaving process. The performance of the composites will be directly impacted by the three-dimensional weaving damage, which in turn results from fiber degradation generated by the weaving damage. Researchers have observed that laminates with the same volume fraction and three-dimensional fabric composites exhibit differences in their in-plane tensile, compressive, and flexural properties. Specifically, the former typically have properties that are 10-20% higher than the latter, and in some cases, the difference can be as high as 50% [54–56]. However, other researchers have noted that the tensile properties of three-dimensional fabric composites are influenced by the characteristics of normal yarns[57,58].

Furthermore, it is worth noting that the rate of performance loss resulting from yarn friction accounts for approximately 9-12% of the overall mechanical property loss rate. This phenomenon typically takes place during the "weft" stage of weaving. During this stage, the reed is responsible



for beating the weft yarns to the weaving mouth. Additionally, the warp and weft yarns are tightly interwoven. While the yarns are repeatedly friction during the process, the abrasion continues to accumulate, and a significant number of "hairiness" can be observed on the surface of the preforms[59]. The composites will experience a loss in their mechanical characteristics as a result of the "hair plume". For this reason, it is essential to investigate the friction and wear behavior of yarns throughout the process of 3D textile precast body forming. This will allow for the quantitative evaluation of yarn damage, the optimization of the process of 3D textile precast body forming, and the enhancement of the mechanical characteristics seen in composites[46,52,53,60].

### 1.3 Friction behavior between yarns/fibers

#### 1.3.1 Friction research status

This section presents a study on the friction properties of fibrous beams in the process of fiber-enhanced phase forming. It provides a summary of the advantages and disadvantages of the test methods used to evaluate the properties of yarn-tool and yarn-yarn beam interactions. The section also analyzes the influence of factors such as friction angle, friction frequency, pre-tension, and loading method on the friction properties of fiber/yarn. Additionally, it discusses the theoretical analysis model of the abrasion behavior of fiber/yarn. This information is valuable for understanding the mechanism and optimizing the forming process. The technical path is depicted in Fig. 1. 5.

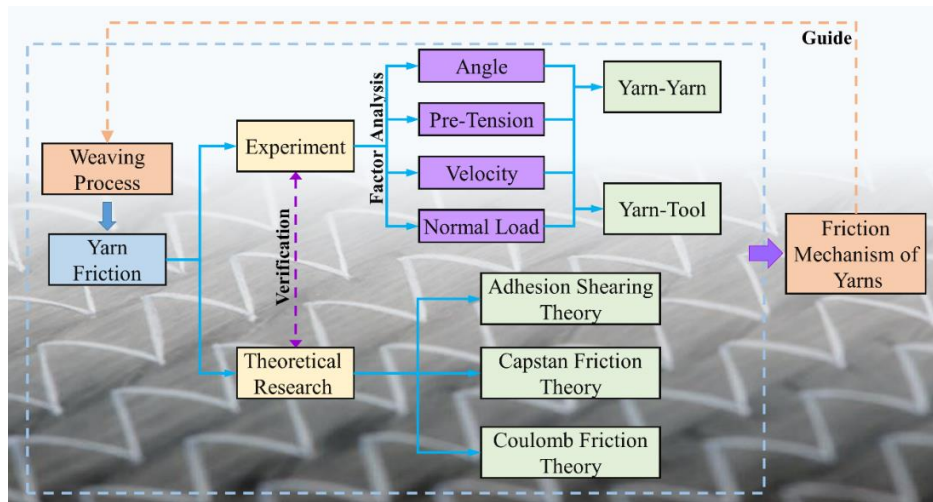


Fig. 1. 5. Technical path of research

#### 1.3.2 Friction test methods

Initially, friction testing for fiber/yarns was carried out in the 1870s by utilizing two yarns that were twisted[61]. This was followed by the introduction of friction testing. According to the contact mode, yarn friction behavior can be divided into three types [32]: point contact [62–64],

in which fibers or yarns rub against a rough surface, and multi-point contact is formed by multiple peaks, line contact [65–67], in which sliding friction occurs between fibers within the yarn; and face contact [68,69], in which yarns rub against the contact surface with sliding friction. At the moment, the study techniques that are most often used for the purpose of examining yarn frictional wear are as follows: the flat plate extraction method [70], the capstan method [71], the rotary reciprocating friction method[72,73], and the orthogonal linear reciprocating friction method[2].

In their study, Xiang Zhong et al [74] examined the advancements in fiber tribology research and conducted an analysis of the distinct features and areas of applicability for various friction testing techniques stated before. Building upon this foundation, the researchers conducted a more in-depth analysis of the friction behavior of yarn. They summarized the scope of application, advantages, and disadvantages of commonly used friction test methods in Table 1. 1. Additionally, they developed test methods [72,75] and modeling schemes [76–78] that align with real-world working conditions. Fig. 1. 6. illustrates the scholarly articles, publications, and references on yarn tribology in the last decade, specifically focusing on the forming process of textile composite preforms. This data suggests that there is a growing interest in studying the frictional properties of yarns, making it a prominent and relevant topic [68,69,79].

Table 1. 1 Application scope, advantages and disadvantages of friction test methods

Way of friction	Range of application	Advantages	Disadvantages	Representative articles
Reciprocating friction	Yarn-Yarn Yarn-Tool	Easy mass production designable	Friction fluctuates; Difficult to tension	Experimental simulation of friction and wear of carbon yarns during the weaving process
Capstan friction	Yarn-Tool Yarn-Yarn	Simple operation High accuracy Controllable processing speed	High environmental requirements	Frictional behavior of high-performance fibrous yarns: Friction experiments
Pull-Out Test	Yarn-Yarn Yarn -Tool	Unlimited workpiece size	Difficult to control speed	Effect of tool surface topography on friction with carbon yarns for composite fabric forming
Fiber Twist method	Yarn-Yarn	Reflects the contact between yarns	Difficult to operate	A new estimate of the yarn-on-yarn friction coefficient
Hanging fiber method	Yarn-Yarn Yarn-Tool	Simple structure	Difficult to control accuracy	Fiber-on-fiber friction measurement using hanging fiber method
Surface friction method	Simple structure	Simple structure	Difficult to control accuracy	Effect of tool surface topography on friction with carbon yarn for composite fabric forming

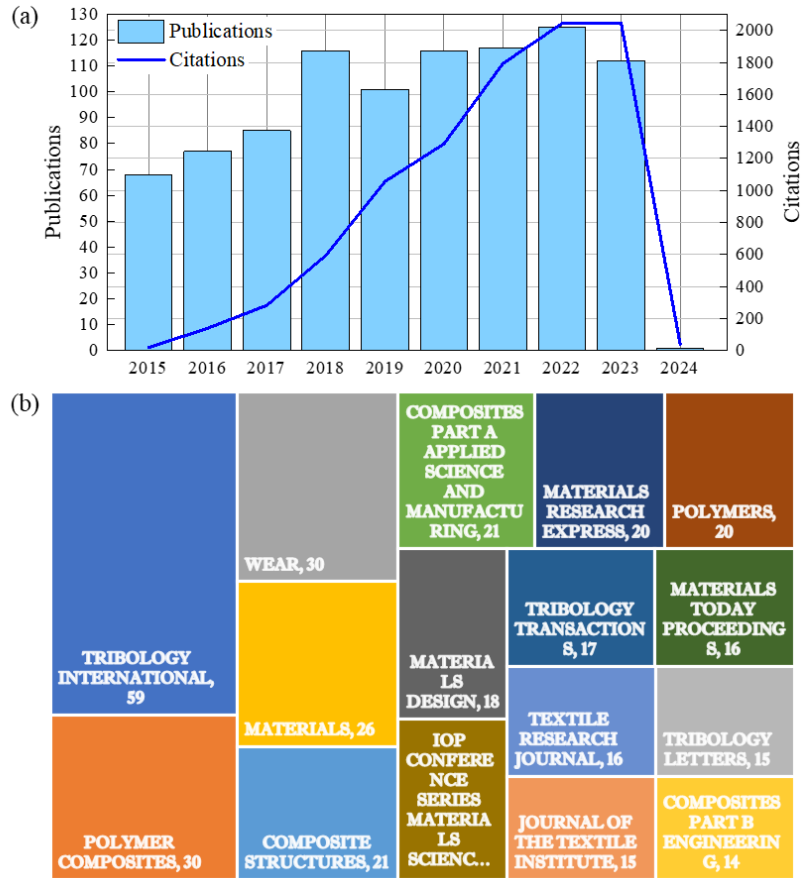


Fig. 1. 6. Research progress of friction methods during textile composites forming for yarns in recent 10 years: (a) published items and citations in each year; (b) key publications of friction methods during textile composites forming for yarns [obtained from the Web of Science Core Collection with the following keywords: friction methods, yarn and fiber (updated on 25/03/2024)]

Two primary categories can be used to classify the friction behaviors that occur during the process of textile precursor forming. The first category is the friction that occurs between the yarn and tool components like reeds and guide rollers. The second category is the friction that occurs between various yarn systems like warp yarns, weft yarns, and normal yarns. Consequently, most of the research that has been conducted on the subject of yarn tribology has focused on two forms of friction: yarn-tool and yarn-yarn [25,80]. The extraction method is an important method for testing the friction properties between the yarn and the tool [81]. As shown in Fig. 1. 7(a), the force that is required for the yarn to be extracted from the flat plate under a specific normal pressure condition is defined as the friction force [82]. After that, the coefficient of friction can be obtained by applying Coulomb's theory[83,84]. During the process of precast body building, this approach can characterize the friction performance of yarns under a variety of situations, including fineness, preloaded tension, and friction frequency. Over the course of the last several years, researchers

have carried out many investigations on the tribological characteristics of yarns by using the extraction technique. As a result, they have garnered a great deal of information that is useful for engineering practice. The researchers Mulvihill et al. [65] conducted a study to examine the frictional behavior of carbon yarns and tool flat plates with roughness ranging from 0.005 to 3.2  $\mu\text{m}$ . They recorded the curves of the friction force  $F$  vs roughness for the contact between the yarn and the tool flat plate. In the case of tool flat plates with a surface roughness of less than 0.1  $\mu\text{m}$ , it was discovered that the friction force rose fast as the surface roughness decreased. However, the variation of friction force with roughness did not show any meaningful relationship for tool flat plates with a roughness that was considered to be higher. An additional technique of testing that may be used for the purpose to determine the frictional qualities of soft materials like yarns is known as the capstan friction method [74]. As seen in Fig. 1. 7(b), the sample is presented in a suspended state on a friction roller that is cylindrical and has a fiber wrap angle. At one end of the yarn, the tension  $T_1$  is applied, and the other end is linked to a load testing instrument. The load is recorded as  $T_2$ , and the friction force is equal to the difference between  $T_1$  and  $T_2$ . Cornelissen et al. [72] designed a gib test setup to discuss the effects of factors related to preform forming on the frictional properties of yarns. The results showed that different normal loads lead to changes in the contact surface morphology. Furthermore, the contact surface morphology is the primary factor that influences the behavior of yarn-tool friction. Furthermore, the trend relationship between friction and normal load is consistent with the law of distribution of the power function [85,86]. The capstan friction technique was used by Abu Obaid et al. [62] to perform cyclic friction testing on aramid yarn (KM2-600<sup>®</sup>) with two different kinds of glass fiber yarns (AGY S2<sup>®</sup> and Owens Corning Shield Strand S<sup>®</sup>). These experiments were based on a handmade wear tester. Based on the findings, the surface slurry has a role in enhancing the abrasion resistance of the yarns. The abrasion resistance is graded from best to worst for the aramid yarns (KM2-600<sup>®</sup>), glass yarns (OCS Strand S<sup>®</sup>), and glass yarns (AGY S2<sup>®</sup>), respectively. Not only is the strand friction technique relevant to the fine scale, but it can also be used to measure the friction of fibers at the microscopic size. Wang et al [87] used a high-precision nano-friction tester to test the friction properties of superconducting *NbTi* material and polyvinyl chloride (PVC) under non-lubricated conditions, and the results were similar to the fine-scale friction behavior, and the fiber fineness, normal load, and friction frequency had significant effects on the friction properties. As the winch friction technique has become more popular, researchers have developed several novel test

methods that are based on the winch friction principle. The goal of these new methods is to make the winch friction method generally relevant to the testing of a variety of materials and circumstances [88]. Chakladar et al. [63] carried out a comprehensive experimental investigation into the frictional behavior of carbon yarns by utilizing a friction apparatus that was constructed at home. The apparatus was depicted in Fig. 1. 7(c), and it consisted of one end of the yarn being connected to a load cell, and the other end being connected to a weight that was mounted around a friction roller. The friction and wear of carbon yarns were explored by Wu et al. [25] using a friction and wear test setup that is shown in Fig. 1. 7(d). The researchers looked at how the friction number, normal load, and friction angle affected the friction and wear of the yarns. When the friction angle was varied in the range of  $30^\circ$  to  $90^\circ$ , the residual tensile breaking strength of carbon fibers decreased with the decrease of friction angle, and when the friction angle was  $0^\circ$ , the residual tensile breaking strength decreased sharply. The studies that were discussed above demonstrated that the wear of carbon fibers gradually increased with the increase in the number of friction instances and the normal load. In addition, several researchers have built various test platforms to better examine the tribological features of yarns. These test platforms take into consideration a variety of factors, including fiber qualities [89], the spinning process [90,91], the forming process [66,92,93], and friction motion [94].

When yarns are deformed by an external force during the process of forming a prefabricated body, relative sliding occurs between the yarns. The friction behavior between yarns can be classified into three different types based on the direction in which the yarns are sliding. These three types are the length-length (l-l) direction, the length-radius (l-t) direction, and the radius-radius (t-t) direction, shown in Fig. 1. 7(e). According to the researchers, the test was designed based on the principle of friction test in the length-length direction (l-l), where the two ends of two stranded yarns were subjected to the same preloaded tension  $P_1$ , as shown in Fig. 1. 7(f). This was done in order to evaluate the friction performance of yarns. Any one of the two yarns ends will progressively apply continuous tension  $P_2$  ( $P_2 > P_1$ ), and when  $P_2$  is less than the maximum static friction between yarns and  $P_1$  total, the helical contact surface between the yarns in the same structure will stay immobile. This is because  $P_2$  is more than  $P_1$ . When  $P_2$  is greater than the maximum static friction between yarns and the total of  $P_1$ , the inter-yarn helical contact surface undergoes a change, and sliding takes place. The length-radius direction friction principle (l-t) has been the subject of a number of investigations that have been conducted by scholars over the past

several years. One of the ends of the yarn FL1 is fixed at point O, as illustrated in Fig. 1. 7(g), while the other end of the yarn FL1 is free to hang over the fixed yarn FL2 under the influence of gravity G. The free end of FL1 is driven to move together under friction when FL2 moves in the horizontal direction. This continues until the free end of FL1 tends to slide. The friction coefficients under the conditions that correspond to these conditions can be obtained by solving according to the variables of deflection angles  $\alpha$  and  $\beta$  and sliding distance  $x$ . Based on this principle, Alirezazadeh et al. [80] investigated the effect of fineness on the friction behavior of polypropylene yarns. They used a high-precision test setup that they had designed themselves, and the findings revealed that the geometry of the contact surface had a more significant impact on the friction behavior of yarns. This was since different fineness results in different contact shapes. Abdellahi et al. [64] employed the finite element approach to numerically simulate the test method illustrated in Fig. 1. 7(g). They discovered that the calculated results were in good agreement with the experimental findings, with a maximum error of around 4.3%. This was the conclusion that they reached after testing the method. The testing procedure that is based on the l-t friction principle is straightforward and easy to implement; however, it is not capable of successfully controlling the circumstances of yarn pre-tension and normal load. As a result, the friction process is subject to noticeable fluctuations, and the accuracy of the technique is poor. As a result of the development of high-precision sensors, researchers have been able to construct test devices that are based on the original equipment and contain variables that can be controlled and have less fluctuation. The friction behavior between two vertical yarns was evaluated by Tournalias et al. [95] using an NTR2 nano tribometer. Additionally, the researchers investigated the effects of friction frequency and normal load on the friction performance of carbon yarns of varying grades. It has been demonstrated via the findings that the frictional behavior of yarns is in accordance with Coulomb's law. The effects of friction frequency and normal load on the coefficient of friction of yarns are not found to be significant. Furthermore, it is of utmost significance to investigate the tribological characteristics of yarns in accordance with the radius-radius (t-t) friction principle. This is in addition to the length-length (l-l) and length-radius (l-t) friction principles. For instance, there are t-t friction behaviors that occur inside the carbon yarns that are of grades T300-12K and T800-6K. Additionally, there are inter-yarn friction behaviors that occur between the yarns that are contained within the textiles themselves in the t-t direction. It is not particularly typical to conduct friction research in accordance with the t-t principle, even though the t-t direction friction

behavior is of great significance in the preform forming process. The friction test configuration that was devised by Shanwan et al. [96] is depicted in Fig. 1. 7(h). In this setup, two yarns that are subjected to the same tensile force are entangled in the direction of  $\beta$ , and the yarns are rotated with an angular velocity designated as  $\theta$ . When the yarns are brought into contact with one another, the rotating motion causes two different kinds of friction to occur. The rotating motion results in the generation of two distinct types of torques: the elastic torque, which is transferred to the contact region between the yarns as a result of the rotational motion, and the resistive torque, which is induced by the tangential friction  $T_1$  and  $T_2$  that occurs between the yarns. The sliding that takes place between the two interwoven yarns is an example of frictional behavior in the t-t direction. This occurs when the elastic torque is the dominant force in the rotation.

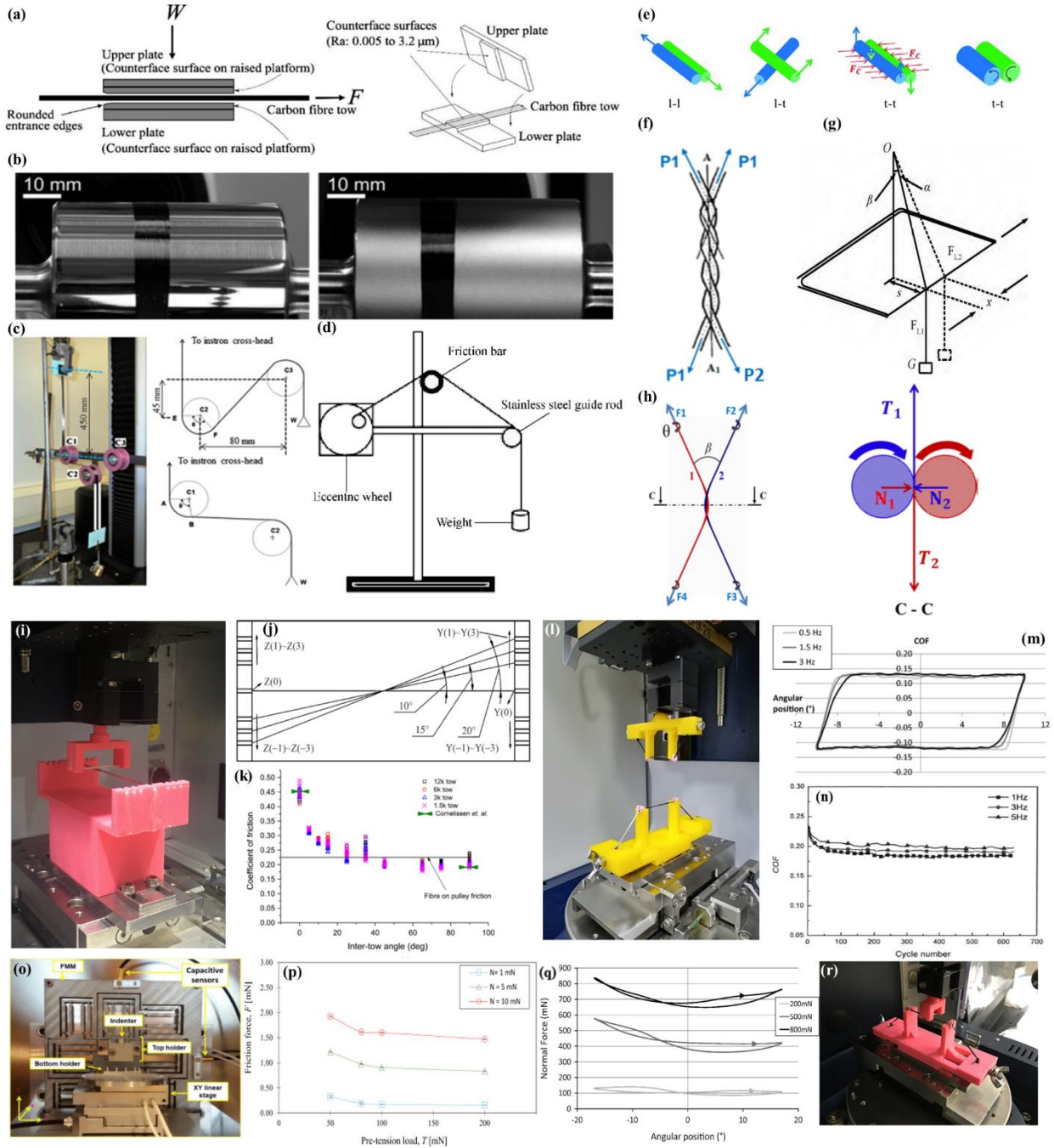


Fig. 1. 7. (a) Schematic diagram of testing method for fiber frictional properties [65]; (b) capstan method for yarns [72]; (c) wear-resistant device schematic [63]; (d) schematic of three angles of wrap; (e) classification of friction according to directions [96]; (f) l-l friction principle [63]; (g) l-t friction principle [97]; (h) t-t friction principle [96]; (i) fixture on machine; (j) schematic diagram of key dimensions of lower fixture; (k) effects of inter-yarn angle on yarn friction [63]; (l) figure of the upper and lower fixture; (m) average cyclic curve of friction coefficient versus angular position for SM single fiber friction with different oscillation frequencies [95]; (n) effect of friction velocity on friction coefficient of carbon yarns; (o) Schematic description of friction experiment between fibers [98]; (p) friction force as a function of pre-tension load [98]; (q) Influence of the normal load on the average cycle in terms of normal force [75]; (r) photograph of experimental rig mounted on friction tester.



### 1.3.3 Friction influence factors

It is possible to effectively characterize the friction performance of yarns during the process of precast body forming by using the friction test. Researchers have conducted a large number of parametric studies to investigate the influence law of each factor on the friction performance of yarns and to analyze the friction and wear mechanism based on the residual breaking strength of yarns after friction.

During the forming process of textile preforms, yarns experience friction and abrasion at various angles, particularly in the forming of 3D preform, where this effect is more pronounced. In the context of the yarn-yarn friction test, the friction angle represents the sharp angle formed between the yarns. This angle may be modified by modifying the beginning location of the fibers. Based on earlier research on friction between yarns, it has been shown that when the friction angle lowers, the contact area rises, leading to a more intense yarn friction behavior and severe wear. Chakladar et al [63] examined the friction characteristics of carbon yarns at a small scale by a combination of tests and simulations. They discovered that the friction behavior between the yarns exhibited an increase, leading to significant wear of the fibers. Additionally, Chakladar et al examined the friction characteristics of carbon yarns at a small scale using both experimental and simulation techniques. They discovered that a reduction in the friction angle between the yarns leads to an expansion in the contact area and a shift in the direction of the traction force. Consequently, this causes an elevation in the frictional force along the direction of friction, resulting in an increase in the coefficient of friction and significant wear. Furthermore, fiber migration and tangling took place due to friction between yarns. It was determined that the coefficient of friction at a friction angle of  $0^\circ$  was twice as high as that at  $90^\circ$ , showed in Fig. 1. 7(k). The precast forming process involves various angles of friction acting on yarns, leading to intricate alterations in contact behavior. Therefore, the primary concern in the precast forming process should be addressing the friction-induced damage caused by the orientation of yarns. This is crucial for minimizing the degradation of mechanical properties and the service life of the resulting molded composites.

When referring to the friction behavior between yarn and tool, the term "friction angle" refers to the angle that exists between the free ends of the yarn and the tool after contact has been made. When the angle between the yarns was between  $30^\circ$  and  $90^\circ$ , the results showed that the residual tensile breaking strength of the carbon yarns showed a decreasing trend with the decrease of the

angle, but the change was not significant. When the pinch angle is  $0^\circ$ , the tensile breaking strength of the carbon yarn drops abruptly, down 84.90% compared with the original sample, this is because that with the decrease of the pinch angle, the carbon yarn in the upper layer and the lower layer of the surface of the friction roller gradually overlap, and the carbon yarn morphology is a flat strip, under the action of the pre-tensioned in the state of elongation, therefore, with the decrease of the pinch angle, the upper and lower layer of the contact area of the carbon f yarn part of the In light of this, the contact area of the top and lower carbon yarns is distinct from one another when the clamping angle lowers. The yarn wear is severe when the friction angle is decreased [99]. This is because the frictional resistance between the yarns increases as the contact area between the yarns increases. This results in more broken fibers on the surface of the yarns after the friction, which causes the wear to be intense. However, the yarn wear is severe when the friction angle is decreased.

In addition to the significant impact that the friction angle has on the behavior of the friction, the friction frequency is of utmost significance in the process of forming reinforced materials. The variation in the friction frequency has a direct influence on the amount of fiber damage that occurs and the efficiency with which the material is formed. This is a physical parameter that describes the speed of friction behavior, and it is referred to as the yarn friction frequency. It is the number of times that the friction behavior between the yarn and the tool or between the yarn and the yarn happens in each unit of time. Previous research has demonstrated that the frequency of friction only has an influence on the amount of time it takes to achieve a state of frictional stability; it does not have a substantial impact on the behavior of friction. Using the fixture depicted in Fig. 1. 7(1), Yang et al investigated to determine the impact of friction frequency on the friction behavior between yarns. Their findings revealed that the change in friction frequency does not have any impact on the friction force  $F_f$  and friction coefficient  $\mu$  of the carbon yarns, shown in Fig. 1. 7(m). which, however, extended the number of cycles that were necessary to achieve stability. This is because the carbon fibers have a high kinetic energy when they are subjected to friction at a frequency of 5 Hz, which causes an increase in the force that is exerted along the frictional sliding direction during the orthogonal reciprocating motion of the carbon yarn. As a result, the number of cycles that are necessary for the fibers to rearrange themselves to form a frictional interface layer that is stable is increased. A yarn friction and wear test fixtures were built, whose fixtures were designed in such a way that the yarns or fibers could be contacted at a certain angle, from the quasi-fiber scale. The purpose of this fixture was to investigate the impact that friction frequency

has on the friction behavior of yarns. According to the findings, the number of friction times per unit of time increases as the frequency of friction increases. Additionally, the amount of time required for fiber rearrangement to reach the steady state decreases. However, the total number of friction times does not change, which is further evidence that the friction frequency does not have a significant impact on the behavior of the friction. Tournalonias et al. [75] simulated the friction behavior of warp yarns under different weaving frequencies and used friction energy as a quantitative indicator of inter-yarn friction and wear performance. Other researchers came to the same result from the standpoint of friction energy but came to a different conclusion. According to the findings, the three frequencies of 1.5, 3.0, and 4.0 Hz did not have a significant impact on the coefficient of friction in relation to the amount of energy that was used by friction. In addition, Tournalonias et al. [95] conducted more experiments with fibers and concluded that the variation patterns between friction coefficients and angular displacements under the three friction frequencies were consistent. This was demonstrated in Fig. 1. 7(n).

The prediction of friction behavior relies heavily on pre-tension, which is closely linked to the normal load according to the principles of mechanical equilibrium. The function of this variable in the composite molding process can result in the deterioration of mechanical qualities or even the complete failure of composite products. Studying the impact of preloaded tension on yarn-yarn friction and wear is crucial for optimizing the forming process of textile reinforcements. The researchers Ismail et al [100] utilized an experimental arrangement, as depicted in Fig. 1. 7(o), to investigate the impact of preloaded tension on the frictional qualities of inter-yarns. The findings indicate a reduction in the friction coefficient as the preloaded tension increases. Due to the study's emphasis on the experimental setup and test procedure, the discussion of pre-tension was not extensively addressed. Ismail et al [98] conducted a study to investigate this matter in more depth. They employed a novel characterization technique and compared it to a theoretical model. The findings, depicted in Fig. 1. 7(p), indicate that friction diminishes as pre-tension increases. This phenomenon occurs because the process of increasing the pre-tension reduces the length of contact between the yarns. Consequently, this reduction in contact length results in a decrease in both the size of the contact area and the amount of friction. Moreover, in the friction test conducted between a yarn and a tool, weights are commonly employed to apply pre-tension to the yarns. Wu et al. [25] designed a tension-controlled friction test apparatus using a UMT-TriboLab friction and wear tester to conduct friction testing between carbon fiber yarn and reed. The test parameters were

established based on the pre-tension applied to the yarn during the weaving process. The study examined the impact of pre-tensions of 0.5, 0.7, and 0.9 N on the friction performance of the carbon yarn-reed. The study revealed that the variations in the friction force and friction coefficient of the yarn were not significant across different pre-tensions. This suggests that the selected range of pre-tensions had a minimal effect on the friction behavior of both the yarn and the reed. The capstan friction technique determines the preload tension by applying an external force to the free end of the yarn, known as the input tension.

Additionally, as was noted earlier, the normal load plays a crucial role in the computation of the friction coefficient since it has a considerable impact on the behavior of the friction. An experimental investigation of inter-yarn friction and wear was conducted by Tournalias et al [75,95] under the condition of friction frequency of 0.5 Hz. The purpose of this study was to explore the influence of starting normal load on the friction force  $F_f$  and friction coefficient. The normal loads used in the study were 200, 500, and 800 mN. The results are displayed in Fig. 1. 7(q), which demonstrates that the friction behavior is stable under the condition of a tiny normal load. The analysis indicates that the phenomena may be described by the theory of adhesive contact; however, this theory is not treated in depth in the study. The fixture depicted in Fig. 1. 7(r) was utilized by Wu et al. [25] studied the impact that normal load had on the friction and wear performance of the yarn-tool combination. All the findings indicate that the friction force and the normal load are in accordance with the power function law, which is comparable to the findings than research of Tournalias. By calculating the contact area of the actual and theoretical contact, it is discovered that the normal load is related to the contact area by a power function, and the exponential difference is 0.004; this is supported by the analysis, which suggests that the contact area serves as a key variable of the normal load that affects the friction performance of the yarn. The proposal made in the research, therefore, the power function that was presented in the research is able to more accurately describe the relationship that exists between friction and normal load. The mechanism that governs the impact of normal load on friction behavior is not only relevant to micron-sized fibers, but it is also quite prevalent in the research of friction involving nanosized fibers. The purpose of Ismail et al. [98] was to investigate the impact of normal load on friction behavior. They did this by plotting the trend of friction force within the range of 1 to 10 mN. The findings of this study were in agreement with the research of Tournalias. [52], which stated that the normal load and friction force have a positive proportional relationship. According to Howell's

theory of capstan friction [97,101], when the fibers are subjected to a larger normal load, the contact area and the friction force during friction are both increased. Wang et al. [87] investigated the effect of normal load on the coefficient of kinetic friction of NbTi microfibers with different diameters, and found that the larger the contact area, the greater the friction force that occurs during friction.

#### 1.3.4 Friction analytical models

Scientists have consistently attempted to apply theoretical principles to experiments to gain a deeper understanding of the friction characteristics of yarns. The analytical model may be categorized into three primary models: the Capstan model, the Coulomb model, and the adhesion model. The capstan friction model is employed as an analytical model in ASTM D3108/D3412 to describe the friction that occurs between the yarn and the circular roller. To counteract the frictional resistance of the yarn around the capstan, the output tension  $T+dT$  needs to exceed the input tension  $T$  at the opposite end. The tension in the yarn generated by the change in the normal force  $N$  may be calculated using formula (1).

$$dN = T \sin\left(\frac{d\theta}{2}\right) + (T + dT) \sin\left(\frac{d\theta}{2}\right) \quad (1)$$

Due to the modest size of  $d\theta$ ,  $\sin(d\theta/2)$  may be approximated as  $d\theta$  while disregarding the higher components. Additionally, the primary cause of the rise in tension  $T$  is friction.

$$\begin{cases} dN = Td\theta \\ dT = \mu Td\theta \end{cases} \quad (2)$$

The equation for the winch is obtained by making  $T=T_1$  and  $T+dT=T_2$ :

$$\int_{T_1}^{T_2} \frac{dT}{T} = \int_0^\theta \mu d\theta \quad (3)$$

Solving the above equation yields the winch equation.

$$T_2 = T_1 e^{\mu\theta} \quad (4)$$

where  $\theta$  is the winding angle,  $T_1$  is the input tension and  $T_2$  is the output tension.

The researchers [102] developed a technique for quantifying the coefficient of friction of yarns using the stranding method. The coefficient of friction of the yarns, denoted as  $\mu_{app}$ , may be determined using equation (5).

$$\mu_{app} = \ln\left(\frac{T_2}{T_1}\right) \frac{1}{2\pi n\alpha} \quad (5)$$

here  $n$  represents the twist of the yarn, whereas  $\alpha$  represents the angle between the yarns. The stranding friction model examines the force exerted on the fiber during stranding and stranding methods. It provides a more comprehensive understanding of the mechanical properties of the fiber and yarn during testing. The capstan equation, commonly referred to as Euler's equation, is derived from Newton's second law of motion. However, the inertia tensor components are greatly influenced by the surrounding environment, which restricts the model's application to a certain range [103].

The Coulomb friction model is a fundamental model used to describe the friction behavior between pairs of surfaces. It is widely employed in many friction test techniques [66,92] and may be represented by Equation (6).

$$\mu = \frac{F_f}{N} \quad (6)$$

The variables in question are  $\mu$ , which represents the friction coefficient, and  $N$ , which represents the normal load. Researchers have extensively studied the relationship between friction and normal load using this model. Howell's nonlinear mathematical model, which describes the friction behavior of fiber assemblies, has been widely accepted. Based on Howell's work, Rao et al.[104] developed a friction model specifically for yarns/fibers, as represented by equation (7).

$$F_f = aN^n \quad (7)$$

The friction force, denoted as  $F_f$ , is typically determined by model constants  $a$  and  $n$ . The value of coefficient  $a$  is often influenced by the physical and chemical properties, as well as the morphological traits, of the sample. The value of the exponent  $n$ , which determines the relationship between material qualities and the deformation process, often falls between 2/3 and 1. When the material experiences entire elastic deformation,  $n$  is equal to 2/3. On the other hand, when the material receives complete plastic deformation,  $n$  is equal to 1.

Bowden and Tabor [105] investigated the friction behavior of fibers and found that the friction force mainly consists of two parts, namely, shear force and furrow force:

$$F_f = A_r \tau + P \quad (8)$$

where  $F_f$  is the friction force;  $A_r$  is the actual contact area of the yarn;  $\tau$  is the interfacial shear strength; and  $P$  is the furrow force.

The friction model described above can be applied to friction between yarns as well as friction between yarns and tools. Even though the fiber model is composed of two parts, the furrow force

that is caused by plastic deformation has a negligible impact on the friction force in the actual behavior of fiber friction, and as a result, the role of  $P$  can be practically ignored:

$$F_f = A_r \cdot \tau \quad (9)$$

By disregarding the influence of  $P$ , the fibers may be seen as being in direct touch with each other. According to the Hertz contact theory[106,107], the actual area of contact between the fibers, denoted as  $A_r$ , can be mathematically stated as:

$$A_r = \pi \left( \frac{3F_N R}{4E^*} \right)^{\frac{2}{3}} \quad (10)$$

where  $F_N$  is the normal load,  $R$  is the equivalent radius, and  $E^*$  is the equivalent modulus, denoted as:

$$\frac{1}{E^*} = \frac{1-\nu_1^2}{E_1} + \frac{1-\nu_2^2}{E_2} \quad (11)$$

where:  $E_1$  and  $E_2$  are the elastic modulus of the friction pair;  $\nu_1$  and  $\nu_2$  are the Poisson's ratio of the friction pair.

Since the fiber cross-section changes from circular to elliptical after contact, the equivalent radius  $R$  is expressed as:

$$\begin{cases} R = \frac{1}{R'} + \frac{1}{R''} & \theta = 0 \\ R = \left( \frac{1}{R'^2} + \frac{1}{R''^2} + \frac{2}{R'^2 R''^2} \cdot \cos(2\theta) \right)^{\frac{1}{2}} & \theta \neq 0 \end{cases} \quad (12)$$

where  $R'$  and  $R''$  are the radii of curvature of the two contacting objects, respectively; and  $\theta$  is the angle between the central axes of the fibers.

Tourlonias et al.[103,108] expressed the actual contact area of the yarn as:

$$\begin{cases} A_{r/tow} = 2nA_r & \theta = 0 \\ A_{r/tow} = n^2 A_r & \theta \neq 0 \end{cases} \quad (13)$$

where  $n$  is the number of fiber roots in the yarn, which is calculated by the following equation:

$$n = \frac{W}{d} \quad (14)$$

where  $W$  is the yarn width and  $d$  is the fiber diameter.

Cornelissen et al.[66,92] conducted a study on the friction characteristics of high-performance fibers. These fibers were employed as materials and primarily focused on the sliding friction and

contact mechanics models between the fibers and tool pairs. The researchers developed a contact mechanics model to explain the friction phenomena of the fibers and used this model to forecast friction behaviors in practical situations. The model utilizes an analytical contact mechanics technique to precisely characterize the friction phenomena. It begins by calculating the nominal contact area using Hertzian contact theory, after identifying the relevant contact loads in the system. The model is iteratively refined and enhanced by incorporating experimental data and the theoretical model to finally get a more precise characterization of the frictional interaction between the fiber and tool pairs. Wang et al[109]. created an innovative analytical model using the Hertzian contact theory to explain the friction characteristics between yarns in both orthogonal and non-orthogonal contact scenarios. This model accurately calculates the actual contact area at small and medium scales, while considering the impact of contact angle and fiber arrangement in yarns with varying twist levels. The model enables the analysis of the friction behavior between yarns under various conditions, such as orthogonal and non-orthogonal contact, identical and different twist levels, and identical and different twist directions. These factors are crucial for optimizing the process of forming textile preforms and improving the mechanical properties of composites.

The effect of fiber rearrangement was not taken into consideration by Tournalonias et al[75,108]. while they were determining the number of fibers that were included inside the yarn. Mulvihill et al[65,99]. investigated the friction behavior of the yarn based on the consideration of the contact angle. The findings revealed that the adhesion friction theory was unable to explain all the friction mechanisms that were involved. This was because the fibers slip each other and rearrange themselves to form new contact surfaces under different contact conditions. The purpose of this investigation was to provide a more in-depth explanation of the adhesion friction theory. This is because the fibers are able to separate from one another under a variety of contact circumstances and then rearrange themselves to generate new contact surfaces. Even though it does not fully express the arrangement law of the fibers, the model that is used to describe the arrangement of the fibers in the bundle continues to make use of the assumption that was made before. Following several friction cycles, the yarns are compressed, which leads to the interpenetration of the fiber contact layer between the yarns. This causes the real contact area to vary, and the theoretical friction calculation is subject to variations. The adhesion friction model has some limitations when it comes to accurately describing the friction behavior of yarns. Additionally, it is only applicable to yarns that have a low fiber orientation and are arranged in a parallel and straight fashion.



Furthermore, the analysis of the friction behavior of yarns that have twisted or plied yarns still needs to be improved.

## 1.4 Modeling and simulation of woven reinforcement

### 1.4.1 Modeling and simulation at micro-scale

Yarn, composed of thousands of fibers, is a crucial component in fabric deformation due to the arrangement and interaction between fibers. The relative motion of fibers within a yarn determines the yarn's cross-section shape[110]. Therefore, the mechanical properties of each fiber must be considered. Each fiber can be modeled as a "mechanical element" that can be bent to simulate the relative motion of fibers, reflecting the change in fabric microstructure. However, establishing a micro model involves modeling the behavior of individual fibers and simulating contact friction interaction between them. Currently, three approaches are used to establish the virtual fiber model: digital element approach (DEA), truss element-based approach, and beam element-based approach. The digital element approach breaks the fiber into discrete elements and models the mechanical properties of each element. The truss element-based approach models the fiber as an assembly of interconnected truss elements. The beam element-based approach models the fiber as a beam with nodes at each end.

Zhou et al[111]. expanded the application of the Digital Element Method (DEA) to the level of individual fibers, resulting in the development of the Multi-Chain Digital Element Method. In this paradigm, every skein is depicted as a collection of fibers, with each fiber being represented as a digital chain. The yarn tension and cross-section are dictated by the tension and arrangement of the fibers. The fiber is represented as an elastic component with a circular shape, composed of small cylindrical segments joined together by nodes that have no friction. Fiber contact occurs when fabric is deformed, and when the length of the rod-element becomes very small, the contact may be represented as the contact of nodes, as shown in Fig. 1. 8(a). If the distance between two nodes on the neighboring fibers is less than the diameter of the fiber, a contact element is included in the area of contact shown in Fig. 1. 8(b). Miao et al[110]. enhanced the calculation formula of the contact element and introduced a static relaxation approach to decrease simulation time by 98%. Huang et al[112,113] devised a dynamic relaxation algorithm for a fabric cell with a periodic boundary. This program employs an explicit mechanism to acquire and modify the locations of nodes, as shown in Fig. 1. 9(a). The simulation halts until all nodes reach a state of equilibrium, with more than 80% of the computational time dedicated to identifying the contact area. Dobrich

et al[114–116]. took into account many yarn factors throughout the weaving process, including warp and weft density, yarn size, yarn crimp, and yarn dimension. The microgeometry of fabric acquired using DEA demonstrates exceptional congruity with the physical structure of the woven fabric. The micro-geometries of the fibers acquired from DEA may be utilized for mechanical research, as shown in Fig. 1. 9(b). However, in order to conduct FEM calculations, the fiber-level geometry must be converted into yarn-level geometry. Mazamuder et al[117]. enhanced the technique for generating finite element meshes by dividing the yarn surface into triangular components, eliminating any overlapping or empty spaces between the yarns. The micro-scale fabric structure produced by DEA is utilized for the simulation and prediction of fabric characteristics.

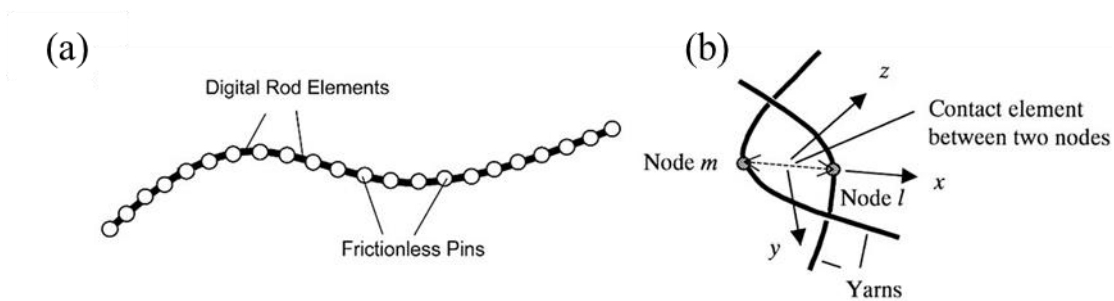


Fig. 1. 8. Basic concepts of the digital element method. (a) Virtual fiber (b) Contact relationship [118].

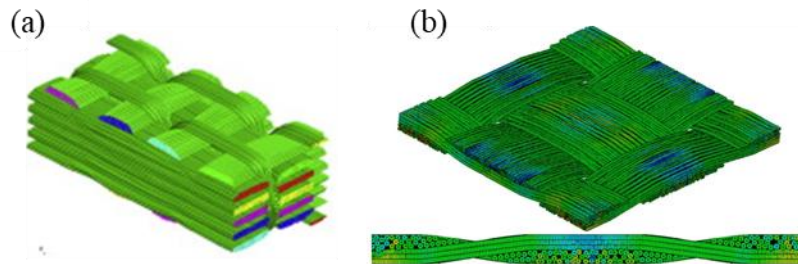


Fig. 1. 9. Different microscopic models based on DEA. (a) Huang's model[113] (b) Döbrich's model[115].

The virtual fiber has a significantly greater diameter compared to the realistic fiber. Therefore, the bending stiffness of the virtual fiber needs to be sufficiently low in order to match the properties of the realistic material. Like the DEA, truss elements likewise possess the property of having zero bending stiffness, and the nodes of truss elements can function as frictionless pins. Daelemans et al[119]. suggested constructing the virtual fiber model using truss elements that have no bending stiffness, as seen in Fig. 1. 10(a). The microgeometry of the 3D woven fabric was created by applying stress to yarn made up of virtual fibers in a loose structure with a circular cross-section. The fabric model was compressed repeatedly until it reached the same thickness as realistic textiles

(Fig. 1. 11(a)). The fabric model exhibited similar mechanical behavior to real woven fabrics, demonstrating the accuracy of the simulation. The Abaqus' general algorithm is utilized to manage the interaction between fibers during the fabric compaction process. Ying et al[120]. utilized a chain consisting of truss components to replicate the characteristics of the fiber, as seen in Fig. 1. 10(b). Within his concept, the physical state following fiber contact may be categorized into two scenarios: relative static and relative sliding, each of which is characterized by distinct frictional relationships. The fiber's equilibrium position is found by computing the nodal force at the contact region. Fig. 1. 11(b) displays the simulated result of the fabric microstructure. Xie et al[121,122]. developed a microscopic model of textiles by utilizing truss elements as virtual fibers to replicate the needling process and compaction characteristics of fabrics, respectively.

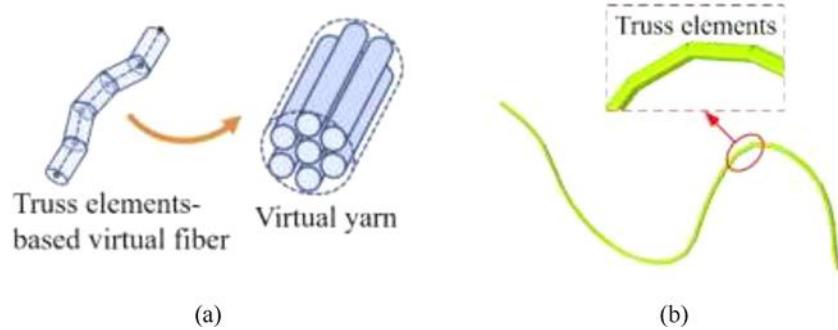


Fig. 1. 10. Diagram of virtual fiber of truss element (a) Daelemans' method[119] (b) Ying's method[120].

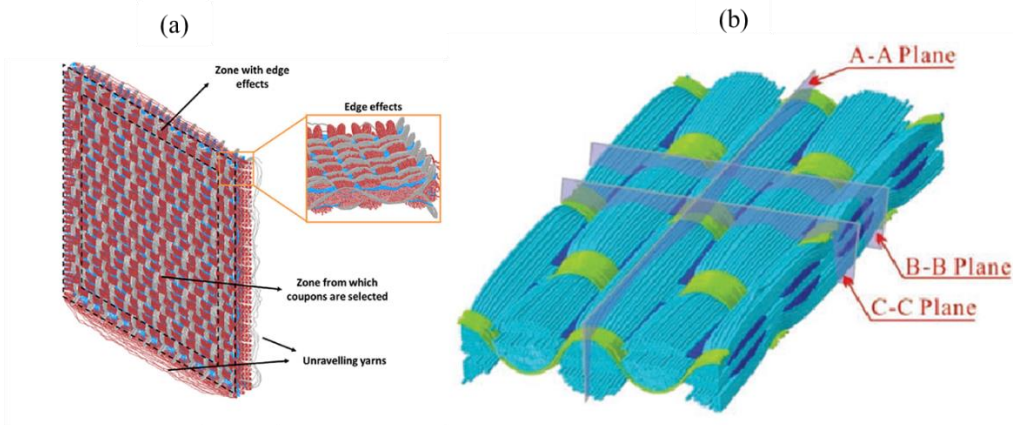


Fig. 1. 11. Different microscopic models based on truss element. (a) Daelemans' model[119] (b) Ying's model[120].

The virtual fibers, constructed using DEA and truss components, have a bending stiffness of zero, leading to an overestimation of the flexibility of the yarn. High-performance yarns possess a certain level of rigidity when subjected to bending, nevertheless, beam components can replicate scenarios involving bending moments. To achieve optimal operational efficiency, the beam element is capable of simulating dozens or even hundreds of virtual fibers, as shown in Fig. 1. 12(a)

and (b). Nevertheless, the virtual yarn possesses significantly greater bending stiffness compared to real yarn, necessitating a reduction in the bending stiffness of the beam element. Mahadi et al[123]. utilized a beam element that lacks pin connections at the nodes to depict the fiber bundle and formulated the kinematic model of a 3D woven fabric. Green et al[124]. enhanced the refinement level of Mahadik's model by reducing it to unit cell size. Durville et al[9,125]. devised an elaborate kinematic beam model that incorporates three vector fields and nine degrees of freedom. This model is capable of accurately replicating the intricate behavior of fibers within a fabric. An essential concern that still should be addressed is the identification and representation of contact friction between fibers. To prevent frequent detection due to the high quantity of fibers, the contact is categorized into two types: local contact between distinct yarns and continuous contact inside the same yarn. A novel geometric contact detection technique is introduced, whereby the contact components are identified inside the region where contact is anticipated. Durville et al[9]. employed this technique to replicate the 3D woven fabric by commencing with an initial arrangement where all strands are situated in a single plane and then progressively diverging following the weaving pattern. The resultant model has the ability to elucidate intricate formations at the fiber level and may be employed to analyze and forecast the mechanical characteristics of textiles. Meier et al.[126] concentrated on the contact algorithm of beam elements and introduced an all-angle contact method that merged the benefits of the current point model and line contact model. This modeling approach allows for the simulation of the mechanical properties of the interior microstructure of the fabric on a fiber-by-fiber basis. However, it requires a significant amount of data for the identification and modeling of contact friction between fibers.

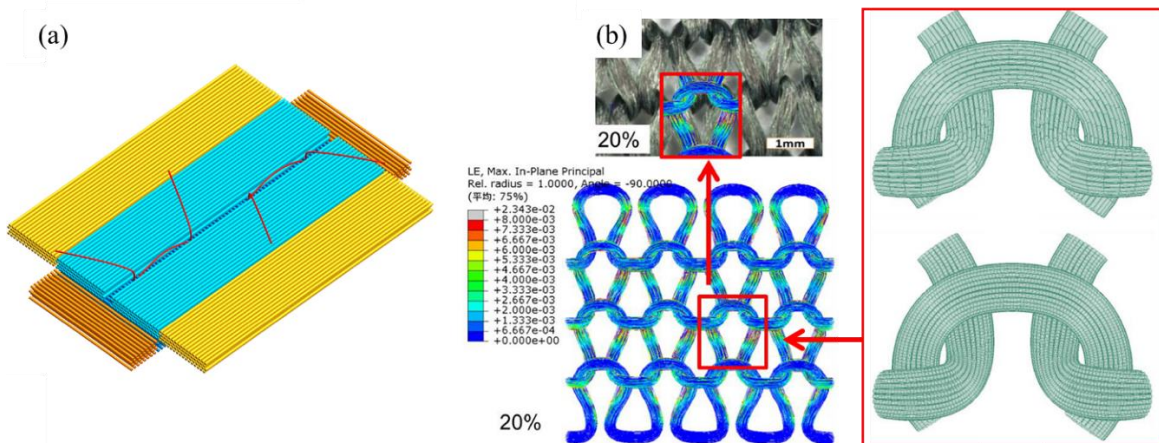


Fig. 1. 12. The virtual fiber models of (a) non-crimp fabric[127] and (b) weft knitted fabric[128].

#### 1.4.2 Modeling and simulation at meso scale

Yarn modeling is a method used to study the internal structure and weaving principle of fabric, aiming to analyze deformation and mechanism at the yarn scale. Mesoscopic yarn models can better describe the discrete internal structure of 3D woven fabric compared to macro modeling. 3D woven fabric has a hierarchical architecture, which can be represented by simple geometries. This allows for a more accurate representation of the fabric's behavior under different conditions, such as tension or compression. By incorporating mesoscopic yarn models into the study of 3D woven fabric, researchers can gain a deeper understanding of its mechanical properties and potential applications[126]. Geometrical approaches are the earliest method applied to the numerical representation of fabrics based on Pierce's model, which idealized assumptions on yarn path and cross-sectional shapes[129,130]. These assumptions are still widely used in textile preprocessing procedures. However, idealized models only consider the topological structure of the fabric and do not consider the complexity of the structure or the contact of the yarn. This can lead to interpenetration at the contact areas between the yarns, resulting in unrealistic fiber volume fractions and voids. Therefore, idealized geometry methods are not accurate for simulating 3D woven fabric. More advanced modeling techniques, such as finite element analysis or computational fluid dynamics, can provide a more realistic representation of the fabric structure by considering the actual physical interactions between yarns. These methods allow for a more accurate prediction of the mechanical properties and behavior of 3D woven fabrics under different conditions.

There are two major challenges: uneven yarn cross-section and interpenetration between yarns. Geometric approaches can control the yarn path and cross-section based on specific geometric rules, use contact algorithms to avoid interpenetration, or reconstruct the yarn geometry structure by CT scanning. These approaches can be classified into three types: analytic geometry, physics-based methods, and reconstruction methods. The analytic geometry approach primarily employs geometric calculations to simulate the variations in the curvature of yarn inside the fabric. By using geometric characteristics obtained from micrographs, it is possible to generate a model that is comparable to the actual fabric. Sagar et al[131]. introduced an improved configuration of the yarn trajectory using polynomial equations, while considering the many ways in which the yarn might deform, including tensile, bending, and compression. This approach is utilized mostly for predicting the non-linear characteristics of yarns that cannot be adequately characterized using

conventional geometric methods. It involves energy minimization. Both the Wisetex and TexGen applications utilize a comparable mechanism for constructing textile Representative Volume Elements (RVEs), based on this approach.

Wisetex was created by Lomov et al[132]. to simulate the structure of several types of 3D woven textiles. When calculating the yarn trajectory, it takes into account several aspects, including yarn characteristics, weave pattern, and mechanical behavior. This is done by reducing the bending energy of the yarns. Nevertheless, the shape of the yarn cross-section remains consistent and optimal, regardless of whether the fabric is deformed or undeformed. This consistency, however, leads to a decrease in the accuracy of predictions in the subsequent finite element processing. Lin et al[133]. proposed a method for representing the geometric characteristics of fabric structure. The trajectory of the yarn was shown using splines and dictated by the fabric's characteristics. The yarn's cross-section was represented as a symmetrical shape and modified in certain areas using the experimental photographs as a reference. The implementation of this strategy was carried out in TexGen. Other researchers used the analytic geometry method is a method used to simulate the curve change of yarn in a fabric through geometric calculation and combining geometric parameters from micrographs[134,135]. Sagar et al[38,120,136]. proposed an improved yarn trajectory geometry utilizing polynomial equations and taking into account deformation phenomena such as tensile, bending, and compression. This method is employed to predict the non-linear characteristics of fibers that cannot be effectively characterized using conventional geometric methods. The final model can be shown as Fig. 1. 13(a). Hivet et al[134]. examined the impact of yarn contact on the shape of their cross-section. The contact region is categorized and shown by distinct curves in order to guarantee the absence of any interpenetration between the warp and weft yarns. The model's parameters are determined based on experimental data utilizing various optical methods, and the spacing between the warp and weft yarns is consistent with real-world conditions. Isart et al[135]. introduced an analytical model that utilized sinusoidal functions to depict the variation in curvature throughout the length of yarns. This model was integrated with the geometric data from micrographs to accurately characterize the fabric's geometry. The resultant elastic characteristics were determined by finite element studies, which corresponded with the geometric structure and fiber area percentage of genuine fabric. The results showed good agreement between the predicted and measured fabric behaviors.

The physical method focuses on treating the contact area to avoid or eliminate interpenetration between yarns.

Wendling et al[137]. developed a CAD based on catia v5 to model the structure of 3D woven fabric at the yarn level, accounting for all contacts and classifying them into weave interlacing, warp lateral, and weft longitudinal contacts. This modeling ensures tangency between yarns and variable cross-section shape along the path, as shown in Fig. 1. 13(b). Wintiba et al[138]. employed implicit geometry to describe yarn movement under different tensions, eliminating residual interpenetration using a level set method and adding a small gap between yarns to achieve a realistic fabric unit cell, as shown in Fig. 1. 13(c). Nilakantan et al[139]. proposed a "thermal growth" approach to generate realistic virtual meso structures of 3D woven fabric. The yarns were modeled with an orthotropic thermoelastic material, and the material properties were defined along the three yarn axes (length direction, width direction, and thickness direction). The contact algorithm was defined on the surface of yarns to prevent interpenetrations. The final simulation result is shown in Fig. 1. 13(d). Pierreux et al[140]. presented an approach to describing cross-section variations in yarns, representing weft and binder yarns by discretized boundary- and inner-line lines based on geometrical frameworks. The shape of yarn with different fiber fraction and tensioning can be obtained, resulting in the simulated RVEs, see Fig. 1. 13(e).

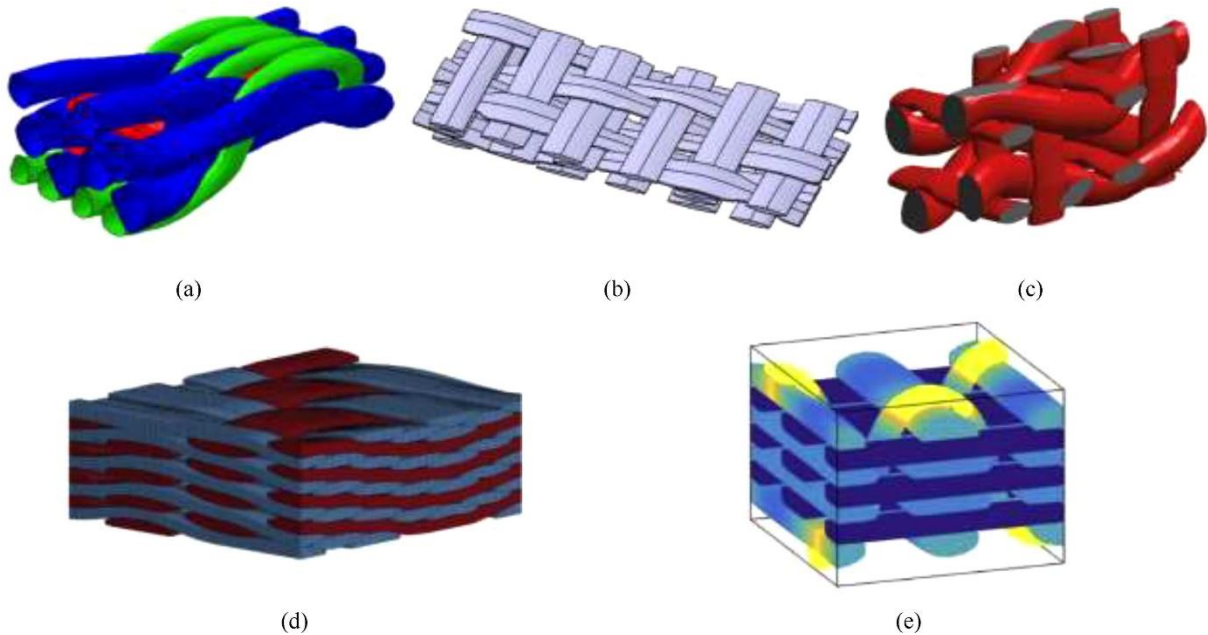


Fig. 1. 13. The simulation results of 3D fabric meso-geometry by different geometric methods. (a) Stig's model[136] (b) Wendling's model[137] (c) Wintiba's model [138] (d) Nilakantan's method [139](e) Pierreux's model[140].

Micro-scanning modeling involves creating a geometric model of fabric using photographs collected using micro-CT. This model is then used to generate a finite element model that can predict the mechanical behavior of the fabric[141]. Fig. 1. 14. displays the scanning reconstruction results of a 3D orthogonal woven fabric as an example. The micro-CT equipment's excellent spatial resolution enables a thorough examination of the fabric's interior structure. Not only can it reconstruct the yarn structure in textiles and preregs, but it can also distinguish between the fibers in the yarn. Furthermore, micro-CT has the further advantage of being able to non-destructively reconstruct the internal structure of the material. This means that the scanning procedure will not do any damage to the original fabric structure. Desplentere et al[142]. investigated the capability of micro-CT to reconstruct the micro-structure of 3D woven cloth. Badel et al[143]. examined the arrangement of fibers in the yarn using microscopic scanning photographs. They also developed a structural model to simulate the deformation of textile materials. Multiple methods are available for reconstructing structures from micro - CT images. Most micro-scanning reconstruction modeling procedures may be divided into four distinct steps: (I) Apply image processing techniques to enhance the quality of the image. (II) Generate a three-dimensional geometric configuration. (III) The process of dividing an image into multiple parts and extracting characteristics to differentiate between the various components and orientations of fibers. (IV) Utilizing finite element analysis to forecast different performances. The distinction among the various approaches mostly lies in the initial three phases. In the process of picture segmentation, it is straightforward to differentiate between warp and weft strands in 2D woven fabric due to their distinct orientations. However, in the 3D fabric, the binder and warp yarns are aligned in the same direction and have extensive contact surfaces, preventing any separation. Naouar et al[144–146]. suggested an image segmentation approach utilizing the Grey Level Co-occurrence Matrix (GLC Matrix) to distinguish between warp, weft, and binder yarns. This method aims to construct a meso-structural model of the 3D orthogonal textile. Fig. 1. 15(a) represents the finite element model shown in Fig. 1. 14. This approach is appropriate for 3D woven textiles that have complex internal structures. It allows for accurate prediction of mechanical properties and behavior under various loading conditions.



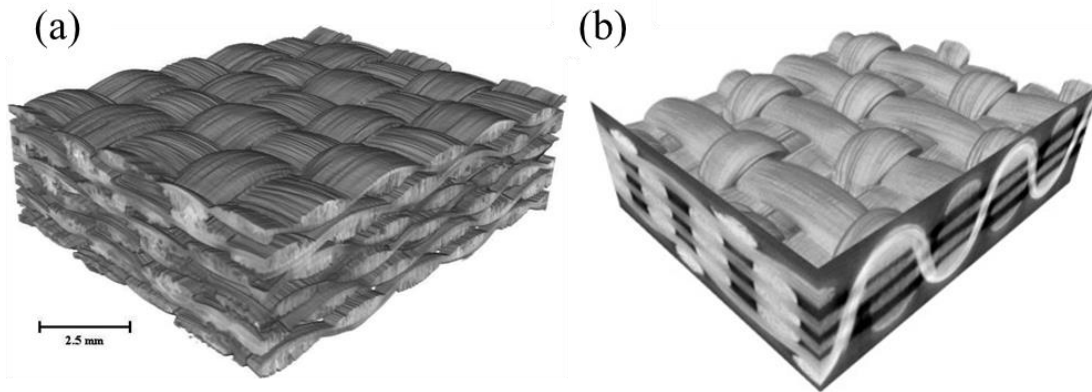


Fig. 1. 14. (a)3D reconstruction of the six layer dry preform[147]; (b) 3D tomography reconstruction of orthogonal non-crimp woven fabric image[144].

Straumit et al[148]. proposed an approach for determining the fiber orientation using a structural tensor. Additionally, the photograph is partitioned into distinct segments through the process of clustering. The yarns may be extracted from the photograph, allowing for differences between yarns that are oriented in various directions. The finite element cell model is automatically generated using the voxel approach, as shown in Fig. 1. 15(b). Huang et al[149]. conducted a study on a method which employed micro-CT scanning to create a geometric model of a textile at the meso-scale. This involved analyzing 3D microscopic photographs, as seen in Fig. 1. 15(c). The investigation also involved the development of a modeling platform named CompoCT. The key aspect of this approach is the ability to segment a photograph at a low resolution and build a set of processes to evaluate the correctness of the geometric model. Nevertheless, manually separating the yarn in the photograph still requires a significant amount of effort. Wijaya et al[150,151]. introduced an approach to distinguishing various pieces of information in CT scan with a relatively low level of detail. The approach utilizes grayscale data from photographs to extract the yarn from the airspace and identifies the warp and weft yarn by employing structural tensor analysis. The outcomes of photograph processing are utilized to generate a finite element model for compaction simulation and a voxel model for flow simulation. Fig. 1. 15(d) shows the finite element model that has been generated. Wintiba et al[152]. introduced a computerized approach for producing meso-structure from micro-CT scans of 3D woven textiles. This approach uses the level set method from the author's earlier research. Fig. 1. 15(e) displays the meso geometric model. The approach utilizes voxel-based smoothing processing to extract the explicit geometry of yarn and then convert it into implicitly smoothed geometry. This approach prevents the interlocking of the yarns and takes into consideration the impact of the local fiber volume ratio. The meso-scale models, utilizing micro-CT scans, precisely simulate the internal structure of the fabric. This approach

allows for the accurate reconstruction of the fabric's geometric structure and effectively prevents the cross-section of yarns. Ricks et al[153]. presents experimental observations of damage states in unnotched and notched 3D orthogonal woven coupons loaded in tension using X-ray computed tomography (CT) scanning and anisotropic analysis. The results of the anisotropic analysis were found to be in good agreement with the experimental data, indicating that the anisotropic analysis provides a reliable method for estimating the damage states of the coupons, shown as Fig. 1. 15(f). Nevertheless, this technique is limited to examining the current fabric and does not possess the capability of predicting aspects. Simultaneously, the expensive nature and the time-consuming nature of post-processing micro-CT image analysis limit the utilization of this approach.

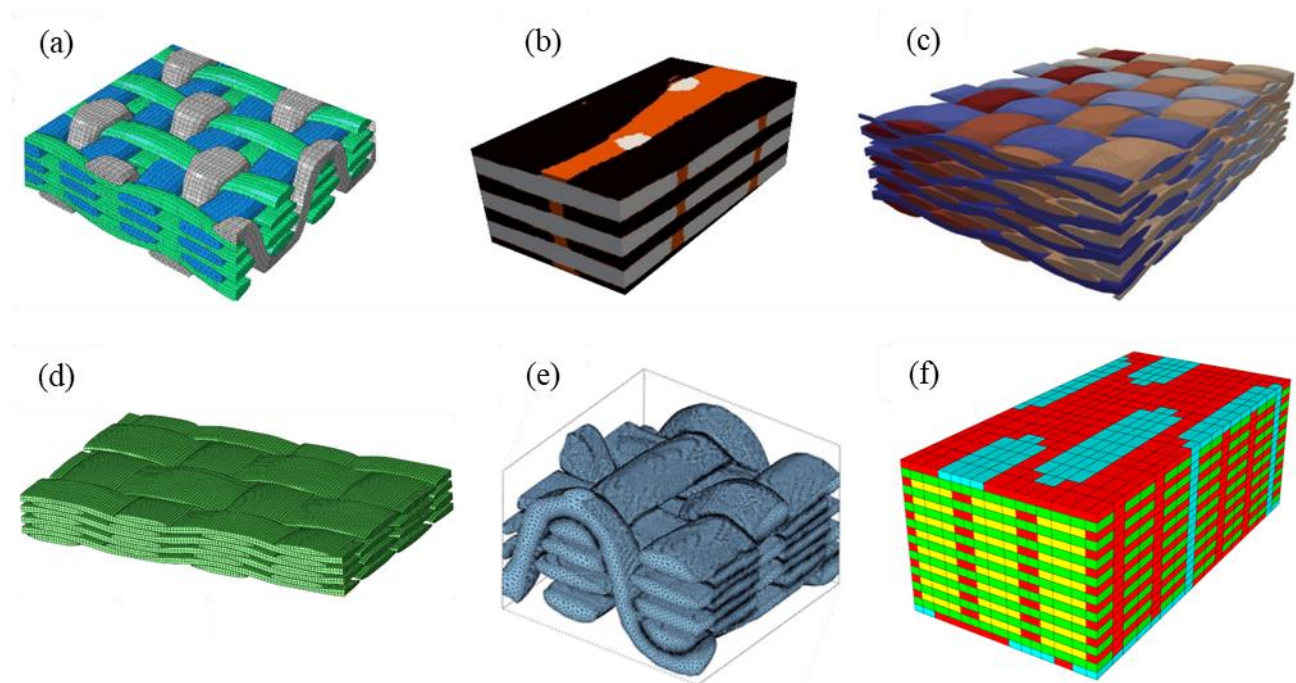


Fig. 1. 15. The different reconstruction results of 3D fabric using micro-CT. (a) Naouar's model[144] (b) Straumit's model[148] (c) Huang's model[149] (d) Wijaya's model [150] (e) Wintiba's model[152] (f) Ricks's model [153].

#### 1.4.3 Modeling and simulation at macro-scale

The macroscopic modeling of 3D woven textiles generally uses traditional finite element models for investigating the deformation behavior and overall fabric behavior[153]. 3D woven fabric is not classified as a thin plate - like 2D fabric due to the inclusion of through - thickness processes. Alternatively, it is represented using 3D solid-shell finite elements, which combine with certain constitutive laws to precisely represent mechanical behavior. The advancement of the macro model involves improving the 3D solid shell finite element model and the constitutive rule. The objective is to predict the phenomenon of wrinkling during deformation, which arises from

the sliding movement between yarns. Tensile stiffness, in-plane shear stiffness, and bending stiffness are three essential factors in the mechanical modeling of fabric deformation[154]. Hence, it is important to consider the impact of bending stiffness and tension-shear coupling while enhancing the model.

The development of three-dimensional (3D) entity shell components in 1998 has had a significant effect on the micro-scale modeling of materials. In the last two decades, several 3D entity shell elements have been suggested, such as the low-order hexahedral entity shell element and the 8-node hexahedral entity shell finite element. De Luycker et al[155]. introduced a unique hexahedral entity shell element composed of fiber segments. This technique, known as semi-discrete modeling, takes into account the dispersion of fibers, as shown in Fig. 1. 16. Bassa et al[156]. introduced a 9-node hexahedral finite element. This element consists of 8 nodes located at the vertices, each having 3 degrees of freedom for translation. Additionally, there is 1 node positioned at the center of the unit cell, which has 1 degree of freedom for translation along the thickness direction. Flores, Ko, and Lee et al[157,158]. have devised numerous elements to deal with shear locking and thickness locking in materials. Flores suggested using a 6-node prismatic element as a means to prevent lateral shear locking and minimize Poisson locking. Ko and Lee [158] proposed the utilization of a 6-node triangular solid-shell element to mitigate shear locking and address thickness locking by employing assumed strain and improved strain strategies. Xiong et al[159]. have recently created a new type of finite element called a 7-node prismatic solid-shell finite element. This element is an improvement on the DKT6 plate finite element and enhances the behavior of the element through its thickness by including a translation factor in the direction of the thickness. This element is utilized for simulating the properties of fiber-reinforced thermoplastic composite prepregs, as shown in Fig. 1. 17.

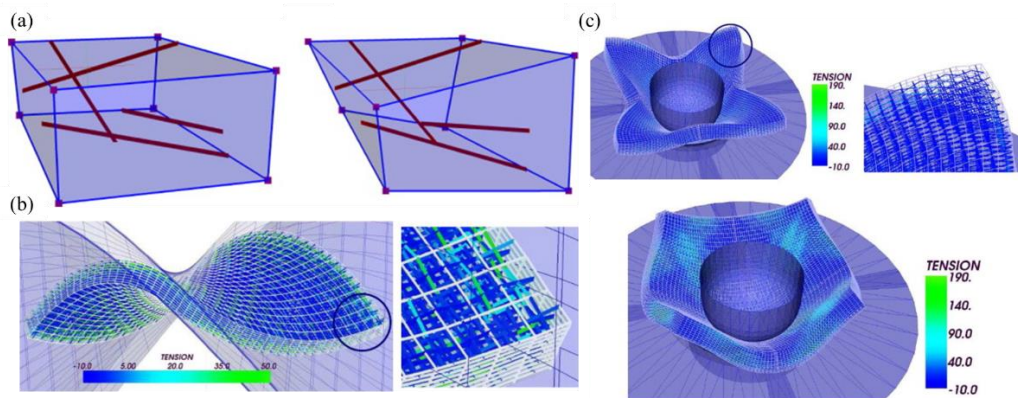


Fig. 1. 16. Height node hexahedral finite element containing fibrous yarns (a) Initial and deformed, (b) Simulation of hemisphere formability and (c) Forming of a twisted plate[155].

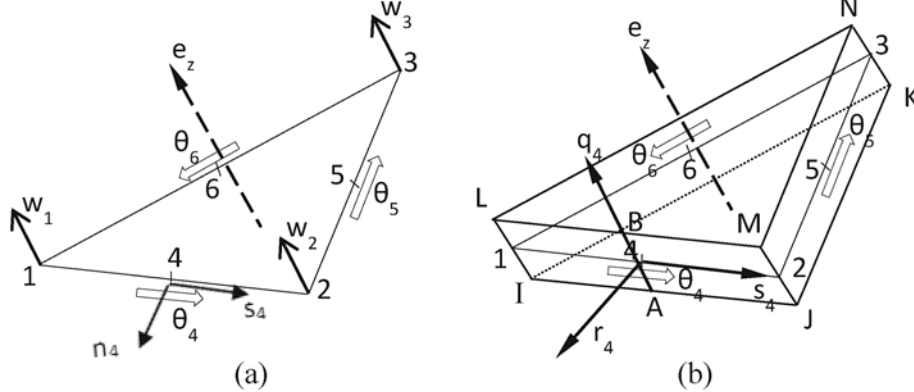


Fig. 1. 17. (a) DKT6 plate finite element, (b) corresponding prismatic element[159].

3D woven fabric, although it seems continuous on a large scale, is distinct from other continuous materials because of its interior individual fibers. Constitutive laws are made that assume the elasticity of fiber-reinforced materials during the forming process so that they can accurately describe their unique mechanical properties. These laws include hypoelastic, hyperelastic, and second-gradient materials[160]. The hypoelastic constitutive law, often referred to as the rate constitutive law, is a commonly employed approach for modeling the mechanical properties of a continuous material under significant strain, specifically for simulating its isotropic behavior. The analysis focuses solely on the tensile stiffness of 3D woven fabric and disregards intricate secondary rigidities such as the transverse compression rigidity of yarn and friction between fibers. De Luycker's model was utilized for the process of producing 3D interlock fabric[155,161]. Khan et al[162]. introduced a hypoelastic constitutive law that depends on warp and weft fiber rotation tensors. In contrast, Dörr et al[163]. provided a viscoelastic method that separates the decoupled bending behavior from the membrane behavior in order to predict wrinkles during the forming process.

Wrinkling arises in the process of creating 3D woven fabric as a result of the fibers moving and having low bending stiffness. Charmetant et al[164]. introduced a transversely isotropic hyperelastic constitutive model to represent the layer-to-layer angle interlock, enabling the simulation of hemisphere formation and three-point bending. Pazmino et al[165]. enhanced this model by including both in-plane and out-of-plane deformation processes to analyze the formability of 3D orthogonal woven fabrics. Mathieu et al[166]. conducted a study on simulating the bending behavior of 3D woven materials. They developed a hyperelastic constitutive law that incorporates local bending stiffness. Yao et al[167]. introduced a hyperelastic constitutive model

that incorporates tension-shear coupling to accurately represent the nonlinear big deformation and tension-shear coupling characteristics. It is possible that the second-gradient constitutive rule can explain the mesoscopic mechanical properties of 3D woven fabric, such as the relative slipping of yarn and shear in the plane. Madeo et al[168]. introduced a 3D second-gradient constitutive equation that takes into account the bending stiffness of yarns, resulting in improved accuracy in predicting macroscopic bending. Barbagallo et al[169]. introduced a mathematical equation for the strain energy density, which is derived from the continuous model using the second-gradient theory. This equation considers the in-plane shear deformation, variations in bending stiffness, and the imaginary elongations in both the warp and weft directions. The constructed model not only aligns with the experimental data but also accurately predicts the deformation. The impact of the model is seen in Fig. 1. 18. Simultaneously, the second-gradient model's ability to accurately predict the macroscopic bending modes was demonstrated, taking into account the unique characteristics of fibers.

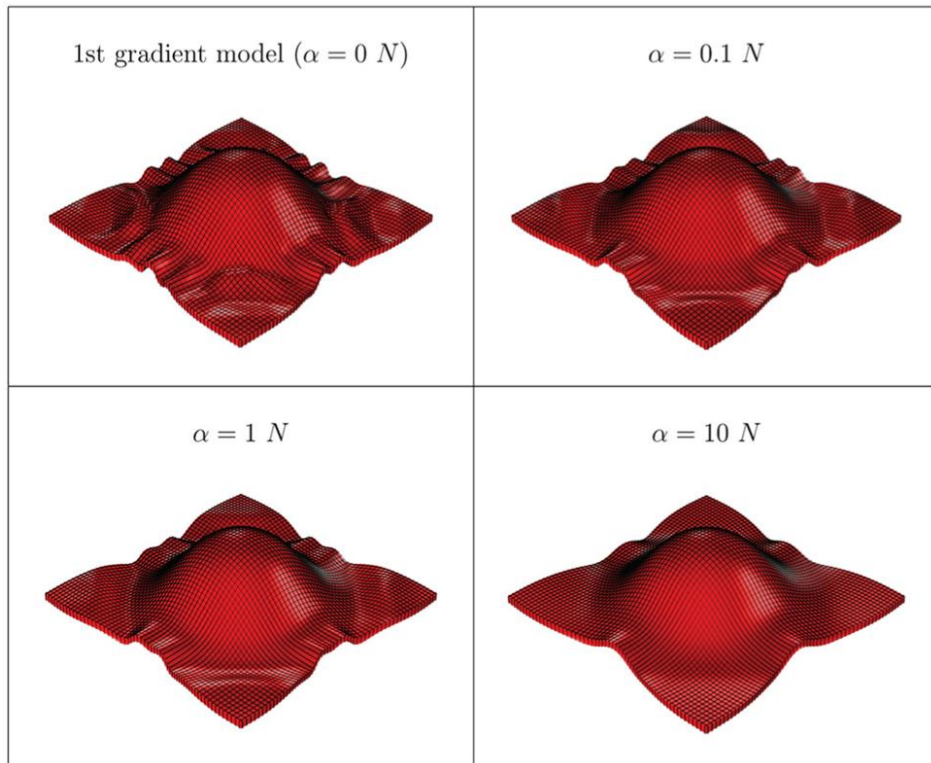


Fig. 1. 18. Influence of shear angle on the onset of wrinkling using the second gradient model[169].  
1.5 Summary of Chapter 1

Textile composites have been widely used in aerospace, automotive, shipbuilding and construction fields due to their high specific strength, high specific modulus and high designability. At present, China has independently developed a variety of complex structure three-dimensional

fabric reinforced composites, which have been successfully applied to the fields of Chang'e satellite, Shenzhou spacecraft, high-speed missiles etc. Preforms are the reinforced skeleton of textile composites, and yarns, as the basic unit of preforms, lose up to 5%-30% of their mechanical properties due to friction, compression and bending in the process of weaving and forming. Among them, the mechanical properties loss rate due to friction is as high as 9%~12%. At present, in order to meet the requirements of component properties design, all production units are forced to use costly yarns to compensate for the loss of mechanical properties of composites caused by friction during weaving. Especially, during the beating stage of the 3D orthogonal weaving process, since multilayer weft yarns need to be introduced all at a time for each beating, it is necessary to apply a larger beating force than the 2D weaving process. Many fuzzes appear on the surface of the fabric. Therefore, a thorough understanding of the frictional behavior at the fiber and yarns level is necessary, especially for complex structures like woven fabrics, braided fabric and tufted fabric, etc. Indeed, the following scientific problems in friction are not discussed and proposed:

- The relationship between contact deformation and friction behavior of yarns under different working conditions.
- The mechanical behavior under different weaving modes.
- The meso-friction digital simulation model was established to verify the weavability of the yarns

In part 1 of this chapter, the research of composites and their practical uses presents a domain replete with both obstacles and prospects. It has a high specific strength, specific modulus, fatigue, corrosion resistance, structural designability, and so on, and many other advantages, at the same time, the textile composites also exhibit good impact resistance, At the same time, this composite also exhibit excellent mechanical properties such as good impact resistance and high damage tolerance. Then, it is essential to investigate the friction and wear behavior of yarns throughout the process of 3D textile precast body forming. This will allow for the quantitative evaluation of yarn damage, the optimization of the process of 3D textile precast body forming, and the enhancement of the mechanical characteristics seen in composites. Finally, the existing numerical methods are summarized in three different scales, and the advantages and disadvantages of each scale are summarized separately. To study the friction behavior in a more complete and detailed way, a multi-scale approach needs to be employed.

# **Chapter 2 Yarn to Yarn Friction Analysis Considering the Weaving Process of Textile Fabrics at micro-meso scale**

## Résumé en français

L'analyse des caractéristiques mécaniques des fibres et des fils est essentielle dans le processus de production des composites renforcés par des fibres. Ce chapitre explore les modèles analytiques et la validation expérimentale de la friction des fils pendant le tissage des tissus textiles. Les dommages subis par les fils sont accentués pendant le processus de tissage, en particulier entre les fils de chaîne et de trame, ainsi qu'entre les fils de liage et de trame dans le tissage tridimensionnel (3D) orthogonal. Les angles de contact entre les fils de trame et de chaîne, qu'ils soient orthogonaux ou non, jouent un rôle crucial dans ces dommages. Environ 5 à 30 % de la résistance mécanique est perdue pendant le tissage en raison de la friction, de la compression et de la flexion, la friction représentant jusqu'à 9 à 12 % de cette perte totale. Ainsi, il est impératif de se concentrer sur le comportement de friction des fibres ou des fils pendant le tissage pour le développement de composites performants.

Les recherches sur les propriétés de friction des fibres ou des fils ont commencé vers le milieu du XXe siècle. Les techniques actuelles de mesure de la friction comprennent le pull-out, le capstan, le yarn-twist, la friction réciproque rotative et la friction réciproque linéaire, offrant une grande précision et une large gamme d'applications. Des études récentes, telles que celles de Tournalias et al., ont démontré que le coefficient de friction diminue avec l'augmentation de la charge normale tout en restant insensible à la fréquence d'oscillation. Ismail et al. ont étudié la friction dynamique entre fibres individuelles sous pré-tension, montrant que la déformation élastique de la zone de contact est plus significative que l'effet d'enroulement, créant ainsi la zone de contact où se produit le cisaillement interfacial.

Pour améliorer la précision des modèles de friction, des études spécifiques sur les paramètres microscopiques tels que la largeur de contact et le nombre de fibres en contact sont nécessaires. Wu et al. ont développé un modèle expérimental pour calculer le nombre de filaments en contact et la surface de contact réelle en utilisant le modèle de contact de Hertz. Les résultats montrent que la force de friction suit une loi de puissance par rapport à la charge normale. De plus, Tournalias et al. ont exploré l'effet de l'angle de contact entre deux fibres et deux fils en utilisant la théorie de l'adhésion pour expliquer les changements observés.

Le comportement mécanique des fils tordus diffère considérablement de celui des fils non tordus, influençant les propriétés de friction de manière significative. La zone de contact des fils est également affectée par l'interaction de nombreuses fibres, la disposition des fibres à l'intérieur des



fil et leurs caractéristiques mécaniques. Des recherches antérieures ont montré que la déformation migratoire se produit dans les fils après la mise en charge, entraînant une disposition complexe des fibres à la surface de contact. Cependant, il y a encore un manque de recherche systématique sur la corrélation quantitative entre les méthodes d'arrangement des fibres et la zone de contact des fils.

L'objectif de cette étude est d'examiner les caractéristiques de friction des fils tordus dans des conditions non parallèles lorsqu'ils sont soumis à une charge normale. Un modèle mathématique a été formulé pour caractériser la transmission de la friction indépendamment des variations d'angles et de torsion. La validité de ce modèle est confirmée par des recherches expérimentales. Le modèle est utilisé pour prédire le comportement de friction des fils avec des niveaux de torsion identiques et variés.

Une analyse expérimentale a été menée pour étudier la variation de la surface de contact des fils sous différentes conditions d'angle de contact et de pré-tension. Les résultats montrent que la surface de contact diminue avec l'augmentation de l'angle de contact et augmente avec l'augmentation de la pré-tension. L'orientation des fibres est un facteur clé influençant la surface de contact entre les fils et les rouleaux. Les résultats expérimentaux ont été comparés aux modèles théoriques basés sur la théorie de contact de Hertz, montrant une bonne concordance, bien que des différences subsistent en raison de l'orientation des fibres.

Un modèle analytique modifié a été développé pour tenir compte de l'orientation des fibres et améliorer la prédiction de la surface de contact des fils. Ce modèle a été validé par des tests expérimentaux, montrant une meilleure correspondance avec les résultats expérimentaux par rapport au modèle de Hertz. La modélisation analytique a également été utilisée pour prédire le comportement de friction des fils avec des torsions similaires et différentes, démontrant l'impact significatif du niveau de torsion et de l'angle de contact sur la force de friction et le coefficient de friction.

En conclusion, l'étude du comportement de friction des fils dans les composites renforcés par des fibres est cruciale pour optimiser le processus de formation des préformes textiles et améliorer les propriétés mécaniques des composites finaux. Les recherches futures devront se concentrer sur le développement de modèles numériques pour quantifier l'effet des processus d'adhésion sur le comportement de friction et explorer les impacts de l'usure et de la taille des fils. Cette étude fournit une base solide pour de futures explorations et analyses de systèmes de couplage complexes,

offrant des perspectives précieuses pour la compréhension des mécanismes sous-jacents et l'amélioration des performances des composites textiles.

## 2.1 Introduction

The mechanical characteristics of fiber and yarn are crucial in the production process and play a significant role in the development of fiber-reinforced composites. The damage to the yarns will be aggravated during the weaving process, especially between the warp and weft yarns, as well as between the binder and weft yarns in three-dimensional (3D) orthogonal weaving[34–36]. The difference lies in the way they come into contact, and they can generally be categorized based on the different contact angles between the weft and warp in a plane coordinate system, namely orthogonal and non-orthogonal. Fig. 2. 1 illustrates typical patterns of damage, which primarily occur during the weaving and beating stages. The contact angle between the weft and warp has a normal distribution, indicating that the yarns in the center region are in orthogonal contact, whereas in other regions, they are in non-orthogonal contact. Approximately 5–30% of the mechanical strength is lost during weaving as a result of friction, compression and bending, with friction accounting for as much as 9–12% of the total loss[2,104,170,171]. Therefore, it is imperative to focus research on the friction behavior of fiber or yarn during the weaving process for the development of composites.

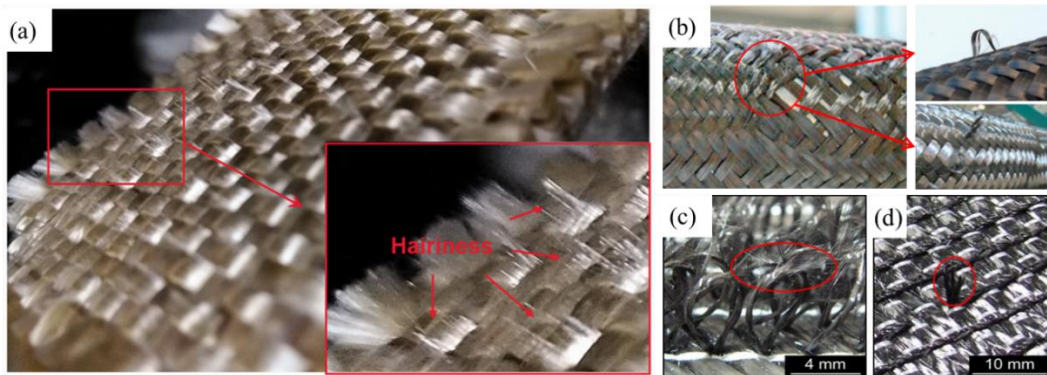


Fig. 2. 1. Evidence of damage on fibers during weaving[59,172].

Investigation into the frictional properties of fibers or yarns commenced around the mid-twentieth century, with many research teams in the textiles industry putting four various measuring techniques [68,173]. Currently, the prevailing research techniques for measuring friction in fibers or yarns include the pull-out [65,66], the capstan [74,174], the yarn-twist [96,175], the rotating reciprocating friction [75,176,177], and the linear reciprocating friction approach [122,173,177], among others. These approaches have a diverse array of applications and exceptional precision. Furthermore, Tournalias et al.[75] conducted a study to investigate the friction interactions between warp yarns and devised a kinematic experiment to accurately replicate the weaving motion of these yarns, particularly under unique working situations. The results demonstrate that

the coefficient of friction diminishes as the normal load increases, while remaining unaffected by the oscillation frequency. Ismail et al. [98] conducted a study on the dynamic friction between fibers, specifically focusing on the interaction between single fibers when subjected to pre-tension. They developed an experimental setup and analytical method to investigate the friction behavior. The study found that the elastic deformation of the contact area is more significant than the 'wrapping effect', and this deformation creates the contact area where interfacial shear occurs. The indicated work is founded on the notion of friction between two fibers in a straight motion to quantify [97,174]. However, the author is unaware of any systematic discussion on the impact of twist on friction behavior under different pre-tension and normal loads, specifically focusing on detailed parameters at the microscale, such as contact width, realistic contact area, and number of contact fibers. Although these parameters have been proposed in certain previous studies [174,178–180], they have not been thoroughly examined.

Regarding the specific parameters involved in the friction process, the only documented study pertains to twistless yarns, namely M55JB, T1100, and T300 from Toray [25,108], as well as HTS40 from Toho Tenax[95,177], etc. Wu et al. [25] established the experimental apparatus and computed the accurate count of contact filaments and actual contact area using the Hertzian contact model. The results show that the friction force  $F$  versus normal load  $N_{tow}$  curves followed power law descriptions,  $F$  being proportional to  $N_{tow}^{0.734}$  for the investigated carbon tow. Tournalias et al. [108] investigated the effects of the contact angle between two fibers and two tows in order to explain the changes achieved via the application of the adhesion theory of friction using a fundamental analytical model. When the fibers are aligned in parallel, the friction is significantly increased. This is because there is a larger contact surface at  $0^\circ$  and the adhesion between fibers at the interface of the tows is enhanced. The mechanical behavior of twisted yarns differs significantly from twistless yarns, resulting in unique properties during friction that are currently not well understood and require further investigation to develop a more precise analytical model. Furthermore, the contact area of the yarn is influenced by the interaction of many fibers. Recent research has focused on how the fibers are arranged inside the yarns and their mechanical characteristics. Bowden and Tabor discovered that migration deformation takes place in yarns after forcing, resulting in a very intricate fibers arrangement inside the contact surface. Mulvihill et al. [65,99] examined the contact surface of monofilaments by using a semi-reflective film on a glass plate, which discovered that the contact area of fibers deviated substantially from the theoretically

estimated value as the normal load increased. Turlonias et al. [108] found that fibers adhered to each other, with maximal contact area occurring at a contact angle of  $0^\circ$ . Previous research has shown a link between fiber and yarn contact surfaces, highlighting the significant impact of fiber contact area on yarn contact area. However, there is not enough research on the quantitative correlation between fiber arranging methods and yarn contact area.

As mentioned in the literature, research on the friction characteristics of yarns requires excluding the influence of wear, which encompasses two fundamental principles in tribology. Therefore, the objective of this study is to investigate the friction characteristics of non-parallel circumstances between twisted yarns when subjected to a normal load. We have formulated a mathematical model that accurately characterizes the transmission of friction, independent of varying angles and twists. The implementation of this model begins by analyzing the contact between fibers. It then applies the Hertzian contact theory to define and calculate the relevant parameters involved in the friction process. In order to enhance the accuracy and simplicity of the calculations, more associated factors are incorporated into this model. Subsequently, the validity of this model is confirmed by experimental research. The model for non-parallel situations is utilized to predict the friction behavior of yarns with both identical and varying twist levels. The friction analysis model we have created, incorporating the twist response, serves as a crucial connection between practical and theoretical study. This model is vital for optimizing the textile preform forming process and improving the mechanical characteristics of composites.

## 2.2 A modified contact model of single non-twisted yarn

To investigate the fiber contact mechanism and improve the prediction accuracy of yarn contact area, in this section, the image analysis method is used to calculate the fiber orientation and fiber contact area in the contact surface; using the self-made friction test device, we study the contact area change rule between carbon fiber yarn and round rollers under different contact angles and pre-tension conditions. A prediction model was established considering the fiber orientation, which provides a theoretical foundation for the research of friction and wear in the weaving process.

### 2.2.1 Modified model based on Hertz contact principle

The Hertz contact theory model is used to validate the experimentally measured yarn-roll contact area [106,170]. Assuming that the fibers are smooth cylinders and that the fibers in the yarn are all aligned in parallel, the contact half-width between the fibers and the contact roll is given by equation (15) [99,181]:

$$a = \left( \frac{3N_{fil}R^*}{4E^*} \right)^{\frac{3}{2}} \quad (15)$$

where  $N_{fil}$  is the normal load acting on the fiber,  $R^*$  is the equivalent radius of the contact surface and  $E^*$  is the equivalent Young's modulus, expressed as equation (16):

$$\frac{1}{E^*} = \frac{1-\nu_1^2}{E_1} + \frac{1-\nu_2^2}{E_2} \quad (16)$$

where  $E_1$  and  $E_2$  are the moduli of elasticity of the fiber and the contact roll,  $\nu_1$  and  $\nu_2$  are the Poisson's ratio of the fiber and the contact roll.

Since the values of Young's modulus and Poisson's ratio are difficult to obtain, the average of the data from the existing studies was used as the reference values [67,108]. The equivalent radius  $R^*$  is expressed as in equation (17) [182,183]:

$$\frac{1}{R^*} = \frac{1}{R_1} + \frac{1}{R_2} \quad (17)$$

where  $R_1$  and  $R_2$  are the radius of fiber and contact roll. The contact area of fiber can be shown:

$$A = 2aL \quad (18)$$

where  $L$  is the length of contact, which can be obtained by:

$$L = \frac{(180 - \theta)\pi r}{180} \quad (19)$$

where the  $\theta$  is the contact angle,  $r$  is the radius of contact roll.

The normal load  $N$  can be calculated by Eq (20):

$$N = F \int \cos\left(90 - \frac{\theta}{2}\right) d\theta = F \int \sin \frac{\theta}{2} d\theta \quad (20)$$

where  $F$  is the pre-tension of yarn.

According to research [99], it is known that the theoretical contact area of a yarn-roller is:

$$A_n = An_{fil} \quad (21)$$

where the number of fibers is  $n_{fil}$ , which is defined by eq (22).

$$n_{\text{fil}} = \frac{D}{d} \quad (22)$$

$$N_{\text{fil}} = \frac{N}{n_{\text{fil}}} \quad (23)$$

where  $D$  is the width of the yarn,  $d$  is the diameter of the fiber.

To modify the difference between theoretical and experimental results due to the fiber orientation, which can be redefined by modifying the equivalent radius  $R'$  as following Eq (24):

$$\frac{1}{R'} = \left( \frac{1}{R_1^2} + \frac{1}{R_2^2} + \frac{2}{R_1 R_2} \cos(2\beta_{\text{tow}}) \right)^{\frac{1}{2}} \quad (24)$$

$L'$  is the modified length of contact surface, which is defined by Eq (25):

$$L' = \frac{(180 - \theta)\pi r}{180} \times \sec(\beta_{\text{tow}}) \quad (25)$$

### 2.2.2 Experiment research for contact behavior

As shown in the schematic of the test device in Fig. 2. 2(a), the frame connects the fixed roller, contact roller and thread guide roller as a complete unit, the fixed roller and thread guide roller are located in the same horizontal plane and equally distance on both sides of the contact roller, during the experiment, both ends of the yarn are connected with the fixed roller and weights respectively, and the middle section is in contact with the contact roller and thread guide roller. The contact angle is changed by adjusting the height of the contact roller, and the yarn pre-tension is adjusted by applying different weights to the yarn. The partially enlarged view of the contact area is shown in Fig. 2. 2(b), which results in the change of fiber arrangement due to the different contact conditions, as shown in Fig. 2. 2(c).

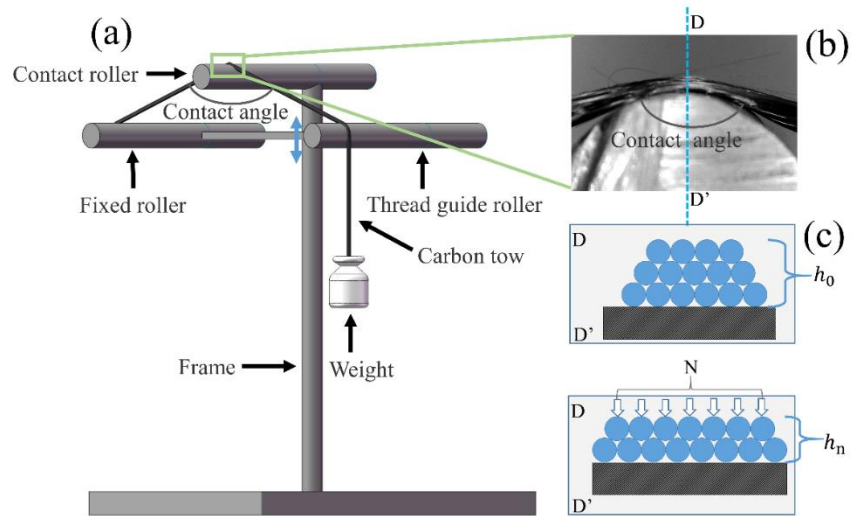


Fig. 2. 2. Experimental figures: (a) schematic of the experimental fig; (b) schematic of yarns mesoscopic contact; (c) schematic drawing of yarns mesoscopic contact

Based on previous yarn contact surface research[25,181,184], yarn contact surface extraction tests were performed as shown in Fig. 2. 3. A silicon film was prepared by combining silicone resin and curing agent in the ratio of 1:5, and about 2 ml of the mixture was dripped onto the surface of the contact rolls and uniformly coated, and the yarn was peeled off after 8 min of contact with the contact rolls to obtain the silicon film carrying the information on the contact surface of the yarns, and the silicon film was analyzed by the 3D Optical Profilers (VR-5200, Japan). The above operations were performed at a temperature of  $25\pm 5$  °C and a humidity of 40%~50%.

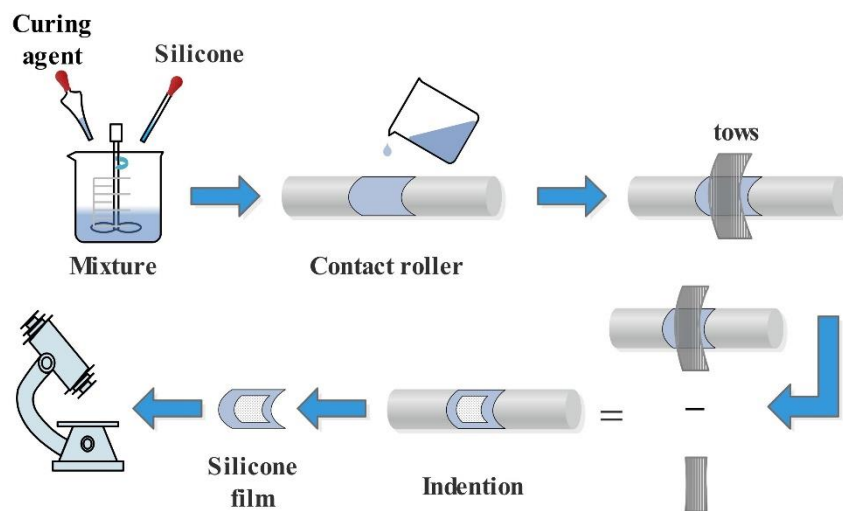


Fig. 2. 3. Experimental method for extracting fiber contact surface.

Image analysis was employed to observe the variation of the yarn contact surface, and the yarn-roll contact area was measured by VR-5200 Analysis software. Before analysis, the pixel size



of each image was first converted to a physical length in millimeters, and then to a grayscale map in order to complete the image scale setting. Fig. 2. 4(a)~(c) demonstrate the contact surface extraction method. According to the contact mechanics model for yarn friction and wear test proposed by Cornelissen et al [72], it can be seen that the yarn exhibits fiber migration from the non-contact layer to the contact layer under different contact conditions, as shown in Fig. 2. 2(c).

The threshold value is employed as an important parameter for determining the contacted and uncontacted layers, in order to accurately select the contacted fibers, the height of the radial direction of the yarn was measured using the experimental setup shown in Fig. 2. 2(a), and the difference between the original sample and the measured value was taken as the image threshold value of the contacted surface of the yarn,  $U$ . This analysis was repeated and the image threshold value was calculated. The actual contact zone was presented for analysis through the image threshold, as shown in Fig. 2. 4(c). Subsequently, the contact area was segmented every 0.5 mm and divided into several profile images, as shown in Fig. 2. 4(d). According to the fluctuation characteristics of each profile image, Image J software was utilized to reconstruct the spatial paths of each contacting fiber Fig. 2. 4(e), and the following characterization parameters were defined. The fiber and the segmentation line intersect at  $O$  and  $a_{i+1}$ , and the projection  $Oa_i$  of the fiber is drawn through  $O$ . The angle between  $Oa_{i+1}$  and  $Oa_i$  is the orientation degree between the segmentation points, denoted by  $\beta_i$ , as shown in Fig. 2. 4(f) shown.

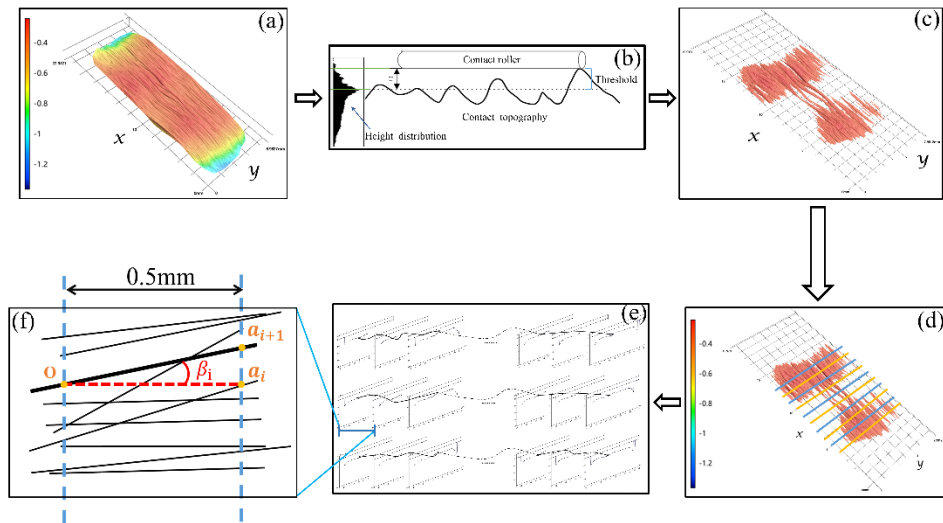


Fig. 2. 4. Contact analysis method

As shown in Fig. 2. 5, the contact fiber orientation  $\beta_{\text{fiber}}$  within the contact surface is standardized in this research according to Eq. (26):

$$\beta_{\text{fiber}} = \sum_{i=1}^n \beta_i / n \quad (26)$$

where  $\beta_i$  is the degree of orientation between contact fiber segmentation points;  $n$  is the number of segments.

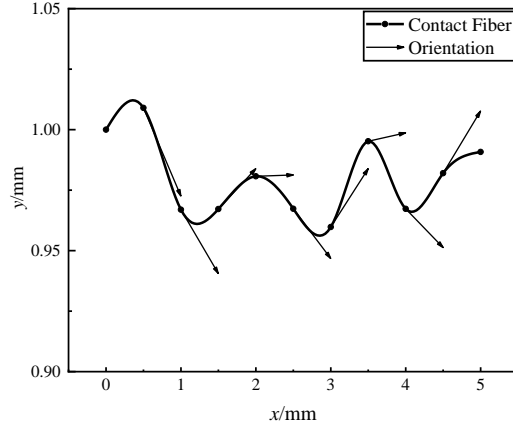


Fig. 2. 5. Schematic of contact fiber track

For further analysis of the yarn orientation, the yarn orientation  $\beta_{\text{tows}}$  was standardized according to Eq. (27), as:

$$\beta_{\text{tows}} = \sum_{i=1}^m \beta_{\text{fiber}} - 180 \times t \quad (27)$$

where the  $\beta$  fiber is the orientation of the fiber,  $t$  is the standardization factor and  $m$  is the number of contacting fiber.  $\beta_{\text{tows}}=0^\circ$  indicates that yarns are not deflected under contact conditions, and  $\beta_{\text{tows}}=\pm 180^\circ$  indicates that yarns are reverse deflected under contact conditions.

### 2.3 A modified analytical model of friction for single twisted yarn

The state of contact pair is vital for the determination of the friction force of a yarn according to the widely accepted adhesion theory of friction[174], which can be explained as Eq. (28):

$$F_T = A_{r/\text{yarn}} \times \tau \quad (28)$$

where  $A_{r/\text{yarn}}$  is the realistic contact area of yarn and  $\tau$  is the specific shear strength.

The implementation of a model describing the variation of the realistic contact area should thus specify the crucial parameters for each state of contact pair during yarn friction. In this way, the Hertzian contact theory was usually utilized to develop this model as shown in Fig. 2. 6, as it can be used to express the friction behavior of yarns with different twists, linear density and twist

direction (the orientation of the surface fiber in relation to yarn axis: S or Z), under different contact angles of yarns.

Assuming that the arrangement of fiber within yarn is incommensurate, that is, the migration of internal fiber does not take place in a static state, especially after the contact interaction. The relationship between the realistic contact area of fiber ( $A_{r/fiber}$ ) and yarn ( $A_{r/yarn}$ ) can be described in Eq.(29):

$$A_{r/yarn} = (m \times n) \cdot A_{r/fiber} \quad (29)$$

where  $n$  and  $m$  are the numbers of contact fibers in the widths of yarns, which will be shown in Fig. 2. 6. The  $A_{r/fiber}$  with a dissimilar contact angle between two fibers has been calculated under the assumption that the fibers are cylindrical and smooth[97,108].

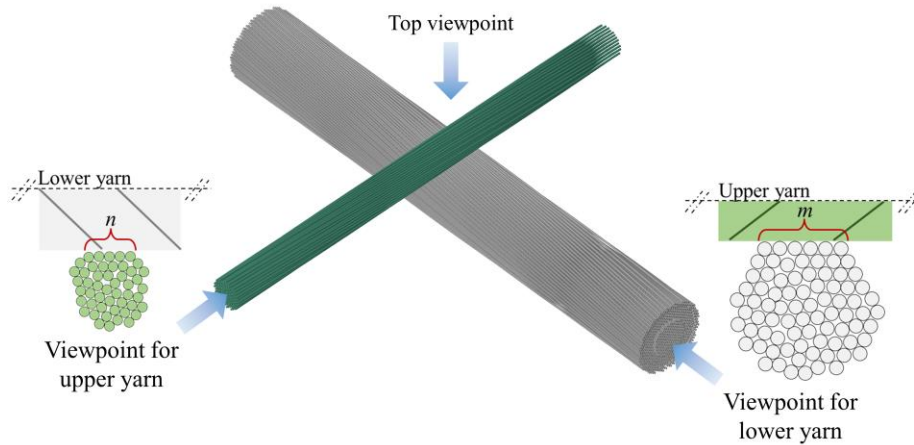
$$A_{r/fiber} = \pi \left( \frac{3f_N R^*}{4E^*} \right)^{2/3} \quad (30)$$

where  $f_N$  is the normal load of fiber.  $R^*$  is the equivalent radius,  $E^*$  is the equivalent Young's modulus expressed as:

$$\frac{1}{E^*} = \frac{1-\nu_1^2}{E_1} + \frac{1-\nu_2^2}{E_2} \quad (31)$$

where  $E_1$  and  $E_2$  are the transverse Young's modulus of two materials rubbing against each other, and  $\nu_1$  and  $\nu_2$  are the Poisson's ratio of two materials rubbing against each other. The transverse Young's modulus and Poisson's ratio of fiber are used in this analytical model and are difficult to obtain. Therefore, the values used are averaged from some earlier research [185,186].

(a)



(b)

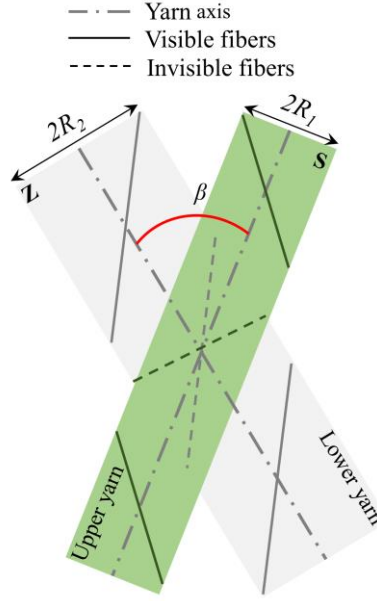


Fig. 2. 6. Schematic diagrams of non-orthogonal contact between twisted yarns: (a) three-dimensional diagram, (b) top viewpoint diagram. (Notes: **S** means the direction from the upper left to the lower right; **Z** means the direction from the upper right to the lower left)

The fibers show an irregular arrangement due to pre-tension and normal loading. The equivalent radius  $R^*$  can be expressed as the following equation:

$$R^* = (R' R'')^{\frac{1}{2}} \quad (32)$$

where  $R'$  and  $R''$  are the major and minor relative radius of curvature on the contact surface, respectively, which can be then possibly obtained by solving Eq. (33)[106].

$$\begin{cases} \frac{1}{R'} + \frac{1}{R''} = \frac{1}{r_{f1}} + \frac{1}{r_{f2}} \\ \frac{1}{R'} - \frac{1}{R''} = \left( \frac{1}{r_{f1}^2} + \frac{1}{r_{f2}^2} + \frac{2\cos(2\alpha)}{r_{f1}r_{f2}} \right)^{\frac{1}{2}} \end{cases} \quad (33)$$

where  $r_{f1}$  and  $r_{f2}$  are radiuses of contact fibers, and  $\alpha$  is the contact angle between the axis of fibers.

The equivalent radius  $R^*$  depends on the angle between the yarn axes ( $\beta$ ). This was discussed in [108], however, the fibers are not normally parallel to the axis of twisted yarn. To precisely describe the friction behavior between the twisted yarns, the contact angle between the fiber axes ( $\alpha$ ), the contact angle between the yarn axes ( $\beta$ ), the twist level and the twist direction of the yarns are taken into account in this research. Regarding the complexity of the twist, a micro-meso scale analysis needs to be performed.

### 2.3.1 Fiber scale modeling

The parameters of the fiber scale model, with the contact angle between the two fiber axes and the number of contact fibers as the main parameters, need to be obtained to clarify the parameters of the yarn scale model. The contact angle between the two fiber axes is dissimilar from  $\beta$  between the axes of the two yarns and the twist angle of yarn  $\gamma$ , whose relationships are shown in Fig. 2. 7. At the same time, with different twist directions,  $\alpha$  is different and indeed this results in the difference in the realistic contact areas. Therefore, it is important to calculate  $\alpha$  by  $\beta$  and  $\gamma$ . In this way,  $\gamma$  should be transformed into a plane coordinate system, however,  $\alpha$  needs to be expressed based on the different directions of twist by the following equations:

$$\alpha = \begin{cases} \beta + \gamma_1 - \gamma_2 & S-S \text{ or } Z-Z \\ -\beta + \gamma_1 + \gamma_2 & S-Z \text{ or } Z-S \end{cases} \quad (34)$$

$$\gamma = \arctan 2\pi RT_t \quad (35)$$

where  $R$  and  $T_t$  are the radius and twist of twisted yarn, **S-S** or **Z-Z** indicates two **S** (or **Z**) yarns in contact, **S-Z** or **Z-S** indicates **S** and **Z** yarns (or **Z** and **S** yarns) in contact.

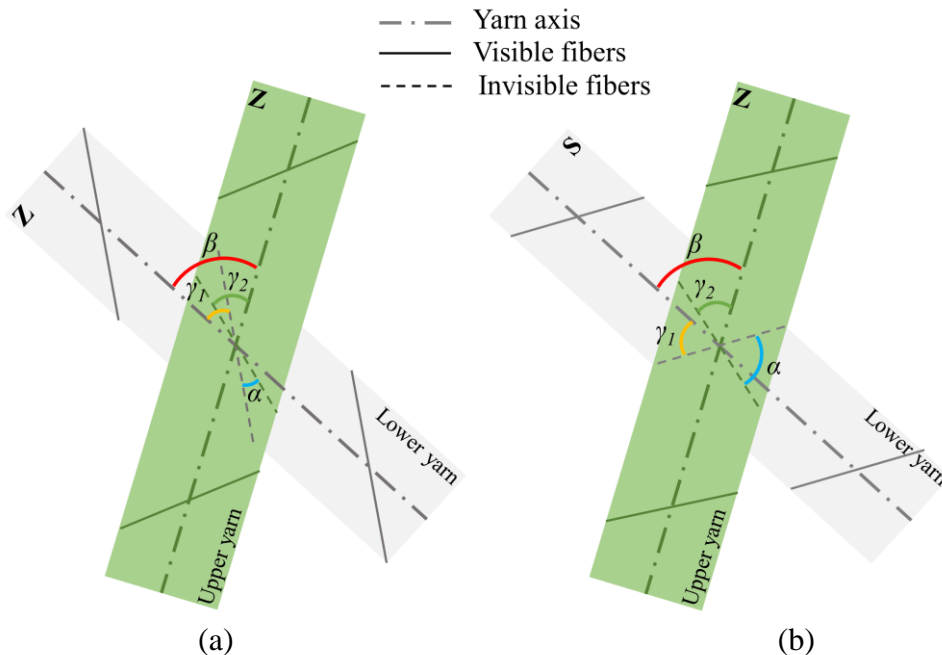


Fig. 2. 7. A diagram of angle analysis during the contact phase of twisted yarns: (a) S-S or Z-Z, (b) S-Z or Z-S.

Then the number of contact fibers  $n$  or  $m$  (c.f. Fig. 2. 6) of each cross-section of yarn during the friction phase can be expressed as:

$$2nr_f + \sum h_i = 2b \quad (36)$$

where  $r_f$  is the radius of the fiber,  $h_i$  is the distance between two neighboring fibers, which can be obtained using the Euclidean distance formula. The half-width of the contact  $b$  is vital to calculate  $n$  under the  $F \cos \theta$ , as shown in Fig. 2. 8, which was described by [187] as Eq. (37).

$$b = \sqrt{\frac{8R^{*2}F \cdot \cos \theta}{\pi} \left( \frac{1}{E_t} - \frac{\nu_{12}^2}{E_l} \right)} \quad (37)$$

where  $E_l$  and  $E_t$  are the longitudinal and transverse modulus of the yarn.  $\nu_{12}$  is the Poisson's ratio of yarn. Based on the assumption of incommensurate structure, the range of  $n$  can be given according to the range of  $h_i$ . When the distance  $h_i$  equals  $2r_f$ , the close homogenous arrangement of fibers is achieved (see Fig. 2. 8), leading to the number of contact fibers being the maximum at this time, marked as  $n_{max}$ . By contrast, when  $h_i$  equals  $4r_f$ , the number of fibers in contact is the minimum, marked as  $n_{min}$ , shown in Fig. 2. 8.

$$n = \begin{cases} \frac{b}{r_f} & h_i = 2r_f \\ \frac{2b - \sum h_i - 2r_f}{2r_f} & 2r_f < h_i < 4r_f \\ \frac{1}{2} \left( \frac{b}{r_f} + 1 \right) & h_i = 4r_f \end{cases} \quad (38)$$

Nevertheless, the situation of the minimum number of fibers cannot be achieved due to the incommensurate arrangement of fiber. When  $h_i$  is located in the range  $(0, 4r_f)$ , the dissimilar  $h_i$  is made a summation to calculate  $n$ . Since  $n$  has a small difference in each section,  $n$  is represented by the average value. Similarly, it is possible to work out the number of contact fibers  $m$  in the width of another yarn. Therefore, the  $A_{r/yarn}$  can be shown, according to the equations above, as a function of the characteristics of the fibers and the contact angle between the fiber axes as described in Eq. (39):

$$A_{r/yarn} = \pi \left( \frac{3r_{f1}r_{f2}\sqrt{mn} \cdot F \cdot \cos \theta}{4} \cdot \left( \frac{1-\nu_1^2}{E_1} + \frac{1-\nu_2^2}{E_2} \right) \right)^{2/3} \cdot (R_1R_2 - 2\cos^2(2\alpha))^{1/3} \quad (39)$$

(a)

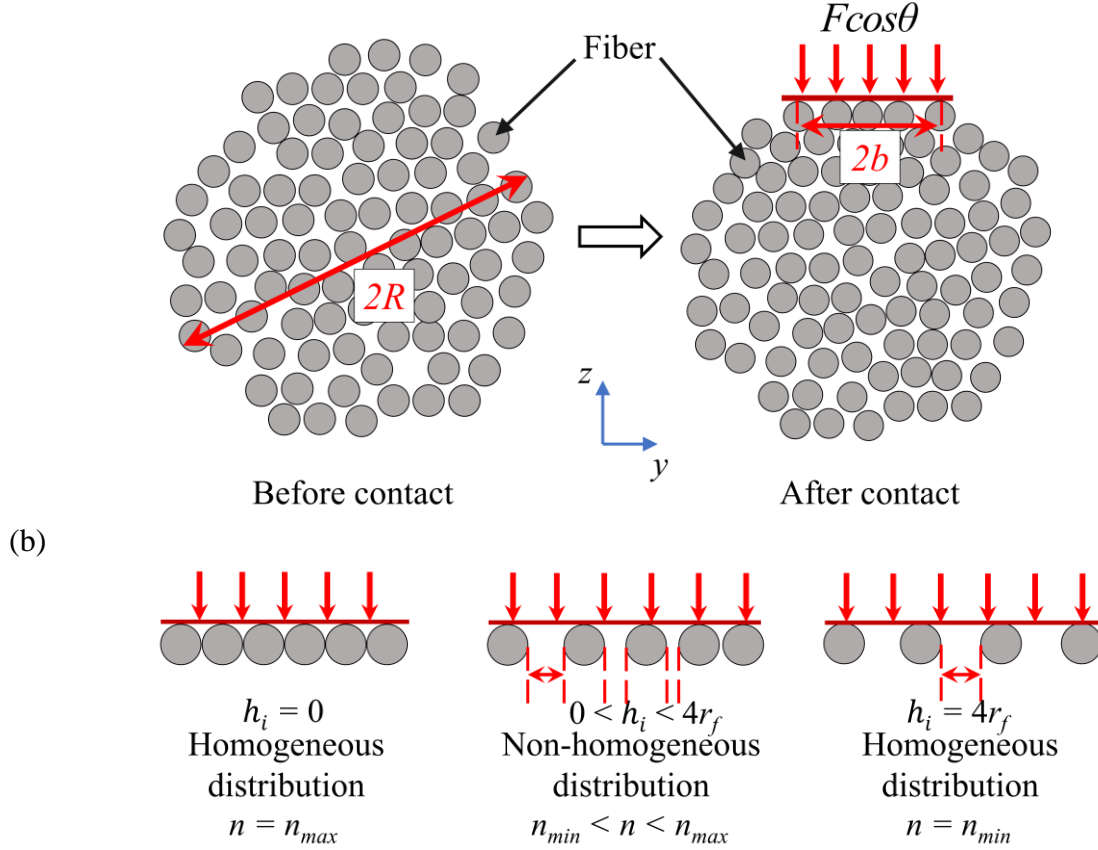


Fig. 2. 8. Enlarged view of the arrangement to arrive at the relationship: (a) a deformation description under the normal load  $F \cos \theta$  and (b) a schema of fiber arrangements (based on the viewpoint in Fig. 2. 6).

### 2.3.2 Yarn scale modeling

To further describe the friction between the yarns, the parameters at the meso-scale must be obtained after the calculation of the realistic contact area of the fibers. As for the calculation of the  $F \cos \theta$ , the dynamic process needs to be identified, that is, the relationship between  $F \cos \theta$  and the contact angle between the axis yarn  $\theta$  (see Fig. 2. 10). In this manner, the normal force  $F$ , related to the pre-tension  $F_p$ , can be projected in two directions (tangential  $\vec{t}$  and normal  $\vec{n}$ ) shown in Fig. 2. 10 and Eq. (40):

$$F = \begin{pmatrix} F_t \\ F_n \end{pmatrix}_{(\vec{t}, \vec{n})} = \begin{pmatrix} F \cdot \sin \theta \\ F \cdot \cos \theta \end{pmatrix} \quad (40)$$

where  $F$  can be expressed as:

$$F = F' - F_p \cdot \sin \theta \quad (41)$$

where  $F'$  is the normal force applied, which is artificially applied. Furthermore,  $F \cos \theta$  can be calculated by Eq (42):

$$F \cdot \cos \theta = F \cdot \cos \left( \arctan \frac{2H}{a-l\sqrt{\frac{a^2+4H^2-l^2}{a^2-l^2}}} \right) \quad (42)$$

The changes in variables  $a$ ,  $H$  and  $l$  had significant effects on  $F \cos \theta$ . More details of formula derivation are presented in Eqs (43)-(48). The changing relationships between  $\theta$  and displacement  $H$  under the action of  $F$  were explained. The normal load  $F_n$  in the kinematic friction process can be further calculated. From Eqs. (40)-(41), the  $\theta$  is obtained as:

$$\tan \theta_1 = \frac{H}{\frac{a}{2}-u} \quad (43)$$

$$\tan \theta_2 = \frac{H}{\frac{a}{2}+u} \quad (44)$$

$$\sqrt{\left(\frac{a}{2}-u\right)^2+H^2} + \sqrt{\left(\frac{a}{2}+u\right)^2+H^2} = l \quad (45)$$

where  $l$  is the length of the yarn sample involved in friction which is obtained from the experiment.  $u$  is the distance between contact point and center of span. More details of dimensional parameters are shown in Fig. 2. 9. Substituting the Eqs. (43) and (44) into (45),  $\theta_1$  and  $\theta_2$  are given as:

$$\theta_1 = \arctan \frac{2H}{a-l\sqrt{\frac{a^2+4H^2-l^2}{a^2-l^2}}} \quad (46)$$

$$\theta_2 = \arctan \frac{2H}{a+l\sqrt{\frac{a^2+4H^2-l^2}{a^2-l^2}}} \quad (47)$$

where  $H$  is displacement under the action of  $F$ , which can be shown by  $F_p$  as:

$$F_n = \left( E_l S \left( \frac{H}{\sin \theta_1} + \frac{H}{\sin \theta_2} - 1 \right) + F_p \right) \cos \theta_1 \quad (48)$$

where  $S$  is the cross-section area of yarn.



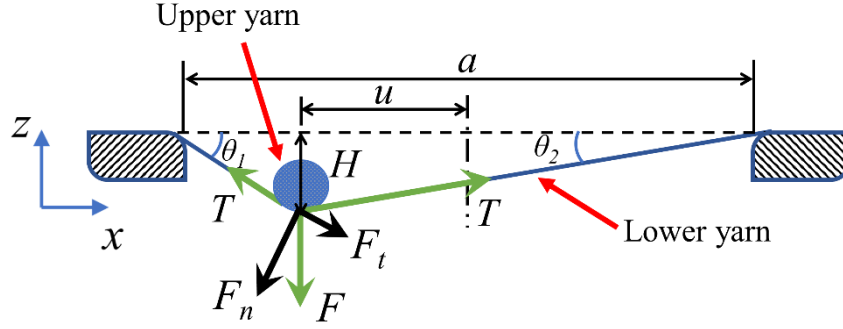


Fig. 2. 9. The description of dimensional parameters during the friction process based on Fig. 2. 10.

Thus, an analytical model describing the friction behavior of the yarn (friction force  $F_T$ ) was established and is shown in Eq (49).

$$F_T = \pi \sin \theta (F' - F_p \cdot \sin^2 \theta)^{5/3} \left[ \frac{3r_{f1}r_{f2}\sqrt{mn}}{4} \cdot \cos \left( \arctan \frac{2H}{a-l\sqrt{\frac{a^2+4H^2-l^2}{a^2-l^2}}} \right) \cdot \left( \frac{1-v_1^2}{E_1} + \frac{1-v_2^2}{E_2} \right)^{2/3} \cdot (R_1R_2 - 2\cos^2(2\alpha))^{1/3} \right] \quad (49)$$

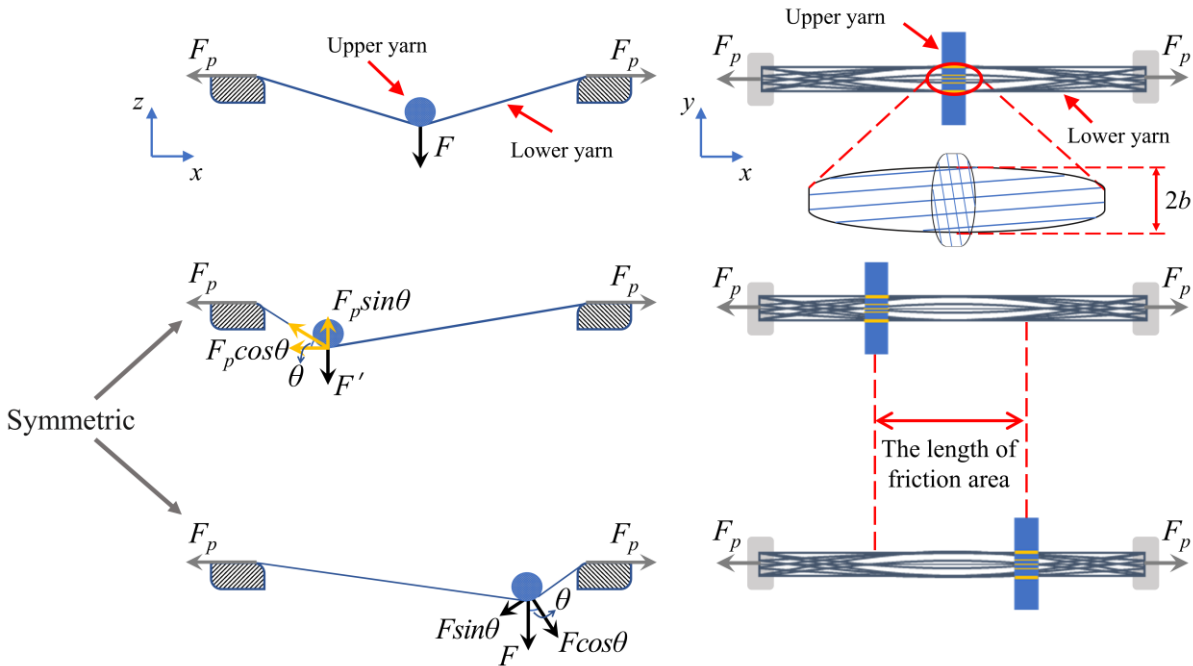


Fig. 2. 10. Kinematic description of the yarn friction process which includes three characteristic locations where force and contact situation are shown.

As an essential parameter of friction behavior, the coefficient of friction ( $COF$ ) is complicated to obtain since the friction process is dynamic, as shown in Fig. 2. 10. To clearly state real-time  $COF$  which was defined as a ratio between the friction force  $F_T$  and the normal load  $F \cos \theta$  at yarn scale in Eq. (50)[97,108].

$$COF = \frac{F_T}{(F \cdot \cos \theta)^k} \quad (50)$$

where  $k$  is the fitting coefficient derived from the experiment, namely  $2/3$  when the two objects undergo complete elastic deformation. For complete plastic deformation, the range of  $k$  is located in  $(0.67, 1)$ .

### 2.3.3 Materials and Experiment

The twisted yarns investigated in this article are HMWPE yarns (Spectra®, Honeywell Company, USA). Four yarn samples were prepared and tested for friction. The samples are named according to the twist. For example, Y-50tpm represents the sample of single yarn with 50 tpm (twist per meter). More samples (Y-100tpm, Y-150tpm, and Y-200tpm) are used in the article. For all samples, both yarns were 135 Tex, characterized according to ASTM D 1907/D 1907M. The main properties related to the tested yarns are noted in Table 2. 1.

**Table 2. 1 Main physical properties of high-molecular-weight polyethylene (HMWPE) fiber and yarns.**

Sample	Linear density (Tex)	Twist level (tpm)	Longitudinal modulus (GPa)	Diameter ( $\mu\text{m}$ )
Fiber	-	-	0.6	17
Y-50tpm	135	50	73.0	998
Y-100tpm		100	83.4	493
Y-150tpm		150	98.4	324
Y-200tpm		200	110.3	238

The friction experiments set-up with two specific carriers, including upper and lower carriers, were designed and are shown in Fig. 2. 11. The carriages are similar in the upper and lower parts and were designed to fix the sample under a pre-tension load. In addition, some threaded holes were designed to maintain pre-tension of sample. During the setting up of the sample, one end of the sample is fixed by screwed clamps. The other end of the sample is screwed within the range of a certain pre-tension for a period, with a single fiber pre-tension of at least 0.15 mN per fiber. The fixed part of the sample was protected by a rubber mat[108]. The position should be such that there is only contact between the upper and lower yarns. The force sensor in Fig. 2. 11 limits the normal load to 20 N and the tangential force to 3 N. The lower carrier is fixed to the base, which is perpendicular to the upper one. This configuration makes it possible to carry out the friction tests for a  $\beta$  of  $90^\circ$ . The length and width of the tested area are chosen as 30 mm and 25 mm (Fig. 2.

11b), which is related to the area in the beating-up. The length of the fixed fiber area is 1 cm, which ensures there is no fiber slippage.

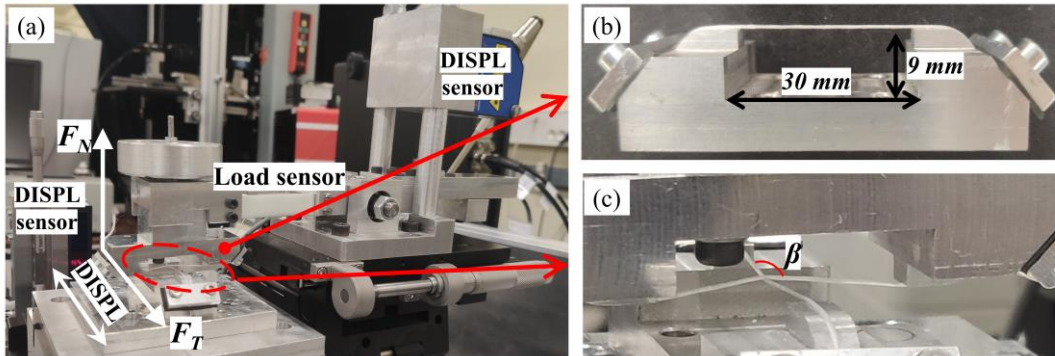


Fig. 2. 11. A picture of the tribometer dedicated to twisted yarn-yarn friction tests.

Once the experiment is set up as shown in Fig. 2. 11, the upper carrier with a force sensor is fixed, and the lower carrier moves reciprocally in the direction of displacement. Fig. 2. 12 presents schematically one cycle of the friction test, which starts from an extreme position of the moving carrier (position 1 in Fig. 2. 12). The different normal loads are applied to maintain the contact between the two tested yarns (c.f. Table 2. 2), which were chosen appropriately at the beginning of the test and remained unchanged during the entire friction test.

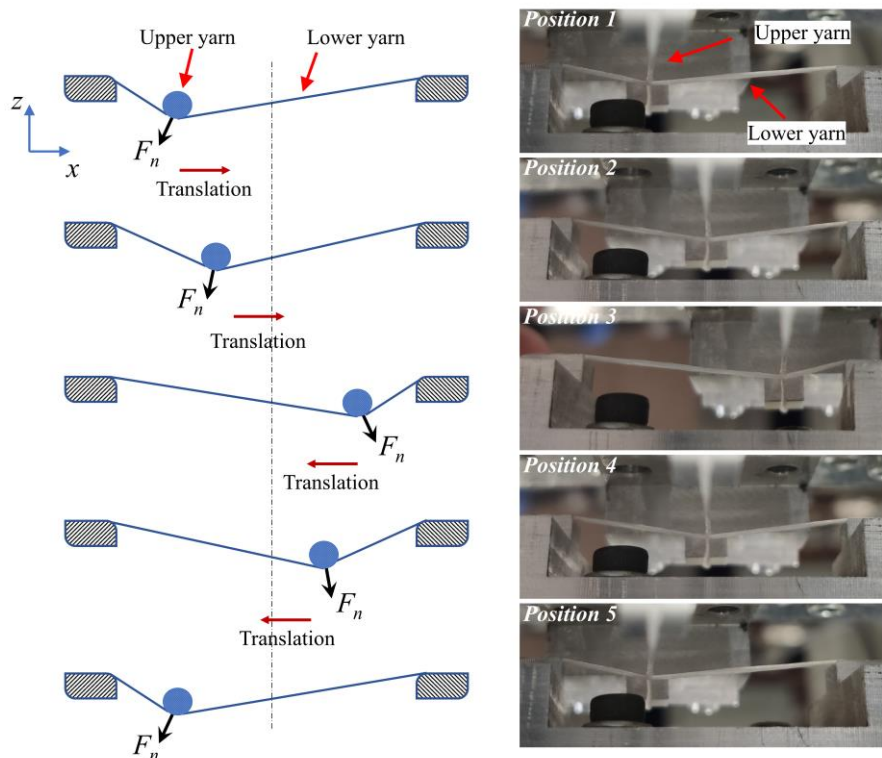


Fig. 2. 12. Schematic diagram of one cycle for the friction test.

All experiments were performed at conditions of  $22 \pm 2^\circ\text{C}$  temperature and  $65 \pm 4\%$  relative

humanity (RH). According to previous research[98,108,188], the weft yarns could be subjected to weaving cycles for 100 mm from the starting position of beating to the fabric (15 mm fabric as an example). Therefore, each test corresponds to 40 friction cycles for each kind of sample under the assumption that there is no secondary friction. The friction tests under different experimental conditions are listed in Table 2. 2.

Table 2. 2 The friction tests with different conditions to validate the developed analytical model.

Test number	$\beta$ (°)	Normal force applied (N)	Pre-tension (N)	Twist (tpm)	Twist direction	Cycle number	Acceleration (mm/s <sup>2</sup> )	Stable velocity (mm/s)
1	90	2.00	0.50	100-200	S-S			
2	70	1.50	1.00	150-150	S-S			
3	50	1.50	0.35	50-100	Z-S	20	20	10
4	90	2.00	1.00	200-200	S-S			

## 2.4 Results and discussion

To achieve multidimensional prediction of friction characteristics utilizing the theoretical model developed, the model assessment is conducted focusing on predictability and accuracy, including the contact area of non-twist yarn and friction response of twisted yarn, which shows the significant effect of contact area on friction in the first subsection. Then, the influence of contact area under different contact conditions are illustrated, including the contact angle and pre-tension. In the second and third subsections, the friction behavior of yarns with the same and different twists is predicted using the model for non-parallel conditions. The friction analysis model we have developed, which takes the twist response into account, could be a bridge linking practical and theoretical analysis, which is essential for optimizing the textile preform forming process and enhancing the mechanical properties of the composites. Moreover, a novel approach and analytical methodology for investigating the frictional characteristics of yarns with identical or different twist angles are presented. The proposed method not only offers valuable insights into understanding the underlying mechanisms but also establishes a solid basis for future exploration and simulation analysis of intricate coupling systems.

### 2.4.1 Consistency analysis

Fig. 2. 13 shows the variation curves of contact area measured by Hertz's contact theory and experiment under different contact angle and pre-tension conditions. Both show the same trend, that is, the contact area decreases with the increase of contact angle and increases with the increase of pre-tension. Using the correlation analysis method to study the relationship between the Hertz

contact theory model and the experiment, the Pearson correlation coefficients are both greater than 0.995, and the significant levels (p-value) are less than 0.01. It can be shown that the experiment can better reflect the yarn-roller contact behavior. In, detail, Table 2. 3 shows the yarn-roll contact area calculated according to the Hertz contact theory model.

Table 2. 3 Hertz contact area between carbon tows and round roller under different contact conditions

Contact Parameter	Parameter value	$L/mm$	$R^*/mm$	$E^*/GPa$	$a/mm$	$A_n/mm^2$
Contact angle/ $^{\circ}$	60	12.54	$3.6 \times 10^{-3}$	17.39	$6.38 \times 10^{-3}$	106.61
	90	9.40			$5.60 \times 10^{-3}$	74.74
	130	5.22			$4.20 \times 10^{-3}$	34.98
	150	3.13			$2.87 \times 10^{-3}$	17.82
	170	1.04			$1.50 \times 10^{-3}$	4.13
Pre-tension/N	0.19	3.13	$3.6 \times 10^{-3}$	17.39	$1.48 \times 10^{-3}$	10.42
	0.39	3.13			$1.92 \times 10^{-3}$	13.13
	0.98	3.13			$2.87 \times 10^{-3}$	17.82
	1.47	3.13			$3.33 \times 10^{-3}$	20.40

However, in comparison, there are some differences between the two results, as shown in Fig. 2. 13(a), the theoretical value of Hertz contacts in the range of  $130^{\circ}$ - $170^{\circ}$  has high comparability with the experimental value, which is due to the contact fiber orientation is low under the condition with larger contact angle, the contact area of the yarn-roller contact area is not significantly affected by the degree of orientation. In the range of  $60^{\circ}$ ~ $130^{\circ}$ , the difference between the theoretical and experimental values of Hertz contact is obvious, which is since under the condition of a smaller contact angle, the contact surface becomes wider, the fibers within the yarn are dispersed, the fiber orientation is larger, and the contact area of the yarn-roller is significantly affected by the orientation. As shown in Fig. 2. 13(b), the difference between the theoretical and experimental values gradually increases with the increase of pre-tension, which is due to the small fiber orientation under the condition of small pre-tension, and the length of contact fibers is approximately equal to the length of non-orientated fibers, that is, the effect of yarn orientation on the pre-tension is small. In summary, it is concluded that the yarn orientation is the key factor affecting the contact area of the yarn-roller, the contact angle and pre-tension affect the yarn orientation in the contact surface, changing the yarn-roller contact area.

The modified contact surface length  $L'$  and equivalent radius  $R'$  are substituted into Eq. (15) to obtain the contact half-width  $a$ , and then the yarn-roller contact area  $A_n$ . Table 2. 4 lists the parameter values of the modified model considering the yarn orientation. Fig. 2. 13 shows the contact area evolution curves of the Hertz contact model, the modified model and the experiment. From the figure, it can be seen that the contact areas obtained from the three models show the same trend with the evolution of the contact angle and the pre-tension, and it is obvious that the modified

model has a better coincidence with the experiment, which is analyzed by the Tukey significance test method for the three models, and its test parameters are shown in Table 2. 5.

Table 2. 4 Modified contact area between carbon tows and round roller under different conditions

Contact Parameter	Parameter value	$L'/\text{mm}$	$R'/\text{mm}$	$A_n/\text{mm}^2$
Contact angle/(°)	60	13.38	3.5837E-03	113.61
	90	9.60	3.5802E-03	76.15
	130	5.27	3.5792E-03	35.20
	150	3.14	3.5786E-03	17.81
	170	1.05	3.5785E-03	4.13
Pre-tension/N	0.19	3.13	3.5789E-03	10.78
	0.39	3.14	3.5787E-03	13.59
	0.98	3.14	3.5786E-03	18.47
	1.47	3.14	3.5785E-03	21.15

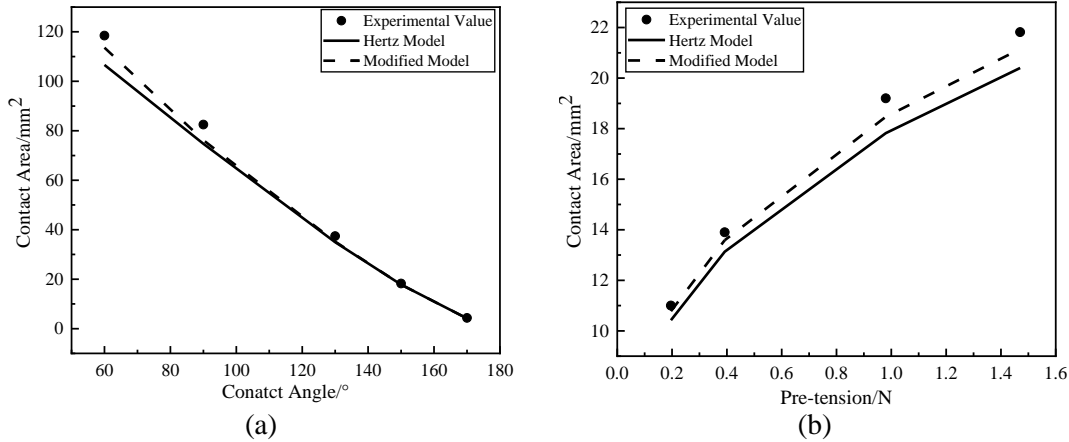


Fig. 2. 13. Hertz model, modified model and experiment contact area under different (a) contact angle and (b) pre-tension

Table 2. 5 Tukey-test parameters of three models under different contact conditions.

Contact Parameter	Tukey-test probability	
	Ex-Hertz	Ex-Mod
Contact angle	0.87	0.92
Pre-tension	0.77	0.89

Note: Ex-Hertz represents experiment and Hertz model; Ex-Mod represents experiment and modified model.

As can be seen from Table 2. 5, the Tukey test probability of Ex-Hertz is smaller than the Tukey test probability of Ex-Mod under both types of contact conditions, which indicates that the improved model is more consistent with the experimental model than the Hertz contact model, so the contact model that considers the orientation of the fibers within the yarn should be employed for the research of the yarn friction and wear behaviors.

The friction response of twisted yarns also is verified by the experiment. Based on the analytical model developed, comparisons were conducted between the analytical and experimental approaches and shown in Fig. 2. 14. The yarn is set to slide with a constant displacement, a sliding

distance of 7.5 mm in the forward and backward directions based on the dissimilar  $\beta$ , to complete one friction cycle. The friction force during the friction test can be divided into decreasing (*I* and *III*) and increasing phases (*II* and *IV*), as shown in Fig. 2. 14. It can be noted that the change in friction force is significantly different in each phase. It is probably due to the sliding velocity between two contact yarns. The variation in relative parameters will occur if the friction is carried out under the condition of acceleration. Therefore, it also reflects the fact that friction has a rate correlation, as described in Fig. 2. 14.

To ensure the experimental value is stable, the average data are selected after the five friction experiments. The friction force of the analytical model is calculated based on the average value of  $n$  and  $m$ . A good agreement between the analytical and experimental friction responses can be seen in Fig. 2. 14(a). However, the variation between each characteristic phase shows a rate correlation in Fig. 2. 14(c). This is probably related to  $\theta$ , which influences the arrangement of the fibers on the contact surface. Furthermore, it can be observed that the analytical and experimental curves separate approximately in the decreasing phase, whose average errors are averagely concentrated at about 21.9% (less than the average experimental error of 36.7%). Meanwhile, the average errors in the increasing phase are about 7.2% (less than the average experimental error of 11.8%).

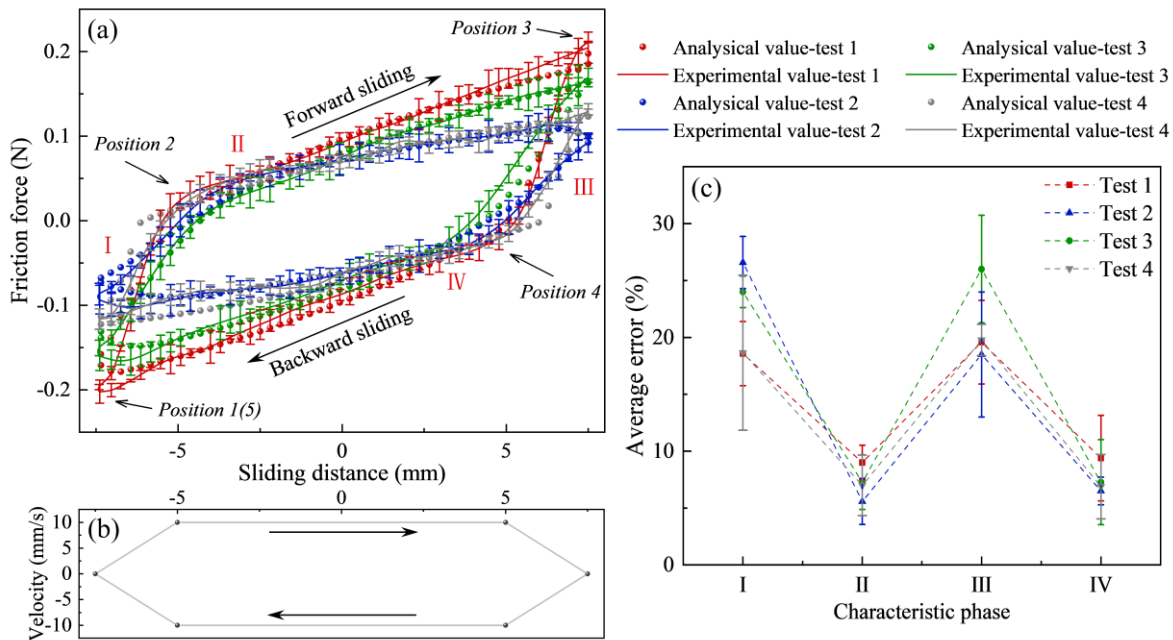


Fig. 2. 14. Comparison of the analytical and experimental results on friction force by different tests mentioned in Table 2. 3 (average of five measurements): (a) one cycle of friction, (b) sliding distance versus velocity curve and (c) average error of friction force in the characteristic area.

#### 2.4.2 Friction behavior between the yarns with the same twist level and the same twist direction

As one essential yarn/yarn friction parameter, the realistic contact area ( $A_{r/yarn}$ ) depends directly on the normal force applied and is influenced by the yarn twist level and the contact angle between the yarn axes ( $\beta$ ). This realistic contact area can be calculated by Eq. (39) and worked out in Fig. 2. 15 in the case of friction between yarns with the same twist. It can be noted that each  $A_{r/yarn}$  of yarns almost shows a nonlinear relation with an identical tendency towards the normal force,  $A_{r/yarn}$  gradually increases as normal force  $F$  increases, but the range of variation is dissimilar, which can be explained by ref. [50,189]. Among the three twist levels, the biggest range of variation can be observed in the case of 50-50 tpm yarns under horizontal comparison (the twist of upper and lower yarns both are 50 tpm). This phenomenon is probably due to the cohesive force of the fibers as the twist increases with increasing cohesive force, which can be confirmed by the research work presented in [50,189]. Regarding the contact angle between the yarn axes ( $\beta$ ), it is imperative to consider the influence of non-orthogonal yarn configurations ( $\beta \neq 90^\circ$ ) which provide a wider representation of the contact area compared to the simplistic scenario of orthogonal yarns ( $\beta = 90^\circ$ ). By incorporating non-orthogonal yarn conditions, a more realistic contact area between yarns can be achieved, leading to a comprehensive understanding of the intricate interplay between yarn geometry and contact behavior. Furthermore, a smaller contact angle  $\beta$  influences a bigger realistic contact area, which can be seen from the different twist levels curves in Fig. 2. 15(a-c).

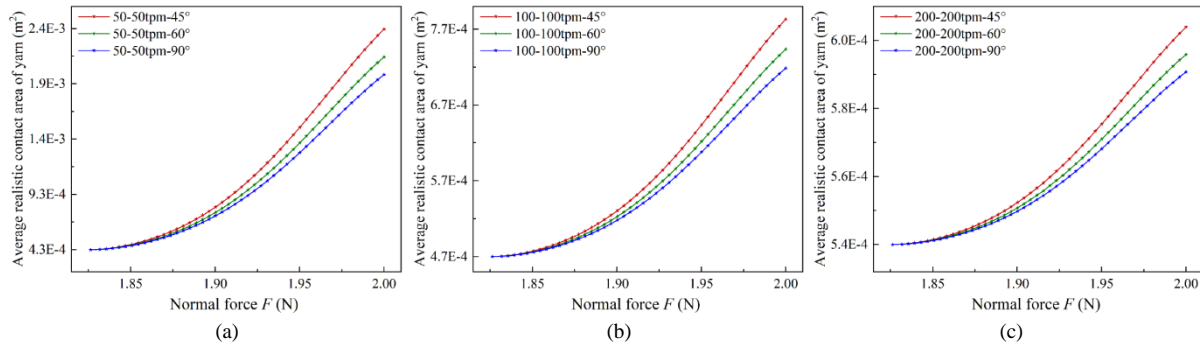


Fig. 2. 15. The realistic contact area of yarn  $A_{r/yarn}$  of a typical friction cycle with the same twist (horizontal comparison: same color in three figures; vertical comparison: three colors in one figure).

Based on the realistic contact area between yarns  $A_{r/yarn}$ , the developed model can predict the friction force  $F_f$  and  $COF$  during the friction test. The friction force and  $COF$  in the function of the sliding distance in one cycle of friction test between two yarns with the same twist are shown in Fig. 2. 16(a-c) and (d-f), respectively. A similar variation can be observed between friction force and  $COF$ . The twist level of yarns and the contact angle between the yarn axes significantly impact the friction force and  $COF$ . The twist leads to an increase in the compression cohesion force in the



circumferential direction of the yarn. Consequently, a higher twist level leads to a dense structure and a smaller contact surface under the same transverse compressive load, which reduces the inter-yarn friction. In addition, the contact angle  $\beta$  changes the realistic contact area of the yarns, with a bigger contact angle generating a smaller realistic contact area on the yarns and a weaker friction force as well as  $COF$ . However, these influences on the friction force and  $COF$  can be noted in the stable friction stages (the sliding velocity remains constant in stages *II* and *IV* shown in Fig. 2. 14a and b).

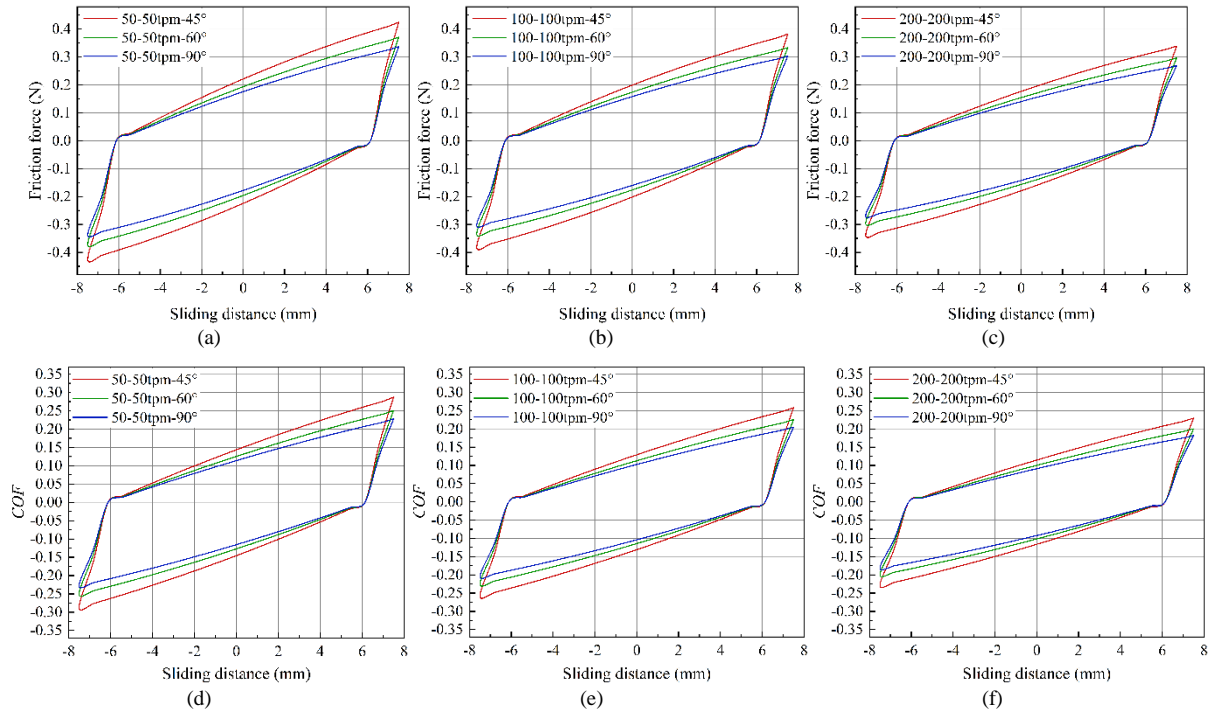


Fig. 2. 16. A typical friction cycle with the same twist: (a-c) friction force and (d-f)  $COF$ . (Note: Friction condition for test 4 was employed to analyze).

### 2.4.3 Friction behavior between the yarns with a different twist level and the same twist direction

The analytical model can predict the friction behavior with a different twist, including the twist levels and direction, analogous to the previous section. Similar relative parameters of friction behavior are selected for analysis. Fig. 2. 17 illustrates a more distinguishing trend with different twists in relative parameters. As shown in Fig. 2. 17(a-c), the  $A_{r/yarn}$  of each twist level calculated by the analytical model are distinct from each other, and the range of variation at the extreme values of the normal force increases with the increasing of twist level. Simultaneously, the range of variation of  $A_{r/yarn}$  increases with the increasing span of twist level. With identical twist levels, the  $A_{r/yarn}$  of non-orthogonal friction is larger than orthogonal friction under vertical comparison, and there is a marked decrease in  $A_{r/yarn}$  as  $\beta$  increases under horizontal comparison due to the tight

arrangement of fibers within the larger twist yarn and the greater number of fibers participating in the friction, the frictional behavior of yarn with different twist levels have larger realistic contact area compared to yarns with same twist level.

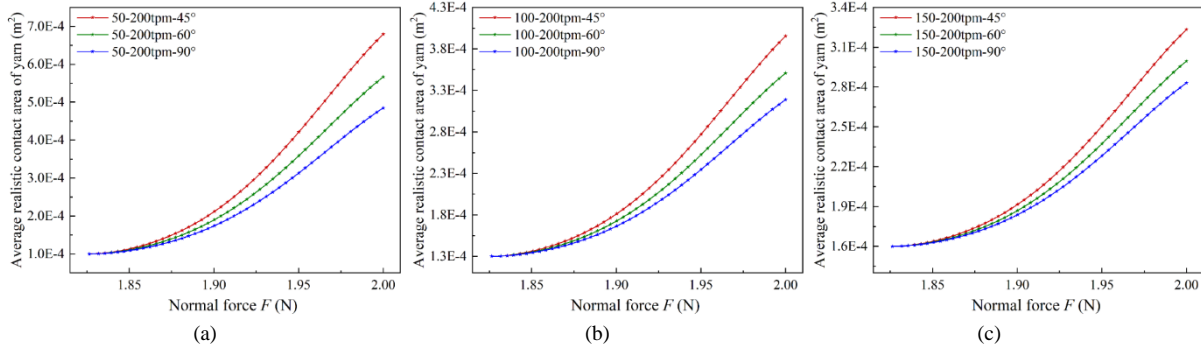
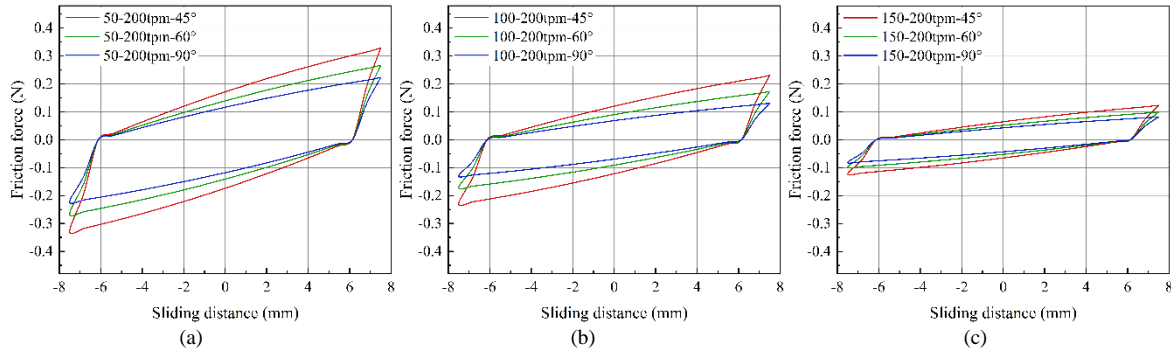


Fig. 2. 17. The realistic contact area of yarn  $A_{r/yarn}$  of a typical friction cycle with the different twist levels.

The evolution of different twist levels on  $F_f$  and  $COF$  is similar to those of the same twist level. In contrast, the range of variation is significant in Fig. 2. 18. For the same  $\beta$ , the 50-200tpm tends to show a greater range of variation than 100-200tpm and 150-200tpm, which may indicate that the span of twist levels plays a role in determining  $F_f$  and  $COF$ . Regarding the comparison of the same span of twist level, the ranges of variation of  $F_f$  and  $COF$  decrease with increasing of  $\beta$ , namely the effect of  $F_f$  is significantly greater than  $F_n$  with a decreasing span of twist level in Fig. 2. 18(a-c) and (d-f), respectively. Moreover, it is obvious that there is also a phenomenal increase as  $\beta$  drops even though the span of twist level is different. The above influences are also apparent during the stable friction stages.



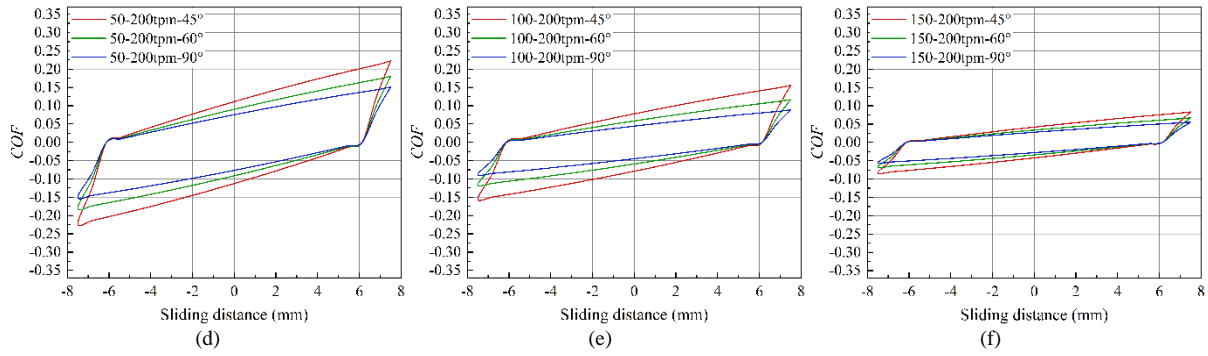


Fig. 2. 18. A typical friction cycle with the different twist levels: (a-c) friction force and (d-f)  $COF$ . (Note: Friction condition for test 4 was employed to analyze).

#### 2.4.4 Friction behavior between the yarns with a different twist level and a different twist direction

Fig. 2. 20 exhibits the evolution of relative parameters during the friction process with different twist directions. The evolution trend of  $A_{r/yarn}$  is also non-linear as is the variation in  $F$ , with both expressing an invariant law that the maximum  $F$  occurs in the middle position, while the minimum  $F$  occurs in transformation positions of direction. And there is no change for  $A_{r/yarn}$  at any  $\beta$  in transformation positions of direction, while the change is significant at the position of maximum  $F$  with the same span of twist level. The  $A_{r/yarn}$  of non-orthogonal friction is larger than orthogonal friction with the same  $\beta$  under horizontal comparison. Additionally, Fig. 2. 20(a-c) show the rate of change is insignificant at an  $F$  of 2.0 N between 100-200tpm-45° and 150-200tpm-45°, while the rate of change of 50-200tpm-45° is about three times as large as 100-200tpm-45°, and the evolution is similar to the  $A_{r/yarn}$  with same twist direction. However, the range of  $A_{r/yarn}$  is obviously indicated due to the different calculations of  $\alpha$ . Therefore, it has commonly been assumed that the rate of change in  $A_{r/yarn}$  increases with increasing span of twist under horizontal comparison, which is available regardless of whether it is orthogonal or non-orthogonal. Under the same span of twist level under vertical comparison, a smaller  $\beta$  influences a bigger  $A_{r/yarn}$ , which can be seen from the three  $\beta$  in each figure (Fig. 2. 20a-c).

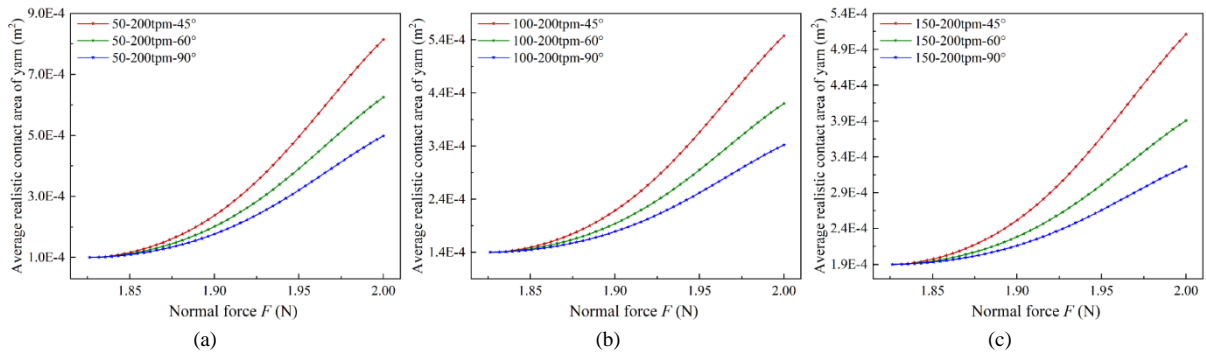


Fig. 2. 19. The realistic contact area of yarn  $A_{r/yarn}$  of a typical friction cycle with the different twist directions.

Fig. 2. 20(a-c) show the evolution of yarn friction force during the friction process. This friction force can characterize the friction behavior of yarns with different twist directions, that is, S-Z or Z-S. The span of twist level increases with the increasing range of friction force. The rate of change under a normal force applied of 2.00 N is more significant than other normal forces and is influenced by  $A_{r/yarn}$ . There is a gradual fall in the range of friction force as  $\beta$  increases, regardless of the span of twist level. Additionally, the trends of  $COF$  calculated by Eq (50) are shown in Fig. 2. 20(d-f) are similar to the friction force. However, the rates of change of  $COF$  and frictional behavior reflected by  $COF$  are different. For different spans of twist level, it can be revealed that the range of friction force decreases with the decreasing span of twist level during the friction process. The  $COF$  rises to a high point and peaks at a normal force applied of 2.00 N, which increases with the decrease of  $\beta$ . In general, the friction behavior is variable regardless of whether the twist is the same or different. The key parameters must thus be considered throughout the friction analysis of yarns.

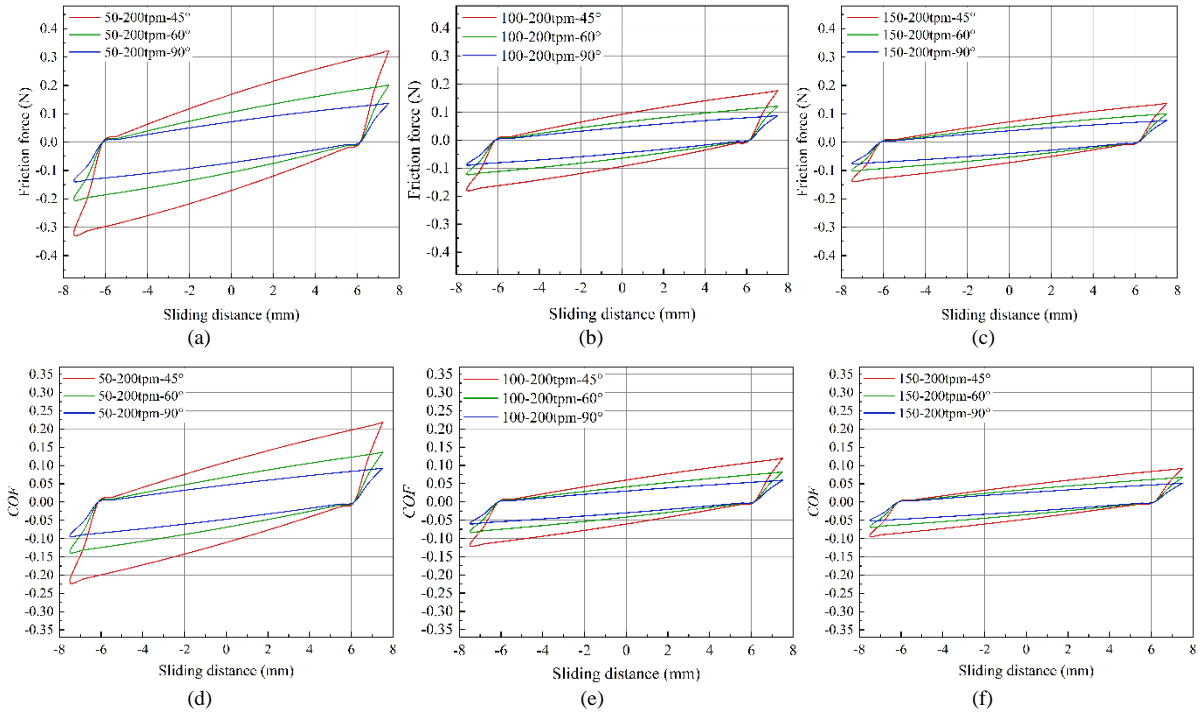


Fig. 2. 20. A typical friction cycle with the different twist directions: (a-c) friction force and (d-f)  $COF$ . (Note: Friction condition for test 4 was employed to analyze).

## 2.5 Summary of Chapter 2

Firstly, to study the contact mechanism of the fiber and improve the prediction accuracy of the contact area of the yarn, the orientation and the contact area of the fiber in the contact surface

are calculated by the image analysis method. The contact area between yarn and roller under different contact angles and pre-tension conditions was investigated by using a self-made contact simulation test device.

The orientation is the key factor affecting the contact area between the yarn and the roller. The contact angle and the pre-tension affect the orientation and change further the contact area between the yarn and roller. When the contact angle increases from  $60^\circ$  to  $170^\circ$ , the orientation of yarn gradually decreases, and the contact area also gradually decreases, and the contact area at  $60^\circ$  is 22 times that at  $170^\circ$ ; When the pre-tension increased from 0.19 N to 1.47 N, the orientation of yarn gradually increased, and the contact area gradually increased, and the contact area of the pre-tension is twice that of the 0.19 N. Furthermore, based on the Hertz theory, the modified model was established considering the orientation of yarn and is verified to be in high agreement with the experimental results.

Furthermore, an analytical model based on Hertzian contact theory at the micro-meso scale was constructed to characterize and predict the relative parameters during the yarn-yarn friction process. On account of the experimental analysis of the friction behavior between non-orthogonal twisted yarns (split into four characteristic phases) and the average error of friction force, the correctness of this model was determined. Furthermore, the analytical model can predict the friction behavior of yarns with the same and different twists regardless of the contact angle between the yarn axes.

In the same twist friction case, regardless of whether the yarns have similar twist levels and directions, the realistic contact area has an uptrend with the increase in normal load. By contrast, in the different twist friction case (different twist level and twist direction), the increase in relative parameters follows the same pattern as the same twist level friction. Regarding  $\beta$  of  $45^\circ$ ,  $60^\circ$  and  $90^\circ$ , a smaller contact angle  $\beta$  influences a bigger realistic contact area. The range of friction force and *COF* increase gradually with the increasing span of twist level regardless of the  $\beta$ . Additionally, the extreme values of the non-orthogonal friction force and *COF* are higher than the corresponding values for orthogonal friction under the same conditions since the realistic contact area of yarn  $A_{r/yarn}$  increases.

The investigation of yarn friction in fiber-reinforced composites is of importance as it is a key factor in optimizing the complex textile preform process and in improving the mechanical properties of the final composite. However, the effects are likely to deviate significantly from

reality due to adhesion processes. To quantify the effect of this mechanism on the friction behavior, a numerical model is required, which will be based on the present model. In addition, whether such a model can adequately account for the effects of wear or yarn size is a matter of interest for future research.

# **Chapter 3 Yarn-to-yarn friction behavior during the manufacturing of woven fabrics at meso-macro scale**

## Résumé en français

Les composites textiles, en tant que type particulier de composites, sont largement utilisés dans les domaines de l'aérospatiale, des navires marins, du biomédical et d'autres secteurs en raison de leurs excellentes propriétés telles qu'une haute résistance spécifique, un haut module spécifique, une légèreté et une grande capacité de conception structurelle. Les tissus, en tant que composant de renforcement des fibres, jouent principalement un rôle dans la prise en charge de la charge. Les caractéristiques mécaniques des tissus, déterminées principalement à l'échelle micro et méso, influencent les propriétés mécaniques des composites. La fabrication de renforts en fibres implique diverses structures de tissus et de fils, qui affectent la performance des composites.

Les dommages causés par la friction, la compression et la flexion des fils peuvent atteindre 5 à 30 % pendant le processus de préparation du renfort en fibres, représentant 9 à 12 % des dommages totaux dus à la friction. La friction entre les fils ou entre les fils et les composants de tissage réduit les propriétés mécaniques du renfort en fibres et affecte la durée de vie des composants composites. Tous ces éléments sont liés aux configurations des fils. Par conséquent, il est nécessaire de se concentrer sur la recherche des caractéristiques de friction des fils ou des fibres pendant le processus de préparation des renforts en raison de la compréhension limitée des recherches actuelles. Pour optimiser le processus de préparation et améliorer les propriétés mécaniques des composites, une compréhension approfondie du principe de friction des fils est requise.

Les recherches antérieures ont réalisé des progrès notables dans l'étude de la friction des fibres, mais présentent encore des lacunes et des défauts. Par exemple, les propriétés de friction des fibres naturelles comme le coton, la laine et les fibres de bambou ont été largement étudiées, tandis que les études de friction des fibres chimiques comme le nylon, le polyester et le polyéthylène augmentent en raison de leurs excellentes propriétés mécaniques. Les chercheurs ont modifié les fibres par des traitements chimiques pour améliorer leurs propriétés de surface. Par exemple, l'utilisation de décharges de plasma atmosphérique pour modifier la surface des fils d'aramide a permis d'améliorer considérablement leur résistance à la traction.

Pour améliorer plus efficacement la performance de friction des fibres, une compréhension approfondie des mécanismes régissant la friction est impérative. Les chercheurs ont mis au point de nombreuses méthodologies de test dédiées à l'examen de la friction des fils. L'évolution de ces techniques a permis un raffinement progressif et une sophistication accrue dans le domaine de la recherche sur la friction des fils, permettant un examen de plus en plus détaillé du sujet. Par



exemple, Turlonias et al. ont présenté une méthode efficace pour mesurer le coefficient de friction en fonction de l'angle de glissement entre 0 et 90° entre les fils ou les tows. Les résultats indiquent que le coefficient de friction diminue avec l'augmentation de l'angle.

En dépit des résultats obtenus dans le domaine de la friction des fils, il reste encore des lacunes, notamment dans l'étude de la tendance du comportement de friction en tenant compte des facteurs structurels. Peu d'études ont été menées pour investiguer la tendance du comportement de friction après avoir pris en compte l'influence des facteurs structurels (ou de la friction de plusieurs fils). De plus, un modèle théorique pour l'effet de la stochastique sur le comportement de friction résiduel après l'usure des fibres n'a pas encore été développé.

Pour combler cette lacune, la présente section a étudié le comportement de friction entre les fils lors du battement sous différentes configurations (tissage plat, satin et sergé) et tensions préalables des fils. Le modèle géométrique de Peirce a été utilisé pour développer un nouveau modèle théorique micro-méso pour prédire les propriétés de friction lorsque les fils sont soumis à la friction. Ensuite, la précision de ce modèle est validée par une analyse expérimentale. Enfin, les comportements de friction des fils en 2D et 3D ont été prédits sur la base du modèle théorique micro-méso.

L'étude utilise des fils de polyéthylène à poids moléculaire élevé (HMWPE, Spectra®) fournis par Honeywell Company, USA, avec des niveaux de torsion spécifiques. Des expériences ont été menées pour analyser le mécanisme de friction des fils pendant la fabrication de tissus tissés avec différentes architectures en utilisant une machine UMT Tribolab équipée d'un capteur de charge de 10 N.

Les résultats montrent que la force de friction moyenne augmente avec l'augmentation de la force de pré-tension pour les configurations S-cell et D-cell. La distribution de la pré-tension peut influencer la propriété de friction dans les renforts avec une plus grande surface de contact, ce qui entraîne une différence de force de friction entre deux distributions augmentant progressivement sous la condition de valeurs de pré-tension équivalentes. La corrélation théorique et expérimentale montre un bon accord pour les configurations de renfort avec plusieurs zones de contact. En outre, le modèle théorique a été utilisé pour prédire les propriétés de friction des fils pendant le battement des renforts en 2D et 3D dans les mêmes conditions.

Les résultats montrent que le coefficient de friction (*COF*) augmente avec l'augmentation de la pré-tension, similaire à la relation observée pour la force de friction (*F<sub>f</sub>*) en raison de la variation

de  $F_f$  par rapport à la surface de contact des fils pour tout renfort en 2D. Par ailleurs, la *COF* moyenne augmente avec l'augmentation du nombre de fils de trame regroupés, pour des raisons similaires à celles observées pour les renforts en 2D.

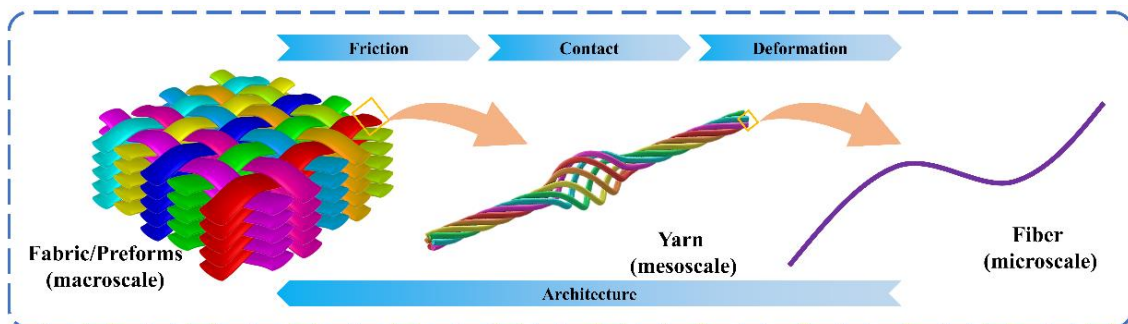
En conclusion, cette recherche fournit une base solide pour la compréhension des mécanismes intrinsèques et établit un fondement robuste pour de futures explorations et analyses de systèmes complexes et couplés. Un système d'évaluation combinant la prédiction des paramètres, la caractérisation géométrique et l'optimisation des paramètres est nécessaire pour une étude approfondie du comportement de friction et d'usure des fils pendant le processus de préparation des renforts textiles.

### 3.1 Introduction

Textile composites, as a special type of composites, are extensively used in aerospace, marine vessels, biomedical and other fields due to their excellent properties such as high specific strength, high specific modulus, lightweight and structural designability, etc.[10,43,190] The preparation process has three scales: macro, meso and micro (Fig. 3. 1(a)) [191,192]. The mechanical characteristics of fabrics, particularly as the primary component of fiber reinforcement, are predominantly determined at the micro and meso scales. At the micro scale, the properties of individual fibers, such as their tensile strength and elasticity, play a crucial role. At the meso scale, the interaction of yarns within the fabric structure significantly impact the overall mechanical performance[3,193], and their design in structure affects composite mechanical properties [34,194]. In general, fiber reinforcement is fabricated through an assortment of methodologies involving the structures of fabrics and yarns, which affect the performance of composites, as shown in Fig. 3. 1(b) [3,27,37]. The architectural impact involves three scales: microscale, mesoscale, and macroscale. Furthermore, the damage caused by friction, compression, and bending of yarns can alter the composite structure significantly, accounting for 9-12% of the total damage caused by friction, with potential increases up to 5-30% [74,83,195,196]. However, friction modes are influenced by contact behavior involving the deformation of fibers, which is significant in friction research[197,198]. Yarn/yarn friction is more complex and involves various phenomena and mechanisms. Yarns are composed of thousands of fibers, which can be twisted, sized, and even damaged[199]. Previous studies have reported the effects of structural reorganization, fiber treatment, and other factors on friction[200]. These elements have not been adequately addressed in the hypotheses or analysis of the experimental and analytical results of yarn/yarn friction. It is crucial to consider these elements to provide a comprehensive understanding of the frictional behaviors observed. The study of friction behavior can optimize the structure and process parameters of composites reinforcement, thereby improving the mechanical properties and durability of the composites. The friction modes of the reinforcements with different structures are different. The friction modes are significantly influenced by the contact behavior involving the deformation of fibers. This aspect is of considerable importance in friction research, yet only a limited number of researchers have delved into this area [108,201,202]. Consequently, it is imperative to thoroughly investigate the friction characteristics of yarn or fabric with varying structures. The current body of research exhibits a notable gap in understanding these dynamics,

underscoring the necessity for focused studies to elucidate the underlying mechanisms and their implications for composites performance.

To optimize the reinforcement preparation process effectively, a profound comprehension of the mechanisms governing friction is imperative. Researchers have developed many yarn friction testing methods to understand deeply sophisticated yarn friction research [74,170,203,204]. Ismail *et al.* [98] developed a new experimental setup to measure the dynamic friction behavior of two single fibers sliding onto each other at 90° to understand the friction mechanism. The results show the friction force increases by approximately 34% as the elastic modulus of the fiber increases, for a range of normal loads from 1 to 10 mN. Besides the experimental methods, researchers have continuously tried to employ analytical models to understand the friction properties of yarns [39,205,206]. Cornelissen *et al.* [66,72] developed a contact model to describe the friction behavior of fibers-metal and predicted friction behavior under various conditions. Specifically, the model employs a theoretical contact mechanics approach to describe this friction behavior, in which the nominal contact area is calculated by Hertzian contact theory after determining the relevant contact loads [106,207]. Wang *et al.* [109] developed a novel analytical model based on Cornelissen’s research to calculate the real contact area and describe the fiber arrangement of yarns under various conditions. Despite extensive research conducted in the field of theoretical models and experimental methods [71,208,209], several significant gaps remain, including scale-dependent friction mechanisms, characterization of contact surface and integration of theoretical and experimental approaches[210–212]. Notably, few studies have explored the impact of architectural factors on friction trends. There is a distinct lack of investigations characterizing the shape modifications of contact surfaces in relation to friction behavior using theoretical approaches. This oversight highlights the need for further research to comprehensively understand how these architectural factors influence friction and to develop more accurate predictive models for frictional behavior.



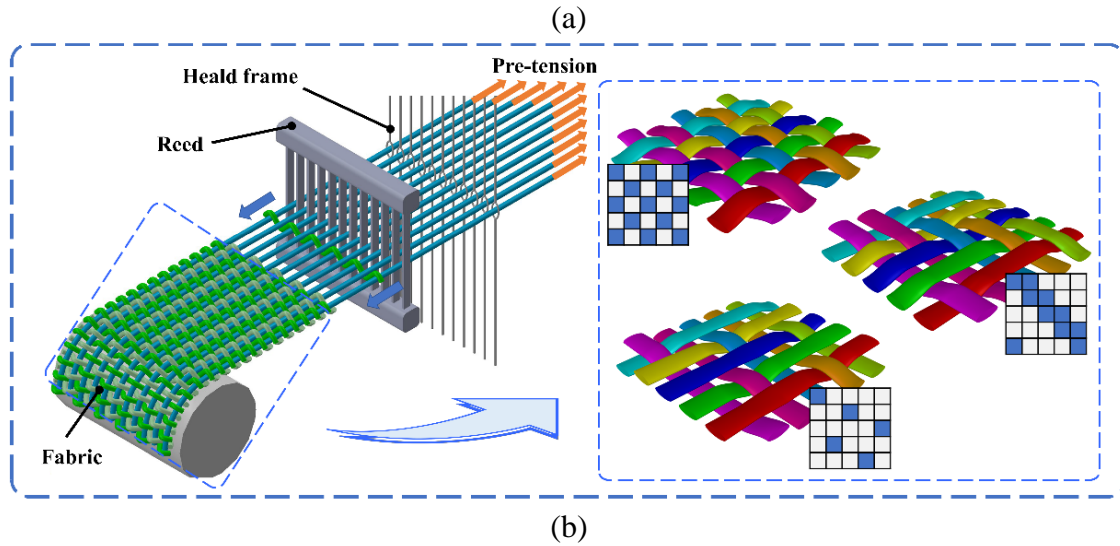


Fig. 3. 1. Multi-scale preparation description of composites: (a) overview of multi-scale; (b) schematic of the weaving process.

To address this gap, the primary interest of this research is to enhance the understanding of how architectural factors influence friction behavior due to the movement of the weft yarn during the beating-up process. The present research investigates the friction behavior between yarns under different woven fabric architectures and yarn pre-tensions. Peirce's geometrical model was utilized to develop a novel micro-meso theoretical model for predicting friction properties when the yarns are subjected to friction during the beating-up process. The accuracy of the model was validated based on experiments. Furthermore, the developed theoretical model can predict the coefficient of friction of yarns, considering the woven fabric's architectures and the yarns' pre-tension response. The developed model and theoretical methodology not only provide valuable insights into understanding the intrinsic mechanisms but also establish a robust foundation for future exploration and simulation analysis of intricate and coupling systems. The primary main objective of the current investigation are as follows:

- Proposing an experimental methodology that considers the mutual response of structure and mechanics for exploring the effect of structure on friction behavior during the weaving process.
- Improving the meso-micro theoretical model based on Peirce's geometrical model, considering the expanded width of contact surface.
- Providing basic data from experimental and theoretical aspects for the friction response of yarns during the weaving process.

### 3.2 Methodology

In this section, the experimental setup and the involved details are introduced in the first and second subsections, including the material, experimental setup and process. Furthermore, in the third subsection, the micro-meso scale theoretical model for the beating-up process of warp and weft yarns is established, taking into account the wrap angle and contact type, classified according to different configurations. Three contact types are involved in a variety of reinforcement configurations, no matter 2D or 3D. The detailed description of the employed theory and assumption behind its selection are described, providing a mechanical foundation for further developing friction behavior and model.

#### 3.2.1 Materials and samples manufacturing

The fiber material used for the experimental research was a product of High-molecular-weight polyethylene yarns (HMWPE, Spectra<sup>®</sup>) with a twist, provided by Honeywell Company, USA. Before being twisted, the fibers were in the form of a tow (no twist or weak twist yarn), with each tow consisting of a thousand single fibers. One yarn sample was prepared and named according to the twist level. Y-50tpm represents the sample of yarn with 50 tpm (twist per meter). The main properties of Y-50tpm yarn and fabric are shown in Table 3. 1. The data originate from the manufacturer and literature sources[185,186].

Table 3. 1 Material properties for HMWPE (Spectra<sup>®</sup> 900) Yarn and Fabric.

Sample	Property Description	Unit	Value
Yarn	Twist	tpm (Twist per meter)	50
	Shape of cross-section	-	circular
	Linear density	Tex	135 (±2.3)
	Density	g/cm <sup>3</sup>	0.97(±0.2)
	Yarn radius	mm	1(±0.1)
	Fiber radius	μm	8.5(±0.2)
	Modulus	Gpa	73
	Elongation	%	3.9
	Ultimate tensile strength	Gpa	2.57(±0.06)
Fabric	Warp yarn density	yarns/cm	6 (±1)
	Weft yarn density	yarns/cm	6 (±1)
	Areal density	g/m <sup>2</sup>	100 (±10)

### 3.2.2 Experiment setup and procedure

To analyze the friction mechanism due to the movement of the weft yarn during the manufacturing process of woven fabrics with different architectures, a characterization setup made by 3D printer technology is employed to study the influence of the interweaving environment on the friction behavior using the UMT Tribolab machine (Bruker company, USA), equipped with a 10 N load sensor ( $\pm 0.5\%$  F.S.). The sensor has a precision of 1 mN, ensuring accurate detection of even small variations in force. The load cells used had a measuring range of 0 to 20 N, covering the typical range of forces encountered in the friction tests. This experimental device consists of two main parts (upper and lower parts), as depicted in Fig. 3. 2. The powerful design capabilities and wide range of applications of the Tribolab, enabling users to develop a wide variety of setups for special experiments, which be utilized to investigate the friction behavior of warp and weft yarns (Fig. 3. 2(a)).

In the present research, the upper fixture is connected to the mechanical sensor, while the lower fixture is fixed to the pedestal, executing a linear reciprocating motion according to user settings. The motors of the tribometer drive the fixtures, which are used to simulate the weft beating-up during the actual weaving process, and the friction force applied to the process is measured by the mechanical sensors. During sample loading, the yarn is initially fixed at one side of the fixture (upper/lower fixture), given a constant pre-tension, and fixed to the opposite side of the fixture. Furthermore, the upper and lower fixtures are assembled into a device for conducting experiments in conjunction with the Tribolab, as illustrated in Fig. 3. 2(b). The pre-tensions with different distribution laws for warp yarn were selected to explore the evolution of friction behavior with LVDT (Linear Variable Differential Transformer). LVDT is measured by a differential transformer of Tribolab, which can characterize the linear displacement of yarn. LVDT has a precision of 1  $\mu\text{m}$ . The measuring range for displacement sensors was 0 to 120 mm, sufficient to capture the full range of motion during the tests.

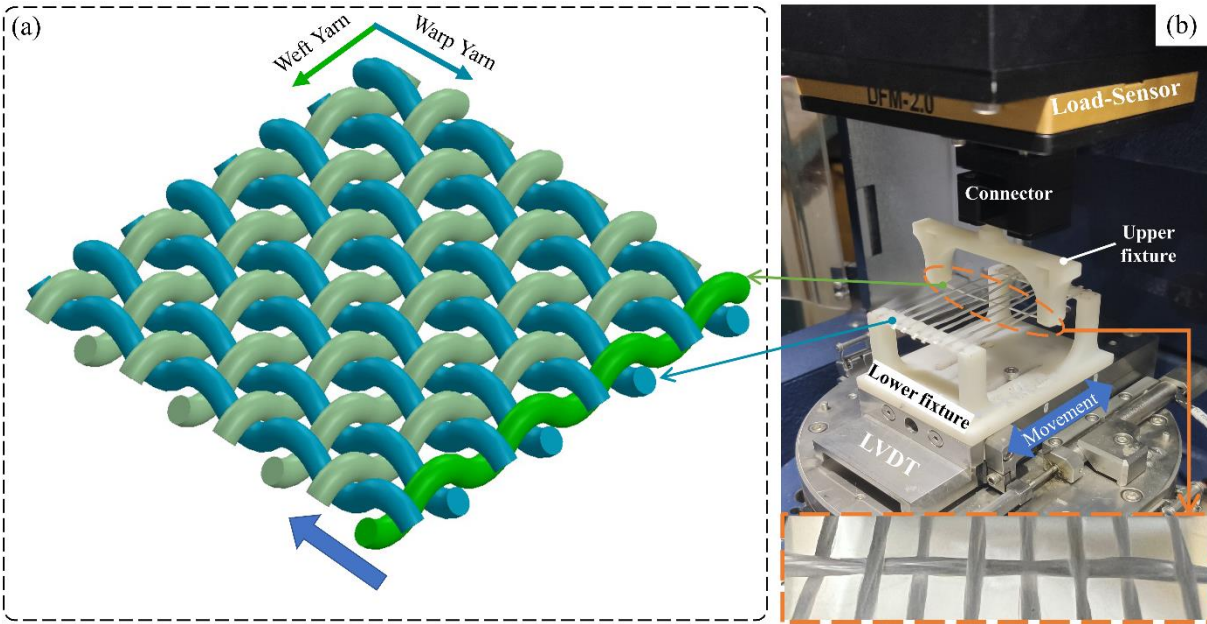


Fig. 3. 2. Friction device with yarn pre-tension dedicated to the beating-up friction test.

As described in previous research [109], an appropriate normal load is applied by displacement to the upper fixture. while maintaining a constant normal load, the top fixture is subjected to reciprocating motion in a straight line. The mechanical sensor measures the process data and accurately represents the friction behaviors of the current yarn situation in a specific arrangement. The cyclic procedure which has a speed of 5 mm/s. The effect of friction speed on the friction force and the coefficient of friction, are minor, which is mainly due to the fact that in the friction dur to the motion of the weft yarns, the actual friction force on the contact surfaces is more dependent on the contact area and the material properties than on the speed of motion. It may be divided into four distinct phases, as shown in Fig. 3. 3. The weft yarn weaves with various warp yarns, guided by the different fabrics' structures. Starting from one end of the warp strand, the weft yarn moves a displacement of 5 cm to reach Position 2. Subsequently, it continues along the length of the warp strand, covering an additional 5 cm until it reaches Position 3, thus completing the first half of the weaving cycle. By reversing its route in the opposite direction, it reaches Position 4 before returning to its initial Position 1, thereby completing the full rhythmic and cyclical process. Fig. 3. 3 displays the top and front perspectives, clearly denoting the path of the weft yarn through the fabric and the direction of the weft insertion process cycle. The blue and green arrows represent this procedure. The load sensor will monitor all loads during the test. To ensure reliability and accuracy, each experiment was repeated multiple times. Specifically, a



minimum of 5 tests were conducted for each configuration to account for variability and to provide statistically significant results.

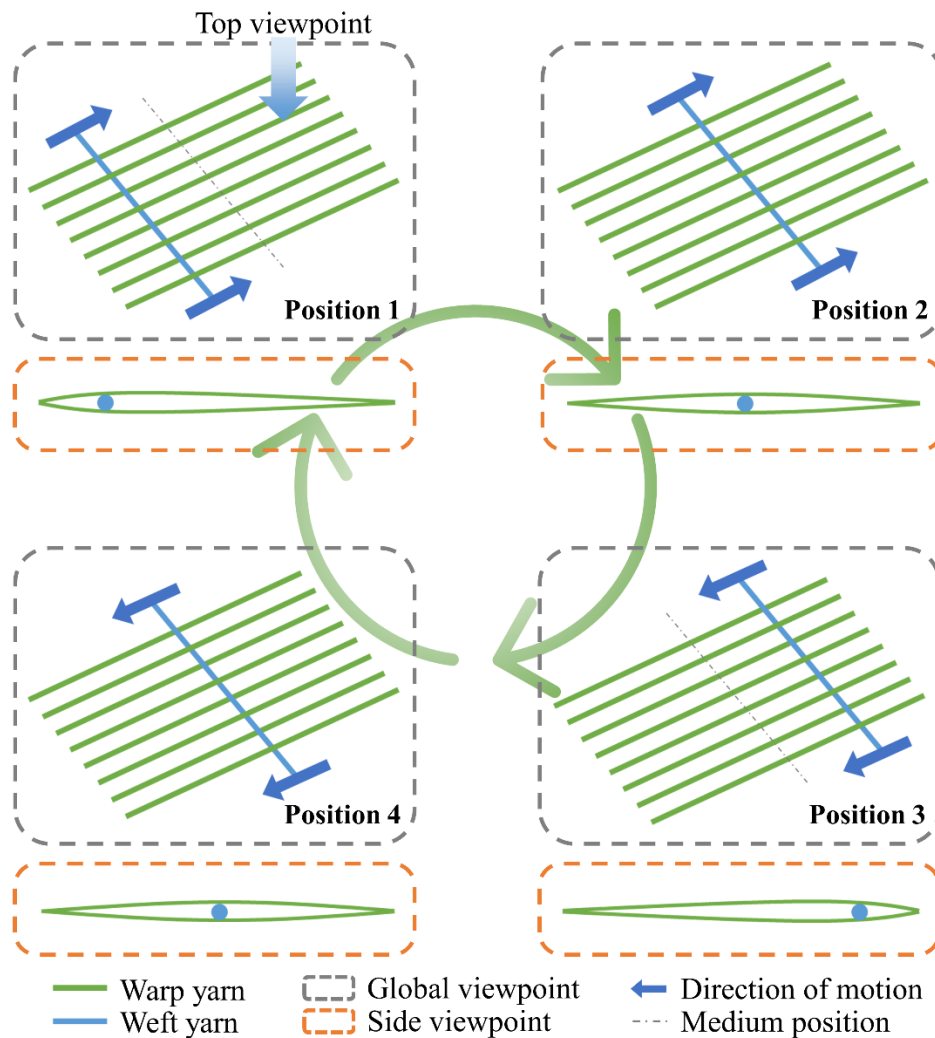


Fig. 3. 3. Schematic diagram of one cycle for the friction test.

### 3.2.3 Micro-meso theoretical model

During the weaving process, frequent friction occurs between the warp and weft yarns. The interstice of fiber engagement plays an essential role in exploring frictional phenomena. It is crucial to thoroughly investigate this subject, taking into account the invaluable details offered by previous research [39,213]. However, within the complex fabric architectures, the contact area of the yarn becomes more intricate compared to surfaces unaffected by structural influences. This complexity arises because the fabric's architecture affects the interweaving state of the yarns at the interlacing points, thereby influencing the contact behavior to varying degrees. The structural configuration exerts a significant impact on how yarns interact and the resulting frictional behavior at these interlacing points, leading to a more nuanced understanding of contact dynamics within

the fabric. To precisely calculate the contact area within a specific architecture and account for the interweaving states of the yarns. The initial yarn is assumed to be an elongated cylinder with uniform circular cross-sections. Upon deformation, the yarn exhibits increased contact areas with yarn. This transformation from a cylindrical shape to one with a larger contact surface is crucial for understanding frictional behavior during the weaving process. Peirce's geometrical model can be utilized to mathematically describe an arrangement of the yarn in the fabric [213,214]. The wave degree in warp ( $e_{warp}$ ) and weft ( $e_{weft}$ ) directions can be characterized by the equation:

$$\begin{cases} e_{warp} = \frac{2h_{warp}}{d_{warp} + d_{weft}} \\ e_{weft} = \frac{2h_{weft}}{d_{warp} + d_{weft}} \end{cases} \quad (51)$$

where  $d_{warp}$  and  $d_{weft}$  represent the effective diameters of individual yarns,  $h_{warp}$  and  $h_{weft}$  denote the wave heights of warp and weft yarns, respectively.

The definition of the yarn angle of circle center  $\alpha$  and the yarns is illustrated from the cross-sectional perspective of the warp yarn in Fig. 3. 4. This figure shows that the modes of contact can be classified into three types based on various values of  $\alpha$ , labeled as type 1, type 2, and type 3, which can be observed across diverse fabric architectures.

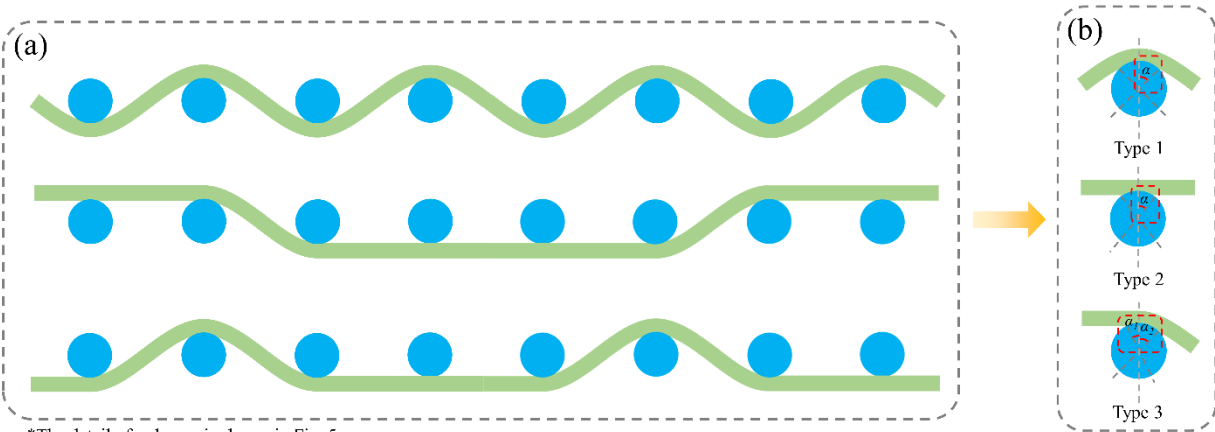


Fig. 3. 4. Overview of the contact types between yarns in different fabric architectures: (a) representative architectures and (b) contact types.

Regarding contact type 1, the relationship between related parameters is illustrated in Fig. 3. 5(a). The  $\alpha$  can be expressed through the geometric model as:

$$\alpha = \arctan \left( \frac{1 - \tan \beta \sqrt{\frac{e_{weft}^2}{\sin^2 \beta} - 1}}{\sqrt{\frac{e_{weft}^2}{\sin^2 \beta} - 1} + \tan \beta} \right) \quad (52)$$

where  $\beta$  is the angle related to  $\alpha$ , which meets the relationship “ $\alpha + \beta \neq \pi$ ” and the Eq.(52) can be employed to calculate  $\alpha$ :

$$\begin{cases} \sin \beta = \frac{e_{warp}}{2} = \frac{h_{warp}}{d_{warp} + d_{weft}} \\ \tan \beta = \frac{h_{warp} (d_{warp} + d_{weft})}{(d_{warp} + d_{weft} + h_{warp})(d_{warp} + d_{weft} - h_{warp})} \end{cases} \quad (53)$$

where  $h_{warp}$  and  $h_{weft}$  are calculated mathematically, see Fig. 3. 5(a) and (b).

Similarly,  $\alpha$  and  $\beta$  need to be met according to the following equations for contact type 2:

$$\begin{cases} \alpha + \beta = \pi \\ \sin \beta = \cos \alpha \end{cases} \quad (54)$$

Using the representative geometry, the contact arc length of warp yarn  $l_{warp}$  corresponding to  $\alpha$  can be obtained by:

$$l_{warp} = d_{warp} \cdot \alpha \quad (55)$$

The contact arc length of the weft yarn  $l_{weft}$  can be obtained individually by the above equation. From the top view, the expanded behavior needs to be considered, with additional details provided in Fig. 3. 5(c). The width spread of the warp and weft yarns, considering the expansion  $\omega$  ( $\omega_{warp}$  and  $\omega_{weft}$ ) is calculated following the existing research [215], which can be viewed as the intersection of two standard circles.

$$\omega = (12A_{trs}T_{hi})^{1/3} \quad (56)$$

where  $A_{trs}$  is the cross-section area of yarn and  $T_{hi} = h - d / 2$  is the thickness of the contact surface.

After deformation, the cross-section of yarn is elliptic. The  $A_{trs}$  can be obtained by approximate method[216,217]:

$$\begin{cases} A_{trs} \approx aE(2\alpha, e) \\ e = \sqrt{1 - (R_b^2 / R_a^2)} \end{cases} \quad (57)$$

where  $E(2\alpha, e)$  is the incomplete elliptic integral.  $e$  is the eccentricity, which can be shown by the semi-major axis  $R_a$  and semi-minor axis  $R_b$  of yarn cross-section deformed.

The contact area increases due to the expanded behavior given by Gauss law:

$$\Delta A = \iiint_{\Omega} \left( \frac{x^2}{\omega_{warp}/2} + \frac{y^2}{\omega_{weft}/2} + \frac{z^2}{T_{hi}} \right) dv \quad (58)$$

where  $dv = dx dy dz$  and  $\Omega$  is defined as:

$$\Omega = \left\{ (x, y, z) \left| \frac{x^2}{\omega_{warp}/2} + \frac{y^2}{\omega_{weft}/2} + \frac{z^2}{T_{hi}} \right. \right\}, \frac{d_{warp}}{2} \leq x \leq \frac{\omega_{warp}}{2}, \frac{d_{weft}}{2} \leq y \leq \frac{\omega_{weft}}{2}, 0 \leq z \leq T_{hi} \quad (59)$$

Consequently, the contact area of one interweaving point should be calculated by:

$$A_r = \alpha \alpha' \cdot d_{warp} d_{weft} + \Delta A \quad (60)$$

where  $\alpha'$  is the angle of the circle center. Mark “'” is denoted as the cross-section view of weft yarn. Finally, the contact area of fabric ( $A_{r,total}$ ) should be calculated by:

$$A_{r,total} = \sum_{i=1}^n A_{ri} = \sum_{i=1}^n i d_{warp} d_{weft} \cdot \arctan \left( \frac{1 - \frac{\sqrt{3} h_{warp} \cdot (d_{warp} + d_{weft})}{(d_{warp} + d_{weft} + h_{warp})(d_{warp} + d_{weft} - h_{warp})}}{\sqrt{3} + \frac{h_{warp} \cdot (d_{warp} + d_{weft})}{(d_{warp} + d_{weft} + h_{warp})(d_{warp} + d_{weft} - h_{warp})}} \right) \cdot \arctan \left( \frac{1 - \frac{\sqrt{3} h'_{warp} \cdot (d'_{warp} + d'_{weft})}{(d'_{warp} + d'_{weft} + h'_{warp})(d'_{warp} + d'_{weft} - h'_{warp})}}{\sqrt{3} + \frac{h'_{warp} \cdot (d'_{warp} + d'_{weft})}{(d'_{warp} + d'_{weft} + h'_{warp})(d'_{warp} + d'_{weft} - h'_{warp})}} \right) \quad (61)$$

Similarly, focusing on contact type 3, the arc length  $l_{warp}$  or  $l_{weft}$  corresponding to  $\alpha$ , which is related to contact types 1 and 2:

$$l_{warp} = \frac{1}{2} d_{warp} (\alpha_1 + \alpha_2) \quad (62)$$

where  $\alpha_1$  ( $\alpha_1'$ ) and  $\alpha_2$  ( $\alpha_2'$ ) are angles of the circle center of two contact types, individually. The meso contact area of one interweaving point should be calculated by:

$$A_r = \frac{1}{4} d_{warp} d_{weft} \cdot (\alpha_1 + \alpha_2) \cdot (\alpha_1' + \alpha_2') + \Delta A \quad (63)$$

Indeed, the meso contact area can be obtained through Eq. (64):

$$\begin{aligned}
A_{r,total} &= \sum_{i=1}^n A_{r_i} \\
&= \frac{1}{4} \cdot \sum_{i=1}^n i \Delta A d_{warp} d_{weft} \cdot \left( \arctan \left( \frac{1 - \frac{\sqrt{3} h_{warp} \cdot (d_{warp} + d_{weft})}{(d_{warp} + d_{weft} + h_{warp})(d_{warp} + d_{weft} - h_{warp})}}{\sqrt{3} + \frac{h_{warp} \cdot (d_{warp} + d_{weft})}{(d_{warp} + d_{weft} + h_{warp})(d_{warp} + d_{weft} - h_{warp})}} \right) + \left( \pi - \arcsin \left( \frac{h_{warp}}{d_{warp} + d_{weft}} \right) \right) \right) \\
&\quad \cdot \left( \arctan \left( \frac{1 - \frac{\sqrt{3} h'_{warp} \cdot (d'_{warp} + d'_{weft})}{(d'_{warp} + d'_{weft} + h'_{warp})(d'_{warp} + d'_{weft} - h'_{warp})}}{\sqrt{3} + \frac{h'_{warp} \cdot (d'_{warp} + d'_{weft})}{(d'_{warp} + d'_{weft} + h'_{warp})(d'_{warp} + d'_{weft} - h'_{warp})}} \right) + \left( \pi - \arcsin \left( \frac{h'_{warp}}{d'_{warp} + d'_{weft}} \right) \right) \right)
\end{aligned} \tag{64}$$

The effects of wrapping angle on contact area have been elucidated. Nevertheless, it is also necessary to consider the significant geometric changes in the load induced by the related angle. According to the widely accepted adhesion theory of friction, it is essential to identify force analysis. Therefore, the relationship between normal load  $F_n$  and  $\alpha$  needs to be established to further characterize the friction behavior between yarns. In this manner, the normal force applied  $F$ , related to the pre-tension  $F_p$ , can be projected in two directions (tangential and normal directions) shown in Fig. 3. 6(a) [109]:

$$\begin{pmatrix} F_t \\ F_n \end{pmatrix}_{(t,n)} = \begin{pmatrix} F \cdot \sin \theta \\ F \cdot \cos \theta \end{pmatrix} \tag{65}$$

where  $F$  can be described using  $F_p$  with the following equation:

$$F = \left[ E_l A_{rs} \left( \frac{H}{\sin \theta_1} + \frac{H}{\sin \theta_2} - 1 \right) + F_p \right] \cdot (\sin \theta_1 + \sin \theta_2) \tag{66}$$

where the  $E_l$  is the longitudinal modulus of warp yarn,  $\theta_1$  and  $\theta_2$  are angles between the warp and horizontal plane, and  $H$  is defined as displacement under the action of  $F$ , which can have a relationship using  $\theta_1$  and  $\theta_2$ . All of the parameters in Eq. (66) can be calculated using the above equations according to previous research [109] in Fig. 3. 6(b):

$$\theta_1 = \arctan \frac{2H}{a - L \sqrt{\frac{a^2 + 4H^2 - L^2}{a^2 - L^2}}} \tag{67}$$

$$\theta_2 = \arctan \frac{2H}{a + L \sqrt{\frac{a^2 + 4H^2 - L^2}{a^2 - L^2}}} \tag{68}$$

$$\sqrt{\left(\frac{a}{2}-u\right)^2+H^2}+\sqrt{\left(\frac{a}{2}+u\right)^2+H^2}=L \quad (69)$$

where the parameters of  $a$  and  $u$  are the span of the sample and the distance between the contact point and center of the span,  $L$  is the length of the warp yarn sample involved in friction which is obtained from the experiment.

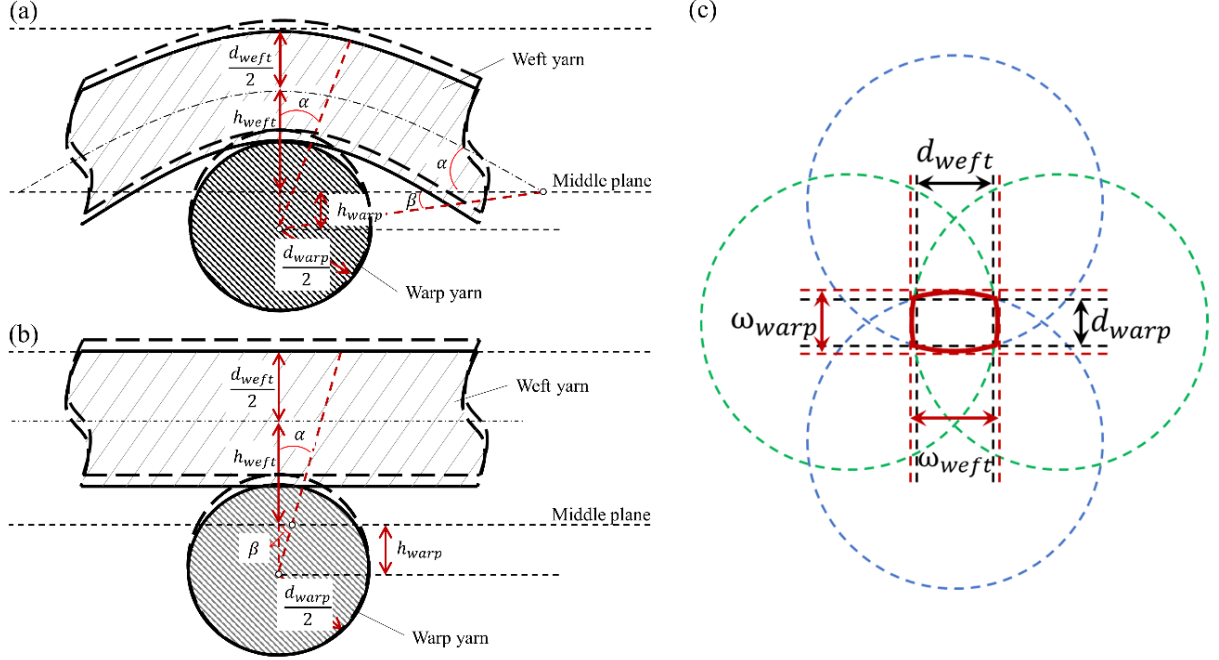


Fig. 3. 5. Geometric diagram of one interweaving point: (a) contact mode type 1, (b) contact mode type 2 and (c) top view for the contact zone.

Based on Eq. (13), the friction force  $F_f$  between yarns can be recalculated using Eq. (70) as presented in [97,218].

$$F_f = A_{r/total} \cdot \tau \quad (70)$$

where  $\tau$  is the specific shear strength.

The real-time coefficient of friction ( $COF$ ) needs clarification, defined as a ratio between the friction force  $F_f$  and the normal load  $F_n$  at the mesoscale. Eqs. (61), (64), (65), (66) and (70) have indicated that the  $COF$  is determined by various related parameters, as shown in Eq. 20:

$$COF = \frac{F_f(e, h, d, l, \alpha, \beta, T_{hi}, \omega)}{F_n^k(E_l, A_{trs}, \theta_1, \theta_2, F_p, H, a, u, L)} \quad (71)$$

where  $k$  is the fitting coefficient, equal to  $2/3$ , obtained experimentally for the friction between two objects undergoing complete elastic deformation.

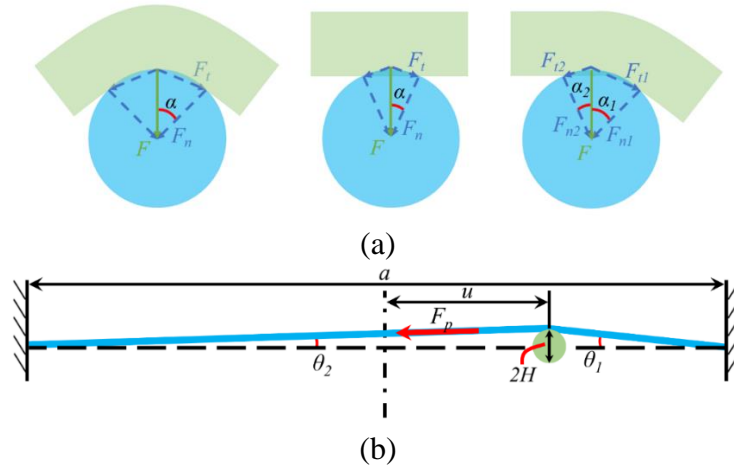


Fig. 3. 6. The key parameters of contact zone from (a) cross-section view of warp yarn and (b) cross-section view of weft yarn.

### 3.3 Significance of configuration on friction behavior based on pre-tension

Even though the friction force can be determined by calculating the contact area, many factors from the multi configurations could make the value of change to form the final contact surface based on different pre-tensions. Three special configurations were first selected, plain, satin and twill. Experiment with a single cell (S-cell) as an example, which is related to the wrapping angle. The contact area between warp and weft yarns was further calculated by counting the contact types in different configurations under different pre-tension conditions in this study. Secondly, Considering the pre-tension distribution law, involving the unique distribution and normal distribution, the friction forces of double cell (D-cell) reinforcement configurations, which are the same configuration as single double, are calculated in this subsection, which will help optimize weaving input parameters.

#### 3.3.1 Influence of S-cell reinforcement configuration

Fig. 3. 7. shows three representative reinforcement configurations, including plain, twill and satin. It can be seen that the type of yarn contact is different in each configuration, for instance, there are three types of contact, Type 1, type 2 and type 3, in the configuration shown in Fig. 3. 7(b). In this study, four warp yarns (green) and one weft yarn (blue) are employed as a cell, with the weft yarns moving back and forth in a special interweaving configuration, whose displacement is 5 cm per cycle. Throughout the entire process, the warp yarn remains in a state of extension due to the influence of the pre-tension force. Under varying tensile conditions, the results of frictional forces are presented in Fig. 3. 8. By comparing the friction test outcomes of three distinct configurations under pre-tension forces of 0.25 N, 0.50 N, and 1.20 N. The effect of pre-tension on the friction behavior between warp and weft yarns under the same S-cell reinforcement

configuration was investigated horizontally, furthermore, the effect of S-cell configuration on the friction behavior between warp and weft yarns was investigated longitudinally under consistent conditions of pre-tension. In the context of identical S-cell reinforcement configurations, it is observed that the average friction force demonstrates an upward trajectory as the pre-tension force increases. This phenomenon is primarily attributed to the amplification of the normal load resulting from the escalation in pre-tension force. Similarly, distinct S-cell reinforcement configurations exhibit varying average coefficients of friction under the same pre-tension conditions, with the plain weave configuration exhibiting the highest friction force, while the twill weave configuration exhibits the lowest. This discrepancy can be predominantly attributed to differences in contact, subsequently leading to variations in the contact area. Moreover, due to the relatively marginal disparities in the coefficients of friction among the three reinforcement configurations, discernible frictional traces cannot be readily observed in the actual observational figure (see Fig. 3. 8(a'), (b'), and (c')).

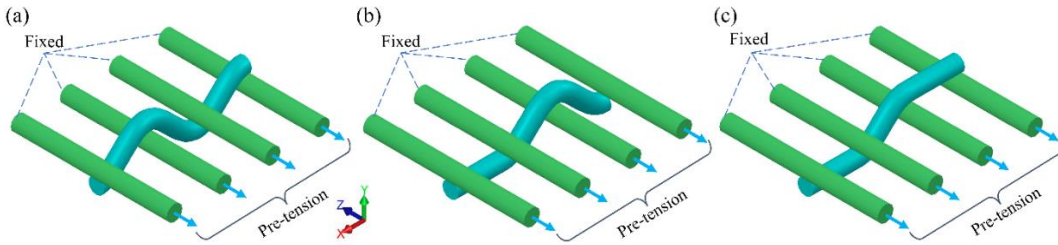


Fig. 3. 7. Single cell of representation reinforcement based on the actual weaving process: (a) plain (b) satin and (c) twill.

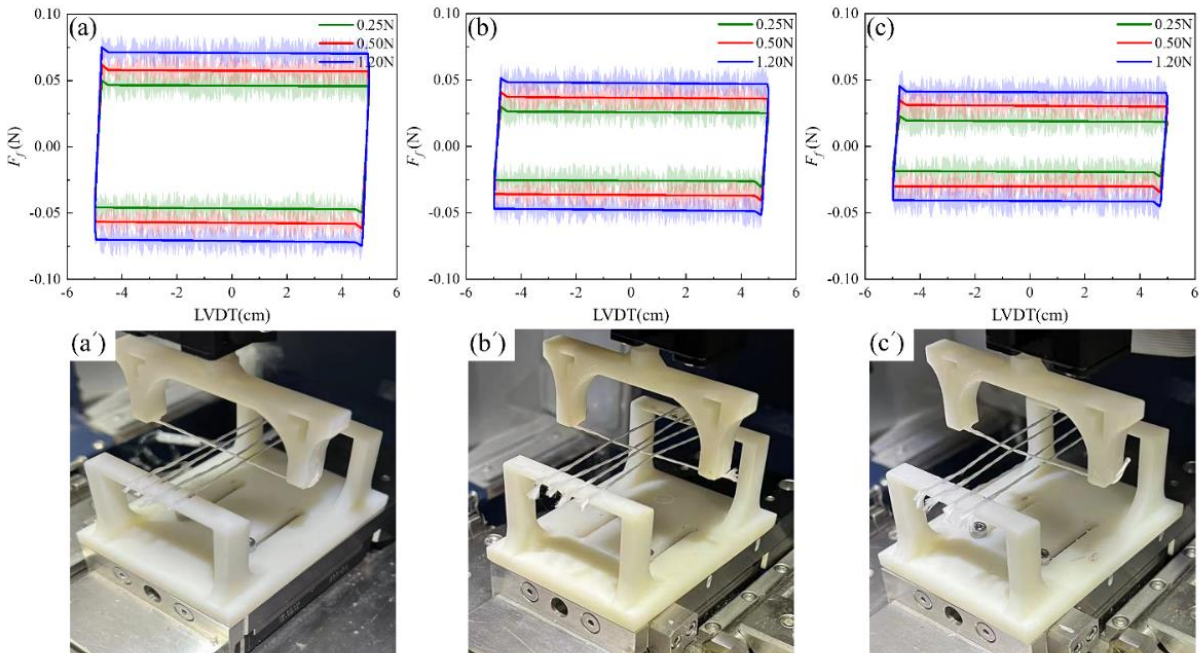




Fig. 3. 8. Influence of Friction behavior as a function on pre-tension: (a)-(c)  $F_f$  vs LVDT and (a')-(c') experimental observation.

### 3.3.2 Influence of D-cell reinforcement configuration

In this section, the friction forces of D-cell reinforcement configurations are conducted to explore the Influence of pre-tension distribution, including the unique and normal distribution. The D-cell reinforcement configurations are shown in Fig. 3. 9, which are the same as the configuration of a S-cell. It can be seen from the figure that the D-cell is the amalgamation of two S-cell reinforcements, which is regarded as one representative element. The unique distribution of pre-tension is also explored to explore the relationship between the number of cells and friction. The relationship between displacement under variable pre-tension distributions and the average frictional force can be observed in Fig. 3. 9. From the diagram, it is evident that under identical tensile stress distribution conditions, the variation in frictional force exhibits a similar trend, while the distinctions in frictional forces along the same displacement are readily discernible. Based on the varying contact types, the average frictional force displays a linear trend with respect to the pre-tension values, which mirrors the behavior observed in S-cell. Within the same reinforcement configuration, the average friction of UD-1.2N is larger than the normal distribution at the same condition. The difference is particularly significant in plain configurations, which is consistent with the findings of a previous study[109].

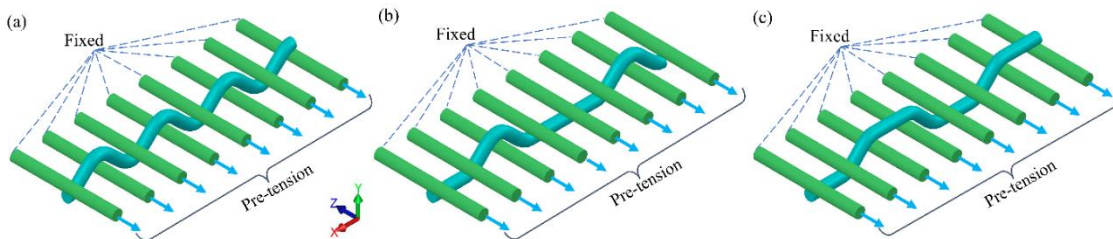


Fig. 3. 9. Double cell of representation reinforcement based on the actual weaving process: (a) plain (b) satin and (c) twill.

Similarly, the  $F_f$  is recorded along the direction of yarn length in Fig. 3. 10. It is noted that under the condition of different pre-tension distribution but the same pre-tension value, the average friction force difference of three types of reinforcement (Fig. 3. 9(a), (b) and (c)) between UD-0.50N and ND-0.50N are representatively  $1.45 \times 10^{-2}$ ,  $9.31 \times 10^{-3}$  and  $3.09 \times 10^{-3}$ . The difference in plain configurations is distinctly apparent. As established in the preceding section, it can be inferred that, under equivalent pre-tension values, the pre-tension distribution may influence the friction property in reinforcements with a larger contact area, which further leads to the difference of friction force between two distributions increasing gradually.

It is proposed to consider appreciated pre-tension when reinforcements with large contact areas are manufactured. Furthermore, the results show that the differences between the S-cells and D-cells did not show multiple relationships by comparing Fig. 3. 8. and Fig. 3. 10, that is,  $2F_{fs-cell} \neq F_{fd-cell}$ . Besides, it can be observed that  $F_{fs-cell}$  is always smaller than  $F_{fd-cell}$ , which may be related to the humidity and temperature of the environment, as well as the roughness of the yarn surface.

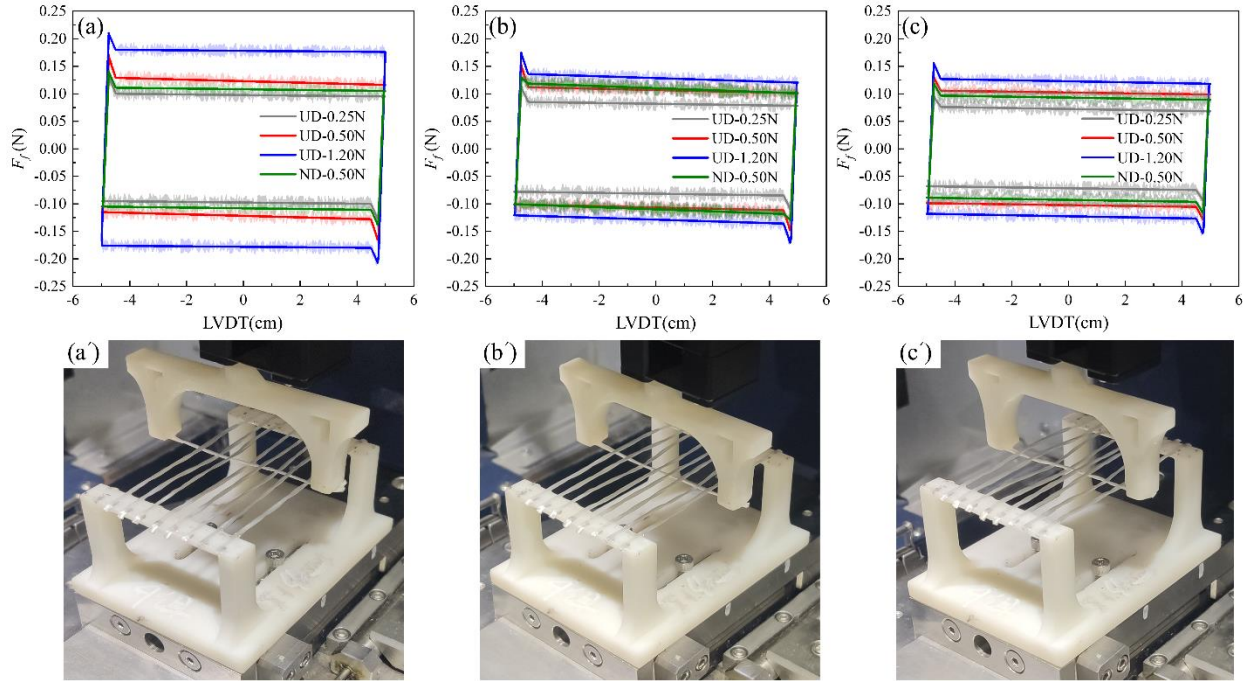


Fig. 3. 10. The friction forces of D-cell of representation configurations under different pre-tension.

### 3.4 Comparison Analysis of the friction behavior

The experimental average  $F_f$  is obtained by Tribolab equipped with self-designed fixtures to verify the theoretical model presented in Eq. (70) using the unique distribution of pre-tension 0.50 N and the normal distribution 0.50 N. The experimental and theoretical correlation of  $F_f$  in plain, twill and satin reinforcements with S-cell and D-cell are shown in Fig. 3. 11. Besides, the model errors of S-cell and D-cell are used and presented based on the research[219,220], respectively.

In Fig. 3. 11, it can be clearly observed that the theoretical values for S-cell often surpass the error range of experimental values. However, the overview of trends is the same as the experimental value, that is, the average friction force decreases as the increasing of contact area of yarns. Besides, the model error is slightly lower for plain than satin and twill. It is further confirmed that the accuracy of the theoretical model for plain is superior to satin and twill clearly for reinforcement configurations with few contact areas. Similarly, the difference in D-cell between theoretical and experimental values also are compared. it can be observed that the trend of the

theoretical values of the average friction for the three configurations on the condition of UD-0.50N is congruent with the experimental values. Apparently, the average value of  $F_f$  obtained by the theoretical model for the UD-0.50N condition lies within the error range of the experimental values, no matter the configuration of reinforcement, which revealed that the theoretical model can predict better reinforcement configurations with multiple contact areas. Indeed, the difference in average friction force of ND-0.50N calculated by the theoretical model is unclear between the three reinforcement configurations, which is similar to the experiment. Likewise, for ND-0.50N, the theoretical value is in the range of the experiment, whose errors are both less than  $\pm 10\%$ . Based on the above reason, the theoretical model can be regarded as highly efficacious in elucidating the structural characteristics of D-cells. However, the trend of average friction force can be obtained simply as a useful message for S-cell reinforcement configurations. The special values of S-cell are not able to be characterized as a reference.

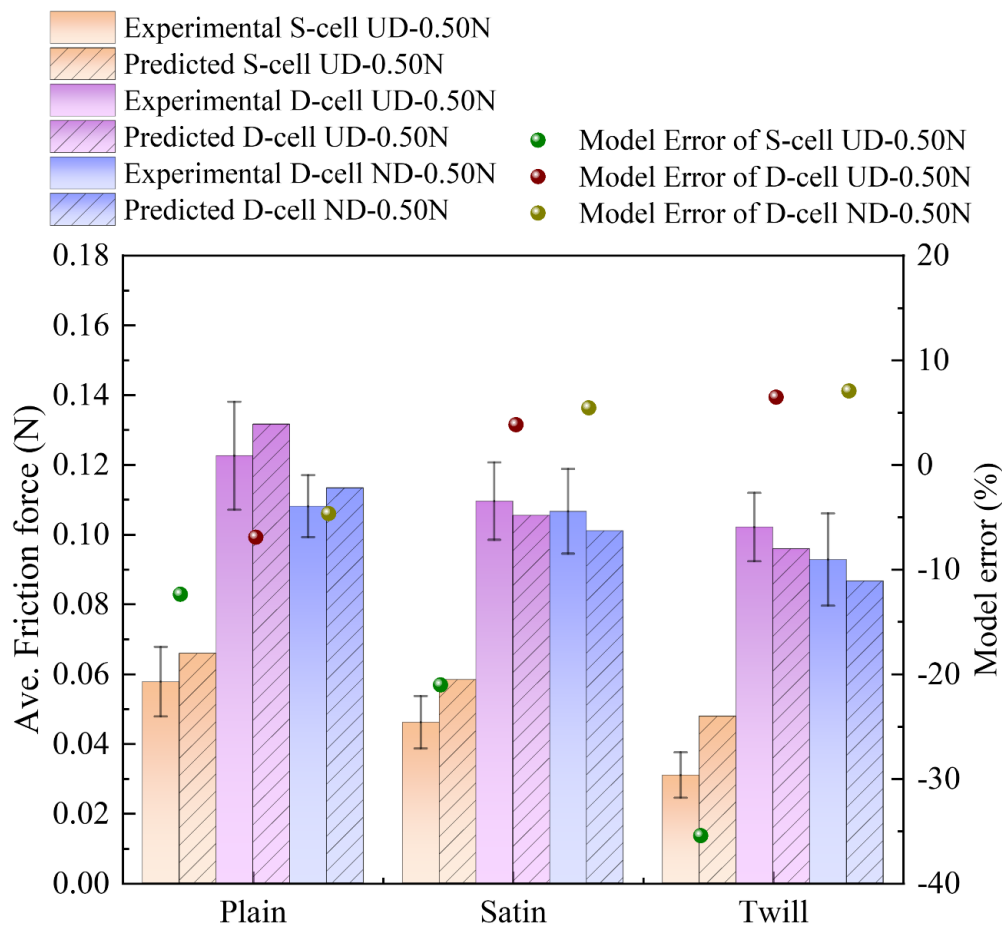


Fig. 3. 11. Comparison of the theoretical and experimental results on friction force under different configurations.

Although the theoretical model is not symmetrical, the yarn pre-tension and reinforcement configuration have a certain strong correlation because the contact area and angle of circle center are affected. Meanwhile, the calculations of friction behavior in theory can be applied to yarn pre-tension and reinforcement configuration. During the weaving process of the reinforcing phase, the situation is rare in the form of S-cells. Consequently, the comparison between experimental results and theoretical calculation can be performed for reinforcement configurations with multiple contact areas, which is enough to use after the variation of accuracy within limited theoretical error.

### 3.5 Approximate solution of friction behavior based on micro-meso analytical model

Employing the micro-meso theoretical model in the 3.3 subsection, the friction force of S-cell and D-cell were predicted. To further characterize the friction properties of different configuration reinforcements, the *COF* also is revised as an important parameter, which can be employed to react to the frictional properties of the reinforcements with  $F_f$ . Additionally, other types of reinforcement configurations were also predicted as examples, involving two directions (2D) and three directions (3D). The detailed parameters of contact properties are recorded, counting the yarn contact type in typical 2D and 3D reinforcements. Indeed, the contact area with different configurations is extensively discussed, and comparative analysis is also performed amongst the predicted results belonging to the typical 2D and 3D reinforcement configurations.

#### 3.5.1 Theoretical examples for 2D configurations

As discussed previously, the friction force can be calculated by the micro-meso theoretical model to characterize friction properties during the reinforcement preparation process between weft and warp yarns. Meanwhile, the *COF* is also used as a parameter to characterize the friction properties, which is calculated according to Eq. (64). Fig. 3. 12 presents the relationship of *COF* and LVDT of three configurations of S-cell on reinforcements under the normal load of 0.25 N during the beating-up stage. Due to the dynamics of the friction process, it is clear that all curves are similar to their corresponding friction. For any configuration of reinforcement, the *COF* increases as the increasing of pre-tension, whose relationship is the same as the  $F_f$ . Since the variation of  $F_f$  with respect to the yarn contact area, in this study, the normal load is invariant. Therefore, considering the definition of *COF*, the main reason for its variation is the contact surface roughness. The *COFs* of various configurations are found to be different, which is tangible in average value. At present, it is possible to obtain the related parameters for future analysis of friction property, particularly in simulation. The *COF* is too high or too low to be used in the

preparation process of actual reinforcements. The appreciated values should be selected to achieve neither yarn damage nor slippage.

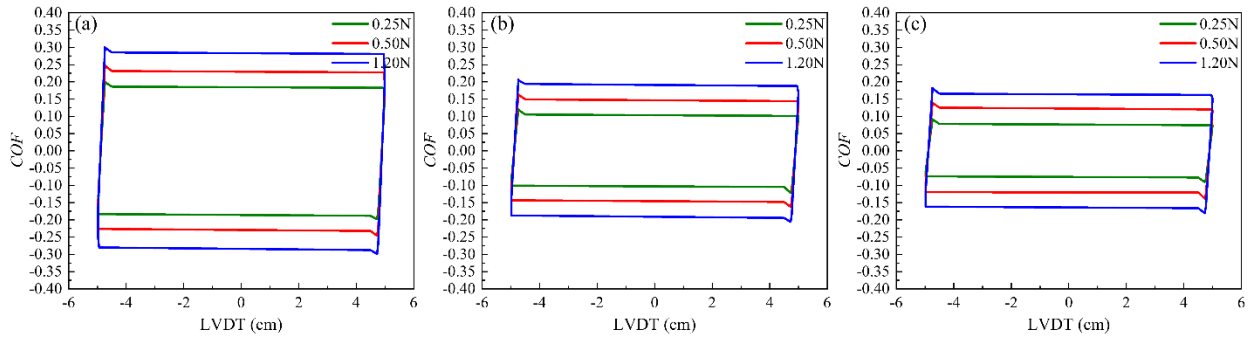


Fig. 3. 12. Predicted trend in *COF* with different S-cell configurations under different pre-tension: (a) plain (b) satin and (c) twill.

### 3.5.2 Theoretical examples for 3D configurations orthogonal

Compared to 2D fabrics, 3D interlock fabrics are increasingly recognized as advanced structural reinforcements in the manufacturing of composites with significant thickness, lightweight, and high-performance parts. Fig. 3. 13 illustrates three classical 3D interlock structures: layer-to-layer, angle and orthogonal structures. With the addition of yarns in the third direction (binder yarns) to link each layer, the friction phenomenon becomes more complex compared to the manufacturing of 2D fabrics. Both the friction of warp and weft yarns in the fabric plane and the friction of binder and warp yarns in cross-section should be considered. In particular, regarding a 3D structure, the cover angles vary in each layer and in different 3D structures, significantly impacting friction and yarn wear behavior.

In LTL Stru 5-3 and A-L Stru 5-3 interlock fabrics (Fig. 3. 13), the weft yarns determine the number of layers of the 3D warp interlock configuration and mostly provide the transverse mechanical properties of multi-layer fabrics [39]. However, the 3D fabric has a different configuration of binder yarns, which results in a difference in contact area. Therefore, each binding yarn, warp and weft, is treated as a cell and its friction characteristics are analyzed. To visualize the positional relationships of the yarns, the schematic diagrams of cross-section along the weft yarn length of the two 3D architectures are shown in Fig. 3. 13(a') and (b').

Fig. 3. 13 presented the typical orthogonal 3D reinforcements Orth.-5-3, where the value of the warp and weft are 3 and 5. And the ratio of binder and warp yarn is 1:2. It can be shown clearly that the warp and weft yarns are in vertical contact and the binding yarns are interwoven throughout the reinforcement. The weft yarns determine the number of layers of the 3D warp interlock configuration and mostly provide the transverse mechanical properties of multi-layer reinforcements[39]. However, the 3D reinforcement has

a different configuration of binder yarns, which results in a difference in contact area. Therefore, each binding yarn, warp and weft, is treated as a cell and its friction characteristics are analyzed. To visualize the positional relationships of the yarns, the schematic diagrams of cross-section along the weft yarn length of the two 3D configurations are shown in Fig. 3. 13 (c') and (d').

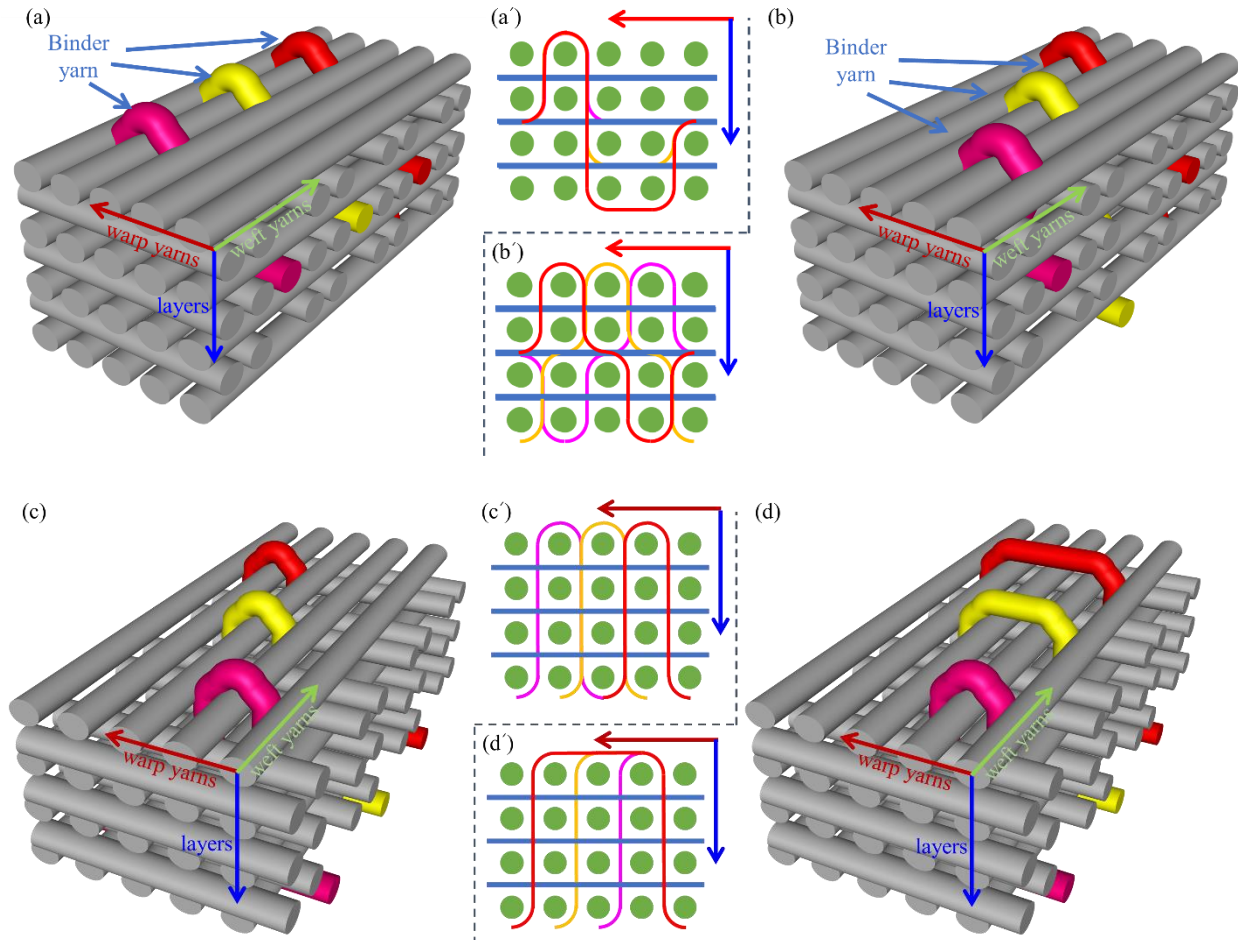


Fig. 3. 13. Schematic diagram of representative 3D fabric architectures (a & b) and weft cross-section (a' & b'): (a) LTL Stru 5-3 (b) A-L Stru 5-3 (c) and (d) Orth. 5-3.

Based on the placement of the binder yarns, the associated configuration cell can be identified. Table 3. 2 illustrates six configuration cells of two typical 3D interlock fabrics, with notes on the weft cross-section and involved contact type. For instance, C-L4-M2-R2 indicates that the binder yarn bundles 4 yarns on the left, 2 yarns in the middle, and 2 yarns on the right. The contact types are determined based on those described in the previous section. It is evident from the weft cross-section figure that for the LTL Structure 5-2, the binder yarn consistently "bundles" 4 yarns on the left, by contrast for the A-L Structure 5-2, 4 yarns in each of the three positions are "bundled".

According to the location of the binding yarn, the cell related can be noted. For example, C-L0-M0-R4 represents the binder yarn bundled the one column of yarn on the right. More cells (C-

L0-M0-R4, C-L0-M4-R4 and C-L4-M4-R4) are used in this section. The weft cross-section and contact type involved are listed in Table 3. 2. The contact types are counted based on the stated in the previous section. It is clear from the figure that the binding yarn only “Bundled” one column of weft yarn (4 yarns) for O-Twill 5-3, in the contract, weft yarns (Number of yarns bound: 8 and 12 yarns, representatively) for O-Twill 5-3. Further, the yarn contact area increases with the number of yarns bundled, which in turn leads to an increase in the contact area.

Table 3. 2 Contact properties of binding warp and weft yarns in representative 3D reinforcement configurations.

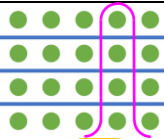
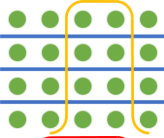
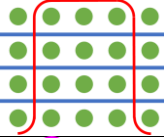
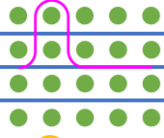
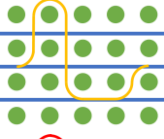
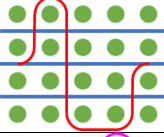
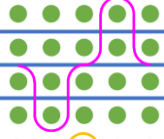
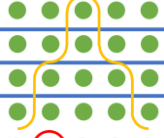
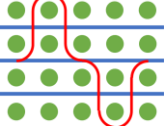
Fabric	Configuration name	Weft cross-section	Contact type			Num. contact zone
			Type 1	Type 2	Type 3	
O-Twill 5-3	C-L0-M0-R4		1	9	2	12
	C-L0-M4-R4		0	9	4	13
	C-L4-M4-R4		0	10	4	14
LTL Stru 5-3	C-L4-M2-R2		1	7	2	10
	C-L4-M1-R1		2	7	2	11
	C-L4-M0-R0		2	10	2	14
A-L Stru 5-3	C-L0-M2-R4		2	6	4	12
	C-L2-M4-R2		1	5	6	12
	C-L4-M2-R0		2	6	4	12

Fig. 3. 14 (a) displays the change law of contact area for different cell configurations under pre-tension of unique distribution of 0.5 N, which firstly indicates a relationship between configuration and mechanical property. To detail this relationship, it can be obtained from the figure that the contact area is independent of the location of the binding yarn, however, is dependent on the number of weft yarns bundled. The contact area of C-L4-M4-R4 is the largest within the whole O-Twill 5-3. After the calculation of The *COF* of all cells both are shown in Fig. 3. 14(b). The evaluations of *COF* are similar, which also present one cycle during the beating-up. The *COF* of cells with same the number of weft yarns bundled is the same. The average *COF* increases as the increasing of the number of weft yarns bundled, whose reason is similar, that is, the increasing of contact area. Generally, the *COF* can indicate the degree of resistance for the contact pair during the friction. The value of *COF* is high, which can be assumed that the friction force is high. In addition, the contact area of C-L4-M0-R0 is the largest within all of the LTL Stru 5-2. The contact areas of three configurations for A-L Stru 5-2 are the same because of the number of "bundled". The *COFs* for all configurations are calculated and depicted in Fig. 3. 14(b). The *COF* serves as an indicator of the resistance experienced by the contact pair during friction. An increase in *COF* usually indicates an increase in friction forces. Therefore, *COF* should be regarded as one critical parameter throughout yarn friction analysis.

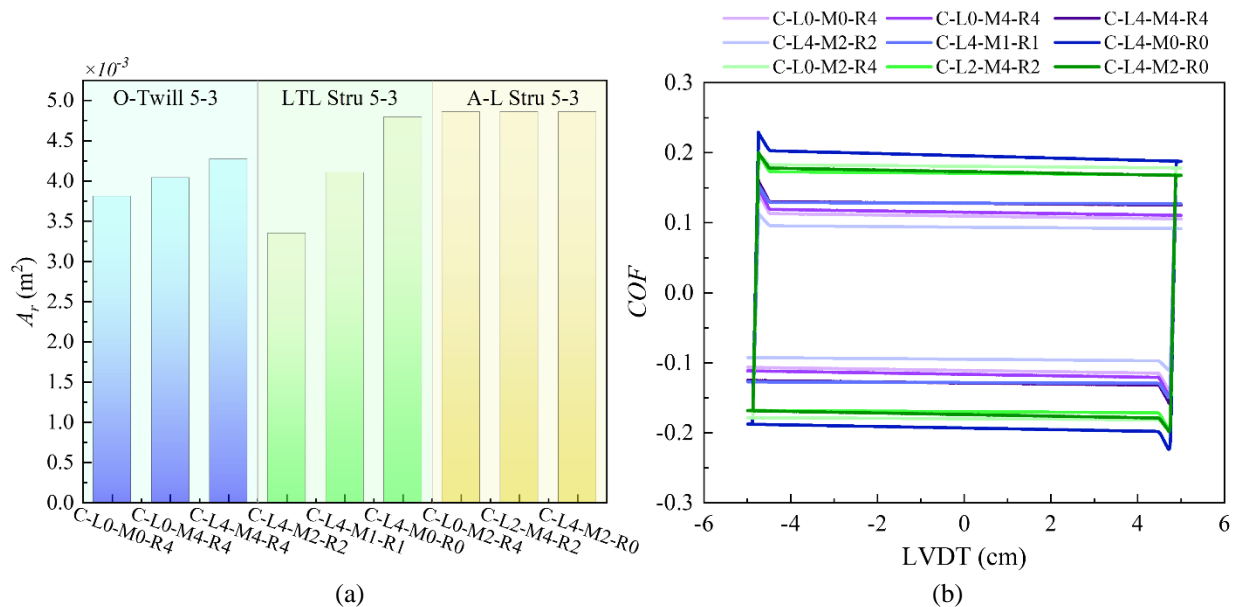


Fig. 3. 14. Predicted contact area (a) and *COF* (b) of representative 3D configurations.



### 3.6 Summary of Chapter 3

The preparation process of fiber reinforcement is a complex process in which several mechanical behaviors of yarns are shown. The principle of friction behavior between yarns, as one of the key mechanical behaviors, is not clear yet involved in configuration regardless of yarn or reinforcement. Therefore, it is critical to focus on the research on the friction characteristics of yarn or fiber during the preparation process of textile-reinforced composites in this research. Firstly, a micro-meso theoretical model for yarn is developed to reveal the friction mechanic. Secondly, two parameters of reinforcement configurations -plain, satin and twill- and pre-tensions of yarns -value and distribution- were employed to explore the friction properties during the beating-up, verifying the developed theoretical model. The results show that the average coefficient of friction demonstrates an upward trajectory as the pre-tension force increases for S-cell and D-cell. The pre-tension distribution may influence the friction property in reinforcements with a larger contact area, which further leads to the difference of friction force between two distributions increasing gradually under the condition of equivalent pre-tension values. The theoretical and experimental correlation is performed and shows a good agreement for reinforcement configuration with multiple contact areas. Furthermore, the theoretical model has been employed to predict the friction property of yarns during the beating-up of 2D and 3D reinforcements with the same conditions, counting on the type of contact for different reinforcement configurations. The results show that the *COF* increases with the increase of pre-tension, whose relationship is the same as  $F_f$  due to the variation of  $F_f$  concerning the yarn contact area for any 2D reinforcement. On the other hand, the average *COF* increases with the increasing number of weft yarns bundled, whose reason is similar to 2D. The friction properties of yarns are mainly characterized by friction force and *COF* during the beating-up. It needs further study to establish an evaluation system, combining parameter prediction, geometric characterization and parameter optimization. Moreover, the mechanical properties of the yarns and the pre-tension applied during weaving are important parameters considered in the predictive theoretical model. Further research is needed to solve the problem of constant yarn cross-sectional area, a nonlinear contact algorithm model is required. The model will consider the dynamic changes in contact area, stress distribution and friction due to the inhomogeneity of the yarn cross-section. By incorporating these nonlinear interactions, the model can more accurately simulate the mechanical and frictional behavior of the yarn, leading to improved prediction and optimization in the weaving process.

## **Chapter 4 Numerical simulation and experimental validation of yarn/yarn friction considering fiber damage and wear prediction**

## Résumé en français

Avec les avancées technologiques, la demande pour les matériaux composites ne cesse d'augmenter. Les composites renforcés de fibres sont largement utilisés dans les industries modernes en raison de leurs propriétés mécaniques supérieures et de leurs caractéristiques personnalisables. Ces composites combinent la haute résistance de diverses fibres avec la ténacité des matériaux de matrice, ce qui donne des produits légers, solides et durables qui surpassent les capacités des matériaux traditionnels. Les processus de conception et de fabrication des composites de fibres peuvent être adaptés aux besoins spécifiques des applications, les rendant indispensables dans des industries telles que l'aérospatiale, la fabrication automobile, les équipements sportifs et la construction.

Dans le domaine de la fabrication de composites de fibres, le contrôle des dommages pendant la phase de renforcement est crucial pour améliorer les propriétés mécaniques du produit final. La phase de renforcement implique généralement des fibres haute performance comme les fibres de carbone, les fibres de verre ou les fibres d'aramide, qui confèrent aux composites une résistance et une rigidité exceptionnelles. Cependant, lors du tissage de ces fibres dans des structures de préformes, elles peuvent subir des étirements, des flexions et des frictions, conduisant à une réduction des performances mécaniques ou même à des ruptures. Cela est particulièrement évident pendant les processus de préformation textile tels que le tissage, le tricotage ou les techniques de tissage avancées, où des interactions fréquentes entre les fils se produisent, causant notamment des dommages par friction. Ces dommages diminuent non seulement la capacité de charge effective des matériaux mais peuvent également entraîner une diminution des performances mécaniques à l'échelle macro, compromettant ainsi l'intégrité structurelle et les performances fonctionnelles des matériaux composites finaux.

Actuellement, la plupart des recherches sur la friction sont réalisées d'un point de vue expérimental. Des chercheurs ont exploré la modélisation avancée des interactions entre les fils lors du surfaçage, introduisant un modèle qui prédit avec précision les angles de tresse en tenant compte de la friction des fils dans le tressage non axisymétrique. D'autres ont examiné le comportement de friction des tissus végétaux et synthétiques pour aborder les défauts de fabrication, mettant en évidence que la friction entre les tows de tissu peut être manipulée en ajustant les motifs de tissage et la tension, conduisant à une meilleure stabilité du tissu et à une réduction des défauts de fabrication. Bien que les méthodes expérimentales puissent refléter efficacement le comportement de friction, les

résultats sont fortement influencés par les conditions de préparation et les procédures expérimentales, introduisant un degré de variabilité. Pour capturer une représentation précise des conditions réelles, plusieurs séries d'expériences sont nécessaires. Cette variabilité est particulièrement prononcée lors de l'étude de la friction fil-sur-fil, car les différences dans les propriétés matérielles des fils, les conditions environnementales et les surfaces de contact de friction peuvent conduire à des résultats divergents à chaque essai.

Pour cette étude, un modèle de simulation numérique a été développé pour investiguer en détail le mécanisme de dommage par friction entre les fils. Des recherches antérieures ont examiné des facteurs influençant la friction des fils/fibres, tels que l'angle de contact, la pré-tension et la vitesse. Cependant, les études se concentrant sur le comportement d'usure dû à la friction et son impact sur la performance matérielle sont relativement rares, résultant en des évaluations de performance incomplètes et des limitations dans l'optimisation de la conception. Pour répondre à cela, notre étude a développé un modèle constitutif des fibres en utilisant la sous-routine utilisateur VUMAT et a établi un modèle de fil à haute précision basé sur la théorie de la poutre de Timoshenko pour résoudre efficacement les problèmes d'intrusion des éléments de poutre. La précision du modèle de simulation numérique, en termes de mécanique et de géométrie, a été validée à l'aide de courbes de déplacement provenant d'une machine de test de friction équipée de dispositifs sur mesure et d'observations par Micro-CT. Le modèle proposé a réussi à prédire le comportement de friction et d'usure en tenant compte des interactions de contact entre les fibres et a examiné l'influence des paramètres géométriques et mécaniques des fils sur ces comportements.

Les résultats de cette étude montrent que la force de friction diminue à mesure que la torsion du fil augmente et augmente à mesure que la charge normale sur le fil augmente. En ce qui concerne l'effet de la pré-tension des fils sur le comportement de friction et d'usure, la force de friction entre deux fils ayant la même pré-tension diminue à mesure que la torsion augmente, tandis qu'elle augmente à mesure que la pré-tension augmente. De même, la force de friction des fils avec des pré-tensions différentes diminue avec l'augmentation de la torsion, tandis qu'elle augmente avec l'augmentation de la pré-tension, bien que les différences soient plus faibles que dans le cas de la même pré-tension. La torsion des fils et le nombre de cycles de friction ont un impact significatif sur la distribution des contraintes et les conditions de rupture. Les fils sont plus susceptibles de se casser après plusieurs cycles de friction, avec des phénomènes de concentration de contraintes notables.

Cette méthodologie et les résultats peuvent guider la conception structurelle des préformes textiles avant leur mise en forme, réduisant ainsi les défauts de pliage des préformes, ce qui est d'une grande importance pour l'amélioration des performances et l'application des matériaux composites finaux. Toutefois, cette étude simplifie la structure transversale et le comportement de friction de contact du modèle de fil virtuel, ce qui sera pris en compte dans les travaux futurs. Le modèle proposé répond efficacement aux effets combinés de la torsion, de la charge normale et de la pré-tension sur le comportement de friction des fils, guidant ainsi la conception géométrique et mécanique pendant la fabrication du renfort, contrôlant ainsi la friction et l'usure des fils, ce qui est d'une grande importance pour l'amélioration des performances et l'application des matériaux composites finaux.

## 4.1 Introduction

With technological advancements, the demand for composite materials continues to rise. Fiber-reinforced composites are widely utilized in modern industries due to their superior mechanical properties and customizable features[3,221]. These composites combine the high strength of various fibers with the toughness of matrix materials, resulting in lightweight, strong, and durable products that surpass the capabilities of traditional materials. The design and manufacturing processes of fiber composites can be tailored to specific application needs, making them indispensable in industries such as aerospace, automotive manufacturing, sports equipment, and construction[10].

In the realm of fiber composite manufacturing, controlling damage during the reinforcement phase weaving is crucial for enhancing the mechanical properties of the final product. The reinforcement phase typically involves high-performance fibers like carbon fibers, glass fibers, or aramid fibers, which provide the composites with exceptional strength and stiffness[49,83,202]. However, during the weaving of these fibers into preform structures, they may experience stretching, bending, and friction, leading to reduced mechanical performance or even breakage[222,223]. This is particularly evident during textile preforming processes such as weaving, knitting, or advanced weaving techniques, where frequent interactions between yarns occur, notably causing friction damage[211]. Such damages not only diminish the effective load-bearing capacity of the materials but can also lead to a macro-level decline in mechanical performance, thus compromising the structural integrity and functional performance of the final composite materials[224].

At present, most friction research is performed from an experimental point of view. Vu et al.[206,210] explored advanced modeling of yarn interactions during overbraiding. A model that accurately predicts braid angles by accounting for yarn friction in non-axisymmetric braiding was introduced. They expand on this model by examining the effects of lubrication on friction, finding that water increases friction due to capillary forces. These insights help refine the overbraiding process, crucial for textile manufacturing in the automotive and aerospace industries. Salem et al.[225] examined the frictional behavior of vegetal and synthetic fabrics to address defects in manufacturing. The research highlights that friction between fabric tows can be manipulated by adjusting weave patterns and tension, leading to improved fabric stability and reduced manufacturing defects. Although experimental methods can effectively reflect friction behavior,

the results are heavily influenced by preparation conditions and experimental procedures, introducing a degree of variability. To capture an accurate representation of actual conditions, multiple sets of experiments are required. This variability is particularly pronounced when studying yarn-on-yarn friction, as differences in yarn material properties, environmental conditions, and frictional contact surfaces can lead to divergent results in each trial. Furthermore, to accurately investigate the frictional wear of yarns/fibers during the reinforcement weaving process, researchers often construct experimental setups or custom fixtures to equip wear testing instruments for precise experiment[69,100,108]. Wang et al.[109] introduced and validated an analytical model to analyze yarn/yarn friction in textile weaving, focusing on twisted yarn interactions by self-made experiment equipment. Guo et al.[226] examined the wear and friction of Z-directional fibers in preforms, using experimental setups to measure the effects of implantation conditions on fiber wear. They found that treatments like silicone oil can significantly reduce wear and enhance tensile strength. Additionally, they developed a friction coefficient model to better understand and optimize the frictional interactions during fiber implantation, contributing to the advancement of digital three-dimensional weaving technologies. This undoubtedly increases the complexity and cost of the study, and these are challenges for the systematic study of yarn friction behavior. Therefore, it is essential to use numerical simulation methods for the study.

Numerical simulation can predict the behavior and performance of materials without the need to manufacture physical samples and conduct experiments[125,205]. This approach can significantly reduce research costs and, by controlling simulation conditions, allows for the precise reproduction and investigation of specific scientific questions, enhancing both research accuracy and data reliability[160,189,227]. Despite its essential role in fiber composite research, the application of numerical simulation to the study of yarn friction behavior remains relatively limited. Current research predominantly focuses on the friction behaviors of fabric-to-fabric or fabric-to-tool interactions, examining the effects of these macro-level friction properties on the overall performance of the fabric[228]. Dutta et al.[229] focuses on the impact of fiber orientation on interply friction in carbon/epoxy prepregs and its implications for simulation methods in composite manufacturing. They demonstrate that fiber orientation significantly influences friction behavior, which varies under different processing conditions. The findings underline the importance of incorporating direction-dependent friction models in forming simulations to achieve more accurate and effective manufacturing outcomes for composite materials. Chu et al.[230] used finite element

modeling to analyze how inter-yarn friction affects ballistic performance in fabrics. Their results show that increasing inter-yarn friction decreases fabric deflection under impact and enhances energy absorption, leading to a more effective distribution of impact forces across the fabric. This adjustment in friction levels directly influences the protective qualities of high-performance fabrics. In this study, the friction damage mechanism between yarns will be investigated in detail by developing and applying a numerical simulation model.

Additionally, previous research has examined factors influencing yarn/fiber friction, such as contact angle, pretension, and speed[36,197,208,231]. However, studies focusing on wear behavior due to friction and its impact on material performance are relatively scarce, resulting in incomplete performance assessments and design optimization limitations. To address this, our study developed a fiber constitutive model using the VUMAT user subroutine and established a high-precision yarn model based on Timoshenko beam theory to effectively resolve beam element intrusion issues. The accuracy of the numerical simulation model, in terms of mechanics and geometry, was validated using displacement curves from a friction test machine equipped with custom devices and Micro-CT observations. The proposed model successfully predicted friction and wear behavior considering fiber contact interactions and examined the influence of yarn geometric and mechanical parameters on these behaviors. In summary, we aim for this model to provide a scientific basis for optimizing the design and manufacturing processes of fiber composites, thereby enhancing the reliability and performance of the final products.

## 4.2 Simulation investigations

### 4.2.1 Fundamental theory

The shear force  $Q$  and bending moment  $M$  of Timoshenko beam element can be defined as follows:

$$Q(x) = \kappa GA \left[ \frac{ds(x)}{dx} + \phi(x) \right] \quad (72)$$

$$M(x) = EI \frac{d\phi(x)}{dx} \quad (73)$$

where  $s(x)$  and  $\phi(x)$  are the deflection and rotation of the beam's cross-section, respectively.  $E$ ,  $G$  and  $I$  denote elastic modulus, shear modulus and inertial moment of cross-section, respectively.  $A$  is the cross-section area,  $\kappa$  means the shearing correction factor, and  $x$  is the coordinate of the neutral axis.



The stiffness matrix of the Timoshenko beam element can be obtained by certain derivations, represented as:

$$K = \frac{EI}{(1+\Phi)L^3} \begin{bmatrix} 12 & 6L & -12 & 6L \\ 6L & (4+\kappa)L^2 & -6L & (2-\kappa)L^2 \\ -12 & -6L & 12 & -6L \\ 6L & (2-\kappa)L^2 & -6L & (4+\kappa)L^2 \end{bmatrix} \quad (74)$$

where  $L$  is the length of the beam. Based on the Timoshenko beam theory, the displacement field of the beam is assumed as:

$$\begin{aligned} u(x) - u_0(x) + \phi(x)x_3 &= 0 \\ w(x) &= w_0(x) \end{aligned} \quad (75)$$

where  $u_0(x)$  is the displacement of the beam centerline,  $x_3$  is the coordinate in the thickness direction of the beam, and  $w_0(x)$  is the transverse displacement of the beam centerline. Then, the stains can be expressed:

$$\varepsilon_{xx} = \frac{du}{dx} = \frac{du_0}{dx} - \phi \quad (76)$$

$$\gamma_{xz} = \frac{dw}{dx} + \frac{du}{dx_3} = \frac{dw_0}{dx} + \frac{du_0}{dx_3} - \phi \quad (77)$$

where  $\varepsilon_{xx}$  and  $\gamma_{xz}$  are the axial strain and shear strain. The stress can be shown by the following equations:

$$\sigma_{xx} = E\varepsilon_{xx} = E\left(\frac{du_0}{dx} - \phi\right) \quad (78)$$

$$\tau_{xz} = G\gamma_{xz} = G\left(\frac{dw_0}{dx} + \frac{du_0}{dx_3} - \phi\right) \quad (79)$$

where  $\sigma_{xx}$  and  $\tau_{xz}$  are axial strain and shear stress.

#### 4.2.2 Virtual Fiber Method

The Virtual Fiber Method is a computational approach used in the field of material science and engineering, particularly in the study of textile composite materials. This method is a predictive near-microscale (virtual fiber scale) technique for textile materials, which mainly is composed of virtual fiber and virtual yarn. In Abaqus software, beam elements are categorized into solid and deformable beam elements. The solid beam element is less efficient than the deformable beam element because of the continuous stresses and the large number of integration

nodes. The deformable beam element is widely used due to its small number of integration nodes and simple modeling operation; however, its cross-section properties and element orientation need to be set artificially, which can be employed for the simulation of different materials. Hence, a deformable beam element has essentially been utilized to establish virtual fiber. Furthermore, the deformable beam element can simulate many types of deformation modes such as bending, tensile, and compression, which are subject to axial forces and bending moments. There are two main types of deformable beam elements, including Euler-Bernoulli beams and Timoshenko beams. The Timoshenko beam theory extends the cross-section assumption of the Euler-Bernoulli beam theory by allowing the cross-section of the beam to be rotated in bending. The Timoshenko beam element considers not only bending deformations but also shear deformations. These are necessary for textile modeling. A virtual yarn can be constructed by number of virtual fibers, which can be modeled with beam elements. Since the diameter of the beam element is larger than the diameter of the actual fiber, considering the computational power of the computer, it is not practical to model a virtual yarn according to the actual amount of fiber filaments in the yarn. Hence, the modified material properties are employed in the simulation process, including the number of virtual fibers and reduced elastic modulus.

#### 4.2.3 Constitutive law

According to the damage-plasticity theory, the strain tensor is split into an elastic part and a plastic part:

$$\varepsilon = \varepsilon^e + \varepsilon^p \tag{80}$$

where the superscripts “e” and “p” denote the elastic part and plastic part, the correlation analytical model see Fig. 4. 1. The parts should be analyzed, respectively.

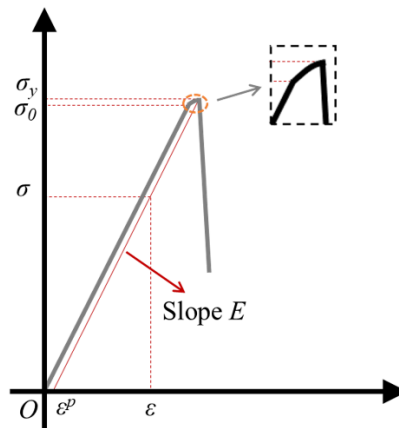


Fig. 4. 1. Typical stress-strain curve of yarn tensile behavior.

For the elastic stage, the stress and strain can be expressed based on the generalized Hooke's law as:

$$\sigma_{ij} = 2G\varepsilon_{ij}^e + \delta_{ij}\lambda \sum_k \varepsilon_{kk}^e, \quad i, j = 1, 2, 3 \quad (81)$$

$$\varepsilon_{ij} = \frac{1}{2G} \sigma_{ij}^e - \delta_{ij} \frac{\nu}{E} \sum_k \sigma_{kk}^e, \quad i, j = 1, 2, 3 \quad (82)$$

where the Lamé parameters ( $G$  and  $\lambda$ ) are defined by:

$$G = \frac{E}{2(1+\nu)} \quad (83)$$

$$\lambda = \frac{\nu E}{(1+\nu)(1-2\nu)} \quad (84)$$

where the  $\nu$  is the poisson ratio.

For the plastic stage, the introduction of a yield function  $\Phi$  can be defined as:

$$\Phi(\sigma_{ij}, \sigma_y) = q - \sigma_y \quad (85)$$

where  $\sigma_y$  is yield stress and  $q$  is equivalent stress, which can be shown as:

$$q = \sqrt{\frac{3}{2}} \|S_{ij}\| \quad (86)$$

where  $S_{ij}$  is the deviatoric stress tensor, which can be expressed as:

$$S_{ij} = \sigma_{ij} - \frac{1}{3} \delta_{ij} \sigma_{kk} \quad (87)$$

It should be noted that, at any stage, no stress level is allowed above the current yield stress, Thus, any admissible stress must satisfy the restriction. Indeed, the yield criterion can be expressed by:

$$\begin{aligned} \Phi(\sigma_{ij}, \sigma_y) < 0 &\Rightarrow \dot{\varepsilon}^p = 0 \\ \Phi(\sigma_{ij}, \sigma_y) = 0 &\Rightarrow \begin{cases} \dot{\varepsilon}^p = 0 & \text{elastic unloading} \\ \dot{\varepsilon}^p \neq 0 & \text{plastic loading} \end{cases} \end{aligned} \quad (88)$$

The plastic strain rate can be obtained, which is positive under tension and negative under compression.

$$\dot{\varepsilon}^p = \dot{\gamma} \text{sign}(\sigma) \quad (89)$$

where  $\gamma$  is termed the plastic multiplier, which is non-negative. Sign is the signum function, which is distinguished +/- . Eventually, a phenomenon, the evolution of the yield stress accompanies the evolution of the plastic strain, is achieved. The yield stress is a given function.

$$\sigma_y = \sigma_y(\bar{\varepsilon}^p) = \sigma_y\left(\int_0^t \dot{\bar{\varepsilon}}^p dt\right) \quad (90)$$

Based on the plastic flow rule, the equivalent plastic strain rate is shown:

$$\dot{\bar{\varepsilon}}^p = \dot{\gamma} = \sqrt{\frac{2}{3} \dot{\varepsilon}_{ij}^p \cdot \dot{\varepsilon}_{ij}^p} \quad (91)$$

The ductile damage degradation model is adopted. The ductile criterion is a phenomenological model for predicting the onset of damage, which is used in current research. The model assumes that the equivalent plastic strain at the onset of damage,  $\bar{\varepsilon}_D^p$ , is a function of stress triaxiality and strain rate:

$$\bar{\varepsilon}_D^p(\eta, \dot{\bar{\varepsilon}}^p), \quad (92)$$

where  $\eta$  is the stress triaxiality, which is defined as:

$$\eta = \frac{\|S_{ij}\|}{q} \quad (93)$$

where  $q$  is the Mises equivalent stress. Furthermore, the displacement at failure can be shown as:

$$\bar{u}_f^p = \frac{2G_f}{\sigma_y} \quad (94)$$

where  $G_f$  is the fracture energy, which can be expressed as:

$$G_f = \int_0^{\bar{\varepsilon}_f^p} \sigma_y d\bar{u}^p \quad (95)$$

A damage variable  $d$  is introduced as:

$$d = \begin{cases} 0 & \sigma \leq \sigma_y \\ \frac{2}{1 + \exp(-d_f (\sigma - \sigma_y)^2)} - 1 & \sigma > \sigma_y \end{cases} \quad (96)$$

where  $d_f$  is the damage factors, which can be explained as an input parameter according to the Weibull distribution law. The yarn stress after initial damage can be defined as:

$$\sigma = (1-d)\sigma_y \quad (97)$$

The detailed derivation process of the damage evolution equation can be referred to the literature[232,233]. The above damage model is carried out by user subroutine VUMAT of Abaqus, shown in Fig. 4. 2.

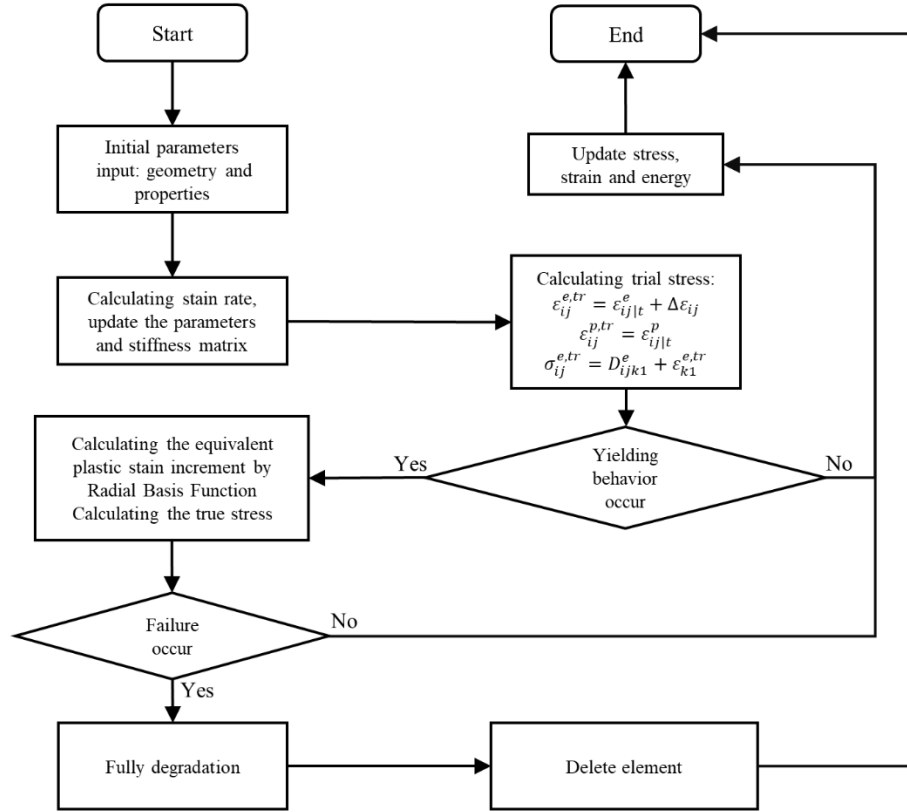


Fig. 4. 2. Flowchart of calling VUMAT in Abaqus as implemented.

#### 4.2.4 Geometric description of virtual yarn

Fiber geometry plays a crucial role in determining the mechanical properties of yarns. Prior research has established that the arrangement of fibers at the quasi-fiber scale affects the geometry of the yarns[196,234]. However, to effectively model the mechanical behavior of yarns, it is important to simulate the virtual yarns with a high degree of accuracy. To achieve this, the authors of this study utilized a virtual yarn to model the mechanical behavior of a realistic yarn. The virtual fiber was modeled using chain-like beam elements in the Abaqus software, with each beam element representing a small segment of the fiber chain. By assembling a certain number of virtual fibers with twist angles, the authors were able to create a twisted yarn using a Python script. The assembly process was executed on Abaqus 2021 to ensure the accuracy of the simulation.

The central routine ( $f(u)$ ,  $g(u)$ ,  $h(u)$ ) and cross-section( $c(w,v)$ ) of fibers is used to establish the geometric model:

$$\begin{cases} X = f(u) + c(\omega, v) \\ Y = g(u) + c(\omega, v) \\ Z = h(u) + c(\omega, v) \end{cases} \quad (98)$$

To maintain the proper alignment of the beam nodes, equations (99) and (100) were employed, which reflected the constraint relationship between them. Fig. 4. 3 illustrates the process of creating a virtual fiber using many beam elements. The use of virtual yarns allowed the authors to model the mechanical behavior of yarns under different conditions and study the impact of fiber geometry on the properties of the yarn. The virtual yarns developed in this study provide a reliable means of simulating the behavior of real-world yarns, enabling researchers to study the impact of different parameters, such as fiber arrangement and twist angles, on yarn properties.

$$\theta_0 = \pi - n \times \arcsin(z_0 / r_{point}) \quad (99)$$

$$\begin{cases} x' = x_0 + \kappa \times Le \\ y' = r_{point} \times \cos(\theta_0 + \kappa\theta_t) \\ z' = r_{point} \times \sin(\theta_0 + \kappa\theta_t) \end{cases} \quad (100)$$

where  $x'$ ,  $y'$  and  $z'$  are coordinates along  $x$ ,  $y$  and  $z$  directions, separately.  $\kappa$  is the number of the element.  $r_{point} = \sqrt{x_0^2 + y_0^2}$  is the distance between the node and the center of the circle on the section.  $\theta_t$  and  $\theta_0$  are the twist of yarns and deflection angle of the element, which usually is normalized by  $n$ . Furthermore, the number of fibers can be obtained by Eq. (101).

$$\pi \times \left( \frac{D_f}{2} \right)^2 \times n_f = \frac{\rho_f}{\phi_f} \quad (101)$$

where  $n_f$  and  $D_f$  are the amount and diameter of virtual fibers in the yarn,  $\phi_f$  and  $\rho_f$  are volume density and linear density of realistic yarn.

Particularly, the equations reflect the constraint relationship between beam nodes based on the Rectangular Coordinates:

$$\begin{bmatrix} y \\ z \end{bmatrix}^T \begin{bmatrix} 1 & 0 \\ a^2 & 1 \\ 0 & b^2 \end{bmatrix} \begin{bmatrix} y \\ z \end{bmatrix} = Q^T A Q = 1 \quad (102)$$

The Eigenvectors of  $A$  can be obtained as:

$$\mu_1 = \begin{bmatrix} 1 \\ 0 \end{bmatrix} \quad \mu_2 = \begin{bmatrix} 0 \\ 1 \end{bmatrix} \quad (103)$$

The assembly of yarn is formed by a multitude of fibers, as seen in the geometric model provided above. The assumption is that the fraction of yarn is sufficiently large to move independently. This research considers the fiber as a material with transverse isotropy, meaning it has physical properties that are symmetric about an axis perpendicular to a plane of isotropy. The transverse plane exhibits infinite planes of symmetry, resulting in uniform material properties in all directions inside this plane. The homogenized material exhibits a directional preference in the same direction as that of the fibers. Analyzed in deformed cross-sections, the spatial distribution of fibers inside the yarn has been analyzed. Generally, each fiber is assigned different properties, which meet the Beta distribution.

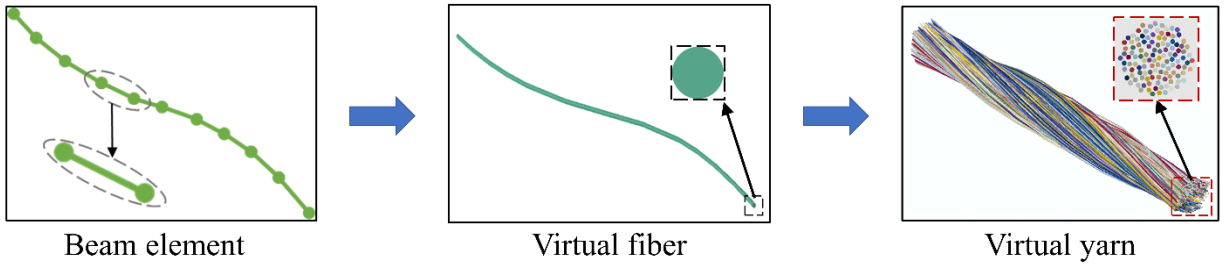


Fig. 4. 3. Virtual fiber and yarn model

#### 4.2.5 Solution to inter penetration problem

To avoid the penetrations when considering contact between yarns, a method was developed in current research. According to the results from Abaqus, a methodology called Active Separation Process (ASP) was developed through Python. As shown in Fig. 4. 4, this is a cross-section view, where each gray circle represents a virtual fiber. A partially enlarged area is displayed and the penetration area is marked.  $d$  is defined as the Euclidean distance of the fiber,  $d_i$  and  $d_j$  are modified distance.

Algorithm 1: Algorithm of node re-arrangement

**Input:**

Two sets of node coordinates: set\_y, set\_z

Elastic modules of each fiber:  $E_i$  or  $E_j$

Poisson's ratio of each fiber:  $\nu_i$

Definition:

**Euclidean distance:**  $D = \sqrt{(y_j - y_i)^2 + (x_j - x_i)^2}$

**Equivalent elastic modulus:**  $\frac{1}{E^*} = \frac{1-\nu_i^2}{E_i} + \frac{1-\nu_j^2}{E_j}$

**GetLinearEquation:**  $a*x+b*y+c = 0$

**Getcoor:** a\_set\_y; a\_set\_z

**Weight:**  $P_i = \frac{E_i}{E^*}$

**for**  $i$  in range(set\_y)

**for**  $j$  in range(set\_z)

**if**  $d < D$

$l = \text{GetLinearEquation}()$

$d_i = (D-d)*P_i$

$d_j = (D-d)*P_j$

      return Getcoor

**else**  $d \geq D$

      break

The algorithmic logic of ASP is shown in Algorithm 1, indeed requiring that the distance between the two circular centers of the fiber be greater than the equal of the radius of a fiber. For the fibers that are very close and not yet in contact, the gap of fibers should equal the sum of the two fibers' radius. However, for the fibers that are not in contact, the gap of fibers should be greater than the sum of fibers' radius. Neither of the above cases needs to be modified as no penetration occurs. On the contrary, for fibers that have been in contact, the distance between the two is less than the radius of the fiber in geometry, which needs to be modified locally by ASP to avoid interpenetration, thereby modifying it to a situation where the gap is greater than or equal. During the gap modification, the Euclidean distance of the representative fibers is calculated as a priority, furthermore, due to the randomness of representative fibers, the equivalent elastic modulus is required to be calculated, which can be used to calculate the modified distance. During the modification, the distance and direction modified of the virtual fiber are defined.  $d_i$  and  $d_j$  can be calculated by a weighting method, and this weight is related to the elastic modulus of the fiber. This code implements an iterative algorithm for rearranging virtual fibers, which can solve the penetration effectively. It considers the distances between nodes from two different sets ("set\_y" and "set\_z") and adjusts their positions based on predefined weights related to material stiffness.



The modified coordinate data of the virtual fibers are outputted and are employed for further simulation.

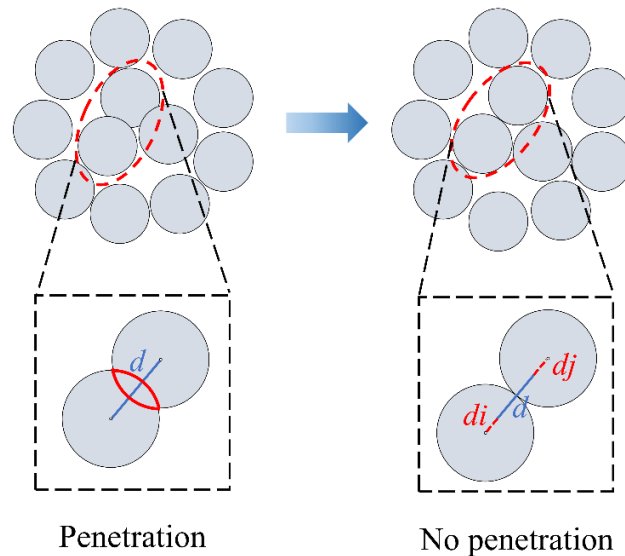


Fig. 4. 4. Simplified procedure on yarn model by active separation process (ASP).

### 4.3 Experimental investigations

#### 4.3.1 Materials preparation

HMWPE (High Molecular Weight Polyethylene) of 135 Tex yarns composed of hundreds or thousands of fibers were selected as experiments object, which is produced by Honeywell International, Inc., USA. All samples are both twisted yarns showed that the strength of high-performance fiber yarns can be improved by a slight twist. The main parameters of tested yarns are listed in Table 4. 1. The labels “tpm” represents twist per meter of yarns. Each twist level of HMWPE yarns exhibits different mechanical properties. 20 yarns for each group were dried at conditions of  $22\pm 2^\circ$  temperature and  $65\pm 4\%$  relative humanity (RH) for 10 h to standardize experimental conditions. The gauge length of each tested yarn is  $100\pm 10$  mm and the cross-sectional area is about  $0.718 \text{ mm}^2$ .

Table 4. 1 The main material parameters of HMWPE.

Sample	Linear density (Tex)	Twist level (tpm)	Longitudinal modulus (GPa)	Diameter ( $\mu\text{m}$ )	Number of fibers
Fiber	-	-	0.5	17	-
Y-50tpm	135	50	73.0	998	100
Y-100tpm		100	83.4	493	
Y-150tpm		150	98.4	324	
Y-200tpm		200	110.3	238	

Note: Data from manufacturer's website and relevant literatures[222,235].

#### 4.3.2 In situ Micro-CT scanning

The Micro-CT technology was used to measure the architecture details of yarn. A sample of the 10 mm was prepared for the Micro-CT scanning, which can obtain high-definition images of yarn samples, shown as Fig. 4. 5(a). The sample with fixture setup is located in the middle of X-ray source and detector. The Micro-CT test was performed using the Xradia 510 Versa X-ray microscope (Zeiss, Germany), with an accelerating voltage of 80 kV and a beam energy of 7 W. The resolution of the Micro-CT scanning was 7  $\mu\text{m}/\text{pixel}$ , which can be decided by adjusting the distance between the sample and X-ray source and detector. The 3D reconstruction of the preform sample was computationally generated by Scout-and-Scan Control System (v14.0, Zeiss), using 1060 CT slices. Next, the image data was analyzed using the Dragonfly software of (version 2020.1, Object Research Systems (ORS) Inc.) for the segmentation, 3D visualization, and quantitative analysis. The overall microstructure is already well presented using 112 virtual fibers, according to the previous research [196,236], which shows a good agreement between simulation and experiment. Hence, in this research, all simulation models were performed with yarns containing 112 virtual fibers.

#### 4.3.3 Friction test

The experiments were carried out on a UMT-TRIBO LAB tribometer (Bruker Nano, Inc., Campbell, CA, USA) presented in Fig. 4. 5(b). It is employed to explore the friction behavior of yarn in conjunction with rig, which is composed of upper and lower setup. The upper setup is connected to the tribometer's sensor which is used to measure the evolution of the forces during the friction process. Similarly, to explore the influence of applied conditions on the frictional behavior of yarns, the sensor also can be utilized to measure the value of the applied parameter. Forces and displacements in all directions during friction can be measured in real-time. The maximum loads of sensor in all directions are  $\pm 20$  N, which offer noise levels at an industry-leading 0.02% of full-scale values.

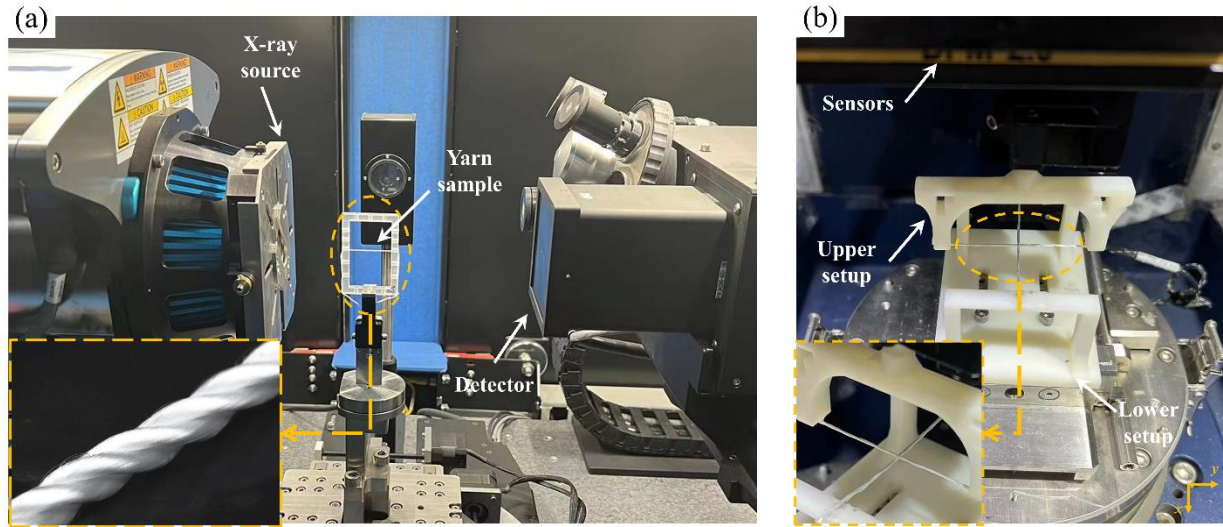


Fig. 4. 5. Experimental equipment and method: (a) Micro-CT testing of yarn and (b) diagram of the tribometer with upper and lower upper setup.

Fig. 4. 5(b) shows the design of the experiment rig. Yarn sample is fixed with upper and lower setup under the given pretension conditions, two yarn samples were placed orthogonally. Due to upper setup and sensor connections, the upper yarn encounters the lower yarn as the sensor moves. Further normal load is applied to the friction pair. When all applied parameters have been configured, the base of tribometer will start to move linearly (along  $x$  direction), that is, orthogonal friction. Upper setup movement and back is called a cycle. Based on previous research [109], to respond to friction behavior efficiently and accurately, friction displacement of 10 mm (5 mm/single direction) and displacement rate of 2.5 mm/s were selected for friction experiments. The data from the contact force and the camera were recorded simultaneously during the experiment at a sampling rate of 100 Hz. Each loading procedure was repeated three times using new yarn.

#### 4.4 Consistency Analysis

##### 4.4.1 Geometric verification

To validate the precision of the model, a thorough analysis was conducted, comparing the simulation results with experimental data. This analysis encompassed several aspects, such as the geometric properties and mechanical response. The intersection area is determined as a distinctive indication of the geometric properties of the yarn. Fig. 4. 6(a) and (b) display a Micro-CT picture and a simulation model of yarns. The statistical data for each cross-section is represented by the cross-section regions, such as in Fig. 4. 6(c), which displays a scattering map that illustrates the link between the Experimental Value and the two averages: the Average of Simulation and the

Average of Experimental data. Each point in the figure corresponds to a distinct intersection value. The blue dot represents the experimental value, the blue line represents the simulation's average, and the green line represents the experimental average. The data illustrates a discrepancy of 7.4% between the average obtained from the experiment and the average obtained from the simulation.

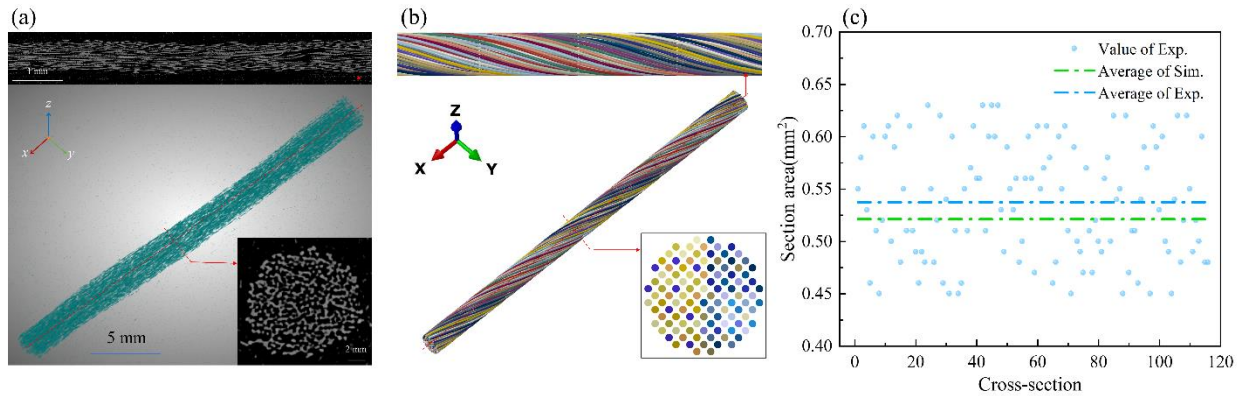


Fig. 4. 6. The geometric comparison results between simulation and experiment: (a) the experimental value, (b) the simulated value and (c) cross-sectional statistics.

Further, the accuracy of the ASP was similarly verified. A set of yarn cross-section data of the contact area was employed as an example to compare the cross-section morphology before and after modification, as described in Fig. 4. 7. Each virtual fiber consists of two parts containing the fiber profile and the center, represented by a red circle and a blue point, respectively. Fig. 4. 7(a) shows the results of the unmodified algorithm, while Fig. 4. 7(b) shows the results of fiber arrangement after modification by ASP. The comparison between the two images suggests that the ASP has influenced the arrangement of the fibers within the yarn. The virtual fibers appear to be more evenly spaced and aligned, with less penetration between fibers. This could suggest that the ASP process has had a beneficial effect on the yarn structure, potentially improving its strength or other properties.

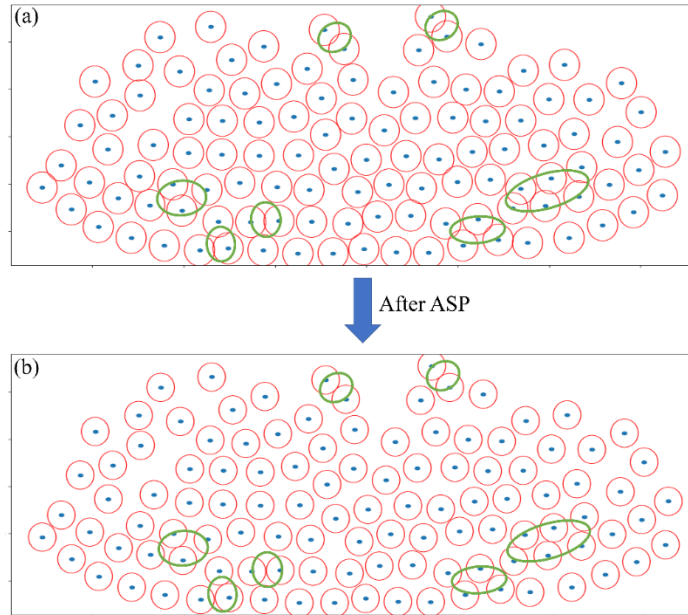


Fig. 4. 7. The comparison of (a) original and (b) modified cross-section viewpoint for yarn.

#### 4.4.2 Mechanical verification

Fig. 4. 8 illustrates the correlation between the friction force and the yarn's displacement under the normal load of 2.8 N and pretension of 1.5-1.5 N. The green and blue core points represent experimental and simulated data points. They clearly illustrate the difference between static and active friction, as well as the turning point or mutation point on the curve. These points indicate the transition from static to motion friction, reflecting a change in the state of the friction force. Generally, the correlation between friction and shift is not always linear, as friction can vary with increasing shift, particularly in situations involving distinct friction stages, such as static and moving friction. To facilitate a comprehensive comparison between the experiment and simulation findings, an adjustment operation was conducted. The experimental and simulation corrections are depicted by the green and blue curves, respectively, in Fig. 4. 8. Additionally, the expected intervals of the results are also displayed. The simulation results may be derived from the diagram, which falls within the expected range of the experiment. This suggests that the simulations exhibit some resemblance to the experiment and provide a more accurate characterization of the yarn friction behavior. The overall friction strength steadily increases as the shift increases, reaching maximum static friction during the active friction phase, and then declines to attain stability. During the time of active friction, there is a 13% disparity in the friction of the wire.

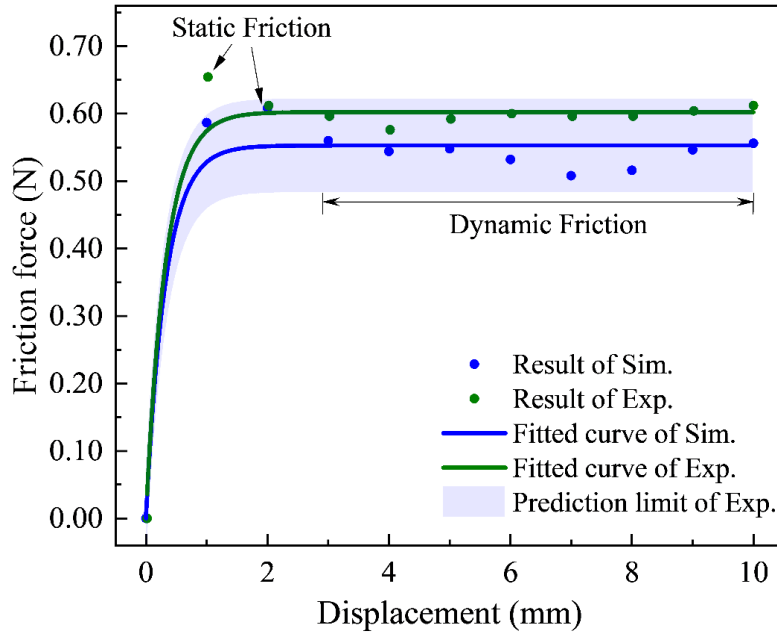


Fig. 4. 8. Representative cycle of the friction experiment and simulation results of yarns at a normal load of 2.8 N and pretension of 1.5-1.5 N.

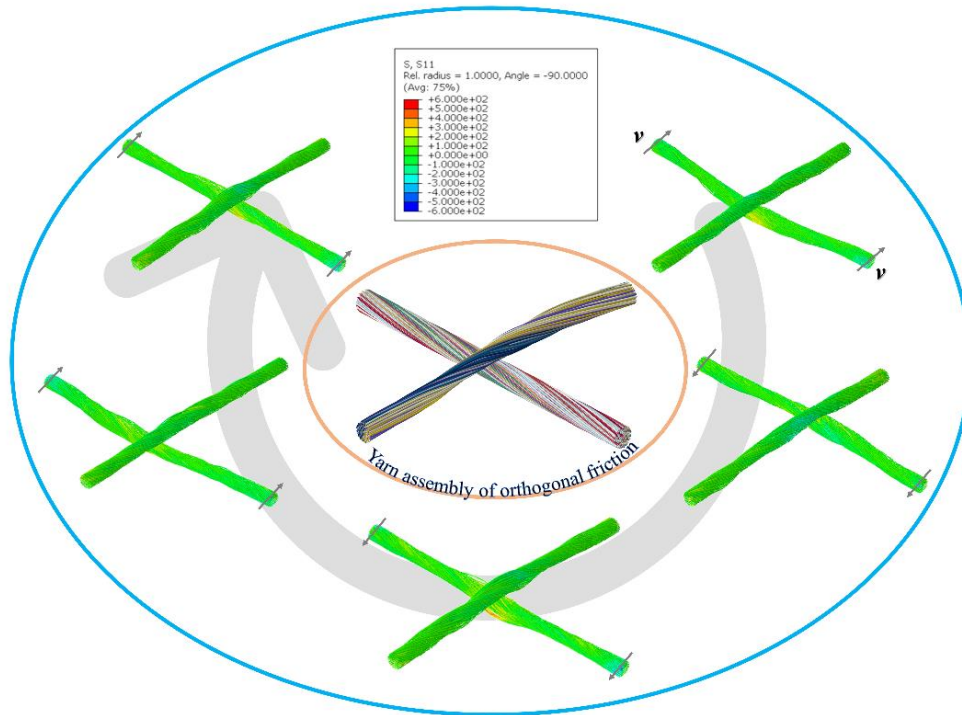


Fig. 4. 9. Morphologies of friction simulation at different stages.

Fig. 4. 9 shows the evolution of stress along the longitude of yarn direction during the orthogonal friction. The upper yarn is applied the normal load by displacement, and the lower yarn is applied the cyclic displacement. The grey arrow indicates the direction of displacement. Due to the stress along the longitude of yarn direction being a key factor during the cycle of orthogonal friction, the

principal stresses of the longitude of yarn (S11) are used to characterize the force on the fibers during orthogonal friction. The maximum longitudinal stress (S11) herein was close to the tensile strength of warp yarns before the breakage. As the friction force increased, the damage accumulation occurs for each fiber. The first cycle of yarn friction is represented, each representative stage of S11 is shown and variation can be clearly observed as the friction process. However, it was not found that the fibers fractured, which is likely because although friction behavior occurred, the fibers had not yet met the criteria for fracture. Therefore, in a cycle, especially the first cycle, there may be no fiber fracture.

#### 4.5 Effect of coupling factors on friction behavior

Factor analysis is very important for friction research, which can be employed to optimize the manufacturing process of composites. And normal load and pretension are important external factors affecting friction behavior. The normal load on the contact surface is significant, and pretension affects the uniformity of yarn. Furthermore, considering the randomness of the mechanical properties of fibers, it is necessary to analyze numerically the mechanism of the influence of the two factors on the friction behavior of yarns with different twist. This research further explores the effects of Normal load and Pretension on the friction behavior of yarns with different twists.

##### 4.5.1 Normal load

Fig. 4. 10 is divided into three sections, each corresponding to a different yarn twist (50, 100, and 200 tpm). Each section contains two subfigures: plots of friction versus displacement (Fig. 4. 10(a-c)), and schematics of yarn structure (Fig. 4. 10(a'-c')). Friction data under three different loads are represented by purple, green, and blue dots, with the corresponding fitted curves shown as solid lines in the same colors. For yarn with 50 tpm, the friction exhibits slight fluctuations with increasing displacement, but the overall trend remains relatively stable. The data presentation for 100 tpm follows the same format as for 50 tpm, with friction during displacement being less than that observed at 50 tpm. Similarly, for yarn with 200 tpm, the differences in friction under various loads are significant; however, the overall friction for the three normal loads is lower than that of yarns with the other two twist levels. The high-twist (200 tpm) yarns possess a denser and more stable structure, as clearly shown in Fig. 4. 10(a'-c'). This reduces fiber slippage, thereby decreasing friction. As the twist increases, the surface roughness of the yarn may decrease, reducing the contact area between the yarn and the surface. A smaller contact area corresponds to reduced friction. The yarn with 200 tpm, having a higher twist, possesses a smoother surface,

which further decreases friction. Additionally, in high-twist yarns, the fibers are more orderly oriented, and this orderly arrangement minimizes the relative movement between fibers, thereby reducing internal friction. This orderliness is particularly pronounced in the yarn at 200 tpm, resulting in further reduction of friction.

The variations in friction under different loads illustrate the impact of load on friction. For the three representative normal loads, friction is lower at a load of 0.5 N and higher at a load of 1.2 N. Using the 100 tpm yarn as an example, the friction data for a normal load of 0.50 N is relatively low, fluctuating between 0.30 and 0.40 N. As the normal load increases, friction also increases, fluctuating between 0.35 and 0.45 N. With a further increase in normal load, friction significantly increases, fluctuating between 0.40 and 0.50 N. This relationship can be explained by the classical law of friction. Moreover, it is related to surface characteristics; as the normal load increases, the degree of compression between the yarn and the contact surface increases, potentially enlarging the contact area and thereby increasing friction.

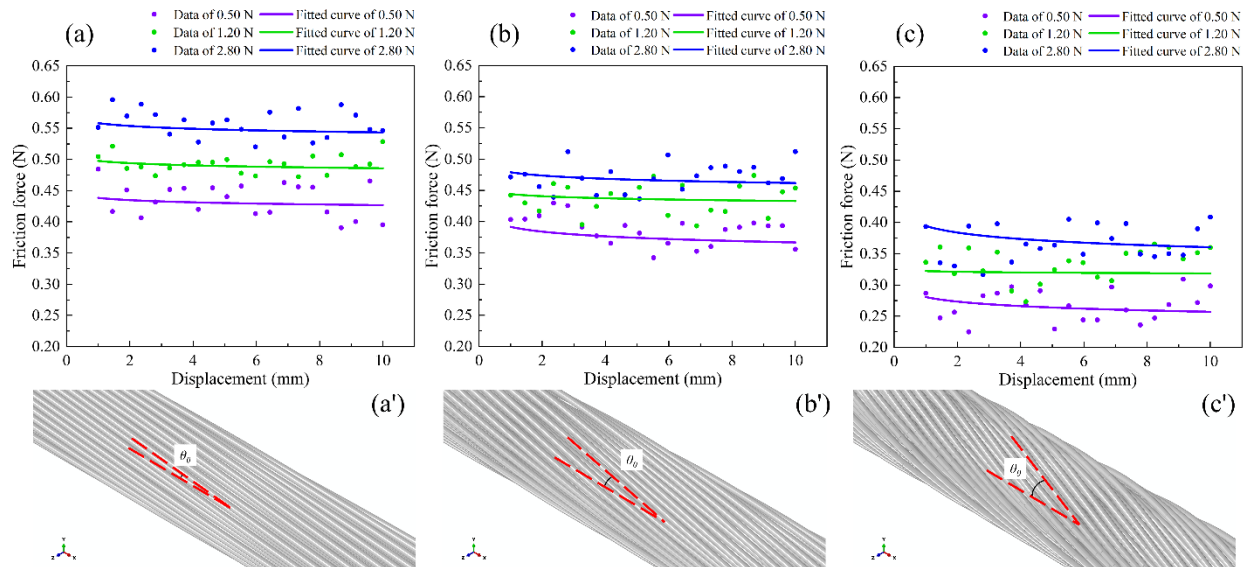


Fig. 4. 10. Evolution of friction force on normal load for different twist yarn (a\* 50tpm; b\* 100tpm; c\* 200 tpm), (a-c) friction force versus displacement and (a'-c') twist angle of different twist of yarn.

#### 4.5.2 Pretension

To explore the effect of pretension on the friction behavior, the uniform normal of 2.8N was selected as the initial parameter. Fig. 4. 11 illustrates the relationship between friction and displacement under different yarn pretensions. The chart is divided into three sections, corresponding to yarn twist levels of 50 tpm, 100 tpm, and 200 tpm. Within each section, two pretension combinations are depicted: uniform pretension across yarns and varying tension across yarns. For each combination, friction data are presented for three different pretension levels, with



specific pretension combinations indicated by purple, green, and blue colors. The data points represent actual measurements, while the curves denote fitted results. Collectively, these data illustrate the relationship between friction and displacement.

For the same pretension combinations, as shown in Fig. 4. 11(a-c), friction decreases with increasing twist due to the larger contact area and contact force between fibers under high pretension, which diminishes the impact of twist on friction. Additionally, the differences in friction for various pretensions progressively decrease. For yarn with 50 tpm, the friction for a pretension combination of 0.3-0.3 N ranges from 0.67 to 0.73 N, whereas for 1.0-1.0 N, it ranges from 0.45 to 0.52 N, with a difference rate of approximately 32%. In contrast, for yarn with 100 tpm, the friction for a pretension combination of 0.3-0.3 N ranges from 0.55 to 0.60 N, while for 1.0-1.0 N, it ranges from 0.4 to 0.45 N, with a difference rate of 20%.

For different pretension combinations, as shown in Fig. 4. 11(d-f), friction decreases with increasing twist, like the case with the same pretension combinations. However, the differences in friction between different pretension combinations are smaller, particularly for high-twist yarns. High twist balances the effects of different pretension combinations, resulting in more uniform friction. This is because, under high twist, the fibers are more tightly arranged, with larger contact force and contact area between fibers, reducing the impact of pretension differences on friction. These findings suggest that twist and pretension significantly complement each other in influencing yarn friction. Under high twist, friction is more stable, with smaller differences in friction between different pretension combinations.

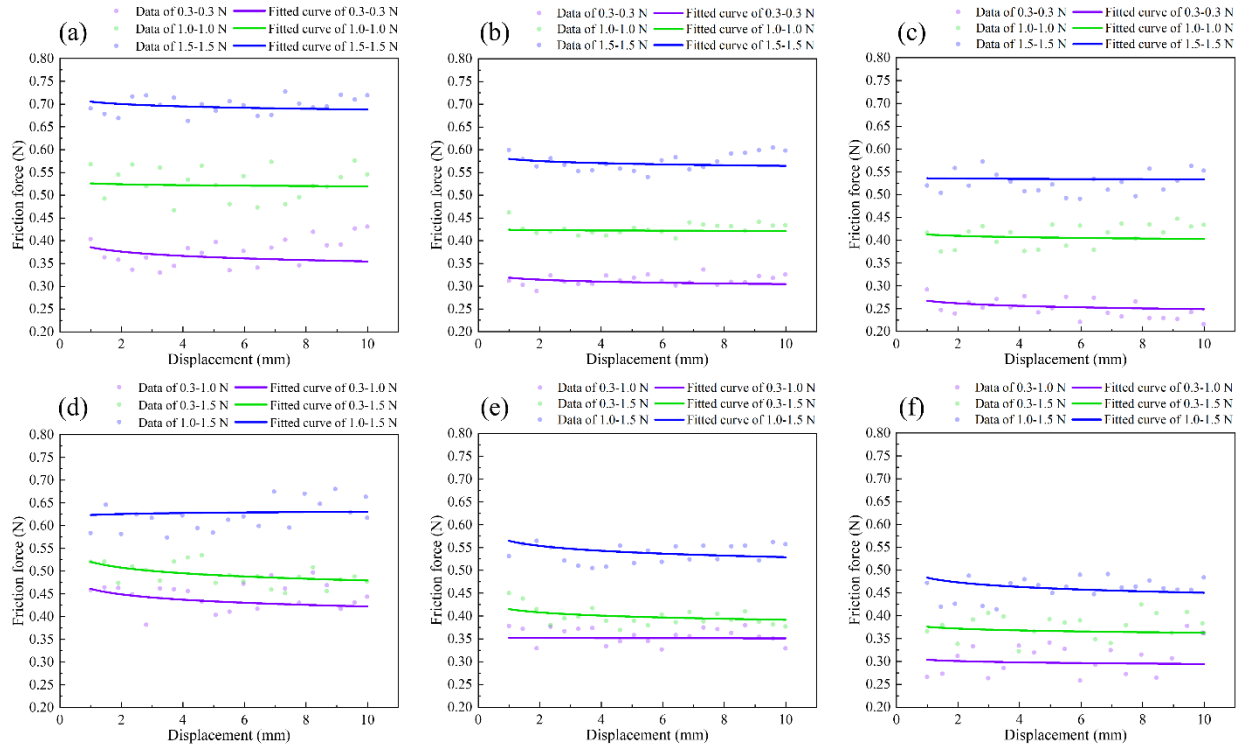


Fig. 4. 11. Evolution of friction force on pretension for different twist yarn (a\* 50tpm; b\* 100tpm; c\* 200 tpm), (a-c) same pretension of yarns and (d-f) different pretension of yarns.

#### 4.6 Damage behavior prediction

Fig. 4. 12 illustrates the results of simulations on different twisted yarns after 0, 25, and 30 cycles during the frictional wear process. Each column represents twists of 50 tpm, 100 tpm, and 200 tpm, respectively, with colors indicating the stress (S11) distribution within the fibers. The figure depicts the changes in stress and the fracture conditions of the fibers under various cycle counts. To compare the extent of damage among different yarns during the friction process, uniform parameters were employed: a normal load of 2.8N and a pretension of 1.5-1.5 N.

Fig. 4. 12 demonstrates that as the yarn twist increases, there is a notable change in the stress distribution during the frictional wear process. For yarn with 200 tpm, stress concentration within the fibers becomes pronounced, especially after 30 cycles, leading to severe fiber fractures. For yarns with a twist of 100 tpm, the number of broken fibers increases significantly with the number of cycles. In contrast, only a few fibers break within the 50 tpm twisted yarn. The fiber fractures mainly occur in areas of stress concentration, typically at the intersection points of the yarn. As the number of cycles increases, the stress in these concentration areas exceeds the fibers' load-bearing capacity, resulting in fractures. Low-twist yarns, due to their small twist angle, cause the

fibers to arrange orthogonally during the friction process, enhancing shear interactions between them.

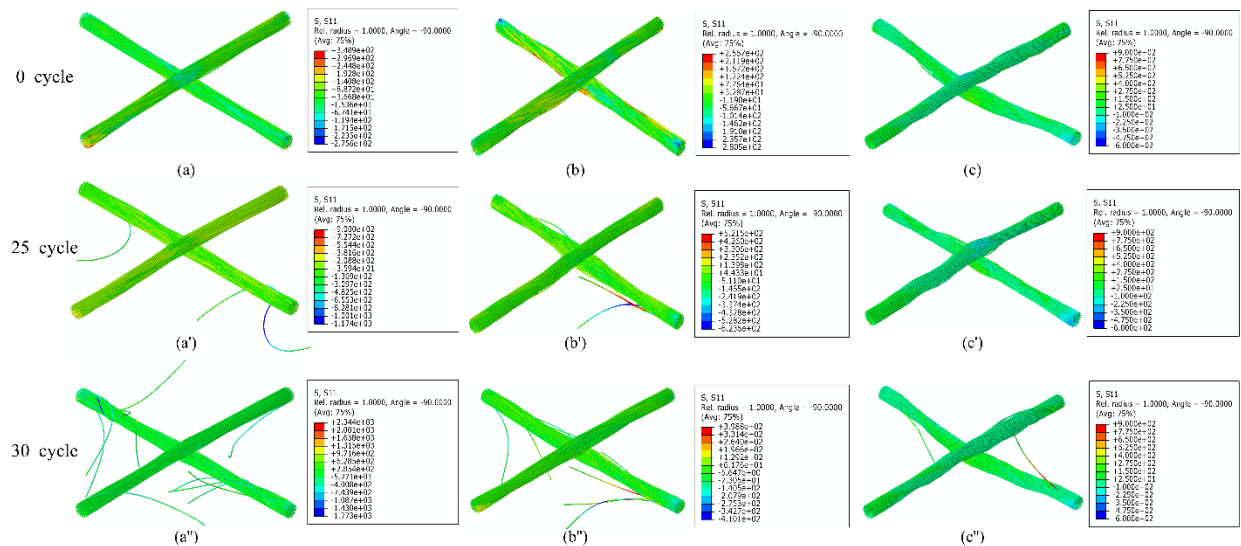


Fig. 4. 12. The results comparison of yarns with different twist for friction and wear behavior before and after 25, 30 cycles (a\* 50tpm; b\* 100tpm; c\* 200tpm).

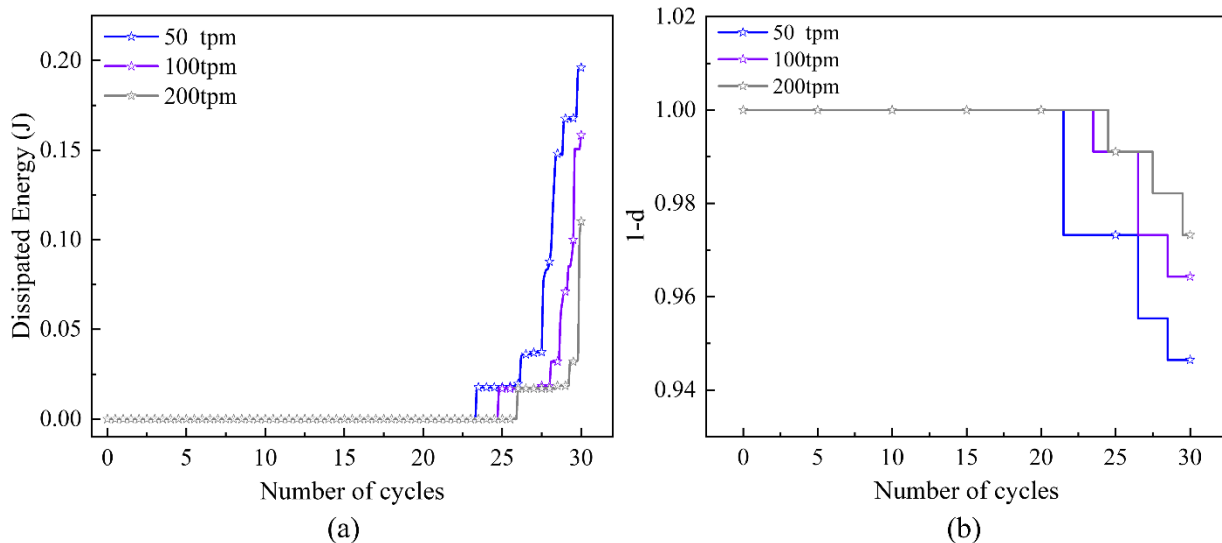


Fig. 4. 13. Number cycles as a function of the dissipated energy(a) and damage variable (b) for different for different twists of yarns.

Fig. 4. 13 illustrates two aspects of fiber damage: (a) dissipated energy and (b) damage variable. In Fig. 4. 13(a), the dissipated energy curve shows a three-stage behavior under applied loading conditions. Initially, all curves are near zero, indicating minimal energy dissipation and suggesting that the fibers are in the elastic deformation stage with negligible internal damage. As the loading increases, the dissipated energy rises significantly, marking the transition from elastic to plastic deformation and the onset and accumulation of internal fiber damage. This critical stage indicates changes in the fiber microstructure as more energy is absorbed. Finally, the curves show

a sharp increase in dissipated energy over a short period, indicating substantial damage accumulation within the yarn fibers. Additionally, the result reveals that yarns with different twist levels exhibit varying fracture energies, with low-twist yarns displaying earlier changes in dissipated energy. This further demonstrates that low-twist yarns have stronger frictional behavior and are more prone to damage.

Fig. 4. 13(b) illustrates the relationship between the damage variable and the number of friction cycles to clarify the correlation between effective stress and actual stress during material damage. The damage variable begins at 0 and increases gradually with loading, then rises sharply, corresponding to a rapid increase in dissipated energy. This critical point marks the onset of fiber damage. As loading continues, the damage variable approaches 1, indicating complete fiber failure. Overall, the parallel trends between dissipated energy and the damage variable underscore the strong correlation between energy absorption and damage accumulation. Understanding these relationships is essential for predicting the lifespan and performance of fiber materials under various loading conditions.

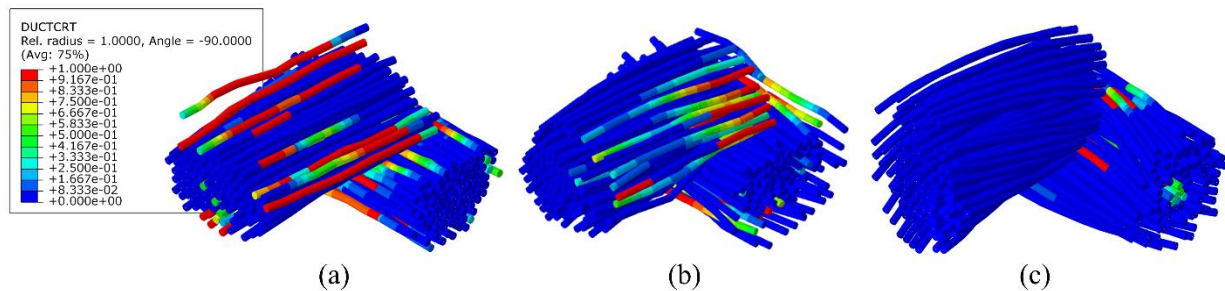


Fig. 4. 14. The DUCTCRT distribution of contact zone of yarns with different twist: (a) 50, (b) 100 and (c) 200 tpm.

In the analysis of the distribution of DUCTCRT under various twist conditions, it is evident that different yarn structures significantly influence DUCTCRT distribution in Fig. 4. 14. Low-twist yarns show a higher incidence of fiber failure. This suggests that optimizing yarn structure can effectively improve internal stress distribution and reduce localized damage. An analysis of these two factors indicates that the energy dissipation and damage characteristics of fibers under different structural conditions are closely interrelated. All three studies highlight the critical importance of optimizing yarn structure. From the simulation results, it can be concluded that during the actual usage of yarns, internal stress accumulates progressively with increased friction cycles, ultimately causing fiber fractures. This highlights that frictional wear is a critical factor affecting yarn lifespan, particularly for low-twist yarns, where attention should be given to the

fracture risk after multiple cycles. It is recommended to select yarns with appropriate twist levels based on the usage environment and to consider their wear resistance to extend the yarns' lifespan.

#### 4.7 Summary of Chapter 4

A yarn model considering fiber damage behavior is developed, based on the Timoshenko beam principle and Ductile Criterion for exploring the friction and wear behavior during the manufacturing of the reinforcement. Moreover, the penetration problem is also effectively solved by self-coding to enhance the accuracy of model. The constitutive model of fibers was developed using user subroutine VUMAT in Abaqus software, and a friction experiment was performed by tribometer equipped with a self-made setup. The accuracy of the numerical simulation model is verified in mechanics and geometry through experimental load-displacement curves and Micro-CT observations. The proposed model can effectively predict the friction and wear behavior considering the contact behavior of fibers according to the experimental and simulation results. The friction behavior of the yarn during the manufacturing of the reinforcement is analyzed. Further, the effect of yarn geometrical and mechanical parameters on friction and wear behavior can be explored. The results are summarized as follows:

- (1) The frictional force decreases as the yarn twist increases and increases as the normal load on the yarn increases.
- (2) Regarding the effect of yarn pretension on friction and wear behavior, the frictional force between two yarns with the same pretension decreases as the twist increases, while it increases as the pretension increases. Similarly, the frictional force of yarns with different pretensions decreases with increasing twist, while it increases with increasing pretension. However, the differences are smaller than in the case of the same pretension.
- (3) The twist of the yarn and the number of frictional cycles significantly impact its stress distribution and fracture conditions. Yarns are more prone to fiber fractures after multiple frictional cycles, with noticeable stress concentration phenomena. The fiber fractures predominantly occur in areas of stress concentration, typically at the contact points within the yarn. Furthermore, increasing the twist generally enhances the yarn's strength, as the cohesion between fibers increases, making the yarn more resistant to breaking during friction. There is a significant correlation between dissipated energy and the damage variable; the rapid increase in dissipated energy corresponds to the rapid rise in the damage variable. This indicates that by optimally designing the yarn's twist, the internal stress distribution and damage accumulation within the

fibers can be better controlled, thereby enhancing the mechanical performance and durability of the fibers.

This research's methodology and findings can guide the structural design of 3DWPs before forming, thereby reducing the forming wrinkle defects of the preform, which is of great significance for the performance improvement and application of the final composite material. However, this research simplifies the cross-sectional structure and contact friction behavior of the virtual yarn model, which will be considered in future work.

The proposed model effectively responds to the combined effects of torsion, normal load and pre-tension on yarn friction behavior, which guide the geometrical and mechanical design during the manufacturing of the reinforcement, thereby controlling friction and wear of yarn, which is of great significance for the performance improvement and application of the final composite material. Future research could utilize the methodology to investigate friction behavior for other situations, e.g., to study the couple effects of geometrical arrangement and virtual weaving simulation. Furthermore, an investigation of the sizing treatment for yarn could also be performed by applying the material property data.

## **Chapter 5 Conclusions and Perspectives**

## 5.1 Conclusions

Textile composites are widely used in industries such as aerospace, automotive, and construction because of their excellent mechanical capabilities and lightweight characteristics. These materials, which are strengthened with high-performance fibers such as carbon fiber and aramid, have notable benefits such as exceptional strength and resistance to corrosion. Nevertheless, the production process is intricate and necessitates stringent regulation to guarantee the best performance of the end products.

Comprehending the friction characteristics of yarns during the weaving process is essential because it directly affects the mechanical properties of the composites. The mechanical characteristics of the yarns can be significantly impaired by friction, compression, and bending, resulting in damage that can compromise up to 30% of their overall performance. The composition of the yarns and the methods used for weaving have a direct impact on the robustness and longevity of the composites. A mathematical model has been devised to comprehend and forecast the friction characteristics of yarns in various arrangements and levels of twist. The model demonstrates that the friction force diminishes as the yarn twist rises, but it intensifies with greater normal loads. This comprehension is further improved by a micro-meso theoretical model that has been verified through experimental methods. This model accurately forecasts the friction characteristics of yarns in both 2D and 3D reinforcement configurations.

Furthermore, in the reinforcing phase, where high-performance fibers are interwoven into preform structures, the fibers may undergo stretching, bending, and friction, resulting in diminished mechanical performance or breaking. This problem is most noticeable in textile preforming processes such as weaving, knitting, or sophisticated weaving methods. In these processes, there are numerous contacts between yarns, which leads to damage caused by friction. These damages reduce the ability of the material to bear weight and can cause a decrease in the mechanical performance of the finished composite materials, which compromises their structural integrity and functional performance.

Due to the constraints of experimental techniques, numerical simulation approaches have become indispensable for investigating the behavior of yarn friction. These simulations forecast the behavior and performance of materials without the requirement for actual sample production, resulting in substantial reductions in research expenses and enabling meticulous control over simulation settings. The fiber constitutive model, constructed utilizing the VUMAT user



subroutine and a high-precision yarn model based on Timoshenko beam theory, successfully resolves beam element incursion problems. This model has been verified using displacement curves obtained from friction test machines that were fitted with customized devices, as well as Micro-CT observations. It has effectively predicted friction and wear behavior by taking into account interactions between fibers in contact.

An analysis was conducted on the friction characteristics of yarns in the process of producing reinforcements. The results indicate that as the twist of the yarn rises, the friction force reduces, whereas greater normal loads lead to an increase in friction force. Moreover, the degree of rotation and the quantity of friction cycles have a substantial influence on the distribution of stress and the circumstances that lead to fractures. Yarns are susceptible to fiber fractures when subjected to repeated friction cycles, resulting in obvious stress concentration phenomena. These findings emphasize the significance of improving the structure of yarn to enhance the dispersion of internal stress and minimize localized damage.

In summary, the research shows that it is essential to comprehend and enhance the friction and wear characteristics of yarns to enhance the mechanical properties of textile composites. The models and validations establish a strong basis for the design and production of fiber reinforcements, with the goal of minimizing harm and optimizing the performance of the final composites. Future research should prioritize the improvement of numerical models to incorporate variables like fiber treatment and ambient circumstances. Additionally, it should investigate novel weaving processes to maximize the effectiveness of textile composites. This comprehensive method will provide guidance for the structural design of textile preforms, resulting in a reduction of flaws and an improvement in the application and performance of the final composite materials.

## 5.2 Perspectives

Future research in the field of textile composites should place a strong emphasis on the development of more advanced numerical models to simulate the friction and wear behaviors of yarns. These simulations are crucial for understanding how yarns perform under a wide range of environmental conditions and treatment processes. By creating more detailed and precise models, researchers can predict how these materials will behave in realistic applications, which is essential for improving their overall performance and longevity.

In addition to modeling, there is a significant potential in exploring new materials and innovative weaving techniques. By experimenting with different materials, researchers can

discover combinations that offer superior strength, flexibility, and resistance to environmental stressors. Similarly, advances in weaving techniques can lead to the creation of textiles with unique properties, such as enhanced durability or specialized functionality, which are not achievable with traditional methods.

Furthermore, the integration of advanced technologies, such as machine learning and artificial intelligence, could revolutionize the design and manufacturing processes of textile composites. These technologies can analyze vast amounts of data to identify patterns and make real-time adjustments, optimizing every aspect of production. This capability not only improves efficiency but also allows for the customization of materials to meet specific requirements, thereby reducing waste and costs.

Collaboration between academia and industry is a critical component in this innovation ecosystem. Such partnerships are necessary to ensure that the latest scientific discoveries are translated into practical, commercially viable solutions. Academic institutions often provide the fundamental research and theoretical knowledge, while industry partners can apply this knowledge in real-world settings, scaling up the innovations for broader use. This synergy can lead to the development of more efficient, robust composite materials tailored for various industrial applications, including in sectors like automotive, aerospace, and construction, where the demands for high-performance materials are ever-increasing.

Overall, the concerted efforts in research, innovation, and collaboration will be instrumental in shaping the future landscape of textile composites. These efforts will ensure that these advanced materials are not only adopted but also optimized for diverse applications, meeting the evolving needs of various industries and contributing to economic and technological growth. As the field progresses, it is expected that textile composites will play an increasingly vital role in a wide range of industrial and consumer products, offering unparalleled benefits in terms of performance, durability, and adaptability.

## References

- [1] Ngo T-D. Introduction to Composite Materials. *Composite and Nanocomposite Materials - From Knowledge to Industrial Applications*, IntechOpen; 2020. <https://doi.org/10.5772/intechopen.91285>.
- [2] Ouyang Y, Wu X. A review on the mechanical properties of textile structural composite T-beams. *Textile Research Journal* 2020;90:710–27. <https://doi.org/10.1177/0040517519871259>.
- [3] Gao Z, Chen L. A review of multi-scale numerical modeling of three-dimensional woven fabric. *Composite Structures* 2021;263:113685. <https://doi.org/10.1016/j.compstruct.2021.113685>.
- [4] Paul R, Gouda K, Bhowmik S. Effect of Different Constraint on Tribological Behaviour of Natural Fibre/Filler Reinforced Polymeric Composites: a Review. *Silicon* 2021;13:2785–807. <https://doi.org/10.1007/s12633-020-00613-z>.
- [5] Liang B, Boisse P. A review of numerical analyses and experimental characterization methods for forming of textile reinforcements. *Chinese Journal of Aeronautics* 2021;34:143–63. <https://doi.org/10.1016/j.cja.2020.09.027>.
- [6] Gennusa ML, Llorach-Massana P, Montero JI, Peña FJ, Rieradevall J, Ferrante P, et al. Composite Building Materials: Thermal and Mechanical Performances of Samples Realized with Hay and Natural Resins. *Sustainability* 2017;9:373. <https://doi.org/10.3390/su9030373>.
- [7] Chinta VS, Ravinder Reddy P, Prasad KE. The effect of stacking sequence on the tensile properties of jute fibre reinforced hybrid composite material for axial flow fan blades: An experimental and finite element investigation. *Materials Today: Proceedings* 2022;59:747–55. <https://doi.org/10.1016/j.matpr.2021.12.500>.
- [8] Chen B, Colmars J, Naouar N, Boisse P. A hypoelastic stress resultant shell approach for simulations of textile composite reinforcement forming. *Composites Part A: Applied Science and Manufacturing* 2021;149:106558. <https://doi.org/10.1016/j.compositesa.2021.106558>.
- [9] Durville D, Baydoun I, Moustacas H, Périé G, Wielhorski Y. Determining the initial configuration and characterizing the mechanical properties of 3D angle-interlock fabrics using finite element simulation. *International Journal of Solids and Structures* 2018;154:97–103. <https://doi.org/10.1016/j.ijsolstr.2017.06.026>.
- [10] Xie J, Guo Z, Shao M, Zhu W, Jiao W, Yang Z, et al. Mechanics of textiles used as composite preforms: A review. *Composite Structures* 2023;304:116401. <https://doi.org/10.1016/j.compstruct.2022.116401>.
- [11] Sayam A, Rahman ANMM, Rahman MdS, Smriti SA, Ahmed F, Rabbi MdF, et al. A review on carbon fiber-reinforced hierarchical composites: mechanical performance, manufacturing process,

- structural applications and allied challenges. *Carbon Lett* 2022;32:1173–205. <https://doi.org/10.1007/s42823-022-00358-2>.
- [12] Zhang J, Lin G, Vaidya U, Wang H. Past, present and future prospective of global carbon fibre composite developments and applications. *Composites Part B: Engineering* 2023;250:110463. <https://doi.org/10.1016/j.compositesb.2022.110463>.
- [13] Moy S. 7 - Advanced fiber-reinforced polymer (FRP) composites for civil engineering applications. In: Uddin N, editor. *Developments in Fiber-Reinforced Polymer (FRP) Composites for Civil Engineering*, Woodhead Publishing; 2013, p. 177–204. <https://doi.org/10.1533/9780857098955.2.177>.
- [14] Riccio A. 2 - Delamination in the context of composite structural design. In: Sridharan S, editor. *Delamination Behaviour of Composites*, Woodhead Publishing; 2008, p. 28–64. <https://doi.org/10.1533/9781845694821.1.28>.
- [15] Vasiliev VV, Morozov EV. Chapter 12 - Optimal composite structures. In: Vasiliev VV, Morozov EV, editors. *Advanced Mechanics of Composite Materials (Third Edition)*, Boston: Elsevier; 2013, p. 745–96. <https://doi.org/10.1016/B978-0-08-098231-1.00012-1>.
- [16] Wazeer A, Das A, Abeykoon C, Sinha A, Karmakar A. Composites for electric vehicles and automotive sector: A review. *Green Energy and Intelligent Transportation* 2023;2:100043. <https://doi.org/10.1016/j.geits.2022.100043>.
- [17] Mohammadi H, Ahmad Z, Mazlan SA, Faizal Johari MA, Siebert G, Petru M, et al. Lightweight Glass Fiber-Reinforced Polymer Composite for Automotive Bumper Applications: A Review. *Polymers* 2023;15:193. <https://doi.org/10.3390/polym15010193>.
- [18] Andrew JJ, Dhakal HN. Sustainable biobased composites for advanced applications: recent trends and future opportunities – A critical review. *Composites Part C: Open Access* 2022;7:100220. <https://doi.org/10.1016/j.jcomc.2021.100220>.
- [19] Katnam KB, Comer AJ, Roy D, da Silva LFM, Young TM. Composite Repair in Wind Turbine Blades: An Overview. *The Journal of Adhesion* 2015;91:113–39. <https://doi.org/10.1080/00218464.2014.900449>.
- [20] Chen J, Wang J, Ni A. Recycling and reuse of composite materials for wind turbine blades: An overview. *Journal of Reinforced Plastics and Composites* 2019;38:567–77. <https://doi.org/10.1177/0731684419833470>.
- [21] Raj EFI, Appadurai M, Ram V, Gnanih AM, Salkuti SR. Natural-Fibre-Reinforced Composite-Based Micro-Size Wind Turbines: Numerical Analysis and Feasibility Study. *Journal of Composites Science* 2023;7:197. <https://doi.org/10.3390/jcs7050197>.

- [22] Diniță A, Ripeanu RG, Ilincă CN, Cursaru D, Matei D, Naim RI, et al. Advancements in Fiber-Reinforced Polymer Composites: A Comprehensive Analysis. *Polymers* 2024;16:2. <https://doi.org/10.3390/polym16010002>.
- [23] Heitkamp T, Girmth S, Kuschmitz S, Klawitter G, Waldt N, Vietor T. Continuous Fiber-Reinforced Material Extrusion with Hybrid Composites of Carbon and Aramid Fibers. *Applied Sciences* 2022;12:8830. <https://doi.org/10.3390/app12178830>.
- [24] Denault J, Vu-Khanh T. Crystallization and fiber/matrix interaction during the molding of PEEK/carbon composites. *Polymer Composites* 1992;13:361–71. <https://doi.org/10.1002/pc.750130505>.
- [25] Wu N, Xie X, Yang J, Feng Y, Jiao Y, Chen L, et al. Effect of normal load on the frictional and wear behaviour of carbon fiber in tow-on-tool contact during three-dimensional weaving process. *Journal of Industrial Textiles* 2022;51:2753S-2773S. <https://doi.org/10.1177/1528083720944615>.
- [26] Minus M, Kumar S. The processing, properties, and structure of carbon fibers. *JOM* 2005;57:52–8. <https://doi.org/10.1007/s11837-005-0217-8>.
- [27] Jiao W, Chen L, Xie J, Yang Z, Guo Z. Deformation mechanisms of 3D LTL woven preforms in hemisphere forming tests. *Composite Structures* 2022;283:115156. <https://doi.org/10.1016/j.compstruct.2021.115156>.
- [28] Charmetant A, Vidal-Sallé E, Boisse P. Hyperelastic modelling for mesoscopic analyses of composite reinforcements. *Composites Science and Technology* 2011;71:1623–31. <https://doi.org/10.1016/j.compscitech.2011.07.004>.
- [29] Syerko E, Comas-Cardona S, Binetruy C. Models of mechanical properties/behavior of dry fibrous materials at various scales in bending and tension: A review. *Composites Part A: Applied Science and Manufacturing* 2012;43:1365–88. <https://doi.org/10.1016/j.compositesa.2012.03.012>.
- [30] Dixit A, Mali HS. Modeling techniques for predicting the mechanical properties of woven-fabric textile composites: a Review. *Mech Compos Mater* 2013;49:1–20. <https://doi.org/10.1007/s11029-013-9316-8>.
- [31] Jiang L, Zulifqar A, Hai AM, Anwar F, Hu H, Liu F, et al. Effect of using alternate elastic and non-elastic yarns in warp on shrinkage and stretch behavior of bi-stretch woven fabrics. *Journal of Engineered Fibers and Fabrics* 2023;18:15589250221137897. <https://doi.org/10.1177/15589250221137897>.
- [32] Wang L, Liu X, Saleemi S, Zhang Y, Qiu Y, Xu F. Bending properties and failure mechanisms of three-dimensional hybrid woven spacer composites with glass and carbon fibers. *Textile Research Journal* 2019;89:4502–11. <https://doi.org/10.1177/0040517519837730>.
- [33] He Y, Jiao Y, Zhou JQ, Lei H, Jia N, Chen L, et al. Ballistic response of ultra-high molecular weight polyethylene laminate impacted by mild steel core projectiles. *International Journal of Impact Engineering* 2022;169:104338. <https://doi.org/10.1016/j.ijimpeng.2022.104338>.

- [34] Jiao W, Chen L, Xie J, Yang Z, Fang J, Chen L. Effect of weaving structures on the geometry variations and mechanical properties of 3D LTL woven composites. *Composite Structures* 2020;252:112756. <https://doi.org/10.1016/j.compstruct.2020.112756>.
- [35] Kashif M, Hamdani STA, Nawab Y, Asghar MA, Umair M, Shaker K. Optimization of 3D woven preform for improved mechanical performance. *Journal of Industrial Textiles* 2019;48:1206–27. <https://doi.org/10.1177/1528083718760802>.
- [36] Hui C, Wang P, Legrand X. Improvement of tufting mechanism during the advanced 3-dimensional tufted composites manufacturing: To the optimisation of tufting threads degradation. *Composite Structures* 2019;220:423–30. <https://doi.org/10.1016/j.compstruct.2019.04.019>.
- [37] Li M, Wang P, Boussu F, Soulat D. A review on the mechanical performance of three-dimensional warp interlock woven fabrics as reinforcement in composites. *Journal of Industrial Textiles* 2022;51:1009–58. <https://doi.org/10.1177/1528083719894389>.
- [38] Li M, Wang P, Boussu F, Soulat D. Investigation of impact performance of 3-dimensional interlock polymer fabrics in double and multi-angle pass stabbing. *Materials & Design* 2021;206:109775. <https://doi.org/10.1016/j.matdes.2021.109775>.
- [39] Li M, Wang P, Boussu F, Soulat D. Effect of Fabric Architecture on Tensile Behaviour of the High-Molecular-Weight Polyethylene 3-Dimensional Interlock Composite Reinforcements. *Polymers* 2020;12:1045. <https://doi.org/10.3390/polym12051045>.
- [40] Chen C, Wang P, Legrand X. Effect of Core Architecture on Charpy Impact and Compression Properties of Tufted Sandwich Structural Composites. *Polymers* 2021;13:1665. <https://doi.org/10.3390/polym13101665>.
- [41] Wu C, Pan Y, Yan L. Mechanical Properties and Durability of Textile Reinforced Concrete (TRC)—A Review. *Polymers* 2023;15:3826. <https://doi.org/10.3390/polym15183826>.
- [42] Amirifard M, Asayesh A. The effect of elastic yarn tension and alignment on the tensile and compression characteristics of weft-knitted spacer fabrics for cushioning applications. *The Journal of The Textile Institute* 2023;114:1476–87. <https://doi.org/10.1080/00405000.2022.2131351>.
- [43] Simon J, Hamila N, Binetruy C, Comas-Cardona S, Masseteau B. Design and numerical modelling strategy to form Tailored Fibre Placement preforms: Application to the tetrahedral part with orthotropic final configuration. *Composites Part A: Applied Science and Manufacturing* 2022;158:106952. <https://doi.org/10.1016/j.compositesa.2022.106952>.
- [44] Xiao S, Wang P, Soulat D, Gao H. An exploration of the deformability behaviour dominated by braiding angle during the forming of the triaxial carbon fibre braids. *Composites Part A Applied Science and Manufacturing* 2020;133. <https://doi.org/10.1016/j.compositesa.2020.105890>.

- [45] Bejan L, Poterasu VF. Woven composite material design by orthotropic compliance averaging method using mathematica. *Computer Methods in Applied Mechanics and Engineering* 1999;179:53–65. [https://doi.org/10.1016/S0045-7825\(99\)00040-7](https://doi.org/10.1016/S0045-7825(99)00040-7).
- [46] Mouritz AP, Bannister MK, Falzon PJ, Leong KH. Review of applications for advanced three-dimensional fibre textile composites. *Composites Part A: Applied Science and Manufacturing* 1999;30:1445–61. [https://doi.org/10.1016/S1359-835X\(99\)00034-2](https://doi.org/10.1016/S1359-835X(99)00034-2).
- [47] Omrani F, Wang P, Soulat D, Ferreira M. Mechanical properties of flax-fibre-reinforced preforms and composites: Influence of the type of yarns on multi-scale characterisations. *Composites Part A: Applied Science and Manufacturing* 2017;93:72–81. <https://doi.org/10.1016/j.compositesa.2016.11.013>.
- [48] Palacio A, Baniyadi M, Kardel K. Investigating Mechanical Properties of Fabricated Carbon-Fiber-Reinforced Composites via LCD Additive Manufacturing. *Polymers* 2023;15:4556. <https://doi.org/10.3390/polym15234556>.
- [49] Wang J, Zhou H, Liu Z, Peng X, Zhou H. Statistical modelling of tensile properties of natural fiber yarns considering probability distributions of fiber crimping and effective yarn elastic modulus. *Composites Science and Technology* 2022;218:109142. <https://doi.org/10.1016/j.compscitech.2021.109142>.
- [50] Hemmer J, Lectez A-S, Verron E, Lebrun J-M, Binetruy C, Comas-Cardona S. Influence of the lateral confinement on the transverse mechanical behavior of tows and quasi-unidirectional fabrics: Experimental and modeling investigations of dry through-thickness compaction. *Journal of Composite Materials* 2020;54:3261–74. <https://doi.org/10.1177/0021998320912809>.
- [51] R'Mili M, Godin N, Lamon J. Flaw strength distributions and statistical parameters for ceramic fibers: The normal distribution. *Phys Rev E* 2012;85:051106. <https://doi.org/10.1103/PhysRevE.85.051106>.
- [52] Rudov-Clark S, Mouritz AP, Lee L, Bannister MK. Fibre damage in the manufacture of advanced three-dimensional woven composites. *Composites Part A: Applied Science and Manufacturing* 2003;34:963–70. [https://doi.org/10.1016/S1359-835X\(03\)00213-6](https://doi.org/10.1016/S1359-835X(03)00213-6).
- [53] Lee L, Rudov-Clark S, Mouritz AP, Bannister MK, Herszberg I. Effect of weaving damage on the tensile properties of three-dimensional woven composites. *Composite Structures* 2002;57:405–13. [https://doi.org/10.1016/S0263-8223\(02\)00108-3](https://doi.org/10.1016/S0263-8223(02)00108-3).
- [54] Brandt J, Drechsler K, Arendts F-J. Mechanical performance of composites based on various three-dimensional woven-fibre preforms. *Composites Science and Technology* 1996;56:381–6. [https://doi.org/10.1016/0266-3538\(95\)00135-2](https://doi.org/10.1016/0266-3538(95)00135-2).
- [55] McIlhagger R, Hill BJ, Brown D, Limmer L. Construction and analysis of three-dimensional woven composite materials. *Composites Engineering* 1995;5:1187–97. [https://doi.org/10.1016/0961-9526\(95\)00005-8](https://doi.org/10.1016/0961-9526(95)00005-8).

- [56] Kuo W-S, Ko T-H, Chen C-P. Effect of weaving processes on compressive behavior of 3D woven composites. *Composites Part A: Applied Science and Manufacturing* 2007;38:555–65. <https://doi.org/10.1016/j.compositesa.2006.02.025>.
- [57] Zhiping Y, Xiaohui P, Zhenyu W, Zhongxiang P, Xiaoying C. Effect of the micro-structure on the compressive failure behavior of three-dimensional orthogonal woven composites. *Composite Structures* 2022;297:115892. <https://doi.org/10.1016/j.compstruct.2022.115892>.
- [58] Leong KH, Lee B, Herszberg I, Bannister MK. The effect of binder path on the tensile properties and failure of multilayer woven CFRP composites. *Composites Science and Technology* 2000;60:149–56. [https://doi.org/10.1016/S0266-3538\(99\)00108-6](https://doi.org/10.1016/S0266-3538(99)00108-6).
- [59] Wu N, Li S, Han M, Zhu C, Jiao Y, Chen L. Experimental simulation of bending damage of silicon nitride yarn during 3D orthogonal fabric forming process. *Journal of Industrial Textiles* 2021;152808372110106. <https://doi.org/10.1177/15280837211010681>.
- [60] Lee B, Leong KH, Herszberg I. Effect of Weaving on the Tensile Properties of Carbon Fibre Tows and Woven Composites. *Journal of Reinforced Plastics and Composites* 2001;20:652–70. <https://doi.org/10.1177/073168401772679011>.
- [61] Ismail NB. An experimental study of friction and adhesion between single aramid fibres. PhD. University of Twente, 2018. <https://doi.org/10.3990/1.9789036545969>.
- [62] Abu Obaid A, Gillespie J. Effects of abrasion on mechanical properties of Kevlar KM2-600 and S glass tows. *Textile Research Journal* 2019;89:989–1002. <https://doi.org/10.1177/0040517518760753>.
- [63] Chakladar ND, Mandal P, Potluri P. Effects of inter-tow angle and tow size on carbon fibre friction. *Composites Part A: Applied Science and Manufacturing* 2014;65:115–24. <https://doi.org/10.1016/j.compositesa.2014.06.002>.
- [64] Abdellahi SB, Naghashzargar E, Semnani D. Meso modeling of silk wire rope scaffolds in tissue engineering. *Journal of Industrial Textiles* 2017;47:377–89. <https://doi.org/10.1177/1528083716648762>.
- [65] Mulvihill DM, Sutcliffe MPF. Effect of tool surface topography on friction with carbon fibre tows for composite fabric forming. *Composites Part A: Applied Science and Manufacturing* 2017;93:199–206. <https://doi.org/10.1016/j.compositesa.2016.10.017>.
- [66] Cornelissen B, Sachs U, Rietman B, Akkerman R. Dry friction characterisation of carbon fibre tow and satin weave fabric for composite applications. *Composites Part A: Applied Science and Manufacturing* 2014;56:127–35. <https://doi.org/10.1016/j.compositesa.2013.10.006>.
- [67] Avgoulas EI, Mulvihill DM, Endruweit A, Sutcliffe MPF, Warrior NA, De Focatiis DSA, et al. Frictional behaviour of non-crimp fabrics (NCFs) in contact with a forming tool. *Tribology International* 2018;121:71–7. <https://doi.org/10.1016/j.triboint.2018.01.026>.



- [68] Sugimoto Y, Shimamoto D, Hotta Y. Evaluation of kinetic friction coefficients between single carbon fibers. *Carbon* 2020;167:264–9. <https://doi.org/10.1016/j.carbon.2020.06.010>.
- [69] Li S, Shan Z, Du D, Zhan L, Guo Z, Du W, et al. Effect of processing parameters on friction and damage of carbon yarn during three-dimensional weaving. *The Journal of The Textile Institute* 2021:1–10. <https://doi.org/10.1080/00405000.2021.1915588>.
- [70] Kärger L, Bernath A, Fritz F, Galkin S, Magagnato D, Oeckerath A, et al. Development and validation of a CAE chain for unidirectional fibre reinforced composite components. *Composite Structures* 2015;132:350–8. <https://doi.org/10.1016/j.compstruct.2015.05.047>.
- [71] Montero L, Allaoui S, Hivet G. Characterisation of the mesoscopic and macroscopic friction behaviours of glass plain weave reinforcement. *Composites Part A: Applied Science and Manufacturing* 2017;95:257–66. <https://doi.org/10.1016/j.compositesa.2017.01.022>.
- [72] Cornelissen B, Rietman B, Akkerman R. Frictional behaviour of high performance fibrous tows: Friction experiments. *Composites Part A: Applied Science and Manufacturing* 2013;44:95–104. <https://doi.org/10.1016/j.compositesa.2012.08.024>.
- [73] Zhai W, Wang P, Legrand X, Soulat D, Ferreira M. Effects of Micro-Braiding and Co-Wrapping Techniques on Characteristics of Flax/Polypropylene-Based Hybrid Yarn: A Comparative Study. *Polymers* 2020;12:2559. <https://doi.org/10.3390/polym12112559>.
- [74] Xiang Z, Liu Y, Zhou X, Wu Z, Hu X. Interlayer contact mechanism of the frictional behavior of glass-fiber woven fabrics and improvements of winding characteristics. *Composite Structures* 2020;233:111497. <https://doi.org/10.1016/j.compstruct.2019.111497>.
- [75] Tournalias M, Bueno M-A. Experimental simulation of friction and wear of carbon yarns during the weaving process. *Composites Part A: Applied Science and Manufacturing* 2016;80:228–36. <https://doi.org/10.1016/j.compositesa.2015.07.024>.
- [76] Bikakis GS. Finite element and analytical modeling to predict the frictional oblique indentation response of GLARE fiber–metal laminates. *Journal of Reinforced Plastics and Composites* 2017;36:797–807. <https://doi.org/10.1177/0731684417690928>.
- [77] Sockalingam S, Gillespie JW, Keefe M. On the transverse compression response of Kevlar KM2 using fiber-level finite element model. *International Journal of Solids and Structures* 2014;51:2504–17. <https://doi.org/10.1016/j.ijsolstr.2014.03.020>.
- [78] Liu J, Chen L, Xie J, Lin Z. Micro-flow model with a new algorithm of random fiber distribution over the transverse cross-section. *Polymer Composites* 2020;41:5006–15. <https://doi.org/10.1002/pc.25770>.
- [79] Vorhof M, Weise D, Sennewald C, Hoffmann G. New method for warp yarn arrangement and algorithm for pattern conversion for three-dimensional woven multilayered fabrics. *Journal of Industrial Textiles* 2020;49:1334–56. <https://doi.org/10.1177/1528083718813530>.

- [80] Alirezazadeh A, Zarrebini M, Ghane M, Soltani P. Fiber-on-fiber friction measurement using hanging fiber method. *The Journal of The Textile Institute* 2018;109:636–46. <https://doi.org/10.1080/00405000.2017.1362746>.
- [81] Schön J. Coefficient of friction and wear of a carbon fiber epoxy matrix composite. *Wear* 2004;257:395–407. <https://doi.org/10.1016/j.wear.2004.01.008>.
- [82] Zhou Y, Ali M, Gong X, Yang D. An overview of yarn pull-out behavior of woven fabrics. *Textile Research Journal* 2019;89:223–34. <https://doi.org/10.1177/0040517517741156>.
- [83] Rubino M, Wielhorski Y, Roux S. Transverse compaction of twisted carbon yarns: Experiment and elasto-plastic Mohr–Coulomb modeling. *Composites Part A: Applied Science and Manufacturing* 2024;176:107873. <https://doi.org/10.1016/j.compositesa.2023.107873>.
- [84] Nian G, Li Q, Xu Q, Qu S. A cohesive zone model incorporating a Coulomb friction law for fiber-reinforced composites. *Composites Science and Technology* 2018;157:195–201. <https://doi.org/10.1016/j.compscitech.2018.01.037>.
- [85] Smerdova O, Sutcliffe MPF. Novel Experimental Method for Microscale Contact Analysis in Composite Fabric Forming. *Exp Mech* 2015;55:1475–83. <https://doi.org/10.1007/s11340-015-0044-y>.
- [86] Peng L, Feng Z-Q, Joli P, Liu J, Zhou Y. Automatic contact detection between rope fibers. *Computers & Structures* 2019;218:82–93. <https://doi.org/10.1016/j.compstruc.2019.03.010>.
- [87] Wang J, Zhang X, Zhou J, Zhou Y-H. Effects of Fiber Diameter and Tribotest Conditions on Nonlubricated Frictional Behavior of a Microsized Metal Fiber. *Tribology Transactions* 2018;61:376–80. <https://doi.org/10.1080/10402004.2017.1328548>.
- [88] Gao X, Wang L, Hao X. An improved Capstan equation including power-law friction and bending rigidity for high performance yarn. *Mechanism and Machine Theory* 2015;90:84–94. <https://doi.org/10.1016/j.mechmachtheory.2015.03.005>.
- [89] Zhang G, Ren T, Zeng X, Van Der Heide E. Influence of surgical suture properties on the tribological interactions with artificial skin by a capstan experiment approach. *Friction* 2017;5:87–98. <https://doi.org/10.1007/s40544-017-0140-3>.
- [90] Kuhm D, Bueno M-A, Knittel D. Fabric friction behavior: study using capstan equation and introduction into a fabric transport simulator. *Textile Research Journal* 2014;84:1070–83. <https://doi.org/10.1177/0040517513515313>.
- [91] Jing H, Yu W. Estimation of fiber orientation and length distribution in cashmere fibrous assemblies. *Textile Research Journal* 2019;89:1084–93. <https://doi.org/10.1177/0040517518763987>.
- [92] Cornelissen B, de Rooij MB, Rietman B, Akkerman R. Frictional behavior of carbon fiber tows: a contact mechanics model of tow–tow friction. *Textile Research Journal* 2014;84:1476–88. <https://doi.org/10.1177/0040517514525876>.

- [93] Allaoui S, Cellard C, Hivet G. Effect of inter-ply sliding on the quality of multilayer interlock dry fabric preforms. *Composites Part A: Applied Science and Manufacturing* 2015;68:336–45. <https://doi.org/10.1016/j.compositesa.2014.10.017>.
- [94] Capdevila FX, Carrera-Gallissà E, Escusa M, Rotela M. Canonical analysis of the Kawabata and sliding fabric friction measurement methods. *The Journal of The Textile Institute* 2020;111:890–6. <https://doi.org/10.1080/00405000.2019.1670924>.
- [95] Tournalias M, Bueno M-A, Poquillon D. Friction of carbon tows and fine single fibres. *Composites Part A: Applied Science and Manufacturing* 2017;98:116–23. <https://doi.org/10.1016/j.compositesa.2017.03.017>.
- [96] Shanwan A, Gassara H-E, Barbier G, Sinoimeri A. New experimental device for measuring the inter-fiber transversal friction. *IOP Conf Ser: Mater Sci Eng* 2017;254:142020. <https://doi.org/10.1088/1757-899X/254/14/142020>.
- [97] Howell HG, Mazur J. Amontons' Law and Fibre Friction. *Journal of the Textile Institute Transactions* 1953;44:T59–69. <https://doi.org/10.1080/19447025308659728>.
- [98] Ismail N, de Rooij MB, de Vries EG, Hilwa Mohd Zini N, Schipper DJ. Friction between single aramid fibres under pre-tension load. *Tribology International* 2019;137:236–45. <https://doi.org/10.1016/j.triboint.2019.04.013>.
- [99] Mulvihill DM, Smerdova O, Sutcliffe MPF. Friction of carbon fibre tows. *Composites Part A: Applied Science and Manufacturing* 2017;93:185–98. <https://doi.org/10.1016/j.compositesa.2016.08.034>.
- [100] Ismail N, Vries EGD, Rooij MBD, Zini NHM, Schipper DJ. An experimental study of friction in fibre-fibre contacts. *International Journal of Materials and Product Technology* 2016.
- [101] Carlene PW. 5—the Measurement of the Bending Modulus of Monofil. *Journal of the Textile Institute Transactions* 1947;38:T38–42. <https://doi.org/10.1080/19447024708659285>.
- [102] Hobbs RE, Ridge IML. A new estimate of the yarn-on-yarn friction coefficient. *The Journal of Strain Analysis for Engineering Design* 2018;53:191–6. <https://doi.org/10.1177/0309324718760883>.
- [103] Tournalias M, Jordan C, Bueno M-A, Poquillon D. Friction of carbon fibre and influence of sizing treatment, Penang, Malaysia: 2017, p. 030030. <https://doi.org/10.1063/1.5008017>.
- [104] Rao MP, Duan Y, Keefe M, Powers BM, Bogetti TA. Modeling the effects of yarn material properties and friction on the ballistic impact of a plain-weave fabric. *Composite Structures* 2009;89:556–66. <https://doi.org/10.1016/j.compstruct.2008.11.012>.
- [105] Bowden FP, Tabor D, Palmer F. *The Friction and Lubrication of Solids* 2014:3.
- [106] Popov VL. Rigorous Treatment of Contact Problems – Hertzian Contact. In: Popov VL, editor. *Contact Mechanics and Friction: Physical Principles and Applications*, Berlin, Heidelberg: Springer; 2017, p. 57–81. [https://doi.org/10.1007/978-3-662-53081-8\\_5](https://doi.org/10.1007/978-3-662-53081-8_5).

- [107] Popov VL. Contact Mechanics and Friction. Berlin, Heidelberg: Springer; 2010. <https://doi.org/10.1007/978-3-642-10803-7>.
- [108] Tournalias M, Bueno M-A, Fassi G, Aktas I, Wielhorski Y. Influence of friction angle between carbon single fibres and tows: Experimental analysis and analytical model. *Composites Part A: Applied Science and Manufacturing* 2019;124:105478. <https://doi.org/10.1016/j.compositesa.2019.105478>.
- [109] Wang Y, Jiao Y, Wang P. Yarn/Yarn Friction Analysis Considering the Weaving Process of Textile Fabrics: Analytical Model and Experimental Validation. *Tribol Lett* 2023;71:91. <https://doi.org/10.1007/s11249-023-01755-y>.
- [110] Miao Y, Zhou E, Wang Y, Cheeseman BA. Mechanics of textile composites: Micro-geometry. *Composites Science and Technology* 2008;68:1671–8. <https://doi.org/10.1016/j.compscitech.2008.02.018>.
- [111] Zhou G, Sun X, Wang Y. Multi-chain digital element analysis in textile mechanics. *Composites Science and Technology* 2004;64:239–44. [https://doi.org/10.1016/S0266-3538\(03\)00258-6](https://doi.org/10.1016/S0266-3538(03)00258-6).
- [112] Huang F, Li K, Kulachenko A. Measurement of interfiber friction force for pulp fibers by atomic force microscopy. *J Mater Sci* 2009;44:3770–6. <https://doi.org/10.1007/s10853-009-3506-8>.
- [113] Huang L, Wang Y, Miao Y, Swenson D, Ma Y, Yen C-F. Dynamic relaxation approach with periodic boundary conditions in determining the 3-D woven textile micro-geometry. *Composite Structures* 2013;106:417–25. <https://doi.org/10.1016/j.compstruct.2013.05.057>.
- [114] Döbrich O, Gereke T, Cherif C. Modelling of textile composite reinforcements on the micro-scale. *Autex Research Journal* 2014;14:28–33. <https://doi.org/10.2478/v10304-012-0047-z>.
- [115] Döbrich O, Gereke T, Cherif C. Modeling the mechanical properties of textile-reinforced composites with a near micro-scale approach. *Composite Structures* 2016;135:1–7. <https://doi.org/10.1016/j.compstruct.2015.09.010>.
- [116] Döbrich O, Gereke T, Hengstermann M, Cherif C. Microscale finite element model of brittle multifilament yarn failure behavior. *Journal of Industrial Textiles* 2018;47:870–82. <https://doi.org/10.1177/1528083716674908>.
- [117] Mazumder A, Wang Y, Yen C-F. A structured method to generate conformal FE mesh for realistic textile composite micro-geometry. *Composite Structures* 2020;239:112032. <https://doi.org/10.1016/j.compstruct.2020.112032>.
- [118] Wang Y, Sun X. Digital-element simulation of textile processes. *Composites Science and Technology* 2001;61:311–9. [https://doi.org/10.1016/S0266-3538\(00\)00223-2](https://doi.org/10.1016/S0266-3538(00)00223-2).
- [119] Daelemans L, Faes J, Allaoui S, Hivet G, Dierick M, Van Hoorebeke L, et al. Finite element simulation of the woven geometry and mechanical behaviour of a 3D woven dry fabric under tensile and shear loading using the digital element method. *Composites Science and Technology* 2016;137:177–87. <https://doi.org/10.1016/j.compscitech.2016.11.003>.

- [120] Ying Z, Hu X, Cheng X, Wu Z. Numerical investigation on the effect of tow tension on the geometry of three-dimensional orthogonally woven fabric. *Textile Research Journal* 2019;89:3779–91. <https://doi.org/10.1177/0040517518821912>.
- [121] Liu C, Xie J, Sun Y, Chen L. Micro-scale modeling of textile composites based on the virtual fiber embedded models. *Composite Structures* 2019;230:111552. <https://doi.org/10.1016/j.compstruct.2019.111552>.
- [122] Xie J, Chen X, Zhang Y, Fang G, Chen L. Experimental and numerical investigation of the needling process for quartz fibers. *Composites Science and Technology* 2018;165:115–23. <https://doi.org/10.1016/j.compscitech.2018.06.009>.
- [123] Mahadik Y, Hallett SR. Finite element modelling of tow geometry in 3D woven fabrics. *Composites Part A: Applied Science and Manufacturing* 2010;41:1192–200. <https://doi.org/10.1016/j.compositesa.2010.05.001>.
- [124] Green SD, Long AC, El Said BSF, Hallett SR. Numerical modelling of 3D woven preform deformations. *Composite Structures* 2014;108:747–56. <https://doi.org/10.1016/j.compstruct.2013.10.015>.
- [125] Saadat MA, Durville D. A mixed stress-strain driven computational homogenization of spiral strands. *Computers & Structures* 2023;279:106981. <https://doi.org/10.1016/j.compstruc.2023.106981>.
- [126] Meier C, Grill MJ, Wall WA, Popp A. Geometrically exact beam elements and smooth contact schemes for the modeling of fiber-based materials and structures. *International Journal of Solids and Structures* 2018;154:124–46. <https://doi.org/10.1016/j.ijsolstr.2017.07.020>.
- [127] Thompson AJ, El Said B, Belnoue JP-H, Hallett SR. Modelling process induced deformations in 0/90 non-crimp fabrics at the meso-scale. *Composites Science and Technology* 2018;168:104–10. <https://doi.org/10.1016/j.compscitech.2018.08.029>.
- [128] Wu L, Zhao F, Xie J, Wu X, Jiang Q, Lin J-H. The deformation behaviors and mechanism of weft knitted fabric based on micro-scale virtual fiber model. *International Journal of Mechanical Sciences* 2020;187:105929. <https://doi.org/10.1016/j.ijmecsci.2020.105929>.
- [129] Lomov SV, Huysmans G, Verpoest I. Hierarchy of Textile Structures and Architecture of Fabric Geometric Models. *Textile Research Journal* 2001;71:534–43. <https://doi.org/10.1177/004051750107100611>.
- [130] F.T.I FTPDS and FIP and. 5—THE GEOMETRY OF CLOTH STRUCTURE. *Journal of the Textile Institute Transactions* 1937. <https://doi.org/10.1080/19447023708658809>.
- [131] Sagar TV, Potluri P, Hearle JWS. Mesoscale modelling of interlaced fibre assemblies using energy method. *Computational Materials Science* 2003;28:49–62. [https://doi.org/10.1016/S0927-0256\(03\)00056-9](https://doi.org/10.1016/S0927-0256(03)00056-9).

- [132] Lomov S, Perie G, Ivanov D, Verpoest I, Marsal D. Modeling three-dimensional fabrics and three-dimensional reinforced composites: challenges and solutions. *Textile Research Journal* 2011;81:28–41. <https://doi.org/10.1177/0040517510385169>.
- [133] Lin H, Zeng X, Sherburn M, Long AC, Clifford MJ. Automated geometric modelling of textile structures. *Textile Research Journal* 2012;82:1689–702. <https://doi.org/10.1177/0040517511418562>.
- [134] Hivet G, Boisse P. Consistent 3D geometrical model of fabric elementary cell. Application to a meshing preprocessor for 3D finite element analysis. *Finite Elements in Analysis and Design* 2005;42:25–49. <https://doi.org/10.1016/j.finel.2005.05.001>.
- [135] Isart N, Mayugo JA, Blanco N, Ripoll L, Solà A, Soler M. Geometric model for 3D through-thickness orthogonal interlock composites. *Composite Structures* 2015;119:787–98. <https://doi.org/10.1016/j.compstruct.2014.09.044>.
- [136] Stig F, Hallström S. Extended framework for geometric modelling of textile architectures. *Composite Structures* 2020;244:112239. <https://doi.org/10.1016/j.compstruct.2020.112239>.
- [137] Wendling A, Hivet G, Vidal-Sallé E, Boisse P. Consistent geometrical modelling of interlock fabrics. *Finite Elements in Analysis and Design* 2014;90:93–105. <https://doi.org/10.1016/j.finel.2014.05.010>.
- [138] Wintiba B, Sonon B, Ehab Moustafa Kamel K, Massart TJ. An automated procedure for the generation and conformal discretization of 3D woven composites RVEs. *Composite Structures* 2017;180:955–71. <https://doi.org/10.1016/j.compstruct.2017.08.010>.
- [139] Nilakantan G. Virtual microstructure generation using thermal growth: Case study of a plain-weave Kevlar fabric. *Finite Elements in Analysis and Design* 2018;147:21–33. <https://doi.org/10.1016/j.finel.2018.05.002>.
- [140] Pierreux G, Van Hemelrijck D, Massart TJ. Automated generation of 3D orthogonal woven composites RVEs including yarn cross-section variations. *Composites Science and Technology* 2019;176:90–102. <https://doi.org/10.1016/j.compscitech.2019.03.023>.
- [141] Ali MA, Umer R, Khan KA, Cantwell WJ. Application of X-ray computed tomography for the virtual permeability prediction of fiber reinforcements for liquid composite molding processes: A review. *Composites Science and Technology* 2019;184:107828. <https://doi.org/10.1016/j.compscitech.2019.107828>.
- [142] Desplentere F, Lomov SV, Woerdeman DL, Verpoest I, Wevers M, Bogdanovich A. Micro-CT characterization of variability in 3D textile architecture. *Composites Science and Technology* 2005;65:1920–30. <https://doi.org/10.1016/j.compscitech.2005.04.008>.

- [143] Badel P, Vidal-Sallé E, Maire E, Boisse P. Simulation and tomography analysis of textile composite reinforcement deformation at the mesoscopic scale. *Composites Science and Technology* 2008;68:2433–40. <https://doi.org/10.1016/j.compscitech.2008.04.038>.
- [144] Naouar N, Vidal-Salle E, Schneider J, Maire E, Boisse P. 3D composite reinforcement meso F.E. analyses based on X-ray computed tomography. *Composite Structures* 2015;132:1094–104. <https://doi.org/10.1016/j.compstruct.2015.07.005>.
- [145] Naouar N, Vasiukov D, Park CH, Lomov SV, Boisse P. Meso-FE modelling of textile composites and X-ray tomography. *J Mater Sci* 2020;55:16969–89. <https://doi.org/10.1007/s10853-020-05225-x>.
- [146] Naouar N, Vidal-Sallé E, Schneider J, Maire E, Boisse P. Meso-scale FE analyses of textile composite reinforcement deformation based on X-ray computed tomography. *Composite Structures* 2014;116:165–76. <https://doi.org/10.1016/j.compstruct.2014.04.026>.
- [147] Yousaf Z, Withers PJ, Potluri P. Compaction, nesting and image based permeability analysis of multi-layer dry preforms by computed tomography (CT). *Composite Structures* 2021;263:113676. <https://doi.org/10.1016/j.compstruct.2021.113676>.
- [148] Straumit I, Lomov SV, Wevers M. Quantification of the internal structure and automatic generation of voxel models of textile composites from X-ray computed tomography data. *Composites Part A: Applied Science and Manufacturing* 2015;69:150–8. <https://doi.org/10.1016/j.compositesa.2014.11.016>.
- [149] Huang W, Causse P, Brailovski V, Hu H, Trochu F. Reconstruction of mesostructural material twin models of engineering textiles based on Micro-CT Aided Geometric Modeling. *Composites Part A: Applied Science and Manufacturing* 2019;124:105481. <https://doi.org/10.1016/j.compositesa.2019.105481>.
- [150] Wijaya W, Ali MA, Umer R, Khan KA, Kelly PA, Bickerton S. An automatic methodology to CT-scans of 2D woven textile fabrics to structured finite element and voxel meshes. *Composites Part A: Applied Science and Manufacturing* 2019;125:105561. <https://doi.org/10.1016/j.compositesa.2019.105561>.
- [151] Wijaya W, Kelly PA, Bickerton S. A novel methodology to construct periodic multi-layer 2D woven unit cells with random nesting configurations directly from  $\mu$ CT-scans. *Composites Science and Technology* 2020;193:108125. <https://doi.org/10.1016/j.compscitech.2020.108125>.
- [152] Wintiba B, Vasiukov D, Panier S, Lomov SV, Ehab Moustafa Kamel K, Massart TJ. Automated reconstruction and conformal discretization of 3D woven composite CT scans with local fiber volume fraction control. *Composite Structures* 2020;248:112438. <https://doi.org/10.1016/j.compstruct.2020.112438>.
- [153] Ricks TM, Pineda EJ, Bednarczyk BA, McCorkle LS, Miller SG, Murthy PLN, et al. Multiscale Progressive Failure Analysis of 3D Woven Composites. *Polymers* 2022;14:4340. <https://doi.org/10.3390/polym14204340>.

- [154] Boisse P, Hamila N, Vidal-Sallé E, Dumont F. Simulation of wrinkling during textile composite reinforcement forming. Influence of tensile, in-plane shear and bending stiffnesses. *Composites Science and Technology* 2011;71:683–92. <https://doi.org/10.1016/j.compscitech.2011.01.011>.
- [155] De Luycker E, Morestin F, Boisse P, Marsal D. Simulation of 3D interlock composite preforming. *Composite Structures* 2009;88:615–23. <https://doi.org/10.1016/j.compstruct.2008.06.005>.
- [156] Bassa B, Sabourin F, Brunet M. A new nine-node solid-shell finite element using complete 3D constitutive laws. *International Journal for Numerical Methods in Engineering* 2012;92:589–636. <https://doi.org/10.1002/nme.4318>.
- [157] Flores FG. Development of a non-linear triangular prism solid-shell element using ANS and EAS techniques. *Computer Methods in Applied Mechanics and Engineering* 2013;266:81–97. <https://doi.org/10.1016/j.cma.2013.07.014>.
- [158] Ko Y, Lee P-S. A 6-node triangular solid-shell element for linear and nonlinear analysis. *International Journal for Numerical Methods in Engineering* 2017;111:1203–30. <https://doi.org/10.1002/nme.5498>.
- [159] Xiong H, Guzman Maldonado E, Hamila N, Boisse P. A prismatic solid-shell finite element based on a DKT approach with efficient calculation of through the thickness deformation. *Finite Elements in Analysis and Design* 2018;151:18–33. <https://doi.org/10.1016/j.finel.2018.08.003>.
- [160] Bussetta P, Correia N. Numerical forming of continuous fibre reinforced composite material: A review. *Composites Part A: Applied Science and Manufacturing* 2018;113:12–31. <https://doi.org/10.1016/j.compositesa.2018.07.010>.
- [161] De Luycker E, Hamila N. Modeling of hyperelastic bending of fibrous media using second-gradient isogeometric analysis: Weaving and braiding applications. *Composites Part A: Applied Science and Manufacturing* 2023;167:107415. <https://doi.org/10.1016/j.compositesa.2022.107415>.
- [162] Khan MA, Mabrouki T, Vidal-Sallé E, Boisse P. Numerical and experimental analyses of woven composite reinforcement forming using a hypoelastic behaviour. Application to the double dome benchmark. *Journal of Materials Processing Technology* 2010;210:378–88. <https://doi.org/10.1016/j.jmatprotec.2009.09.027>.
- [163] Dörr D, Schirmaier FJ, Henning F, Kärger L. A viscoelastic approach for modeling bending behavior in finite element forming simulation of continuously fiber reinforced composites. *Composites Part A: Applied Science and Manufacturing* 2017;94:113–23. <https://doi.org/10.1016/j.compositesa.2016.11.027>.
- [164] Charmentant A, Orliac JG, Vidal-Sallé E, Boisse P. Hyperelastic model for large deformation analyses of 3D interlock composite preforms. *Composites Science and Technology* 2012;72:1352–60. <https://doi.org/10.1016/j.compscitech.2012.05.006>.



- [165] Pazmino J, Mathieu S, Carvelli V, Boisse P, Lomov SV. Numerical modelling of forming of a non-crimp 3D orthogonal weave E-glass composite reinforcement. *Composites Part A: Applied Science and Manufacturing* 2015;72:207–18. <https://doi.org/10.1016/j.compositesa.2015.02.013>.
- [166] Mathieu S, Hamila N, Dupé F, Descamps C, Boisse P. Stability of 3D Textile Composite Reinforcement Simulations: Solutions to Spurious Transverse Modes. *Appl Compos Mater* 2016;23:739–60. <https://doi.org/10.1007/s10443-016-9483-6>.
- [167] Yao Y, Peng X, Gong Y. Influence of tension–shear coupling on draping of plain weave fabrics. *J Mater Sci* 2019;54:6310–22. <https://doi.org/10.1007/s10853-019-03334-w>.
- [168] Madeo A, Ferretti M, dell’Isola F, Boisse P. Thick fibrous composite reinforcements behave as special second-gradient materials: three-point bending of 3D interlocks. *Z Angew Math Phys* 2015;66:2041–60. <https://doi.org/10.1007/s00033-015-0496-z>.
- [169] Barbagallo G, Madeo A, Morestin F, Boisse P. Modelling the deep drawing of a 3D woven fabric with a second gradient model. *Mathematics and Mechanics of Solids* 2017;22:2165–79. <https://doi.org/10.1177/1081286516663999>.
- [170] Cornelissen B, de Rooij MB, Rietman B, Akkerman R. Frictional behaviour of high performance fibrous tows: A contact mechanics model of tow–metal friction. *Wear* 2013;305:78–88. <https://doi.org/10.1016/j.wear.2013.05.014>.
- [171] Abteu MA, Boussu F, Bruniaux P, Loghin C, Cristian I, Chen Y, et al. Yarn degradation during weaving process and its effect on the mechanical behaviours of 3D warp interlock p-aramid fabric for industrial applications. *Journal of Industrial Textiles* 2020;152808372093728. <https://doi.org/10.1177/1528083720937288>.
- [172] Ebel C, Mierzwa A, Kind K. 13 - Yarn damage during braiding of reinforcement fibers for composites. In: Kyosev Y, editor. *Advances in Braiding Technology*, Woodhead Publishing; 2016, p. 319–54. <https://doi.org/10.1016/B978-0-08-100407-4.00013-2>.
- [173] Engelfried M, Aichele B, Middendorf P. Investigation of the Friction between Dry and Wetted Carbon Filaments. *Procedia Manufacturing* 2020;47:60–4. <https://doi.org/10.1016/j.promfg.2020.04.130>.
- [174] Roselman IC, Tabor D. The friction and wear of individual carbon fibres. *J Phys D: Appl Phys* 1977;10:1181–94. <https://doi.org/10.1088/0022-3727/10/8/018>.
- [175] Gassara HE, Barbier G, Wagner Kocher C, Sinoimeri A, Pumo B. Experimental evaluation of transverse friction between fibers. *Tribology International* 2018;119:112–22. <https://doi.org/10.1016/j.triboint.2017.10.035>.
- [176] Smerdova O, Sutcliffe MPF. Multiscale tool–fabric contact observation and analysis for composite fabric forming. *Composites Part A: Applied Science and Manufacturing* 2015;73:116–24. <https://doi.org/10.1016/j.compositesa.2015.03.009>.

- [177] Turlonias M, Bueno M-A, Jordan C, Poquillon D. Influence of Wear on the Sizing Layer and Desizing of Single Carbon Fibre-to-Fibre Friction. *Wear* 2018;402–403:64–70. <https://doi.org/10.1016/j.wear.2018.02.003>.
- [178] Gupta BS. *Friction in Textile Materials*. Elsevier; 2008.
- [179] Bowden FP, Leben L. The nature of sliding and the analysis of friction. *Proceedings of the Royal Society of London Series A Mathematical and Physical Sciences* 1939;169:371–91. <https://doi.org/10.1098/rspa.1939.0004>.
- [180] He C, Ge J, Chen Y, Lian Y. Concurrent multiscale virtual testing for 2D woven composite structures: a pathway towards composites design and structure optimization. *Composite Structures* 2022;116406. <https://doi.org/10.1016/j.compstruct.2022.116406>.
- [181] Komori T, Itoh M. A Modified Theory of Fiber Contact in General Fiber Assemblies. *Textile Research Journal* 1994;64:519–28. <https://doi.org/10.1177/004051759406400905>.
- [182] Williams J. *Contact between surfaces*. Engineering Tribology, Cambridge University Press; 2005, p. 73–131.
- [183] Johnson KL. *Contact mechanics*. Cambridge university press; 1987.
- [184] Cornelissen B, de Rooij MB, Rietman B, Akkerman R. Frictional behaviour of high performance fibrous tows: A contact mechanics model of tow–metal friction. *Wear* 2013;305:78–88. <https://doi.org/10.1016/j.wear.2013.05.014>.
- [185] Bazan P, Mierziński D, Bogucki R, Kuciel S. Bio-Based Polyethylene Composites with Natural Fiber: Mechanical, Thermal, and Ageing Properties. *Materials* 2020;13:2595. <https://doi.org/10.3390/ma13112595>.
- [186] Han L, Cai H, Chen X, Zheng C, Guo W. Study of UHMWPE Fiber Surface Modification and the Properties of UHMWPE/Epoxy Composite. *Polymers* 2020;12:521. <https://doi.org/10.3390/polym12030521>.
- [187] Kawabata S. Measurement of the Transverse Mechanical Properties of High-performance Fibres. *The Journal of The Textile Institute* 1990;81:432–47. <https://doi.org/10.1080/00405009008658721>.
- [188] Walther J, Bessette C, Decrette M, Turlonias M, Bueno M-A, Osselin J-F, et al. Yarn Damage Conditions Due to Interactions During Interlock Weaving Process: In-situ and In-lab Experiments. *Appl Compos Mater* 2022;29:245–62. <https://doi.org/10.1007/s10443-021-09950-7>.
- [189] Daelemans L, Tomme B, Caglar B, Michaud V, Van Stappen J, Cnudde V, et al. Kinematic and mechanical response of dry woven fabrics in through-thickness compression: Virtual fiber modeling with mesh overlay technique and experimental validation. *Composites Science and Technology* 2021;207:108706. <https://doi.org/10.1016/j.compscitech.2021.108706>.

- [190] Huang S, Yan L, Kasal B, Wei Y. Moisture diffusion and tensile properties of epoxy-based and polyurethane-based flax-glass hybrid FRP under hygrothermal and weathering environments. *Composites Part B: Engineering* 2023;111049. <https://doi.org/10.1016/j.compositesb.2023.111049>.
- [191] Friedrich K, Fakirov S, Zhang. Polymer composites: from nano- to macro-scale. *Choice Reviews Online* 2006;43:undefined-undefined. <https://doi.org/10.5860/choice.43-2821>.
- [192] He C, Ge J, Qi D, Gao J, Chen Y, Liang J, et al. A multiscale elasto-plastic damage model for the nonlinear behavior of 3D braided composites. *Composites Science and Technology* 2019;171:21–33. <https://doi.org/10.1016/j.compscitech.2018.12.003>.
- [193] He Y, Jiao Y, Zhou JQ, Zhang D, Lei H, Chen L. Influence of projectile physical state on ballistic energy absorption capacity of UHMWPE laminate: Experiment and simulation. *Composite Structures* 2023;326:117607. <https://doi.org/10.1016/j.compstruct.2023.117607>.
- [194] Yang Z, Jiao Y, Xie J, Jiao W, Chen L, Zhu L, et al. Effect of weaving parameters on fiber structure of 3D woven preforms: A Micro-CT investigation. *Journal of Composite Materials* 2022;56:2609–20. <https://doi.org/10.1177/00219983221101173>.
- [195] Gutkin R, Costa S, Olsson R. A physically based model for kink-band growth and longitudinal crushing of composites under 3D stress states accounting for friction. *Composites Science and Technology* 2016;135:39–45. <https://doi.org/10.1016/j.compscitech.2016.09.002>.
- [196] Wang Y, Jiao Y, Wu N, Xie J, Chen L, Wang P. An efficient virtual modeling regard to the axial tensile and transverse compressive behaviors of the twisted yarns. *Journal of Industrial Textiles* 2022;52:15280837221137353. <https://doi.org/10.1177/15280837221137353>.
- [197] Smerdova O, Benchekroun O, Brunetiere N. Transversal friction of epoxy-lubricated and dry carbon tows: From initial stages to stabilised state. *Composites Part A: Applied Science and Manufacturing* 2021;143:106263. <https://doi.org/10.1016/j.compositesa.2020.106263>.
- [198] Walther J, Turlonias M, Decrette M, Bueno M-A. Influence of multifilament yarn twist on yarn-to-yarn friction behaviour: Application to carbon fibre weaving. *Composites Part A: Applied Science and Manufacturing* 2023;174:107737. <https://doi.org/10.1016/j.compositesa.2023.107737>.
- [199] Liu Y, Ge C, Su Z, Chen Z, Gao C, Gong H, et al. Enhancing the Spun Yarn Properties by Controlling Fiber Stress Distribution in the Spinning Triangle with Rotary Heterogeneous Contact Surfaces. *Polymers* 2023;15:176. <https://doi.org/10.3390/polym15010176>.
- [200] Sohbatzadeh F, Shakerinasab E, Mirzanejhad S. Surface modification of aramid yarn by atmospheric pressure plasma: Reinforcement and floating properties. *Polymer Testing* 2023;117:107836. <https://doi.org/10.1016/j.polymertesting.2022.107836>.

- [201] Li A, Ehab Moustafa Kamel K, Wintiba B, Remmers JJC, Geers MGD, Massart TJ. A level set-based procedure for the cohesive modeling of yarn–yarn contacts in woven composite RVEs. *Composite Structures* 2023;304:116356. <https://doi.org/10.1016/j.compstruct.2022.116356>.
- [202] Bessette C, Decrette M, Turlonias M, Osselin J-F, Charleux F, Coupé D, et al. In-situ measurement of tension and contact forces for weaving process monitoring: Application to 3D interlock. *Composites Part A: Applied Science and Manufacturing* 2019;126:105604. <https://doi.org/10.1016/j.compositesa.2019.105604>.
- [203] Xiao S, Wang P, Soulat D, Minet J, Zemni L, Gao H. Analysis of the in-plane shear behaviour of non-orthogonally textile reinforcements: Application to braided fabrics. *Composites Part B: Engineering* 2018;153:159–66. <https://doi.org/10.1016/j.compositesb.2018.07.040>.
- [204] Liu Y, Xiang Z, Wu Z, Hu X. Experimental investigation of friction behaviors of glass-fiber woven fabric. *Textile Research Journal* 2023;93:18–32. <https://doi.org/10.1177/00405175221115468>.
- [205] Simon J, Comas-Cardona S, Binétruy C, Masseteau B, Hamila N. An analytical friction model for fibre tow slippage in Tailored Fibre Placement preforms based on pull-out experiments. *Composites Part B: Engineering* 2023;264:110906. <https://doi.org/10.1016/j.compositesb.2023.110906>.
- [206] Vu AN, Groupe WJB, de Rooij MB, Akkerman R. A mesoscopic model for inter-yarn friction. *Composites Part A: Applied Science and Manufacturing* 2024;180:108070. <https://doi.org/10.1016/j.compositesa.2024.108070>.
- [207] Chaouachi F, Rahali Y, Ganghoffer JF. A micromechanical model of woven structures accounting for yarn–yarn contact based on Hertz theory and energy minimization. *Composites Part B: Engineering* 2014;66:368–80. <https://doi.org/10.1016/j.compositesb.2014.05.027>.
- [208] Bai R, Ma Y, Lei Z, Feng Y, Zou J, Liu D. Shear deformation and energy absorption analysis of flexible fabric in yarn pullout test. *Composites Part A: Applied Science and Manufacturing* 2020;128:105678. <https://doi.org/10.1016/j.compositesa.2019.105678>.
- [209] Mermouli SE, Sorbo PD, Durville D, Tranquart B, Coupé D. Simulation of Frictional Contact Interactions Between Warp Yarns and Heddles Within Jacquard Harness for 3d Weaving. 14th WCCM-ECCOMAS Congress 2020 2021;1000-Manufacturing and Materials Processing. <https://doi.org/10.23967/wccm-eccomas.2020.306>.
- [210] Vu AN, Groupe WJB, Warnet LL, Akkerman R. Modeling anisotropic friction in triaxial overbraiding simulations. *Composites Part A: Applied Science and Manufacturing* 2023:107958. <https://doi.org/10.1016/j.compositesa.2023.107958>.
- [211] Brunetière N, Narayanappa KB, Smerdova O. From mixed to hydrodynamic regime in lubricated sliding of carbon fiber tows. *Composites Part A: Applied Science and Manufacturing* 2024;180:108088. <https://doi.org/10.1016/j.compositesa.2024.108088>.

- [212] Wu N, Xie X, Yang J, Feng Y, Jiao Y, Chen L, et al. Effect of normal load on the frictional and wear behaviour of carbon fiber in tow-on-tool contact during three-dimensional weaving process. *Journal of Industrial Textiles* 2020;152808372094461. <https://doi.org/10.1177/1528083720944615>.
- [213] Mertova I, Neckar B, Ishtiaque SM. New method to measure yarn crimp in woven fabric. *Textile Research Journal* 2016;86:1084–96. <https://doi.org/10.1177/0040517514551464>.
- [214] Peirce FT. 5—the geometry of cloth structure. *Journal of the Textile Institute Transactions* 1937;28:T45–96. <https://doi.org/10.1080/19447023708658809>.
- [215] Wilson SDR. Lateral spreading of fibre tows. *Journal of Engineering Mathematics* 1997:19–26. <https://doi.org/10.1023/A:1004253531061>.
- [216] Bulirsch R. Numerical calculation of elliptic integrals and elliptic functions. II. *Numer Math* 1965;7:353–4. <https://doi.org/10.1007/BF01436529>.
- [217] Carlson BC. Numerical computation of real or complex elliptic integrals. *Numer Algor* 1995;10:13–26. <https://doi.org/10.1007/BF02198293>.
- [218] Mercer EH, Makinson KR. 20—the Frictional Properties of Wool and Other Textile Fibres. *Journal of the Textile Institute Transactions* 1947;38:T227–40. <https://doi.org/10.1080/19447024708659307>.
- [219] Li J, Hamila N, L’Hostis G, Wang P. Shear deformation characteristics under tensile stress during forming of tubular braided fabrics. *Composites Part A: Applied Science and Manufacturing* 2023;167:107458. <https://doi.org/10.1016/j.compositesa.2023.107458>.
- [220] Xu Q, Xiao S, Gao H, Shen H. The propagation of fibre–matrix interface debonding during CFRP edge milling process with the multi-teeth tool: A model analysis. *Composites Part A: Applied Science and Manufacturing* 2022;160:107050. <https://doi.org/10.1016/j.compositesa.2022.107050>.
- [221] Parsons AJ, Chen S, Ryder A, Bradley D, Warrior NA, Harper LT. Thermoplastic composite injection-overmoulding with indirectly-loaded reinforcement: Design for manufacture. *Composite Structures* 2024;118056. <https://doi.org/10.1016/j.compstruct.2024.118056>.
- [222] Yamamoto G, Oshima K, Ramadhan RA, Lim T, Megra YT, Suk JW, et al. Tensile strength prediction of unidirectional polyacrylonitrile (PAN)-based carbon fiber reinforced plastic composites considering stress distribution around fiber break points. *Composites Part A: Applied Science and Manufacturing* 2024;183:108234. <https://doi.org/10.1016/j.compositesa.2024.108234>.
- [223] Xu L, Huang Y, Zhao C, Ha SK. Progressive failure prediction of woven fabric composites using a multi-scale approach. *International Journal of Damage Mechanics* 2018;27:97–119. <https://doi.org/10.1177/1056789516663613>.
- [224] Aldroubi S, Kasal B, Yan L, Bachtiar EV. Multi-scale investigation of morphological, physical and tensile properties of flax single fiber, yarn and unidirectional fabric. *Composites Part B: Engineering* 2023;259:110732. <https://doi.org/10.1016/j.compositesb.2023.110732>.

- [225] Salem MM, De Luycker E, Delbe K, Fazzini M, Ouagne P. Experimental investigation of vegetal and synthetic fabrics cohesion in order to prevent the tow sliding defect via frictional and pull-out test. *Composites Part A: Applied Science and Manufacturing* 2020;139:106083. <https://doi.org/10.1016/j.compositesa.2020.106083>.
- [226] Guo Z, Shan Z, Huang J, Wang D, Huang H, Xue D, et al. Study on friction and wear of preform Z-directional fiber. *Polymer Composites* 2022;pc.26574. <https://doi.org/10.1002/pc.26574>.
- [227] Yang Z, Shi L, Jiao Y, Xie J, Cheng X, Wu Z, et al. Numerical analysis of L-shaped wrinkling behavior of 3D woven preforms based on a novel hybrid element yarn model. *Composite Structures* 2024;340:118207. <https://doi.org/10.1016/j.compstruct.2024.118207>.
- [228] Lawrence GD, Chen S, Warrior NA, Harper LT. The influence of inter-ply friction during double-diaphragm forming of biaxial NCFs. *Composites Part A: Applied Science and Manufacturing* 2023;167:107426. <https://doi.org/10.1016/j.compositesa.2023.107426>.
- [229] Dutta A, Hagnell MK, Åkermo M. Interply friction between unidirectional carbon/epoxy prepreg plies: Influence of fibre orientation. *Composites Part A: Applied Science and Manufacturing* 2023;166:107375. <https://doi.org/10.1016/j.compositesa.2022.107375>.
- [230] Chu Y, Chen X. Finite element modelling effects of inter-yarn friction on the single-layer high-performance fabrics subject to ballistic impact. *Mechanics of Materials* 2018;126:99–110. <https://doi.org/10.1016/j.mechmat.2018.08.003>.
- [231] Das A, Choong GYH, Dillard DA, De Focatiis DSA, Bortner MJ. Characterizing friction for fiber reinforced composites manufacturing: Method development and effect of process parameters. *Composites Part B: Engineering* 2022;236:109777. <https://doi.org/10.1016/j.compositesb.2022.109777>.
- [232] He C, Ge J, Zhang B, Gao J, Zhong S, Liu WK, et al. A hierarchical multiscale model for the elastic-plastic damage behavior of 3D braided composites at high temperature. *Composites Science and Technology* 2020;196:108230. <https://doi.org/10.1016/j.compscitech.2020.108230>.
- [233] Hai L, Li J. Modeling tensile damage and fracture of quasi-brittle materials using stochastic phase-field model. *Theoretical and Applied Fracture Mechanics* 2022;118:103283. <https://doi.org/10.1016/j.tafmec.2022.103283>.
- [234] Yang Z, Jiao Y, Xie J, Chen L, Jiao W, Li X, et al. Modeling of 3D woven fibre structures by numerical simulation of the weaving process. *Composites Science and Technology* 2021;206:108679. <https://doi.org/10.1016/j.compscitech.2021.108679>.
- [235] Wang H, Shen Y, Wei J, Long Y, Zhu M, Liu J, et al. Dynamic Behavior of Twisted UHMWPE Yarns. *Composites Part A: Applied Science and Manufacturing* 2024;184:108242. <https://doi.org/10.1016/j.compositesa.2024.108242>.

[236] Wang Y, Li X, Xie J, Wu N, Jiao Y, Wang P. Numerical and Experimental Investigation on Bending Behavior for High-Performance Fiber Yarns Considering Probability Distribution of Fiber Strength. *Textiles* 2023;3:129–41. <https://doi.org/10.3390/textiles3010010>.